Author:
Marangos, Christos

Title:
Wave interaction with metamaterials and cracked ice sheets

WAVE INTERACTION WITH METAMATERIALS AND CRACKED ICE SHEETS

By

Christos Marangos

School of Mathematics
University of Bristol

A thesis submitted to the University of Bristol in accordance with the requirements for award of the degree of Doctor of Philosophy in the Faculty of Science.

September 2021

Abstract

This thesis is dichotomised into two main types of problems which are briefly introduced in Chapter 1. In the first, linear water wave theory is used to understand the interaction of small amplitude gravity waves with a particular type of submerged metamaterials in finite water depth. Within this study, metamaterials are viewed as arrays of closely-spaced thin vertical barriers protruding from the sea bed.

A summary of linear water wave theory in the framework of this study, is provided in Chapter 2, followed by the problem of scattering of obliquely-incident plane waves by a submerged metamaterial, in Chapter 3. Three different barrier orientations are analysed, whose solutions require different mathematical techniques. Whereas these all ultimately require numerical computation, simplified expressions for the reflected and transmitted wave amplitudes are derived explicitly under a shallow water assumption. The focus of this chapter relates to the unusual wave propagation properties of the plate array, particularly that of negative refraction. In Chapter 4 we consider a final example of wave interaction with an immersed plate array. The plate array is made to extend fully through the water depth and occupies periodic arrangement of triangular inclusions embedded into a wall. The inclusion of damping in a water wave setting or an analogous acoustic setting allows us to consider the broadbanded absorption characteristics of this device.

In the second part of this thesis, the scattering of incident waves by an open water lead in an otherwise infinite and thin ice sheet on water, is considered. A variety of problems, with different degree of complexity are solved with the ultimate goal being to derive a model capable of describing energy loss due to viscous effects in narrow gaps between ice floes. The scattering problem of an obliquely-incident flexural wave across a crack of finite width, is considered in Chapter 5. A much simpler closed-form solution is derived in the case when the two semi-infinite ice sheets are separated by a narrow crack. Finally, the fluid in the narrow gap between the two vertical faces of opposing ice sheets is replaced by a viscous fluid which complicates the interaction between the ice sheet and the fluid and introduces dissipation. A basic outline calculation is made to determine if this proposed model for energy dissipation fits reported field data for wave attenuation in regions of broken ice.

Acknowledgements

I extend my thanks to Professor Richard Porter for his supervision and continued help during this study and the financial support of the Engineering and Physical Sciences Research Council under the grant no. EP/N509619/1.

I am grateful to my mother for her support and guidance throughout my life. I would also like to thank everyone who made my life easier when I needed help, particularly Antonis, Evangelia and Max. Additionally, I would like to thank Christiana, Giorgos, Marina, Steven and Yiannis for their continuous emotional support while I was preparing my thesis during the Covid-19 pandemic (January 2020 until present).

Finally, this thesis owes a great deal to M for her patience, encouragement and inspiration.

Author's Declaration

I declare that the work in this dissertation was carried out in accordance with the requirements of the University's Regulations and Code of Practice for Research Degree Programmes and that it has not been submitted for any other academic award. Except where indicated by specific reference in the text, the work is the candidate's own work. Work done in collaboration with, or with the assistance of, others, is indicated as such. Any views expressed in the dissertation are those of the author.

SIGNED: Christos Marangos

DATE: 16/03/2022

Contents

List of Figures

List of Tables

Chapter 1

Introduction

In this thesis, semi-analytical methods are used to find important features of the solution to a variety of boundary-value problems arising from the application of linear water and acoustic wave theory to scattering problems.

In chapters 2 to 4, the interaction of water waves (in some cases sound waves as well) and some particular metamaterials is examined. The term metamaterial is used to describe a physical medium which propagates information in a manner not generally associated with a natural material[4][5]. One of their principal features that is responsible for these abnormal properties, is that they possess a microstructure that has some form of periodicity, with a period much smaller than the lengthscale of variations in the underlying macroscopic field variable [6][7]. This is the main metamaterial feature that allows this medium to have an effect upon the macroscale and to create unusual characteristics. These typically include a spatially varying anisotropy of a quantity which one normally associates with being isotropic. Therefore, metamaterials owe their properties to subwavelength structural details rather than to their chemical composition and their freedom of design allow us to create phenomena that are difficult or impossible to find in nature.

The science of metamaterials has developed rapidly over the last years predominantly in response to applications emerging from the study of electromagnetic waves and their manipulation. Metamaterials have led to the realisation of phenomena such as negative refraction, invisibility cloaking and sound absorption [8][9][10]. Negative refraction is a phenomenon usually related to electromagnetics, whereby the change of direction of a wave passing from one medium to another is not the

one typically observed to natural materials' refractive properties. For example, [6] maintained negative refraction by considering the scattering of a Gaussian beam by a square lattice of platonic clusters in a thin elastic plate. Also, [8] showed that using a silver slab that behaved as a metamaterial with a negative refractive index, one is able to control the wave and to focus light intensely onto some regions of an image plane via unusual routes. Some other important findings on electromagnetic invisibility cloaking, were the ones of [4] and [9], where the principal idea was to use the metamaterial to modify parameters like permittivity and permeability in such a way so as to bend waves around it, so that the metamaterial renders another object invisible to the observer. Another invisibility cloaking device was the one of [5], where a woodpile photonic crystal with a tailored polymer filling fraction was able to hide a bump in a gold reflector. Owing to the similarity between governing equations describing different physical applications, many of the techniques and results developed for electromagnetic wave scattering, have found analogues in acoustics, elasticity and, to a lesser extent, in water waves.

It is the development of metamaterials for water waves that inspire this study [11]. The physical setting for water waves differs from the other field theories previously mentioned on account that waves exist due to the action of gravity which acts in one direction (aligned with the depth) and that waves exist only due to the presence of a domain boundary (the free surface) of the background medium (the fluid). However, when the fluid is of constant depth, apart from vertical structures which have constant cross-section throughout the depth, then the depth dependence can be factorised from the field equation and the two-dimensional wave equation results. [7] exploited this and was able to adopt techniques from two-dimensional electromagnetics and acoustics to design an annular metamaterial water-wave cloak. The metamaterial structure used for the cloaking device consisted of a doubly periodic circular array of small vertical posts whose approximate effect predicted by homogenisation theory, was to produce the spatially varying anisotropic wave speeds required for a cloak. Inspired from this idea of controlling waves via a fluid bed that act as a device for producing anisotropic and spatially varying wave speeds, many other mechanisms have been proven to produce similar water wave scattering phenomena. The idea of small closely spaced cylindrical obstacles was also adopted in [12] to produce the effect of negative refraction and ultra-refraction for water waves. A numerical comparison between multipole expansions and finite element methods was made followed by an experimental verification of a flat "water lens". Notable work in this context is the one of [13] who designed a microstructured corrugated bed to act as a water-wave metamaterial and used as a means of perfectly transmitting waves through a sharp-angled junction of two-dimensional channel of uniform width.

The experimental design of the metamaterial was based on a theoretical calculation using homogenisation methods applied to a particular approximation to the water wave equations, namely shallow water theory [14][15]. However, standard shallow water theory requires that the bed gradients are continuous and vary slowly when compared to the ratio of local wavelength to depth and its use therefore appears incompatible with a corrugated bed metamaterial. In spite of this, [13] produced experimental results which matched the theoretical predictions reasonably well for reasons explained later in this thesis. Part of this success may be explained by the subsequent work of [1] who revisited the issue of the adoption of standard shallow water theory as the foundation for the realisation of a metamaterial bed. Instead, a new approach was taken involving the application of homogenisation theory to the full three-dimensional (depth-dependent) water wave equations while continuing to work under the assumptions of shallow water theory (the depth to wavelength ratio forms the small parameter used in the homogenisation methodology). The result of that model was a reduced, depth-independent, wave propagation model very much like the shallow water model but with coefficients in the diagonal depth tensor (of rank 2) which were based on a fully three-dimensional potential theory calculation. [1] showed that one of these coefficients was identical to the predictions of the earlier shallow water model of [13], whilst the other coefficient was in terms of an averaged velocity potential associated to a simple potential flow problem. As their problem was able to predict the effective depths for any spacing between the barriers that made the corrugated bed, they verified numerically that when the spacing was increasing, the effective depth tended to that of [13]. Subsequently, this new theory was adopted by [16] to determine the reflection and the transmission of obliquely-incident plane waves by a metamaterial bed of finite width. The principal new feature in this work was the derivation and application of matching conditions at the junction between a flat bed and the metamaterial. These matching conditions, which apply through the depth of the fluid, had to be applied in conjunction with the use of the depth averaged model devised by [1] and required the extension of the homogenisation theory to second order in the small parameter in order to mitigate against discontinuities in the fluid surface.

The work described in the previous paragraph assumes the small parameter (needed for the application of homogenisation methods) to be the depth to wavelength ratio and thus constrains the results for use in the shallow water regime. In this thesis, the same corrugated metamaterial bed configuration is considered, but now another small parameter (ratio of the separation between the corrugations and the wavelength) is chosen as well. Thus, a metamaterial bed with narrow fluid-filled gaps between closely spaced protrusions is envisaged, similar to the one considered

by [11]. This approach also allows homogenisation theory to simplify the effect of the microstructure, but in an arguably much more straightforward way. Thus, the region occupied by the metamaterial is governed by a reduced Laplace equation allowing us to solve the three-dimensional problem directly using standard separation of variables and mode-matching methods. The interface conditions between the fluid and the metamaterial bed are derived using the same principles used for the homogenisation in the bulk. Following [16], the scattering by a finite width of metamaterial bed is considered and also a more general configuration is allowed in which the corrugated structure forming the bed can be oriented in an arbitrary direction. This is particularly useful as it allows us to connect with the work of [11] who considered a rotated corrugation involving infinitely-thin protrusions from the flat bed which extends throughout the depth. He showed that this full-depth metamaterial could act as an all-frequency negative refraction medium for plane waves having incident angles exactly opposed to the angle of orientation of the array. Thus, one of the purposes for this work is to examine this effect when the metamaterial only partially extends throughout the depth. To complement the fully three-dimensional problem outlined above, a shallow water equation (SWE) for a corrugated bed based on the same close-spacing assumption is also derived. Unlike the earlier work, the model is derived from first principles taking into account the rapid discontinuities in depth whilst allowing for a slow variation in the vertical extent of the corrugations. Like the traditional SWE for normal isotropic depths [14][15], the equation for a corrugated bed is a reduced (or depth-averaged) model which will be shown to provide the spatially-varying anisotropy required of the metamaterial and provides a much simpler method for determining solutions to scattering problems. This gives rise to explicit solutions that can be compared with both the work of [1] and with the results of our three-dimensional approach. Numerical results are contained in Chapter 3 where one of the main tasks is to determine the conditions under which the shallow water theory can effectively be deployed by comparing the same results for full linear theory.

Metamaterials found applications into acoustics as well. For example, [17] manage to cloak an acoustic wave around an incompressible cylindrical scatterer surrounded by a cloaking shell to mimic the electromagnetic analogue of [9]. Another important effect of acoustic metamaterials is sound absorption. Such absorbers can be found in nature too. Moth wings have a membrane that forms a metamaterial, made by an intricate scale layer that acts as an ultrasound absorber. This sound absorber provides them with an acoustic camouflage against echolocating bats [18]. Also, the work of [10] showed (both theoretically and experimentally) that an ultrathin acoustic metamaterial rigid panel made of a periodic distribution of thin closed

slits whose upper wall is loaded by Helmholtz resonators, can be used for perfect and quasi-omnidirectional absorption. The resonators produce a slow sound propagation, shifting the resonance frequency of the slit to subwavelength regime and thus by controlling the geometry of the problem the viscothermal losses can be tuned in a way so that the so-called metasurface, acts as a high-efficiency absorber. This is the most common metamaterial design used for acoustic absorption – multi-coiled metasurface absorbers composed of "labyrinthine" narrow passages like the one of [19]. Similar sound absorbers found applications on noise transfer reduction through car body panels [20]. An even simpler absorber is the one used in [21] where the reflection and transmission of acoustic waves along a waveguide of uniform width, is considered. A metamaterial cavity is attached to the waveguide and is comprised of a closely spaced array of micro-channels separated by thin plates between which the field may be damped. Some results have demonstrated that this metamaterial cavity is an extremely effective broadbanded absorber for an acoustic wave.

Inspired from these problems, a similar idea will be examined in this thesis. An obliquely-incident wave will interact with a metamaterial wall made of a sequence of triangular shaped arrays similar to the one described above. Within those arrays, parallel barriers that extend throughout the vertical direction will be oriented at an arbitrary acute angle. The vertical symmetry of the geometry allows the problem to be applicable to water, acoustic and electromagnetic waves due to the similarity of the governing equations (2D Helmholtz equation). A linear damping model will be derived for the effective medium within the cavity. In the case of water waves, [22] identifies a number of ways to model the damping within a cylindrical metamaterial that extends throughout the depth. In the first, it was assumed that the fluid's surface was covered by a thin layer of a porous medium. Within the layer, the vertical velocity and the pressure gradient are related through the Darcy's Law. Then by matching pressures across the boundary of the thin layer and assuming that the vertical velocity is linearly related to the surface velocity through a blockage coefficient [23], the new linear surface condition that arises, adds a small imaginary part to the angular velocity found in the standard surface condition. The same kind of effect upon the angular velocity (found in the surface condition), happen also when the surface is covered by a doubly periodic configuration of closely spaced small cylindrical buoys that act as energy converter mechanisms [24]. Finally, the setting which is most similar to our problem is the one of [25] and [26] (Section 9, Exercise 9.2). They showed the effect of viscosity near the walls of a narrow channel due to a wave travelling within it, shifts the wavenumber by a small imaginary part.

In the case of sound waves, the derivation will start from the standard acoustic wave equations [27] and finding an expression for the tangential shearing

stress near a vertical wall by solving the Stokes boundary layer problem. Then, according to the pioneering work of [28], the tangential shearing stress expression, which is in terms of a far field velocity, can be used in the narrow duct problem (presence of two parallel walls) with the background velocity be replaced by the actual wave velocity across the duct. It will turn out that the governing equation for the velocity along the duct will coincide with the 1D Helmholtz equation but again the wavenumber will be complex valued with a small imaginary part.

By formulating the problem including the thermoviscous effects within the metamaterial, then it will allow comparisons on how the numerical results are affected even by a small damping contribution [21]. Also, it will be shown that the number and amplitudes of the reflective modes can be manipulated by changing the geometry of the structure and in some cases the metamaterial will act as an effective broadbanded absorption wall. As this problem allows an arbitrary direction of incidence and channel orientation, it will be shown that in some cases the metawall will violate the reflection law to the eyes of a far-field observer.

The second part of this thesis follows in Chapter 5 and it involves the interaction between flexural waves in thin floating ice sheets and ocean water waves. An obliquely-incident flexural wave propagates within an ice floe, in a direction towards a crack of uniform width in a sea of finite depth. The fluid within the crack interacts with the incident wave, causing scattering modes to the adjacent ice sheets.

Over the last few years, scientists want to understand the cause of energy dissipation of a flexural wave within a multi-cracked ice floe. A number of field data sets collected over several decades have all shown that the energy in waves, originating in the open seas and passing through large regions of broken ice (the Marginal Ice Zone - MIZ) are attenuated with distance [2][3][29]. There is good evidence to suggest a robust relationship between the attenuation and the wave period although the different ice conditions make the data noisy and hard to analyse. The answer to the question as to what causes this attenuation is not known.

One of the goals of this thesis is to derive a model which might be capable of reproducing this natural effect. Since the width of those cracks is typically small with respect to the thickness of the ice sheets, then the fluid in between those cracks can be assumed to be viscous. The fluid viscosity within the small crack will have an effect upon the motion of the ice floes. The existence of a viscous fluid within the small cracks is an assumption based on physical grounds as when the separation distance of the ice sheets becomes small, then the fluid within the gap is expected to have an intermediate state between liquid and solid (its density and temperature lie within the ones of water and ice). In order to arrive at the point where this problem will be presented, first a series of simpler problems will be considered.

The study of problems involving thin rigid bodies that cover a part of the sea surface, has a long history. Many authors studied the influence of a rigid dock on water waves, using a variety of solution methods. The common feature of those methods was that the velocity potential solution was assumed to possess a line source at the edge of the dock presented by a logarithmic singularity (see [30], pg.11). In the case of a semi-infinite dock, the boundary value problems yield explicit solutions. For example, [31] used the Wiener-Hopf technique to study the interaction of water waves in the free surface with a straight-edged dock in a fluid of finite depth. In the case of infinite depth [32] showed that the solution can be found using complex variable theory and a method related to Laplace transforms. In the case of a finite dock in infinite depth, the solution to the boundary value problem for the velocity potential can be reduced to an integral equation which can be solved by making an appropriate choice for the value of the potential on the dock (typically involving a Green's function). For instance, in the series of papers of [33][34], it was shown that the kernel of this integral equation of the second kind vanishes in the limit of small ratio between the wavelength and the dock width. Therefore, the solution was maintained through short-wave asymptotics to the original problem. Years later, [35] solved the finite dock problem at finite depth, using a method called residue calculus technique (RCT), which is a very useful tool to solve a linear system of equations of infinite size. This method applies only to problems of finite water depth and it works best as an approximate tool for large spacings between end points, but for small spacings you have to solve larger and larger systems of equations. However, it is the solution method of [36] that is mostly related to the solution of the finite crack (in ice sheets) problem, studied in this thesis. [36] solved the so-called finite dock problem at infinite depth by creating an integral equation maintained from the Fourier transform of the scattering part of the velocity potential. The Fourier transform method works well for small spacings as it provides explicit approximations but requires numerical solutions with larger matrix truncation sizes for larger spacings. So, this is the reason why this method is used in this thesis as the interest lies upon small gaps between ice sheets. The solution presented in Chapter 5 for the finite crack problem, is calculated by creating an integral equation whose kernel can be found by making an appropriate choice of the free surface velocity in the crack.

Now when the floating body from rigid becomes elastic, then a new boundary condition between the water and the elastic sheet must be imposed. There is a long literature for the modelling of a floating ice floe as a thin elastic plate. [37] was the first who adapted this idea to create a dispersion relation based on Euler-Bernoulli beam theory. The derivation of the linear ice-water boundary condition can be found in [38] together with the conditions on the edge of an elastic plate. [39]

adopted the Wiener-Hopf technique to examine the scattering of a water wave and a single straight-edged semi-infinite ice sheet at finite depth. The finite gap problem (two semi-infinite ice sheets at a distance) was solved again by [40] using the RCT (for finite water depth), allowing comparisons of numerical results of the problem solved in this thesis. In Chapter 5, the finite gap problem will be decomposed into symmetric and antisymmetric parts due to the geometrical symmetry of the problem and solved using Fourier sine and cosine transforms respectively. This is an idea adopted from [41] where he considered the trapping of waves by a thin floating ice sheet. The first difference between the problem solved in [41] and the one of this thesis is that the regions of open sea and ice-covered sea are inverted. The advantage of finite depth in the problem solved in this thesis is that it allows the semi-infinite integrals that are part of the solution, to be written as infinite sums through the Cauchy's residue theorem. The sum representation of the solution is much more computationally efficient than the integral representation.

When the crack between the two semi-infinite ice sheets becomes small in the sense that limit ratio between the gap and the ice thickness is infinitesimal, then the problem achieves an explicit solution. For example, [42] derived closed-form expressions for the reflection and transmission coefficients of a single small crack in the case of normal incidence at infinite depth, using a Green's function approach. The extension to oblique incidence of the same problem, can be found in [43]. In the case of finite depth, the Wiener-Hopf technique was used by [44] to extend the work of their own paper of the same year [39], for the scattering by a narrow crack, by adding another semi-infinite ice floe at an infinitesimal distance from the other. Their work was adopted from [45]. It is worth noting that the closed-form solution for the scattering coefficients of the single small crack problem at finite depth found in Chapter 5, is identical to the one of [46]. The symmetry of the geometry allowed their solution to be written as a sum of symmetric and antisymmetric solutions, which are simpler to calculate using a Green's function approach (a method much different than the one used in this thesis). However, the symmetric and antisymmetric velocity potential decomposition is an idea adopted in all the problems of Chapter 5. The explicit solutions of the scattering coefficients for the small crack problem, are calculated in the same chapter by making a single term approximation in the free surface velocity in the crack. This method will allow numerical comparisons with all the work discussed above.

Then, in order to understand how energy dissipates through a multi-cracked ice floe, a new linear surface condition is derived that describes the effect of viscous fluid within a single narrow crack, on the two adjacent ice sheets. In this derivation, the assumption of small ratio between the ice sheets gap and thickness is used,

allowing the application of lubrication theory. Similarly, to the inviscid small crack problem, a single term approximation to the fluid's velocity in the gap is used.

After maintaining the scattering coefficients for the single viscous ice crack, then the scattering coefficients for multiple cracks can be found through the scattering matrix. This is a concept that can be applied in the context of any type of waves travelling through a sequence of scatterers [47][48]. In the context of water waves travelling over a periodically rippled bed, the application of the scattering matrix can be found in [49] and [50]. Now if the scatterers are placed in an equal distance from each other, then instead of calculating the scattering matrix to the power of the number of scatterers, a simplification due to a matrix decomposition can be imposed [51]. In the context of waves in ice floes, the more recent work of [52] extends the problem of [46], from single to multiple narrow cracks, by creating a finite-dimensional linear system of equations for the jumps in the displacements and gradients across each crack, through the scattering matrix. However, the methods used in this thesis will be slightly different than the ones discussed above as they do not assume energy conservation after the interaction at each crack.

The dissipation of waves within ice floes was modelled by many authors, trying to match experimental results. For example, the scheme of [53] assumes that the cause of wave dissipation is the turbulence near the ice-water boundary which is represented by an eddy viscosity parameter. Also, [54] modelled ice as a viscoelastic layer and some years later [55] simply added a small imaginary part to the actual wavenumber, that represents the exponential decay rate of amplitude in space, i.e. $\hat{k} = k + ik_i$ where $k = 2\pi/\lambda$ (λ is the wavelength) and $k_i \ll k$. A value for k_i can be extracted from the viscoelastic layer model introduced in [54]. Neither of these models are close in predicting the relationship observed in the experimental data between the attenuation rate and the wave period. Such experimental results can be found from [2], in which buoy measurements of wave spectra were used to analyse the dissipation of wind-generated waves in pancake and frazil ice in the Arctic Ocean. The optimal k_i from the viscoelastic ice sheet model, was determined in a variety of situations to provide a match to the buoy spectrum.

Working on the assumption that attenuation is caused by a physical damping mechanism, then the possibility that this may be due to the forces that exist in the small gaps between adjacent ice floes that are typical in the MIZ, is investigated. Additionally, it is often the case that the fluid trapped in the cracks between floes is a slushy mixture of ice and water which has a higher viscosity than pure sea water. Thus, the model used in this thesis to characterise the wave dissipation in a multi-cracked ice floe, is based on the assumption that the fluid within the narrow cracks is viscous. After calculating the reflection and transmission coefficients for a single

crack, then by using the scattering matrix the multi-cracked scattering coefficients are calculated. From the result, an analogue value for k_i as specified above from [55], can be derived in terms of the single crack scattering coefficients, the incident wavenumber and the crack spacing. Therefore, numerical comparisons for k_i will be achieved with the experimental results reported in [2][3][29].

Chapter 2

Background Theory

2.1 Conservation laws for a fluid

In this section, the mass and the momentum conservation law are derived. First, a fluid of density ρ is considered to flow through an arbitrary volume V (see figure 2.1 below). Thus, the instanteneous mass of the fluid contained in V is given by

$$m(t) \equiv \int_V \rho(\mathbf{r}, t) dV, \tag{2.1.1}$$

where $\mathbf{r}$ is the integrating space variable and t is time. Now in a short time δt, the mass leaving δS (small part of the boundary of V) is $\delta m = \rho \mathbf{u} \cdot \hat{\mathbf{n}} \delta t \delta S$, where $\mathbf{u}$ is the velocity of the fluid and $\mathbf{u} \cdot \hat{\mathbf{n}}$ is the speed in the direction of $\hat{\mathbf{n}}$ (outward pointing normal to V). So, the rate of change of mass leaving V through δS is $\rho \mathbf{u} \cdot \hat{\mathbf{n}} \delta S$. Therefore, the total flux into V is

$$Q(t) \equiv -\int_S \rho \mathbf{u} \cdot \hat{\mathbf{n}} dS. \tag{2.1.2}$$

Using the fact that the fluid is neither created or destroyed in a closed system, then the rate of change of mass in V must be equal to the rate of change of mass into V through S. Or algebraically $\dot{m}(t) = Q(t)$ and so by using (2.1.1), (2.1.2), then

$$\frac{d}{dt}\int_V \rho(\mathbf{r},t)dV = -\int_S \rho\mathbf{u}\cdot\hat{\mathbf{n}}dS, \tag{2.1.3}$$

according to [56]. Using that V is fixed in space and time and by applying the

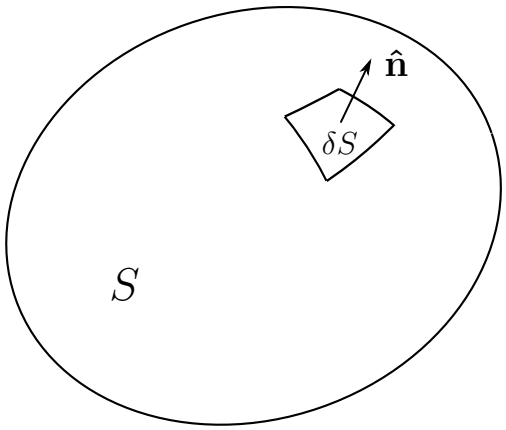

Figure 2.1: Arbitrary volume V bounded by S, with $\hat{\mathbf{n}}$ be the unit normal to the surface that points outwards of V and δS be the elemental small surface on S.

divergence theorem to the right-hand side of (2.1.3), then

$$\int_V \left(\frac{\partial\rho}{\partial t} + \nabla\cdot(\rho\mathbf{u})\right)dV = 0 \tag{2.1.4}$$

and since V was chosen arbitrarily, then the integrand of (2.1.4) must be identically equal to zero. So, the mass conservation law becomes

$$\frac{\partial\rho}{\partial t} + \nabla\cdot(\rho\mathbf{u}) = 0. \tag{2.1.5}$$

Now for the momentum conservation law, the total momentum of the fluid within V is considered, namely

$$\int_V \rho \mathbf{u} dV. \tag{2.1.6}$$

Also, in the short time δt, the momentum through δS is $\delta m\mathbf{u} = \rho\mathbf{u}(\mathbf{u}\cdot\hat{\mathbf{n}})\delta t\delta S$, according to the δm expression stated above. So, the rate of change of momentum leaving V through δS is $\rho\mathbf{u}(\mathbf{u}\cdot\hat{\mathbf{n}})\delta S$. Therefore, by applying the Newton's Law in V using (2.1.6), then

$$\frac{d}{dt}\int_V \rho u_i dV = -\int_S \rho u_i u_j \hat{n}_j dS - \int_S P_{ij}\hat{n}_j dS + \int_V f_i dV, \tag{2.1.7}$$

where $-P_{ij}$ represents the fluid stress tensor and f_i is an external force density (like the gravitational force). By using the space-time independence of the volume V and the divergence theorem on the surface integrals of (2.1.7), then

$$\int_V \frac{\partial}{\partial t}(\rho\mathbf{u})dV = -\int_V \nabla\cdot(\rho\mathbf{u}\otimes\mathbf{u})dV - \int_V \nabla\cdot\mathbf{P}dV + \int_V \mathbf{f}dV. \tag{2.1.8}$$

The first integral of the right-hand side is found by applying the divergence theorem componentwise, on the first surface integral of the right-hand side of (2.1.7). Again, since the fixed volume V was arbitrary, then

$$\frac{\partial}{\partial t}(\rho\mathbf{u}) + \nabla\cdot(\rho\mathbf{u}\otimes\mathbf{u}) + \nabla\cdot\mathbf{P} = \mathbf{f}. \tag{2.1.9}$$

Choosing $\mathbf{P} = p\mathbf{I} - \mu[\nabla\mathbf{u} + (\nabla\mathbf{u})^T] + \frac{2}{3}\mu(\nabla\cdot\mathbf{u})\mathbf{I}$ where p is the fluid's pressure, μ is the dynamic viscosity and $\mathbf{I}$ is the identity matrix, according to [27][56] and using (2.1.5), then the momentum conservation law becomes

$$\rho\frac{D\mathbf{u}}{Dt} = -\nabla p + \mathbf{f} + \mu\nabla^2\mathbf{u} + \frac{1}{3}\mu\nabla(\nabla\cdot\mathbf{u}). \tag{2.1.10}$$

2.2 Derivation of the linear water wave equations

In this section the water wave equation and the boundary conditions of an inviscid fluid of constant density ρ in a domain $\mathcal{V}$ are derived. Cartesian coordinates are chosen such that $z = 0$ coincides with the undisturbed fluid's surface. $\mathcal{V}$ is bounded above by the free surface and bounded below by a rigid, not necessarily flat bed at $z = -h(x, y)$ (see figure 2.2 below). Using that the density is constant, then from the mass conservation (2.1.5), it yields that $\nabla \cdot \mathbf{u} = 0$. Now assuming that the flow is irrotational, i.e. $\nabla \times \mathbf{u} = \mathbf{0}$, then the flow is potential or algebraically there exists a scalar function $\Phi(x, y, z, t)$ (called the velocity potential) such that $\mathbf{u} = \nabla\Phi$. From now on, instead of dealing with three unknowns to the problem (three velocity components), is much easier to solve for the velocity potential and find the velocity field through its gradient. Also $\hat{\mathbf{n}}$ is the unit normal to the bed, pointing out of the fluid and it can be related to h, via $\hat{\mathbf{n}} = -\nabla S/|\nabla S|$ with $S = z + h(x, y)$. Writing the mass conservation and the no flow condition through the bed (namely $\mathbf{u} \cdot \hat{\mathbf{n}} = 0$ at $z = -h(x, y)$) in terms of the velocity potential, then

$$\nabla^2\Phi = 0 \quad \text{in} \quad \mathcal{V}, \tag{2.2.1}$$

$$\frac{\partial\Phi}{\partial z} + \big(\nabla_h\Phi\big) \cdot \big(\nabla_h h\big) = 0 \quad \text{on} \quad z = -h, \tag{2.2.2}$$

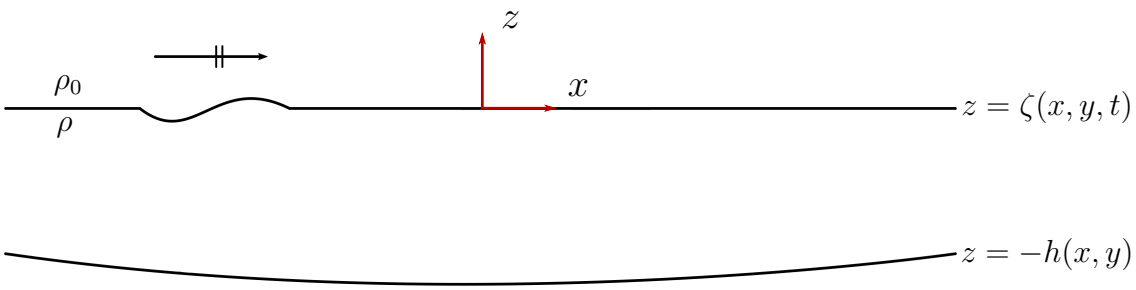

Figure 2.2: Inviscid water of constant density ρ bounded by $-h(x, y) \leq z \leq \zeta(x, y, t)$ below air of density ρ_0 (with $\rho \gg \rho_0$).

where $\nabla^2 \equiv \nabla \cdot \nabla$ is called the Laplacian operator and $\nabla_h = (\partial_x, \partial_y)$ is the two dimensional version of ∇.

So, now only the kinematic and dynamic boundary condition of the moving surface $\zeta(x, y, t)$ should be derived. There are many sources for this derivation, but the one of [26] will be followed here. By letting $S(x, y, z, t) = z - \zeta(x, y, t)$ and requiring $\frac{DS}{Dt} = 0$ on $z = \zeta(x, y, t)$, then

$$\left.\frac{\partial \Phi}{\partial z}\right|_{z=\zeta} = \frac{\partial \zeta}{\partial t} + \left.\frac{\partial \Phi}{\partial x}\right|_{z=\zeta} \frac{\partial \zeta}{\partial x} + \left.\frac{\partial \Phi}{\partial y}\right|_{z=\zeta} \frac{\partial \zeta}{\partial y}. \tag{2.2.3}$$

Now, taking the momentum conservation (2.1.10), writing it in terms of the potential through $\mathbf{u} = \nabla\Phi$, substituting $\mathbf{f} = -\rho g\hat{\mathbf{z}}$ and $\mu = 0$, then it becomes

$$\nabla\Big[\rho\frac{\partial \Phi}{\partial t} + p + \rho g z\Big] = -\rho\big(\mathbf{u}\cdot\nabla\big)\mathbf{u}. \tag{2.2.4}$$

Now, linearisation can be allowed by assuming small amplitudes and steepness to the free surface in the sense of $|\nabla\zeta| \sim U \equiv A\lambda^2/H^3 \ll 1$, where A is the local amplitude, λ is the horizontal wavelength and H is the mean depth. $U \ll 1$ is called the Ursell's number and it was proposed by [57]. One could neglect the acceleration term $\big|\big(\mathbf{u}\cdot\nabla\big)\mathbf{u}\big|$ of the right hand side based on the small wave slope assumption [26]. Thus, dividing by ρ, integrating and setting $z = \zeta$, then

$$\left.\frac{\partial \Phi}{\partial t}\right|_{z=\zeta} + \frac{p_{atm}}{\rho} + g\zeta = C(t), \tag{2.2.5}$$

where $C(t)$ is the integration constant and $p_{atm} = p(x, y, \zeta, t)$ is the atmospheric pressure. Since Φ satisfies the Laplace's equation (2.2.1), the no flow condition (2.2.2) and the kinematic surface condition (2.2.3), then if any time dependent term is added to the solution is still a solution. Thus, relabelling Φ by $\Phi - \frac{p_{atm}}{\rho}t + \int^t C(\tau)d\tau$, then equation (2.2.5) reads

$$\Phi_t + g\zeta = 0 \quad \text{on} \quad z = 0, \tag{2.2.6}$$

$$\Phi_z = \zeta_t \quad \text{on} \quad z = 0, \tag{2.2.7}$$

where the second equation is (2.2.3) but with the products of motion terms at the surface neglected (as they are assumed to be small). These two equations are the dynamic and kinematic boundary conditions on the sufrace respectively. Note that they are evaluated on $z = 0$ instead of $z = \zeta$. But these evaluations of the potential, are proven to be equal at leading order by Taylor expanding Φ_z and Φ_t about $z = 0$, evaluating them at $z = \zeta$ and neglecting products of motion terms. The last two equations can be combined into a single surface condition, by eliminating ζ. Thus, by taking a time derivative of the dynamic condition (2.2.6) and eliminating ζ_t from the kinematic condition (2.2.7), then

$$\Phi_{tt} + g\Phi_z = 0 \quad \text{on} \quad z = 0. \tag{2.2.8}$$

This well-known condition is also derived by many authors e.g. [14][15][26].

Since the equations (2.2.1), (2.2.2) and (2.2.8) satisfied by Φ are linear, then any time-solution can be inferred via inverse Fourier transforms of frequency domain solutions as

$$\Phi(x, y, z, t) = \Re\{\phi(x, y, z)e^{-i\omega t}\}, \tag{2.2.9}$$

for ω be angular frequency of a time-harmonic incident wave. So, under this substitution, the governing equation of the potential Φ gives $\cos(\omega t)\Re\{\nabla^2\phi\}+\sin(\omega t)\Im\{\nabla^2\phi\} = 0$, for any time t. Therefore, we must have $\Re\{\nabla^2\phi\}, \Im\{\nabla^2\phi\} = 0$. So, $\phi(x, y, z)$ must satisfy

$$\begin{gathered} \nabla^2\phi(x, y, z) = 0, \\ \phi_z + \big(\nabla_h\phi\big) \cdot \big(\nabla_h h\big) = 0 \quad \text{on} \quad z = -h, \\ \phi_z = K\phi \quad \text{on} \quad z = 0, \end{gathered} \tag{2.2.10}$$

where $K \equiv \omega^2/g$ and then the total wave potential in the time domain can be found from (2.2.9).

Chapter 3

Wave interaction with a submerged bottom-mounted metamaterial

3.1 Introduction

This chapter is concerned with the scattering of linear water waves by a certain type of a submerged microstructure in finite depth. Problems involving the control of water waves through microstructures sitting in the fluid's bed have a recent history [11][13][58]. The microscale possessed by the submerged structure has an effect upon the macroscale (incident wave). This is the underlying feature of those structures, often called metamaterials as they typically affect the waves in ways not necessarily associated with natural (isotropic) materials. Often the metamaterial can be proven to act as an effective medium by using homogenisation methods with the small parameter frequently associated with the ratio of the structural periodicity and the incident wavelength. The validity of this approximation (homogenisation theory) was tested against exact results [16][22].

Typically, the submerged structure looks like a doubly periodic array of closely spaced vertical posts or barriers. If the long-wave limit (or equivalently the shallow water regime) is assumed, then the model can be simplified and a closed-form solution can be calculated. The simplified formula for the solution can be manip-

ulated accordingly through the other variables such as structural lengths, incident frequency and direction. For example, [59] have considered a periodic array of vertical cylinders placed on the fluid's bed. It was shown that in the long-wave limit, the structure gave rise to an effective depth and an effective gravitational constant that depended on the filling ratio of the cylinders, leading to wave focusing phenomena. [60] achieved surface wave focusing in a channel by adopting an idea from the focusing lens in electromagnetics and acoustics, called the gradient index lens (GRIN) which can be achieved by a periodic array of vertical cylinders at the sea bed where the filling fraction was gradually modified. Also, [61] investigated both numerically and experimentally, the effect of an "invisibility carpet" made of vertical poles of trapezoidal cross-section on an incident water wave travelling parallel to a channel with a curved wall at the end. They achieved the so-called wave cloaking in the channel as in the absence of the "invisibility carpet" the scattered wave would be a "rippled" wave due to the curved wall. However, through a choice of geometrical parameters of the carpet, the response wave was manipulated in a way as if the end wall was flat (cloaking). Recently, [62] used a network of narrow water channels which were coupled at junctions to create a medium supporting wave propagation with metamaterial qualities. Their metamaterial can be thought of as vertical posts which occupy a large fraction of the available domain leaving small channels. It turned out that the metamaterial was acting as a negative refraction medium for small oblique angles.

In this chapter, an attempt of creating similar phenomena through metamaterials of similar type in deep water, will be made. For example, it will be shown later that negative refraction can be achieved for all oblique angles (not just small), when the effective medium was made by closely spaced thick barriers perpendicular to the bed. This is expected on physical grounds, as the fluid motion within closely spaced plates is restricted at a greater degree than in medium of closely spaced vertical posts, because of less openings. Therefore, such metamaterials (vertical plates) achieve the behaviour of a negative refraction medium much easier.

The main purpose of the problems solved in this section, is to what extent a plate array which extends partially through the depth is able to reproduce the negative refraction results shown by [11] whose metamaterial plate array extended uniformly through the depth. An example of a such remarkable result produced by the author was that for certain angles of incidence there was all-frequency perfect transmission with negative refraction. However, the only literature that deals with metamaterials formed by submerged barriers are only under the shallow water regime. For example, [13] have considered the submerged layered structure made of vertical barriers in shallow water, to bend an incident water wave in a waveguide and align it

with the bending angle of the channel. The idea behind the modelling of the effective medium, was to use homogenisation theory on the standard shallow water equation to derive a new equation where the scalar depth was replaced by a diagonal 2×2 tensor (of rank 2) with entries the effective depths of a wave travelling in directions parallel and perpendicular to the barriers. Then [1], used homogenisation theory but now starting from the full linear potential problem and managed to derive the same effective depth tensor equation in shallow water, at leading order. However, one of the diagonal elements of the depth tensor was found to be different than the one of [13]. It turned out that this element was in terms of an integral over the "unit cell" (due to the structural periodicity) of a velocity potential associated to a simple potential flow problem. Two years later, [16] used a similar homogenisation theory to derive the matching conditions across the metamaterial interfaces to higher order of the small parameter associated with the ratio between the structural periodicity and the incident wavelength. The new matching conditions at the metamaterial boundaries were derived by accessing inner and outer asymptotic expansions near the vertical interface of the effective medium. This idea was also adopted in [63] and in [64] (leading and second order respectively) to derive continuity relations for similar type of metamaterials but in the context of electromagnetics.

However, this section starts by considering the full linear potential problem for the scattering of surface waves by a layered medium of arbitrarily oriented thick vertical barriers that cover a region of the fluid. An effective medium equation arises by applying a perturbation theory using a small parameter (structural periodicity to wavelength ratio). The derivation of the effective equation satisfied by the velocity potential and the matching conditions through the metamaterial interfaces, is based on the work of [11], where the barriers had zero thickness and they extended throughout the depth. The effective conditions will correspond to the continuity of pressure and normal flux on the effective medium boundaries. Using the fact that the structure extends uniformly in one direction and that the only "forcing" to the problem is a time-harmonic obliquely-incident wave that propagates from the far-field, then the time and the space dimension, which is aligned with the extension of the structure, can be factored out of the problem, in the same manner as the incident wave. Then after applying the far-field conditions, the procedure follows by calculating vertical eigenfunctions over the open-sea and metamaterial regions which can be sought through separation of variables and roots of certain dispersion relations coming from the boundary conditions in the vertical direction. Then it remains to apply the matching conditions on the vertical interfaces of the submerged structure. This matching procedure needs different approaches depending on the orientation of the barriers. Three cases for different barrier orientations will be considered later in

this section.

Cartesian coordinates are chosen such that $z = 0$ is aligned with the undisturbed free surface of the sea. The metamaterial sits on the flat sea bed $z = -h$ and cover the region $|x| < b$, $-\infty < y < \infty$ and $z \in [-h, -d]$ (where $d > 0$ is a constant). The structure will consist of parallel closely spaced barriers of length $2L$ and of thickness θl, where l is the periodicity of the structure in the direction perpendicular to the barriers and $\theta \in [0, 1)$ is a dimensionless parameter which describes the filling fraction. Thus, $(1 - \theta)l$ is the spacing between the walls with the gaps closing when $\theta \to 1$ and the barriers become infinitely thin when $\theta \to 0$. The barriers will be perpendicular to the sea bed and oriented at some angle $\delta \in [0°, 90°]$ with the positive x-axis. Since those barriers will not extend throughout the depth then there will be no uniformity in depth that typically simplify the problem into 2D (as in [11]). A tilted two-dimensional coordinate system (X, Y) is employed in the metamaterial region and it can be maintained by rotating counterclockwise the Cartesian coordinates (x, y), such that X is aligned with the barrier orientation and Y is perpendicular to the barriers.

An incident water wave of wavenumber k and angular frequency ω propagates from $x \ll -b$, in a direction $\theta_0 \in (-90°, 90°)$ with the positive x-axis and interacts with the submerged structure and causes some reflection and transmission to the problem.

Solutions to the full microstructured problem within the metamaterial region, can be calculated using Bloch-Floquet theory to the problem involving an infinite periodic medium, to find the velocity potential everywhere in terms of the value it takes in a fundamental cell of the array. One can then derive an integral equation over the barrier within that cell whose solution can be numerically calculated. Evidently this is a complicated approach [65].

Alternatively, using the periodicity of the structure and the underlying assumption that the separation between barriers is small both with respect to the wavelength and the plate length ($kl \ll 1$, $l/L \ll 1$), then the region within the metamaterial can be replaced by an effective medium in which the wave field will satisfy a homogenised equation. A more general derivation of the one of [11] will follow. Due to the generality that comes from the barrier thickness and height, new matching conditions through the $x = \pm b$ and $z = -d$ metamaterial interfaces, must be taken into account.

Three different problems will be analysed into this chapter, each one solved with a different method. The geometry of those problems differ just by the orientation of the barriers, i.e. $\delta = 0°$, $\delta = 90°$ and $\delta \in (0°, 90°)$. One would question the necessity of the first two problems as they can be covered in the general case of

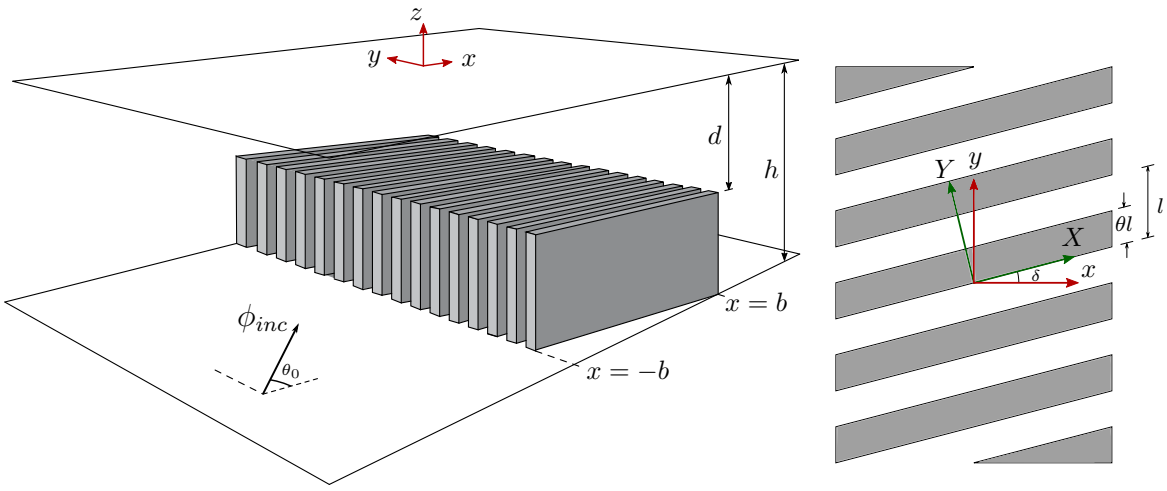

Figure 3.1: Geometry of the submerged metamaterial made of tilted thick barriers. The incident direction θ_0 and the barrier orientation δ are measured counterclockwise from the positive x-axis. In the figure on the left, a negative value of δ was chosen and on the right a positive one.

$\delta \in [0°, 90°]$. The issue with starting directly from an angle $\delta \in (0°, 90°)$, is that the matching conditions of the wave across the top interface of the metamaterial, will produce a dispersion relation whose roots (that give important information about the waves within $|x| < b$) lie on the complex plane but off the real and imaginary axes. Therefore, the 2D Newton's method will be used, which is applicable to functions of two variables, like $f(x+iy)$ for real x, y (see equation (3.2.73)). This method requires initial guesses for each root position which must be relatively close to the roots. But there will be no way to make a good initial guess for the approximated position of each root of the complicated dispersion relation. However, when δ is 0° or 90°, those roots lie on the axes and they can be captured very efficiently using the bisection method on small intervals of those axes (which is applicable on 1D functions like $f(x)$ or $f(iy)$ with real x, y). Thus, if the dispersion roots for an acute δ are required, the numerical code will first capture the $\delta = 0°$ roots and then by shifting δ from 0° to the desired angle in small intervals, it will use 2D Newton's method in each step, with initial guesses the roots of the previous δ-iteration. Without loss of generality, one could capture the $\delta = 90°$ roots first, and then shift δ at small intervals from 90° down to the required angle. The difference is that the dispersion relation in the initial case of $\delta = 90°$ has a simpler form and its roots can be captured easier as

they lie in certain known intervals. Also, it is worth noting that when the barriers are aligned with the y-axis ($\delta = 90°$) a different approach is taken into account when it comes to the wave matching across $x = \pm b$, compared to the other orientations. This method involves solutions to integral equations using variational principles and the Galerkin method [66]. In that case ($\delta = 90°$), when the incident wave arrives at the first barrier at $x = -b$, it would "feel" a rigid step. Such problems are solved using the Galerkin method and this is the technique that will be adopted in that case.

Then, the same problem will be solved in the shallow water regime allowing comparisons with the literature discussed in the beginning of this section (barrier metamaterial in the shallow water regime). The simplification that typically occurs under the shallow water assumption (equation becoming independent of the vertical coordinate), allows us to make the generality of spatially varying metamaterial interfaces. Starting from first principles of the 3D problem, a coordinate transformation will be followed such that the coordinate in the direction perpendicular to the barriers consists of a macroscale and a microscale (due to the local effects of the closely spaced barriers that might occur). Then a mixed perturbation analysis over three small parameters will be carried out - water shallowness, barrier spacing to wavelength ratio and surface amplitude to depth ratio. The first two will be coupled together through some particular relation so that the barrier separation is much smaller than the depth. It will turn out that at leading order the result will be the standard shallow water equation (over a slowly varying depth), but now the depth will be replaced by a diagonal 2×2 tensor (of rank 2) with elements the effective depths for waves travelling parallel and perpendicular to the barriers. This is a typical result according to the literature, but the two diagonal elements differ from the ones of [1][13][16]. One reason for that is because the theory used in this thesis is based on the assumption of closely spaced barriers. Further differences and numerical comparisons will be discussed later through the chapter.

Then, using as starting point the fact that the depth in the shallow water equation becomes a diagonal tensor in the presence of a metamaterial, some new effective depths in the directions parallel and perpendicular to the barriers are derived starting from 3D linear theory. This is a different approach than the model derived from first principles. It turns out that the effective depth in the direction perpendicular to the barriers is the same as the one of the derived model described in the previous paragraph. However, the effective depth in the direction parallel to the barriers will be slightly different than the one before. Algebraic and numerical comparisons between the two models will be discussed later.

3.2 Scattering problems using full linear theory

3.2.1 Effective medium equations

In this section, the wave governing equation describing the metamaterial medium will be derived. Also, the matching conditions of the wave across any interface of the metamaterial will be employed. This is similar to the work of [11] but the barriers now cover a portion of the fluid's depth and a non-zero barrier thickness fraction θ is allowed.

To derive the effective equation within the medium shown in figure 3.1, we consider the region far enough from the metamaterial boundaries so that we can assume there is no influence from the edges. The tilted orthogonal coordinates (X, Y) are employed within the structure, such that X is aligned with the barrier orientation and they are related to (x, y) via

$$\begin{pmatrix} X \\ Y \end{pmatrix} = \begin{pmatrix} \cos\delta & \sin\delta \\ -\sin\delta & \cos\delta \end{pmatrix} \begin{pmatrix} x \\ y \end{pmatrix}. \tag{3.2.1}$$

Therefore under this coordinate transformation, the Laplace equation and the no flow condition through the flat bed found in (2.2.10) to be satisfied by the time-independent potential, become

$$\begin{gathered} \Big(\partial_{XX} + \partial_{YY} + \partial_{zz}\Big)\phi(X, Y, z) = 0, \\ \phi_Y = 0 \ \text{ on } \ Y - Y_n = l\theta, \ -L < X - (l\theta + Y_n)\tan\delta < L, \ z \in (-h, -d), \\ \text{and on } \ Y - Y_n = l, \ -L < X - (l + Y_n)\tan\delta < L, \ z \in (-h, -d), \\ \phi_z = 0 \ \text{ on } \ z = -h, \end{gathered} \tag{3.2.2}$$

where now the depth at $z = -h$ is assumed to be constant, with $L = b\text{sec}\delta$ and $Y_n = nl$, for $n \in \mathbb{Z}$, where n stands for the n^{th} channel. The remaining equations represent the no flow through the vertical faces of the barriers and the sea bed. Letting $\epsilon = l/L \ll 1$ with $kL \sim \mathcal{O}(1)$ (so that $kl = \epsilon kL \sim \mathcal{O}(\epsilon) \ll 1$), then under the transformation $X = Y_n \tan\delta + LX'$, $Y = Y_n + lY'$ and $z = Lz'$, equation (3.2.2)

becomes

$$\begin{gathered}\Big(\epsilon^2\partial_{X'X'}+\partial_{Y'Y'}+\epsilon^2\partial_{z'z'}\Big)\phi_n=0,\\ \partial_{Y'}\phi_n=0 \text{ on } \ Y'=\theta,\ -1<X'-\epsilon\theta\tan\delta<1,\ z'\in(-h',-d'),\\ \text{and on } Y'=1,\ -1<X'-\epsilon\tan\delta<1,\ z'\in(-h',-d'),\\ \partial_{z'}\phi_n=0 \ \text{ on } \ z'=-h',\end{gathered} \tag{3.2.3}$$

where $(h,d)=L(h',d')$ and $\phi(X,Y,z)=\phi_n(X',Y',z')$ is the potential in the n^{th} channel. In the second equation above (no flow through the vertical faces of the barriers), ϵ can be neglected from the range of X'. Thus, since there are only even powers of ϵ in (3.2.3) after this assumption, then by expanding the potential $\phi_n\approx\phi_n^{(0)}+\epsilon^2\phi_n^{(1)}$, the leading order $\mathcal{O}(\epsilon^0)$ gives

$$\phi_n^{(0)}\equiv\phi_n^{(0)}(X',z') \ \text{ with } \ \partial_{z'}\phi_n^{(0)}=0 \ \text{ at } \ z'=-h'. \tag{3.2.4}$$

This is a standard result in multiscale asymptotic expansions - the leading order terms are typically independent of the microscale Y [67]. Proceeding to the next order $\mathcal{O}(\epsilon^2)$ of (3.2.3), the following yields

$$\partial_{Y'Y'}\phi_n^{(1)}+\Big(\partial_{X'X'}+\partial_{z'z'}\Big)\phi_n^{(0)}=0 \ \text{ with } \ \partial_{Y'}\phi_n^{(1)}=0 \ \text{ on } \ Y'=\theta,\ 1. \tag{3.2.5}$$

Integrating the latter result in $\theta<Y'<1$ and using the boundary condition of $\phi_n^{(1)}$ on $Y'=\theta$, 1, then

$$\Big(\partial_{X'X'}+\partial_{z'z'}\Big)\phi_n^{(0)}(X',z')=0 \ \text{ with } \ \partial_{z'}\phi_n^{(0)}=0 \ \text{ at } \ z'=-h', \tag{3.2.6}$$

which is what was expected on physical grounds - the waves at leading order (neglecting $\mathcal{O}(\epsilon^2)$) are confined to propagate only in the direction parallel to the barriers and the amplitudes in different channels are independent. [11] assumed that these independent amplitudes (call them C_n), can be represented as discrete evaluations of

continuous functions of the macroscale coordinate (replace C_n by $C(Y_n)$ where $C(Y)$ is continuous). This approximation was justified by [22] when comparing the solution of the continuum model with the exact solution (using boundary element method). This means writing $C_n = C(Y_n)$ and consequently when $d > 0$ (barriers covering a portion of the fluid's depth) then $C(Y_n) = C(Y)$ by assuming that the smoothness of the wave field just above the structure forces the smoothness of the "field" within the homogeneous effective medium. Then, by writing $\phi_n^{(0)} \approx \phi_n$ (to leading order) in (3.2.6), going back to (X, Y, z) coordinates and using the assumption on the amplitude's Y-variation described above, then the homogeneous equation in the effective medium becomes

$$\Big(\partial_{XX} + \partial_{zz}\Big)\phi(X, Y, z) = 0. \tag{3.2.7}$$

Now we have to deal with the matching conditions across the metamaterial interfaces. In [11] (same problem but for thin plates that extend throughout the depth), it was shown that the leading order (in the small parameter) conditions, matching solutions inside the plate array to the domain outside was the local matching of pressure and flux i.e. $\phi(-b^-, y, z) = \phi_n(-L^+, Y, z)$ and $\phi_x(-b^-, y, z) = \cos\delta\partial_X\phi_n(-L^+, Y, z)$, where ϕ_n is the potential inside the n^{th} channel (expressed in the coordinate system of figure 3.1 and in the language used in this section). These conditions were derived by solving for the potential in two regions - in the thin rectangular strip parallel to the barriers within a single channel and the thin rectangular strip parallel to the x-axis that is attached to the channel opening (Bloch-Floquet theory was used for the potential across the two long sides of the strip). Then, using the equations satisfied by the potential within the triangular region that connect those strips and application of the Green's identity, the potential and normal mass flux matching specified before, were derived. Finally, since the metamaterial occupies a homogeneous medium, then these matching conditions can be assumed that they can be imposed continuously throughout the interface (not only at a single channel opening).

Now since in our case a barrier thickness is included, then a factor of $(1-\theta)$ must be introduced to the flux within the narrow channel. Therefore, starting from the top horizontal interface, by concentrating only in the "unit cell" again, it can be seen that the fluxes just outside and inside are $l\phi_z$ and $l(1-\theta)\phi_z$ to leading order respectively. Now applying the same idea onto the vertical interfaces at $x = \pm b$, the barrier orientation must be taken into account. Thus, the fluxes just outside and inside those interfaces are $l\text{sec}\delta\phi_x$ and $l(1-\theta)\phi_X$ respectively. Thus, the matching

conditions will be

$$\begin{aligned}
\phi\big|_{z=-d^+} = \phi\big|_{z=-d^-} \quad \text{and} \quad \phi_z\big|_{z=-d^+} = (1-\theta)\phi_z\big|_{z=-d^-} \quad \text{in} \quad |x| < b, \\
\phi\big|_{x=\pm b^\pm} = \phi\big|_{x=\pm b^\mp} \quad \text{in} \quad z \in (-h, 0), \\
\phi_x\big|_{x=\pm b^\pm} = \begin{cases} \phi_x\big|_{x=\pm b^\mp}, & z \in (-d, 0), \\ (1-\theta)\cos\delta\phi_X\big|_{x=\pm b^\mp}, & z \in (-h, -d), \end{cases}
\end{aligned} \tag{3.2.8}$$

using the same idea used in [11] - extending the condition throughout the homogenised medium. A formal derivation of these matching conditions in the shallow water regime, using matched asymptotic expansions will follow in section 3.3.

Problems of this type, can be simplified even further. Although these problems are 3D due to vertical non-uniformity in the presence of the metamaterial, the y coordinate dependence can be factored out under some reasonable assumptions. The model in the regions outside the submerged structure, can be simplified using that the y variation of the incident wave can be separated from the propagating field (factored out) due to the constant cross-sections in the y direction within those regions. Therefore since the incident wave that propagates from $x \ll -b$ towards the structure is of the form of $\phi_{inc}(x, y, z) = e^{i\beta x}e^{i\alpha y}\psi_0(z)$, with $\beta = k\cos\theta_0$, $\alpha = k\sin\theta_0$ and $\psi_0(z)$ (specified later) that satisfies the surface condition $\psi_0'(0) = K\psi_0(0)$ and the flat-bed condition $\psi_0'(-h) = 0$ coming from (2.2.10), then the whole response field can be assumed to have its y variation separated through $e^{i\alpha y}$ as the incident wave drives the total motion of the scattering field. Now since within the metamaterial structure the wave field was shown to satisfy a homogeneous effective equation, then the cross-section in the y direction is assumed to be constant again. Therefore the y variation of the field within that region can be assumed to be also $e^{i\alpha y}$, to be compatible with the forcing of the incident wave outside that region. That is to say that the total wave field is compatible with the variation in y of the incident wave. Thus, in the simplification of (2.2.9), y can be dropped as well by arguing that $\phi(x, y, z)$ can be replaced by $e^{i\alpha y}\phi(x, z)$. Therefore, the analogue of (2.2.10) in the y-independent domain is

$$\begin{aligned}
(\nabla^2 - \alpha^2)\phi(x, z) = 0, \\
\phi_z = 0 \quad \text{on} \quad z = -h, \\
\phi_z = K\phi \quad \text{on} \quad z = 0,
\end{aligned} \tag{3.2.9}$$

which can be applied to the problem involving any barrier orientation (the invariance of the geometry in the y direction holds for any δ).

Also, the problem must be supplied with a far field-condition. Using the idea of single scattered wave in $x < -b$ and $x > b$, described above, then

$$\phi(x,z) \sim \begin{cases} \phi_{inc}(x,z) + R\phi_{inc}(-x,z), & x \to -\infty, \\ T\phi_{inc}(x,z), & x \to \infty, \end{cases} \tag{3.2.10}$$

where now $\phi_{inc}(x,z) = e^{i\beta x}\psi_0(z)$ and R, T are the reflection and transmission coefficients which they satisfy $|R|^2 + |T|^2 = 1$ (conservation of energy).

3.2.2 Barriers normal to the side interfaces

By inspection of figure 3.1, one could see that when $\delta = 0^\circ$ and $\delta = 90^\circ$ the geometry of the problem becomes symmetric about the yz-plane. Therefore problems with such symmetric structural geometries, like the one solved in this section ($\delta = 0^\circ$), can be decomposed into two easier problems to solve [68][69]. First, we define the following velocity potentials as

$$\phi^s(x,z) = \phi(x,z) + \phi(-x,z), \quad \phi^a(x,z) = \phi(x,z) - \phi(-x,z), \tag{3.2.11}$$

where the superscripts s, a stand for the symmetric and antisymmetric potential. It follows that $\phi^{s,a}$ satisfy the same governing equations and boundary conditions as the actual potential ϕ. This was expected as the geometry is symmetric about $x = 0$. Further, it can be easily shown that

$$\phi^s(x,z) = \phi^s(-x,z), \quad \phi^a(x,z) = -\phi^a(-x,z), \tag{3.2.12}$$

which implies that ϕ^s is even and ϕ^a is odd. Also since ϕ and ϕ_x are assumed to be continuous at $x = 0$, it follows that

$$\phi^s_x(0,z) = 0, \quad \phi^a(0,z) = 0. \tag{3.2.13}$$

It is therefore sufficient to consider the problems for $\phi^{s,a}$ only in $x > 0$ (or $x < 0$) supplemented by (3.2.13). Also (3.2.11), implies that

$$\phi(x,z) = \frac{1}{2}\Big[\phi^s(x,z) + \phi^a(x,z)\Big], \quad \phi(-x,z) = \frac{1}{2}\Big[\phi^s(x,z) - \phi^a(x,z)\Big], \tag{3.2.14}$$

which provides the total potential in $x > 0$ and $x < 0$ respectively, in terms of $\phi^{s,a}$ only in $x > 0$ (or $x < 0$).

Therefore, back to the scattering problem when the barriers are aligned the x-axis ($\delta = 0°$), then the four equations of (3.2.8) will give us the coupled system of equations for the four sets of unknowns - two sets of Fourier coefficients in $|x| < b$ and one set for each scattered wave (reflection and transmission). This will be very complicated to solve. Instead, by the yz-plane symmetry of the problem, the potential can be decomposed into symmetric and antisymmetric problems (even and odd functions in x) and be solved only in the semi-infinite domain $x < 0$. Thus, the two problems in the semi-infinite domain $x < 0$, translate to

$$\begin{gathered}(\nabla^2 - \alpha^2)\phi^{s,a}(x,z) = 0, \quad \phi^{s,a}_z(x,-h) = 0, \quad \phi^{s,a}_z(x,0) = K\phi^{s,a}(x,0), \\ \phi^{s,a}(x,z) \sim \phi^{s,a}_{inc}(x,z) + R^{s,a}\phi^{s,a}_{inc}(-x,z) \quad \text{as} \quad x \to -\infty,\end{gathered} \tag{3.2.15}$$

for the region outside the metamaterial, with $\phi^{s,a}_{inc}(x,z) = \phi_{inc}(x,z)$ (the factor of $1/2$ can be neglected without the loss of generality as the governing equation and its boundary conditions are linear). This decomposition would not be possible if the geometry was not symmetric. This is because according to the decomposition of the potential, the boundary conditions in $x > 0$ and $x < 0$ must be the same in order to be satisfied by $\phi(x,z)$ and $\phi(-x,z)$ simultaneously. The differential equation and boundary conditions satisfied by ϕ, will be the same for $\phi^{s,a}$ most of the times since all the x-derivatives are typically of even order (zeroth, second or sometimes fourth order) and so $\phi(\pm x, z)$ remains invariant under those operators. Note that in the semi-infinite problems there are only reflection coefficients (R^s and R^a) which according to (3.2.10) are related to the original scattering coefficients by

$$R = \frac{R^s + R^a}{2}, \quad T = \frac{R^s - R^a}{2}, \tag{3.2.16}$$

by carrying out a simple algebra.

The effective medium equation within the metamaterial, specified in (3.2.7), becomes

$$\Big(\partial_{xx}+\partial_{zz}\Big)\phi^{s,a}(x,z)=0, \tag{3.2.17}$$

by going back to Cartesian coordinates, dropping y-dependence through $e^{i\alpha y}$ and substituting $\delta=0^\circ$. The corresponding matching conditions across the interfaces from (3.2.8), are

$$\begin{gathered}\phi^{s,a}\big|_{z=-d^+}=\phi^{s,a}\big|_{z=-d^-}\ \text{and}\ \phi^{s,a}_z\big|_{z=-d^+}=(1-\theta)\phi^{s,a}_z\big|_{z=-d^-}\ \text{in}\ |x|<b,\\ \phi^{s,a}\big|_{x=\pm b^\pm}=\phi^{s,a}\big|_{x=\pm b^\mp}\quad\text{in}\quad z\in(-h,0),\\ \phi^{s,a}_x\big|_{x=\pm b^\pm}=\begin{cases}\phi^{s,a}_x\big|_{x=\pm b^\mp}, & z\in(-d,0),\\ (1-\theta)\phi^{s,a}_x\big|_{x=\pm b^\mp}, & z\in(-h,-d).\end{cases}\end{gathered} \tag{3.2.18}$$

The two semi-infinite boundary-value problems, are now supplied with all the information needed from equations (3.2.15) to (3.2.18). The total wave in $x<-b$ is comprised of the incident and response wave. The incident wave $\phi^{s,a}_{inc}(x,z)=e^{i\beta x}\psi_0(z)$ satisfies all the equalities of (3.2.15) and the response wave can be found by separating variables in the reduced Laplace equation. Thus,

$$-\frac{Z^{s,a}(z)''}{Z^{s,a}(z)}=-\kappa^2\quad\text{with}\quad Z^{s,a}(-h)'=0\quad\text{and}\quad Z^{s,a}(0)'=KZ^{s,a}(0), \tag{3.2.19}$$

$$\frac{X^{s,a}(x)''-\alpha^2X^{s,a}(x)}{X^{s,a}(x)}=-\kappa^2\quad\text{with}\quad X^{s,a}(x)\sim R^{s,a}e^{-i\beta x}\quad\text{as}\quad x\to-\infty, \tag{3.2.20}$$

where $-\kappa^2$ is the separation constant. Solving (3.2.19) and applying the boundary condition on the sea bed, then the z variation of the response wave is $Z^{s,a}(z)=A^{s,a}\cosh[\kappa(z+h)]$. The unknown κ can be found by the surface condition to satisfy $\kappa\tanh(\kappa h)=K$ (water wave dispersion relation). The only real solutions to this dispersion relation are $\pm k$ and the infinite non-real solutions lie on the imaginary axis (symmetric about zero as the relation is even). Those roots may be called $\pm k_n$ for $n\in\mathbb{N}_0$, where $k_0=k$ and $k_n=i\xi_n$ with $\xi_n\in\mathbb{R}_{>0}$, for all $n\in\mathbb{N}$. In this thesis, the set of natural numbers $\mathbb{N}$ is defined to be $\{1,2,3,...\}$, i.e. excluding zero and thus

$\mathbb{N}_0 \equiv \mathbb{N} \cup \{0\}$. The non-existence of complex roots is a well-known result [70][71]. Solving the differential equation in (3.2.20), with κ replaced by k_n, then

$$X_n^{s,a}(x) = a_n^{s,a} e^{-i\gamma_n x} + b_n^{s,a} e^{i\gamma_n x} \quad \text{for} \quad \gamma_n = \sqrt{k_n^2 - \alpha^2}, \tag{3.2.21}$$

where it can be verified that $\gamma_0 = \beta$ and $\gamma_n = i\sqrt{\xi_n^2 + \alpha^2}$ for $n \in \mathbb{N}$. Since the response wave must travel only in the negative x direction and must be bounded as $x \to -\infty$, then $b_n^{s,a} = 0$ for all $n \in \mathbb{N}_0$. Combining the information given in the last three equations, then the total wave potential in $x < -b$, will be

$$\begin{gathered} \phi^{s,a}(x,z) = e^{i\beta x}\psi_0(z) + \sum_{n=0}^{\infty} a_n^{s,a} e^{\beta_n(x+b)}\psi_n(z), \\ \psi_n(z) = N_n^{-1/2}\cosh[k_n(z+h)], \\ \text{with } N_n = \frac{1}{2} + \frac{\sinh(2k_n h)}{4k_n h},\ \beta_n = \sqrt{\xi_n^2 + \alpha^2}, \end{gathered} \tag{3.2.22}$$

where $a_n^{s,a}$ was rescaled by $e^{\beta_n b}$ for numerical purposes, $\beta_0 = -i\beta$, $a_0^{s,a} = R^{s,a}e^{i\beta b}$ and $N_n^{-1/2}$ (the normalised factor of the orthogonal eigenfunctions $\psi_n \in \mathbb{R}$), was chosen that way so that

$$\int_{-h}^{0} \psi_n(z)\psi_m(z)dz = h\delta_{nm}, \tag{3.2.23}$$

where δ_{nm} is the Kronecker delta function that takes the value of 1 if $n = m$ and 0 otherwise. This is a standard representation for the depth eigenfunctions over a constant bed [26]. Problems of this type that are supported with self-adjoint boundary conditions (Sturm–Liouville problem of equation (3.2.19)), are guaranteed to have an unbounded sequence of eigenvalues (wavenumbers k_n) each associated with a normalised eigenfunction (ψ_n defined in (3.2.22)) from Sturm–Liouville theory. The normalised eigenfunctions are also guaranteed to form an orthonormal basis under an inner product. The sum in (3.2.22) corresponds to a single reflective wave ($n = 0$) and to an infinite sequence of decaying or evanescent modes ($n > 0$), which are included to describe the fluid motion near the metamaterial. Normally the sum, should be over all the integers. However, the symmetry of β_n and ψ_n about k_n allows this simplification, due to the symmetry of the dispersion relation over a flat bed.

Now for the potential $\hat{\phi}^{s,a}(x,z)$ in $x \in (-b,0)$, the regions within and above the metamaterial will be considered separately.

$$(\nabla^2 - \alpha^2)\hat{\phi}^{s,a}(x,z) = 0, \quad \hat{\phi}^{s,a}_z(x,0) = K\hat{\phi}^{s,a}(x,0) \ \text{ in } \ z \in L_g, \tag{3.2.24}$$

$$\Big(\partial_{xx} + \partial_{zz}\Big)\hat{\phi}^{s,a}(x,z) = 0, \quad \hat{\phi}^{s,a}_z(x,-h) = 0 \ \text{ in } \ z \in L_b, \tag{3.2.25}$$

with the conditions (3.2.13) on $x = 0$, be satisfied throughout the depth. The depth partitions $L_g = (-d,0)$ and $L_b = (-h,-d)$ stand for "gap" and "barrier" respectively. This is a notation owed to [72], from problems involving scattering by thin barriers throughout the depth with gaps. Also the first two equations of (3.2.18) must be considered, as the potential must be matched across the horizontal interface of the metamaterial. Proceeding to the separation of variables in (3.2.24) and (3.2.25), then

$$\begin{aligned} -\frac{Z^{s,a}_g(z)'' - \alpha^2 Z^{s,a}_g(z)}{Z^{s,a}_g(z)} = -\mu^2, \quad Z^{s,a}_g(0)' = KZ^{s,a}_g(0), \\ -\frac{Z^{s,a}_b(z)''}{Z^{s,a}_b(z)} = -\mu^2, \quad Z^{s,a}_b(-h)' = 0, \end{aligned} \tag{3.2.26}$$

$$\frac{X^{s,a}(x)''}{X^{s,a}(x)} = -\mu^2, \quad X^s(0)' = X^a(0) = 0, \tag{3.2.27}$$

where the subscripts g and b in the depth functions stand for the regions L_g and L_b respectively within $x \in (-b,0)$. Now the matching conditions through the horizontal interface of the metamaterial read $Z^{s,a}_g(-d) = Z^{s,a}_b(-d)$ and $Z^{s,a}_g(-d)' = (1-\theta)Z^{s,a}_b(-d)'$. The solutions of (3.2.26), (3.2.27), after the application of their boundary conditions are

$$\begin{aligned} Z^{s,a}_g(z) = A^{s,a}_g\Big[\cosh\left(z\sqrt{\alpha^2+\mu^2}\right) + \frac{K}{\sqrt{\alpha^2+\mu^2}}\sinh\left(z\sqrt{\alpha^2+\mu^2}\right)\Big], \\ Z^{s,a}_b(z) = A^{s,a}_b\cosh[\mu(z+h)], \end{aligned} \tag{3.2.28}$$

$$X^s(x) = a^s \frac{\cos(\mu x)}{\cos(\mu b)}, \quad X^a(x) = a^a \frac{\sin(\mu x)}{\sin(\mu b)}, \tag{3.2.29}$$

where the multiplicative constants in the functions of x were chosen like that to avoid numerical instabilities. The unknown coefficients μ can be found by applying the matching conditions at $z = -d$ on the depth functions. This is because if the two matching conditions are applied to find $A_g^{s,a}$, $A_b^{s,a}$, then it yields that

$$\begin{aligned} A_g^{s,a}\Big[\cosh\left(d\sqrt{\alpha^2+\mu^2}\right) - \frac{K}{\sqrt{\alpha^2+\mu^2}}\sinh\left(d\sqrt{\alpha^2+\mu^2}\right)\Big] &= A_b^{s,a}\cosh\left[\mu(h-d)\right], \\ A_g^{s,a}\Big[K\cosh\left(d\sqrt{\alpha^2+\mu^2}\right) - \sqrt{\alpha^2+\mu^2}\sinh\left(d\sqrt{\alpha^2+\mu^2}\right)\Big] & \\ = A_b^{s,a}\mu(1-\theta)\sinh\left[\mu(h-d)\right]. & \end{aligned} \tag{3.2.30}$$

Therefore for non-zero z-variations ($A_g^{s,a}, A_b^{s,a} \neq 0$), the determinant of the linear system in (3.2.30) must be zero. This gives rise to the dispersion relation

$$\begin{aligned} \mu(1-\theta)\tanh\left[\mu(h-d)\right]\left\{\frac{K\tanh\left(d\sqrt{\alpha^2+\mu^2}\right)}{\sqrt{\alpha^2+\mu^2}} - 1\right\} & \\ = \sqrt{\alpha^2+\mu^2}\tanh\left(d\sqrt{\alpha^2+\mu^2}\right) - K. & \end{aligned} \tag{3.2.31}$$

It is worth noting that in the case of normal incidence and thin plates ($\theta_0 = 0^\circ$ and $\theta = 0$), the equation above transforms to $z\tanh(zh) = K$ which is what was expected on physical grounds i.e., the wave travels through the thin plates uneffected. The roots of (3.2.31) (call them $\pm\mu_n$) are located only on the real and imaginary axes in the same manner as $\pm k_n$, with $\mu_0 \in \mathbb{R}_{>0}$ and $\mu_n = i\chi_n$ with $\chi_n \in \mathbb{R}_{>0}$ for $n \in \mathbb{N}$ (see discussion in Appendix A.1).

Therefore, the depth functions in $x \in (-b, 0)$ are

$$\begin{aligned} \hat{\psi}_n(z) &= \hat{N}_n^{-1/2}\begin{cases}\cosh(r_n z) + \frac{K}{r_n}\sinh(r_n z), & z \in L_g, \\ D_n\cosh[\mu_n(z+h)], & z \in L_b,\end{cases} \\ \text{where} \quad D_n &= \frac{r_n\cosh(r_n d) - K\sinh(r_n d)}{r_n\cosh\left[\mu_n(h-d)\right]},\ r_n = \sqrt{\alpha^2+\mu_n^2}, \end{aligned} \tag{3.2.32}$$

where D_n was chosen by setting $A_g^{s,a} = 1$ into the first equation of (3.2.30) and the normalisation factor $\hat{N}_n^{-1/2}$ was chosen as

$$\begin{aligned}\hat{N}_n = \frac{d}{h}\left[\frac{1}{2} + \frac{\sinh(2r_n d)}{4r_n d}\right] - \frac{K^2 d}{r_n^2 h}\left[\frac{1}{2} - \frac{\sinh(2r_n d)}{4r_n d}\right] - \frac{K}{r_n^2 h}\sinh^2(r_n d) \\ + \frac{h-d}{h}(1-\theta)D_n^2\left[\frac{1}{2} + \frac{\sinh\big(2\mu_n(h-d)\big)}{4\mu_n(h-d)}\right],\end{aligned} \tag{3.2.33}$$

so that the eigenfunctions satisfy an orthogonality relation, specified later. Also, one can observe that μ_n represent the wavenumbers of the propagated modes in the metamaterial region. Note that $\hat{\psi}_n \in \mathbb{R}$ for all $n \in \mathbb{N}_0$ (using that $\hat{N}_n$ and D_n are real as well) and it is independent of the superscripts s, a, as the depth functions will have the same form in the symmetric and antisymmetric problem. Also, it will be shown in the Appendix B.1 that these eigenfunctions are orthogonal but not with respect to the inner product defined in (3.2.23). This is due to the fact that this inner product involves an integral over $(-h, 0)$ and there is a gradient discontinuity of the eigenfunctions at $z = -d$ (according to the matching conditions). Thus the orthogonality relation of the eigenfunctions in $|x| < b$ is

$$\langle\hat{\psi}_n, \hat{\psi}_m\rangle \equiv \int_{-d}^{0} \hat{\psi}_n(z)\hat{\psi}_m(z)dz + (1-\theta)\int_{-h}^{-d} \hat{\psi}_n(z)\hat{\psi}_m(z)dz = h\delta_{nm}, \tag{3.2.34}$$

due to the choice of the normalisation factor in (3.2.33).

Thus, the general solution of the potential in $x \in (-b, 0)$ is

$$\hat{\phi}^s(x,z) = \sum_{n=0}^{\infty} \hat{a}_n^s \frac{\cos(\mu_n x)}{\cos(\mu_n b)}\hat{\psi}_n(z), \quad \hat{\phi}^a(x,z) = \sum_{n=0}^{\infty} \hat{a}_n^a \frac{\sin(\mu_n x)}{\sin(\mu_n b)}\hat{\psi}_n(z). \tag{3.2.35}$$

Again, as in (3.2.22), the solution is written over a semi-infinite sum from the symmetry of μ_n. Also, a key feature of this problem is that the y-independent potentials are symmetric in θ_0 (and therefore, so does the solution).

The final step of this problem is the matching of the potential across $x =$

$-b$ as stated in the last two equations of (3.2.18). These two conditions create a coupled linear system for $a_n^{s,a}$ and $\hat{a}_n^{s,a}$ after taking an inner product (either (3.2.23) or (3.2.34)). Therefore, by applying the inner product defined in (3.2.23) on the matching conditions, then the result in vectorial form is

$$\begin{aligned}
&e^{-i\beta b}\mathbf{J}+\mathbf{a}^{s,a}=\mathbf{A}^{s,a}\hat{\mathbf{a}}^{s,a},\quad -e^{-i\beta b}\mathbf{J}+\mathbf{a}^{s,a}=\mathbf{B}^{s,a}\hat{\mathbf{a}}^{s,a},\\
&\text{with}\quad J_n=\delta_{n0},\quad A^s_{nm}=G_{nm}+B_{nm},\quad A^a_{nm}=-A^s_{nm},\\
&B^s_{nm}=\frac{\mu_m\tan(\mu_m b)}{\beta_n}\Big(G_{nm}+(1-\theta)B_{nm}\Big),\\
&B^a_{nm}=\frac{\mu_m\cot(\mu_m b)}{\beta_n}\Big(G_{nm}+(1-\theta)B_{nm}\Big),\\
&G_{nm}=\frac{1}{h}\int_{-d}^{0}\psi_n(z)\hat{\psi}_m(z)dz,\quad B_{nm}=\frac{1}{h}\int_{-h}^{-d}\psi_n(z)\hat{\psi}_m(z)dz,
\end{aligned}\tag{3.2.36}$$

where $A^{s,a}_{nm}$ and $B^{s,a}_{nm}$ come by integrating throughout the depth, the pressure and normal flux matching conditions (last two equations of (3.2.18)). The complicated integrals G_{nm}, B_{nm} (standing from integral over the "gap" and "barrier" respectively) are calculated analytically in the Appendix B.3 as

$$\begin{aligned}
G_{nm}=\frac{N_n^{-1/2}\hat{N}_n^{-1/2}D_m}{(k_n^2-r_m^2)h}\Big\{&(1-\theta)\mu_m\cosh\big[k_n(h-d)\big]\sinh\big[\mu_m(h-d)\big]\\
&-k_n\sinh\big[k_n(h-d)\big]\cosh\big[\mu_m(h-d)\big]\Big\},\\
B_{nm}=\frac{N_n^{-1/2}\hat{N}_n^{-1/2}D_m}{(k_n^2-\mu_m^2)h}\Big\{&k_n\sinh\big[k_n(h-d)\big]\cosh\big[\mu_m(h-d)\big]\\
&-\mu_m\cosh\big[k_n(h-d)\big]\sinh\big[\mu_m(h-d)\big]\Big\}.
\end{aligned}\tag{3.2.37}$$

Elimination between $\mathbf{a}^{s,a}$ and $\hat{\mathbf{a}}^{s,a}$ from the system above, results to

$$\begin{aligned}\hat{\mathbf{a}}^{s,a} &= 2e^{-i\beta b}(\mathbf{A}^{s,a}-\mathbf{B}^{s,a})^{-1}\mathbf{J},\\ \mathbf{a}^{s,a} &= e^{-i\beta b}\Big[2\mathbf{A}^{s,a}(\mathbf{A}^{s,a}-\mathbf{B}^{s,a})^{-1}-\mathbf{I}\Big]\mathbf{J},\end{aligned} \tag{3.2.38}$$

where $\mathbf{I}$ is the identity matrix, while using $R=(R^s+R^a)/2$ and $T=(R^s-R^a)/2$ from (3.2.16) (the reflection and transmission coefficients) with $R^{s,a}=a_0^{s,a}e^{-i\beta b}$ then

$$R=\frac{1}{2}e^{-i\beta b}(a_0^s+a_0^a),\quad T=\frac{1}{2}e^{-i\beta b}(a_0^s-a_0^a). \tag{3.2.39}$$

Now, an alternative way to get the unknown Fourier coefficients (3.2.38), is to use the orthogonality of $\hat{\psi}_n$, namely (3.2.34). Therefore, by taking the matching conditions at $x=-b$ (continuity of ϕ and normal flux), multiplying them by $\hat{\psi}_m$ now and applying the (3.2.34) inner product in the first and the (3.2.23) in the second, then

$$\begin{aligned}&\hat{\mathbf{a}}^{s,a}=e^{-i\beta b}\hat{\mathbf{J}}_1^{s,a}+\hat{\mathbf{A}}^{s,a}\mathbf{a}^{s,a},\quad \hat{\mathbf{a}}^{s,a}=-e^{-i\beta b}\hat{\mathbf{J}}_2^{s,a}+\hat{\mathbf{B}}^{s,a}\mathbf{a}^{s,a},\\ \text{with}\quad &\hat{A}^s_{nm}=G_{mn}+(1-\theta)B_{mn},\quad \hat{A}^a_{nm}=-\hat{A}^s_{nm},\quad \hat{J}^{s,a}_{1,n}=\hat{A}^{s,a}_{n0},\\ &\hat{B}^s_{nm}=\beta_m(G_{mn}+B_{mn})\cot(\mu_n b)/\mu_n,\\ &\hat{B}^a_{nm}=\beta_m(G_{mn}+B_{mn})\tan(\mu_n b)/\mu_n,\quad \hat{J}^{s,a}_{2,n}=\hat{B}^{s,a}_{n0},\end{aligned} \tag{3.2.40}$$

where the expressions of G_{nm} and B_{nm} can be found from (3.2.37). Through elimination of the two equations above, the unknown scattering coefficients in vectorial form are

$$\begin{aligned}\mathbf{a}^{s,a} &= e^{-i\beta b}\Big(\hat{\mathbf{B}}^{s,a}-\hat{\mathbf{A}}^{s,a}\Big)^{-1}\Big(\hat{\mathbf{J}}_1^{s,a}+\hat{\mathbf{J}}_2^{s,a}\Big),\\ \hat{\mathbf{a}}^{s,a} &= e^{-i\beta b}\left[\hat{\mathbf{A}}^{s,a}\Big(\hat{\mathbf{B}}^{s,a}-\hat{\mathbf{A}}^{s,a}\Big)^{-1}\Big(\hat{\mathbf{J}}_1^{s,a}+\hat{\mathbf{J}}_2^{s,a}\Big)+\hat{\mathbf{J}}_1^{s,a}\right].\end{aligned} \tag{3.2.41}$$

Note that this method requires a matrix inversion to find $\mathbf{a}^{s,a}$ directly (which is the main goal because it includes the reflection and transmission coefficients) while the previous method required an inversion to find $\hat{\mathbf{a}}^{s,a}$ and then using this approximation to get $\mathbf{a}^{s,a}$. Although the two methods must be equivalent, since there will be truncation of infinite systems of equations in numerical solutions we expect small differences in computed results which we shall compare later.

The scattering coefficients to the physical problem (R and T) can be found again from (3.2.39).

3.2.3 Numerical results

In this section, numerical results for the problem involving the submerged metamaterial made of vertical thick barriers oriented normally to the side interfaces are considered. The numerical strategy is to take the general solution of the wave field found in (3.2.22) and (3.2.35) and find their unknown Fourier coefficients through the linear truncated systems (3.2.36) or (3.2.40), depending on which eigenfunction orthogonality is used (ψ_n or $\hat{\psi}_n$ orthogonality).

N	$\lvert R\rvert$	$\lvert T\rvert$	p_e	f_e
8	0.00783954889	0.9999692702643	5.6×10^{-6}	4.1×10^{-6}
16	0.xxxxxx46140	0.xxxxxxxx10502	1.0×10^{-6}	2.0×10^{-6}
32	0.xxxxxxx4144	0.xxxxxxxx11067	8.5×10^{-7}	1.1×10^{-6}
64	0.xxxxxxx3597	0.xxxxxxxxxx497	6.2×10^{-7}	5.2×10^{-7}
128	0.xxxxxxxx461	0.xxxxxxxxxx603	3.7×10^{-7}	2.7×10^{-7}
256	0.xxxxxxxxx26	0.xxxxxxxxxxx31	9.3×10^{-8}	1.4×10^{-7}
512	0.xxxxxxxxx17	0.xxxxxxxxxxxx7	7.6×10^{-8}	7.6×10^{-8}
1024	0.xxxxxxxxxx5	0.xxxxxxxxxxxx9	5.1×10^{-8}	4.6×10^{-8}

Table 3.1: Scattering coefficients convergence and matching error against truncation size N using the orthogonality of ψ_n. The geometrical parameters are $kb = 0.1$, $\theta_0 = 30^\circ$, $d/h = 0.6$, $b/h = 1$ and $\theta = 0.1$.

Starting from the comparison of two methods, we consider the table 3.1. It can be verified that $N = 1024$ gives an accuracy of 10 decimal places to the scattering coefficients $|R|$ and $|T|$. The last two columns of the table represent the error of the

pressure and flux matching conditions at $x = -b$, namely

$$p_e \equiv \frac{1}{M+1}\sum_{j=0}^{M}\left|\phi(-b,z_j)-\hat{\phi}(-b,z_j)\right|^2, \quad f_e \equiv \frac{1}{M+1}\sum_{j=0}^{M}\left|\phi_x(-b,z_j)-f_j\right|^2,$$
$$\text{for} \quad z_j = -0.01jh \quad \text{and} \quad f_j = \begin{cases} \hat{\phi}_x(-b,z_j), & z_j > -d, \\ (1-\theta)\hat{\phi}_x(-b,z_j), & z_j \leq -d, \end{cases} \tag{3.2.42}$$

for $M = 10^7$. A variety of geometrical choices were tested and the resulting truncation error was the same. Also, the $\hat{\psi}_n$ orthogonality method was not included in the table as for the same choice of geometrical parameters and truncation, the numbers were found to be the same with the numbers of the ψ_n orthogonality method (as shown in the table). Therefore, from now on the truncation size will be chosen to be $N = 1024$ and the ψ_n orthogonality method will be used as there is no significant difference between the two methods.

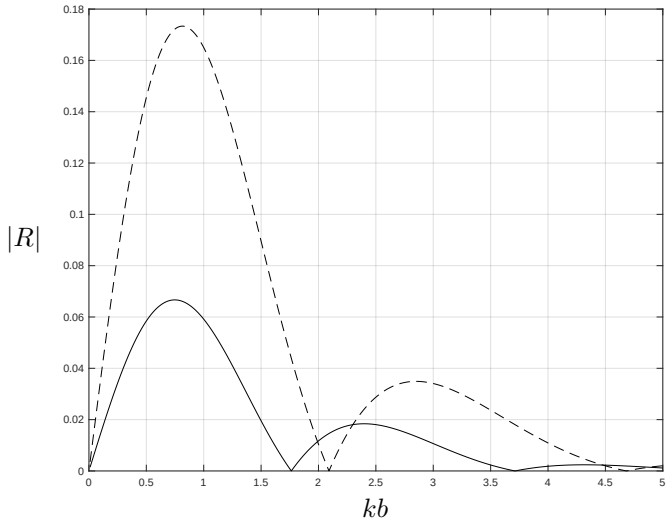

Figure 3.2: $|R|$ against kb, with $d/h = 0.5$, $b/h = 1$ and $\theta = 0$, for incident directions $\theta_0 = 30^\circ$ (full) and $\theta_0 = 45^\circ$ (dashed).

Moving on to the calculation of $|R|$, figure 3.2 shows how reflection varies with the dimensionless parameter kb. The zero-thickness barriers cover 50% of the depth and their width is twice the depth ($2b = 2h$). The two curves represent two different incident directions i.e., $\theta_0 = 30^\circ$ and $\theta_0 = 45^\circ$. Firstly, a common feature of

this kind of plots is that the larger interaction (as in curve modulation) happens for smaller kb and it decays as kb increases. This has to do with the penetration of the motion of the fluid. In the case of long waves (λ/b large or kb small), the energy decay of the wave from the surface to the bed is small. This can be seen from the fact that the z variation of a wave travelling over a flat bed looks like $\cosh[k(z+h)]$ and so small k means small decay as z goes from 0 to $-h$. By the same analogy, large kb (short waves) corresponds to larger energy decay. This is expected on physical grounds as the energy in a fluid column decays exponentially away from the surface with an exponential inversely proportional to wavelength and therefore short waves do not get affected (significantly) from submerged obstacles to the bed. Also, another typical characteristic of such plots is that reflection vanishes as $kb \to 0$. This is because the equivalent limit $\lambda/b \to \infty$ corresponds to an undisturbed surface. The features of the reflection modulus found in our problem, can also be found in [68] and [73] where the scattering problem by a submerged, rigid and horizontal plate is analysed. Moreover, another typical feature of such plots is that the level of interaction depends on the direction of the incident wave. It can be seen from figure 3.2 that as the incident direction approaches the direction of the barriers orientation, then the interaction is smaller. This is again what was expected, as when θ_0 varies from 0° to 90°, the sliding ability of the wave through the barriers reduces.

Next, the reflection modulus is plotted against the dimensionless parameter λ/b in figure 3.3. The array size is now larger as $d/h = 0.1$, $b/h = 1$ and the direction of incidence is $\theta_0 = 60^\circ$. The curve shows that the interaction is larger not only because the incident wave is more oblique than the previous plot, but also because the barriers are now higher. Actually, the barriers now occupy almost all the depth (90%). If the barriers were extended throughout the depth ($d/h = 0$), then the problem becomes two-dimensional. This problem was solved in [11] for thin barriers of general orientation. Also, the reflection coefficient here has the same behaviour under the variation λ/b, as before. More reflection is always expected at larger wavelengths and the reflection vanishes for $\lambda/b \to 0$ as the energy decay of the wave across the depth becomes much larger and so the submerged obstacles do not have a great effect on the wave. Another key feature of this kind of plots, is that $|R|$ and $|T|$ have an oscillatory behaviour of a non-constant period as the wavelength varies. This shift in periodicity is expected from the dispersion relation.

In figure 3.4(i), it can be seen that as kb increases $|T|$ converges to 1 as expected. Also, as θ increases the scattering coefficients "approach" the solution of the rigid step problem. Results of indicating the scattering by a submerged rigid step will be computed in the numerical section of the problem where the barriers are aligned with the y-axis. We derive those results later, as the metamaterial of the

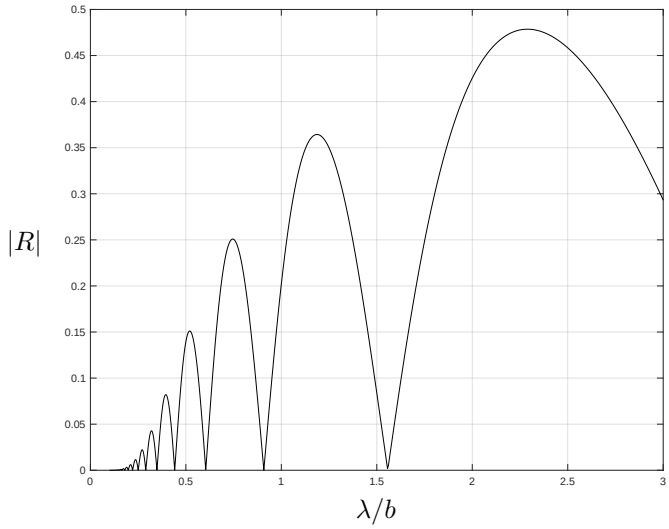

Figure 3.3: Variation of $|R|$ with λ/b, for $\theta_0 = 60°$, $d/h = 0.1$, $b/h = 1$ and $\theta = 0$.

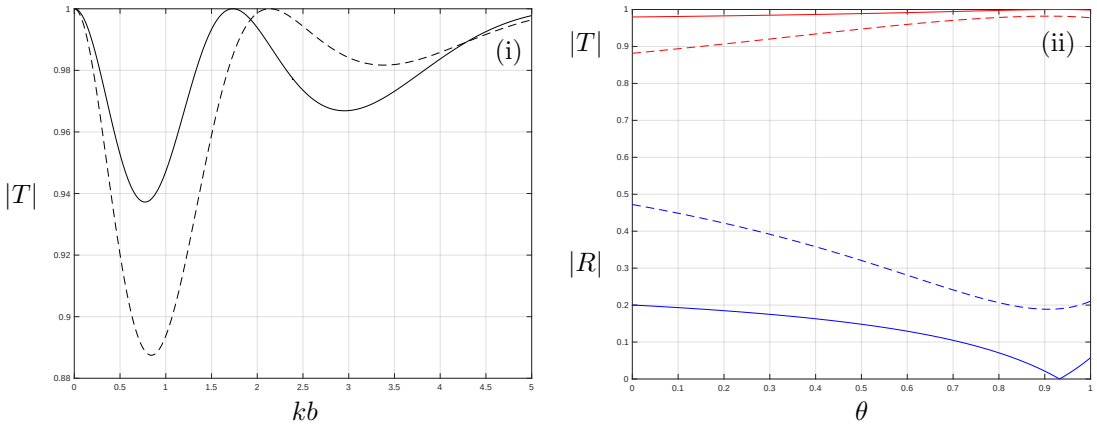

Figure 3.4: (i) $|T|$ against kb, for $\theta = 0.1$ (dashed) and $\theta = 0.5$ (full) with $d/h = 0.3$, $b/h = 1$ and $\theta_0 = 60°$. (ii) $|R|$ (blue) and $|T|$ (red) against θ, for $kb = 0.2$ (full) and $kb = 1$ (dashed) with d/h, b/h and θ_0 same as in (i).

next section behaves like a rigid step, not only when $\theta \to 1$ but also when $\theta_0 \to 0°$ (normal incidence). Also, in the same figure, one can see that even if the array covers 70% of the depth and the angle between the incident wave and the barriers is 60°, the transmission is still high. In this problem it is very difficult to drop the local minima

of $|T|$ while in the metamaterial described in the next section, it will be easier even for the same array height. This happens from the nature of this particular metamaterial which has more openings than the metamaterial whose barriers are aligned with the y-axis i.e. the wave energy escapes the metamaterial from the two side interfaces and the one top interface while in "y-aligned metamaterial", only from the top.

In figure 3.4(ii), kb is now fixed to 0.2 (full line) and 1 (dashed line) and θ now varies in $[0, 1]$ and thus reflection does not go through the origin as happened at $kb \to 0$. Here it can be seen that the interaction is smaller for larger kb. It seems that this contradicts the fact discussed in figure 3.2, but it is not. The largest interaction in figure 3.2, that happens in smaller kb, occur at certain frequencies. Due to the oscillatory behaviour of the scattering coefficients, there is a possibility to pick a largest wavenumber that corresponds to a smaller reflection coefficient and this case is demonstrated in figure 3.4(ii).

Next the surface plot of the elevation $\zeta(x, y, t)$ for some t, is considered in figure 3.5(i) with its cross-section at $y = 0$ in figure 3.5(ii). The free surface elevation can be found from the linear dynamic boundary condition at $z = 0$ in (2.2.6) namely $\eta(x) = (i\omega/g)\phi(x, 0)$ for $\zeta(x, y, t) = \Re\{\eta(x)e^{i\alpha y}e^{-i\omega t}\}$. Therefore, the surface elevation can be found in terms of the complex potential as $\zeta(x, y, t) = -(\omega/g)\Im\{\phi(x, 0)e^{i\alpha y}e^{-i\omega t}\}$ where ϕ can be taken from (3.2.14). The unknown coefficients of the symmetric and antisymmetric potential, namely $\mathbf{a}^{s,a}$, $\hat{\mathbf{a}}^{s,a}$, can be found from (3.2.38). The x and y axes are non-dimensionalised by b so that the metamaterial covers the "small" region $|x/b| < 1$.

This kind of results are similar (not the same due to particular barrier orientation) to the ones of [16]. In $x/b > 1$, there is a single mode travelling in the direction of incidence ($\theta_0 = 60^\circ$) and in $x/b < -1$ there is a periodic pattern of nodes and antinodes due to multiple interference of the incident mode and the reflected wave. Also, it is known that within the metamaterial array, the wave is confined to travel in the x-direction. Therefore, if the barriers covered 100% of the depth ($d \to 0$) then within $|x/b| < 1$, the wave would be confined to travel in the direction parallel to the barriers. It is also known that if $d \to h$ (short barrier limit), the wave will be scattered unaffected in the direction of incidence (this can be verified also by taking this limit in (3.2.31)). Therefore, by the continuity of d, it is expected that for $0 < d < h$, the wave bends at a direction somewhere between the direction of the barrier orientation and the incident direction. One could also calculate the direction of the phase speeds of the two waves in $|x| < b$ as $\theta_p^{(1)} \approx 42.41^\circ$ with $\theta_p^{(2)} = -\theta_p^{(1)}$ from the symmetry of the real roots μ_n of the dispersion relation (3.2.31) - angles calculated as $\arctan\big[\alpha/(\pm\mu_0)\big]$. However, phase speeds say nothing about refraction. Certain refraction properties will be shown though the wave's group velocity later

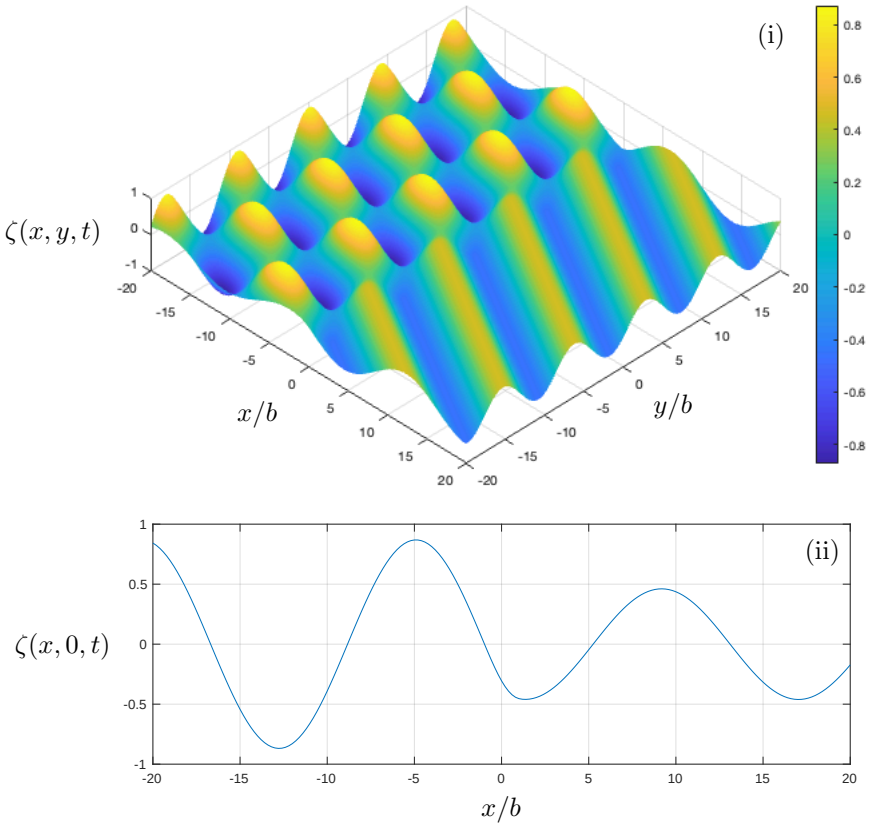

Figure 3.5: (i) Instantaneous surface elevation and (ii) wave profile at $y = 0$, for $kb = 0.8$, $\theta_0 = 60°$, $d/h = 0.1$, $b/h = 1$ and $\theta = 0$.

under the shallow water approximation. The closed-form solution of this simplified problem, will allow us to define and understand the so-called negative refraction.

Now in figure 3.5(ii), it can be seen that the wave amplitude was almost halved after passing the metamaterial medium. It can be seen also from here that when the barriers are aligned with the x-axis, it is very difficult to maintain low transmission because of the multiple openings of the structure. Even with barriers that cover 90% of the depth, a structure width which is double the size of the depth and an oblique incidence, the transmitted wave energy was found to be $|T|^2 \approx 68\%$ of the incident wave energy.

3.2.4 Barriers parallel to the side interfaces

In this section, the barriers have an orientation of $\delta = 90°$. Therefore, the barriers now have infinite length (this can be seen also from $L = b\sec\delta$ from (3.2.2)) and they extend uniformly in the y-direction. Also, this problem can be generalised by assuming that the lower metamaterial interface is located at $z = -c$ for $0 < d < c, h$, instead of $z = -h$. In the case of $c < h$ the metamaterial sits on a flat step of height $h - c$ and in the case of $c > h$, the barriers of height $c - d$ are sunken in the sea bed by a distance of $c - h$. This generalisation can be assumed without making the algebra harder, because the incident wave has no direct contact through $x = -b$, $z \in (-h, -d)$ with the wave within the metamaterial, in contrast to the previous problem. Since the first barrier located at $x = -b$ acts like a wall, then only through $z = -d$, $|x| < b$ (vertical interface) the wave inside and outside the metamaterial exchange information. Therefore, the alternating depths within $|x| < b$ can be set to be $z = -d$ and $z = -c$ instead of $z = -h$. It is not straightforward to make this

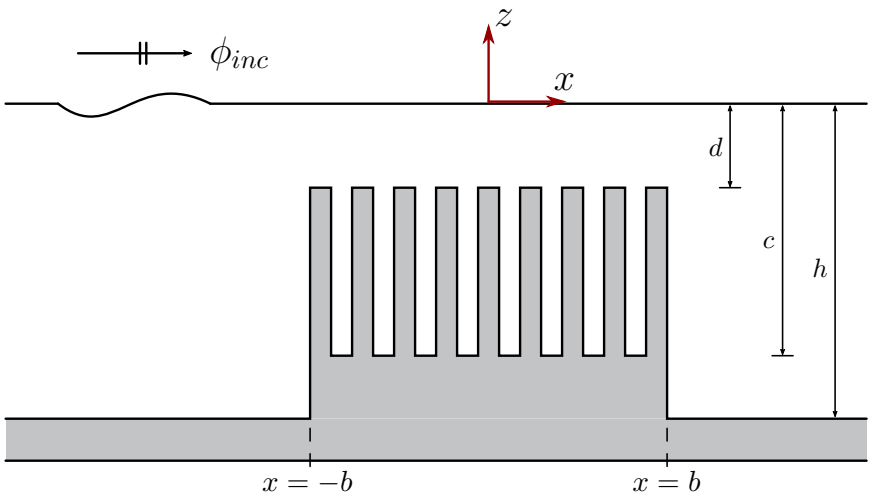

Figure 3.6: Geometry of the metamaterial for $\delta = 90°$ with alternating interfaces at $z = -d, -c$. The lower interface could be below the sea bed level ($0 < d < c, h$).

generalisation to any other barrier orientation ($\delta \neq 90°$) as the matching through the vertical interfaces ($x = \pm b$) must be separated in three cases instead of two, depending on the vertical level.

This problem is similar to the one of [1][16], as the alternating depths within the metamaterial can be different from the depth outside. The difference lies upon the fluid's shallowness assumption. The geometry of the problem is symmetric about

the yz-plane, even for this barrier orientation and this allows the decomposition into symmetric and antisymmetric problems specified in equations (3.2.13) to (3.2.15). Again, due to the time-harmonicity of the problem and the global y-compatibility with the incident wave, the total wave field is assumed to be compatible with the t and y variation of the incident wave. Therefore, the solution to the reduced Laplace equation in (3.2.15) is again

$$\phi^{s,a}(x,z) = \left(e^{i\beta x} + R^{s,a}e^{-i\beta x}\right)\psi_0(z) + \sum_{n=1}^{\infty} a_n^{s,a} e^{\beta_n(x+b)}\psi_n(z) \quad \text{in} \quad x < -b, \tag{3.2.43}$$

using separation of variables, where ψ_n, β_n are defined in (3.2.22).

Within $x \in (-b, 0)$, the governing equation for the potential will be different in the regions L_g and L_b where now $L_g = (-d, 0)$ and $L_b = (-c, -d)$. In L_g, the model will be the reduced Laplacian equation combined with the free surface condition (all specified in (3.2.24)) and in L_b according to (3.2.7), the effective medium equation within the metamaterial becomes

$$\left(\partial_{zz} - \alpha^2\right)\hat{\phi}^{s,a}(x,z) = 0, \tag{3.2.44}$$

by dropping y and t dependence again through the wave field proportionality of $e^{i\alpha y}e^{-i\omega t}$. This equation is combined with the no flow condition at the sea bed and a Neumann/Dirichlet condition at $x = 0$ must be applied throughout the depth for the symmetric/antisymmetric problem (equation (3.2.13)). By separating variables in $x \in (-b, 0)$ throughout $L_g \cup L_b$, it follows that

$$\begin{gathered} -\frac{Z_g^{s,a}(z)'' - \alpha^2 Z_g^{s,a}(z)}{Z_g(z)} = -\mu^2, \quad Z_g^{s,a}(0)' = K Z_g^{s,a}(0), \\ Z_b^{s,a}(z)'' = \alpha^2 Z_b^{s,a}(z), \quad Z_b^{s,a}(-c)' = 0, \end{gathered} \tag{3.2.45}$$

$$\frac{\hat{X}^{s,a}(x)''}{\hat{X}^{s,a}(x)} = -\mu^2, \quad \hat{X}^s(0)' = \hat{X}^a(0) = 0, \tag{3.2.46}$$

where $-\mu^2$ is again the separation constant. The solutions to $Z_g^{s,a}(z)$ and $X^{s,a}(x)$ are

identical to the ones in (3.2.28) and (3.2.29) and the solution to the depth function in L_b is

$$Z_b^{s,a}(z) = A_b^{s,a} \cosh\big[\alpha(z+c)\big]. \tag{3.2.47}$$

The wavenumbers μ will be different than the ones of the previous problem as the dispersion relation satisfied by them will not be the same due to the μ-independent depth function within the barriers, specified in (3.2.47). Also, note that for normal incidence ($\theta_0 = 0°$), the depth function becomes constant within the barriers suggesting that the vertical velocity (potential gradient) will vanish. This is what was expected on physical grounds as the fluid is assumed to be incompressible and the distance between the barriers is much smaller than all the underlying variables of the problem (wavelength and depth). A wave that propagates in a direction perpendicular to the narrow gap, will have no z variation within the barriers. However, if it makes a non-zero angle θ_0 with the gap, then the difference in phase will create some vertical fluctuation of the fluid within the metamaterial. Therefore, for normal incidence the metamaterial acts as a rigid step at a depth $z = -d$.

Matching the depth functions in the same way as in (3.2.30), then the new dispersion relation is

$$\begin{aligned} \alpha(1-\theta)\tanh\big[\alpha(c-d)\big]\left\{\frac{K\tanh\big(d\sqrt{\alpha^2+\mu^2}\big)}{\sqrt{\alpha^2+\mu^2}} - 1\right\} \\ = \sqrt{\alpha^2+\mu^2}\tanh\big(d\sqrt{\alpha^2+\mu^2}\big) - K. \end{aligned} \tag{3.2.48}$$

Those roots (call them $\pm\mu_n$) are shown in the Appendix A.1 to be located only on the real or imaginary axes of the complex plane as before, with $\mu_0 \in \mathbb{R}_{>0}$ and $\mu_n = i\chi_n$ with $\chi_n \in \mathbb{R}_{>0}$ ($n \in \mathbb{N}$). Now the depth functions within $x \in (-b, 0)$ are chosen in a slightly different manner, as

$$\begin{aligned} \hat{\psi}_n(z) &= \begin{cases} \hat{N}_n^{-1/2}\Big(\cosh(r_n z) + \frac{K}{r_n}\sinh(r_n z)\Big), & z \in L_g, \\ \hat{N}_n^{-1/2} D_n \cosh\big[\alpha(z+c)\big], & z \in L_b, \end{cases} \\ &\text{with } D_n = \frac{r_n\cosh(r_n d) - K\sinh(r_n d)}{r_n\cosh[\alpha(c-d)]}, \\ \hat{N}_n &= \frac{1}{2}\left(1 - \frac{K^2}{r_n^2}\right) + \frac{\sinh(2r_n d)}{4r_n d}\left(1 + \frac{K^2}{r_n^2}\right) - \frac{K}{r_n^2 d}\sinh^2(r_n d), \end{aligned} \tag{3.2.49}$$

where again $r_n = \sqrt{\alpha^2 + \mu_n^2}$. Note, that the rigid step behaviour of the metamaterial described above (when $\theta_0 = 0°$) can be achieved also if $\theta = 1$ or $c = d$ for any θ_0. Geometrically, this translates to letting the filling fraction of the barriers (metamaterial contrast) to be 100% or the metamaterial interfaces to have the same level. Algebraically, this can be seen from (3.2.48) as if $\theta = 1$ or $c = d$, the dispersion relation becomes $r_n \tanh(r_n d) = K$, which coincides with the standard water wave dispersion relation over a flat bed at $z = -d$. In contrast to the previous problem ($\delta = 0°$) now D_n was chosen by setting $A_g^{s,a} = 1$ in the first equation of the analogue of (3.2.30). Note that again the z-variation is independent of the symmetric/antisymmetric problem. The multiplicative constant $\hat{N}_n \in \mathbb{R}$ was chosen that way so that the orthogonality condition (shown analytically in Appendix B.2) of the depth eigenfunctions $\hat{\psi}_n \in \mathbb{R}$ becomes

$$\int_{-d}^{0} \hat{\psi}_n(z)\hat{\psi}_m(z)dz = d\delta_{nm}. \tag{3.2.50}$$

Finally, the solutions to the potential within $x \in (-b, 0)$ and $z \in L_g \cup L_b$ for each subproblem, are found to be

$$\begin{aligned} \hat{\phi}^s(x,z) &= \hat{a}_0^s \cos(\mu_0 x)\hat{\psi}_0(z) + \sum_{n=1}^{\infty} \hat{a}_n^s \frac{\cosh(\chi_n x)}{\cosh(\chi_n b)}\hat{\psi}_n(z), \\ \hat{\phi}^a(x,z) &= i\hat{a}_0^a \sin(\mu_0 x)\hat{\psi}_0(z) + \sum_{n=1}^{\infty} \hat{a}_n^a \frac{\sinh(\chi_n x)}{\sinh(\chi_n b)}\hat{\psi}_n(z), \end{aligned} \tag{3.2.51}$$

where $\hat{a}_0^{s,a}$ are rescaled in a way that simplifies the forthcoming algebra a bit. Here, it can be verified again that the y-independent potentials are even in θ_0 from the μ_n dispersion relation and thus the scattering coefficients as well.

A very simple and computationally inexpensive variational approach was used in [72] for the scattering by a single line vertical barriers with gaps. It relies on using the matching conditions on the interfaces to yield two integral equations of the first kind for two functions typically related to the unknown horizontal velocity across the gaps and the pressure difference across the barrier. This follows the principle adopted by [74]. These integral equations are solved using the Galerkin method,

specified in [72].

This method can be applied here as it requires the existence of orthogonal functions in both $|x| < b$ and $|x| > b$. For example in the next section (arbitrary oriented barriers), the eigenfunctions will not be orthogonal in $|x| < b$ and thus the problem can be only solved using mode matching methods. Mode matching could be used here as well. However the new conditions at $x = \pm b$ imply the existence of a flow over a step-like structure and [72] showed that the Galerkin method (with orthogonal eigenfunctions) gives more accurate and efficient results. The validity of this approximation will be verified later by comparing results of the problem in section 3.2.7 which is solved using mode matching methods. It will be shown that by taking the limit $\delta \to 90^\circ$ (where δ is the orientation angle of the barriers), the results converge to the ones of this section.

First, for the symmetric problem, the method starts by defining the following functions

$$\phi_x^s(-b,z) = \hat{\phi}_x^s(-b,z) = \begin{cases} U^s(z), & z \in L_g, \\ 0, & z \in L_b, \end{cases} \tag{3.2.52}$$

$$P^s(z) = \phi^s(-b,z) - \hat{\phi}^s(-b,z), \tag{3.2.53}$$

which they represent the velocity and the pressure jump at the interface $x = -b$ respectively. Concentrating on the two representations of the velocity function, by multiplying the first by $\psi_m(z)$ and integrate throughout the depth and multiplying the second by $\hat{\psi}_m(z)$ and integrate in L_g, then

$$\begin{aligned} i\beta\big(e^{-i\beta b} - R^s e^{i\beta b}\big) &= \frac{1}{h}\int_{L_g} U^s(z)\psi_0(z)dz, \\ \beta_n a_n^s &= \frac{1}{h}\int_{L_g} U^s(z)\psi_n(z)dz \quad (n \in \mathbb{N}), \\ \hat{a}_0^s \mu_0 \sin(\mu_0 b) &= \frac{1}{d}\int_{L_g} U^s(z)\hat{\psi}_0(z)dz, \\ -\chi_n \hat{a}_n^s \tanh(\chi_n b) &= \frac{1}{d}\int_{L_g} U^s(z)\hat{\psi}_n(z)dz \quad (n \in \mathbb{N}), \end{aligned} \tag{3.2.54}$$

using the orthogonality relations of ψ_n and $\hat{\psi}_n$ specified in (3.2.23), (3.2.50).

It is crucial to understand how the integration "throughout the depth" is executed in (3.2.54). In the case of $c < h$ the metamaterial sits on a rigid step. Thus, ψ_n is defined in $(-h, 0)$ from (3.2.22) and so must $\hat{\psi}_n$. Therefore in the case of $c < h$, $\hat{\psi}_n$ from (3.2.49) is defined over $(-h, 0)$ by adding an extra case of $\hat{\psi}_n = 0$ in $(-h, -c)$ in its definition (as there is no flow within that region) and the integral equations above were derived by integrating in $(-h, 0)$. Now in the case of $c > h$, the metamaterial is buried in the ground. Therefore, in this case the opposite trick happens i.e. $\hat{\psi}_n$ is defined over $(-c, 0)$ from (3.2.49) and now ψ_n must be redefined over $(-c, 0)$. Thus, $\psi_n(z)$ can be defined to be $N_n^{-1/2} \cosh\big[k_n(z+h)\big]$ over $(-h, 0)$ and $\psi_n = 0$ over $(-c, -h)$ so that the integral equations above, come by integrating in $(-c, 0)$. The result is the same independently of the sign of $c - h$.

Now concentrating on the pressure jump function specified in (3.2.53), using the fact that $P^s(z) = 0$ in $z \in L_g$, then

$$\begin{aligned} &\big(e^{-i\beta b} + R^s e^{i\beta b}\big)\psi_0(z) + \sum_{n=1}^{\infty} a_n^s \psi_n(z) \\ &= \hat{a}_0^s \cos(\mu_0 b)\hat{\psi}_0(z) + \sum_{n=1}^{\infty} \hat{a}_n^s \hat{\psi}_n(z) \text{ in } z \in L_g. \end{aligned} \tag{3.2.55}$$

Eliminating the Fourier coeffiecients inside the sums from (3.2.54), then

$$\begin{aligned} &-\big(e^{-i\beta b} + R^s e^{i\beta b}\big)\psi_0(z) + \hat{a}_0^s \cos(\mu_0 b)\hat{\psi}_0(z) = \int_{L_g} U^s(t) K^s(z,t) dt, \\ &\text{for } \; K^s(z,t) = \sum_{n=1}^{\infty} \left[\frac{\psi_n(z)\psi_n(t)}{\beta_n h} + \frac{\hat{\psi}_n(z)\hat{\psi}_n(t)}{\chi_n d \tanh(\chi_n b)} \right]. \end{aligned} \tag{3.2.56}$$

By introducing the functions $u_1^s(z)$ and $u_2^s(z)$ to satisfy $\langle u_1^s, K^s \rangle = \psi_0$ and $\langle u_2^s, K^s \rangle = \hat{\psi}_0$ with the inner product defined as $\langle f, g \rangle \equiv \int_{L_g} f(t) g(t) dt$, then it can be seen that $u_1^s, u_2^s \in \mathbb{R}$ since $\psi_0, \hat{\psi}_0, K^s \in \mathbb{R}$. It is worth noting that K^s is a linear, positive definite, self-adjoint operator over the inner product discussed above. It can also be observed that equation (3.2.56) is satisfied by choosing $U^s(t) = -\big(e^{-i\beta b} + R^s e^{i\beta b}\big)u_1^s(t) + \hat{a}_0^s \cos(\mu_0 b) u_2^s(t)$. Therefore, by substituting this particular choice of

U^s in the first and third equation of (3.2.54), then

$$\begin{aligned} i\beta h\big(e^{-i\beta b} - R^s e^{i\beta b}\big) &= -\big(e^{-i\beta b} + R^s e^{i\beta b}\big)\langle u_1^s, \psi_0\rangle + \hat{a}_0^s \cos(\mu_0 b)\langle u_2^s, \psi_0\rangle, \\ \hat{a}_0^s \mu_0 d \sin(\mu_0 b) &= -\big(e^{-i\beta b} + R^s e^{i\beta b}\big)\langle u_1^s, \hat{\psi}_0\rangle + \hat{a}_0^s \cos(\mu_0 b)\langle u_2^s, \hat{\psi}_0\rangle. \end{aligned} \tag{3.2.57}$$

Next, $\hat{a}_0^s$ can be eliminated in the system above, by solving the second equation for $\hat{a}_0^s \cos(\mu_0 b)$ and substituting it into the first equation. Therefore,

$$\frac{i\beta h\big(e^{-i\beta b} - R^s e^{i\beta b}\big)}{e^{-i\beta b} + R^s e^{i\beta b}} = \frac{\langle u_1^s, \hat{\psi}_0\rangle\langle u_2^s, \psi_0\rangle}{\langle u_2^s, \hat{\psi}_0\rangle - \mu_0 d \tan(\mu_0 b)} - \langle u_1^s, \psi_0\rangle \equiv A^s \in \mathbb{R}\ , \tag{3.2.58}$$

where A^s is real since all the inner products in (3.2.58) are real. By rearranging, then

$$R^s = e^{-2i\beta b}\frac{i\beta h - A^s}{i\beta h + A^s}, \tag{3.2.59}$$

leaving the only unknown to the scattering problem to be A^s. One of the advantages of this method is that conservation of energy is automatically satisfied. This can be seen by using the fact that A^s is real and so $|R^s| = 1$. Note that once R^s is calculated from (3.2.59) then all the other unknown Fourier coefficients to the problem can be found. For example, $\hat{a}_0^s$ can be found from the system (3.2.57) and a_n^s and $\hat{a}_n^s$ from (3.2.55) by using the orthogonality of ψ_n, $\hat{\psi}_n$ accordingly. However, the interest of this section lies upon the reflection coefficient R^s only.

Now it remains to choose the unknown functions u_1^s and u_2^s appropriately. This is done using the Galerkin's method which involves an integral equation $\mathcal{K}u = f$ where $\mathcal{K}$ is an integral operator (equation of the (3.2.56) form). The approximate solution u can be expanded into some finite orthogonal basis u_n. The idea of this method is to assume that the error of that solution is orthogonal to the space of functions described by the expansion basis. That is

$$\left\langle \sum_{n=0}^{N} \sigma_n \mathcal{K} u_n - f, u_m \right\rangle = 0, \tag{3.2.60}$$

where σ_n are the unknown expansion coefficients and the first component of the

inner product is the solution error. From now on, the procedure follows from [72]. Therefore, by expanding the unknown functions in a finite orthogonal basis as $u_1^s(z) \approx \sum_{n=0}^{N} \sigma_n^s v_n^s(z)$ and $u_2^s(z) \approx \sum_{n=0}^{N} \tau_n^s v_n^s(z)$, with $\sigma_n^s, \tau_n^s, v_n^s \in \mathbb{R}$, then the equations $\langle u_1^s, K^s \rangle = \psi_0$ and $\langle u_2^s, K^s \rangle = \hat{\psi}_0$ become

$$\begin{gathered}\sum_{m=0}^{N} K_{nm}^s \sigma_m^s = F_{n0}^s \quad \text{and} \quad \sum_{m=0}^{N} K_{nm}^s \tau_m^s = \hat{F}_{n0}^s, \quad \text{for} \quad F_{nm}^s = \langle v_n^s, \psi_m \rangle, \\ \hat{F}_{nm}^s = \langle v_n^s, \hat{\psi}_m \rangle, \quad K_{nm}^s = \sum_{r=1}^{\infty} \left[\frac{F_{nr}^s F_{mr}^s}{\beta_r h} + \frac{\hat{F}_{nr}^s \hat{F}_{mr}^s}{\chi_r d \tanh(\chi_r b)} \right],\end{gathered} \tag{3.2.61}$$

after taking an inner product with $v_n^s(z)$. Now the continuous problem became discrete and that is the essence of this method. Note that the sum in K_{nm}^s, is really running over the purely imaginary dispersion roots of k_r and μ_r. Using the same procedure in (3.2.58), then

$$\begin{gathered}\tilde{A}^s \approx A^s = \frac{\left(\hat{\mathbf{f}}^s \cdot \boldsymbol{\sigma}^s\right)\left(\mathbf{f}^s \cdot \boldsymbol{\tau}^s\right)}{\left(\hat{\mathbf{f}}^s \cdot \boldsymbol{\tau}^s\right) - \mu_0 d \tan(\mu_0 b)} - \mathbf{f}^s \cdot \boldsymbol{\sigma}^s, \\ \text{for} \quad \left[\mathbf{f}^s\right]_n = F_{n0}^s, \quad \left[\hat{\mathbf{f}}^s\right]_n = \hat{F}_{n0}^s, \quad \left[\boldsymbol{\sigma}^s\right]_n = \sigma_n^s, \quad \left[\boldsymbol{\tau}^s\right]_n = \tau_n^s,\end{gathered} \tag{3.2.62}$$

where $\boldsymbol{\sigma}^s$ and $\boldsymbol{\tau}^s$ can be eliminated using the linear systems in(3.2.61). The $\tilde{A}^s$ term is a numerical approximation (because of the truncated/approximated solution) of A^s. Thus, by elimination

$$\tilde{A}^s \approx \frac{\left(\hat{\mathbf{f}}^{s^T} \mathbf{K}^{s^{-1}} \mathbf{f}^s\right)\left(\mathbf{f}^{s^T} \mathbf{K}^{s^{-1}} \hat{\mathbf{f}}^s\right)}{\left(\hat{\mathbf{f}}^{s^T} \mathbf{K}^{s^{-1}} \hat{\mathbf{f}}^s\right) - \mu_0 d \tan(\mu_0 b)} - \mathbf{f}^{s^T} \mathbf{K}^{s^{-1}} \mathbf{f}^s \quad \text{for} \quad \left[\mathbf{K}^s\right]_{nm} = K_{nm}^s. \tag{3.2.63}$$

It remains to choose the finite basis v_n^s. So from inner product definitions in (3.2.61),

$$\begin{aligned} F_{nm}^s &= N_m^{-1/2}\left[\cosh(k_m h)\int_{-d}^{0} v_n^s(z)\cosh(k_m z)dz + \sinh(k_m h)\int_{-d}^{0} v_n^s(z)\sinh(k_m z)dz\right], \\ \hat{F}_{nm}^s &= \hat{N}_m^{-1/2}\int_{-d}^{0} v_n^s(z)\cosh(r_m z)dz + \frac{K\hat{N}_m^{-1/2}}{r_m}\int_{-d}^{0} v_n^s(z)\sinh(r_m z)dz, \end{aligned} \tag{3.2.64}$$

after expanding the hyperbolic cosine term of $\psi_n(z)$. Now by writing $v_n^s(z) = f_n^{s'}(z)$, for $f_n^s(z) = \int_{-d}^{z} v_n^s(t)dt$ and integrating by parts the second terms of each equation in (3.2.64), then

$$\begin{aligned} F_{nm}^s &= N_m^{-1/2}\cosh(k_m h)\int_{-d}^{0}\left[v_n^s(z) - Kf_n^s(z)\right]\cosh(k_m z)dz, \\ \hat{F}_{nm}^s &= \hat{N}_m^{-1/2}\int_{-d}^{0}\left[v_n^s(z) - Kf_n^s(z)\right]\cosh(r_m z)dz, \end{aligned} \tag{3.2.65}$$

using $f_n^s(-d) = 0$ and $k_m\sinh(k_m h) = K\cosh(k_m h)$, from the dispersion relation. Therefore, a choice for $\hat{v}_n^s(z) \equiv v_n^s(z) - Kf_n^s(z)$ needed to be made.

Firstly, $\hat{v}_n^s$ must satisfy a Neumann's boundary condition on the surface as $v_n^{s'}(0) = Kv_n^s(0)$. Also, an analysis of the flow close to the edge of the barrier would reveal that $v_n^s(z) \sim (d^2 - z^2)^{-1/2}$ as $z \to -d^+$ (see the work of [72]). The same asymptotic behaviour must hold for $\hat{v}_n^s$. So an appropriate choice for $\hat{v}_n^s(z) \in \mathbb{R}$ satisfying the properties described above is

$$\hat{v}_n^s(z) = \frac{2(-1)^n}{\pi\sqrt{d^2 - z^2}}T_{2n}\Big(\frac{z}{d}\Big), \quad z \in L_g, \tag{3.2.66}$$

where the orthogonal functions T_{2n} for $n = 0, ..., N$, are the even Chebyshev polynomials of the first kind. These properties, namely $\hat{v}_n^{s'}(0) = 0$ and $\hat{v}_n^s(z) \sim (d^2 - z^2)^{-1/2}$ as $z \to -d^+$, can be verified using that $T_n'(x) = nU_{n-1}(x)$ straight from their trigono-

metric forms (where U_n are the Chebyshev polynomials of the second kind) and the special values $T_{2n}(0) = (-1)^n$, $T_{2n}(1) = 1$, $U_{2n-1}(0) = 0$ from [75] §22. Substituting (3.2.66) into (3.2.65), then

$$F^s_{nm} = (-1)^n N_m^{-1/2} \cosh(k_m h) I_{2n}(k_m d), \quad \hat{F}^s_{nm} = (-1)^n \hat{N}_m^{-1/2} I_{2n}(r_m d), \tag{3.2.67}$$

using the cosine integral transform for the even Chebyshev polynomial with respect to the weight function $(d^2-z^2)^{-1/2}$ from [76] §1.10 combined with $J_{2n}(ix) = (-1)^n I_{2n}(x)$ from [75] §9 (where J_n and I_n are the Bessel and Modified Bessel function respectively). Thus, R^s can be found from (3.2.59) with $A^s \approx \tilde{A}^s$ from (3.2.63), using F^s_{nm}, $\hat{F}^s_{nm}$ from (3.2.67).

The same procedure starting from (3.2.52), is followed for the antisymmetric problem as well. So after a considerable, but almost identical algebra, the expressions for $R^{s,a}$ and everything else needed for their calculation, are

$$\begin{gathered}
R^{s,a} = e^{-2i\beta b} \frac{i\beta h - A^{s,a}}{i\beta h + A^{s,a}} \text{ with } A^{s,a} \in \mathbb{R} \text{ which implies } |R^{s,a}| = 1, \\
\tilde{A}^s \approx A^s = \frac{\left(\hat{\mathbf{f}}^T \mathbf{K}^{s^{-1}} \mathbf{f}\right)\left(\mathbf{f}^T \mathbf{K}^{s^{-1}} \hat{\mathbf{f}}\right)}{\left(\hat{\mathbf{f}}^T \mathbf{K}^{s^{-1}} \hat{\mathbf{f}}\right) - \mu_0 d \tan(\mu_0 b)} - \mathbf{f}^T \mathbf{K}^{s^{-1}} \mathbf{f} \quad \text{for} \quad f_n = F_{n0}, \\
\tilde{A}^a \approx A^a = \frac{\left(\hat{\mathbf{f}}^T \mathbf{K}^{a^{-1}} \mathbf{f}\right)\left(\mathbf{f}^T \mathbf{K}^{a^{-1}} \hat{\mathbf{f}}\right)}{\left(\hat{\mathbf{f}}^T \mathbf{K}^{a^{-1}} \hat{\mathbf{f}}\right) + \mu_0 d \cot(\mu_0 b)} - \mathbf{f}^T \mathbf{K}^{a^{-1}} \mathbf{f} \quad \text{for} \quad \hat{f}_n = \hat{F}_{n0}, \\
F_{nm} = (-1)^n N_m^{-1/2} \cosh(k_m h) I_{2n}(k_m d), \quad \hat{F}_{nm} = (-1)^n \hat{N}_m^{-1/2} I_{2n}(r_m d), \\
K^s_{nm} = \sum_{r=1}^{\infty} \left[\frac{F_{nr} F_{mr}}{\beta_r h} + \frac{\hat{F}_{nr} \hat{F}_{mr}}{\chi_r d \tanh(\chi_r b)} \right], \quad K^a_{nm} = \sum_{r=1}^{\infty} \left[\frac{F_{nr} F_{mr}}{\beta_r h} + \frac{\hat{F}_{nr} \hat{F}_{mr}}{\chi_r d \coth(\chi_r b)} \right].
\end{gathered} \tag{3.2.68}$$

Note that the superscripts from $\mathbf{f}^{s,a}$, $\hat{\mathbf{f}}^{s,a}$, $F^{s,a}_{nm}$, $\hat{F}^{s,a}_{nm}$, were dropped as those expressions happen to coincide in both problems. Also, it is worth mentioning that the only impact of the lower metamaterial interface at $z = -c$ on the solution of this problem, is on the μ_n dispersion relation (3.2.48). However, the reflection and transmission for general metamaterial interfaces, can be found from (3.2.16) using the reflection coefficients specified in the previous equation.

3.2.5 Numerical results

In this section, computational results for the scattering problem of section 3.2.4 are provided. Note that the solution for the scattering coefficients $R^{s,a}$ can be found numerically only by truncating the vectors $\mathbf{f}$, $\hat{\mathbf{f}}$ and the square matrix $\mathbf{K}^{s,a}$ from (3.2.68) at some truncation parameter M, where $M+1$ represents the number of modes taken to the velocity expansion in $z \in L_g$. But since each element of the matrix $\mathbf{K}^{s,a}$ can be found through an infinite sum over the dispersion roots of the regions $|x| > b$ and $|x| < b$, then the infinite sum must be truncated at an independent truncation parameter N. Also, the energy conservation is satisfied for every choice of parameters as expected from $|R^{s,a}| = 1$.

N	$\lvert R\rvert$	M	$\lvert R\rvert$	N	$\lvert T\rvert$	M	$\lvert T\rvert$
8	0.06901334	2	0.07046862	8	0.91184888	2	0.910082293763
16	0.xxx41031	4	0.xxx11516	16	0.xx071942	4	0.xxx310297682
32	0.xxx91521	6	0.xxxx0149	32	0.xxx47045	6	0.xxxx25196762
64	0.x7007521	8	0.xxx09879	64	0.xxx37985	8	0.xxxx27834733
128	0.xxxx9161	10	0.xxxxx792	128	0.xxxx2969	10	0.xxxxx8425663
256	0.xxxxx707	12	0.xxxxxx57	256	0.xxxxx877	12	0.xxxxxx548724
512	0.xxxxxx33	14	0.xxxxxx37	512	0.xxxxxx59	14	0.xxxxxxx65945
1024	0.xxxxxxx4	16	0.xxxxxxx4	1024	0.xxxxxxx6	16	0.xxxxxxxxxxx6

Table 3.2: The geometrical parameters used for the reflection $|R|$ calculation are $(\theta_0, d/h, b/h, c/h, \theta, kb) = (30°, 0.9, 1, 2, 0.1, 0.2)$ and for the $|T|$ calculation are $(\theta_0, d/h, b/h, c/h, \theta, kb) = (60°, 0.1, 1, 1, 0, 1.5)$. When N is varying, M is fixed at 16 and when M is varying, N is fixed at 1024.

Moving to the truncation convergence table, one can see from 3.2 that the choice of $(N, M) = (1024, 16)$ gives a truncation error of at least 7 decimal places. It can be seen from the last column, the when the gap between the metamaterial structure and the free surface became smaller ($d/h = 0.1$), then fewer modes M were needed to get the accuracy of 7 decimal places. This is because M represents the number of modes needed to characterise the normal velocity through the gap L_g. Therefore, from now on the truncation parameters will be chosen to be $(N, M) = (1024, 16)$. The choice of N can be also be verified as the terms inside the infinite sum of $\mathbf{K}^{s,a}$ goes like r^{-2} as $r \to \infty$, (since $k_r, \mu_r \to r$, for sufficiently large r) and that the sum of the reciprocals of square numbers typically needs 2^{10} terms to converge to 7 decimal places of accuracy.

Starting from figure 3.7, the reflection modulus $|R|$ is plotted against the

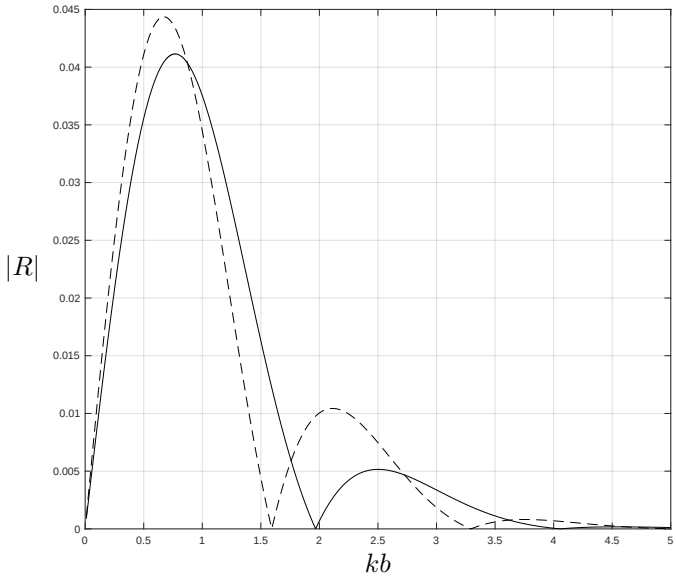

Figure 3.7: $|R|$ against kb, with $d/h = 0.9$, $c/h = b/h = 1$ and $\theta = 0$, for incident directions $\theta_0 = 45°$ (full) and $\theta_0 = 30°$ (dashed).

dimensionless wavenumber kb. It can be seen that the interaction for $\theta_0 = 30°$ is higher than the one of $\theta_0 = 45°$. As in the previous problem, this has to do with the incident wave sliding ability through the thin barriers (as $\theta = 0$). Also, $|R|$ shares a similar behaviour with the previous problem, as it passes through the origin, decays at infinity and it is oscillatory with a non-constant period in kb, for reasons explained in section 3.2.3.

Moving on to the interaction of obliquely-incident waves with a metamaterial sitting on a step, then the figure 3.8 is analysed. One can see that there is more interaction than previous figures due to the larger height of the barriers i.e., as in the limit $d \to 0$ the first barrier at $x = -b$ tends to be a block wall which implies total reflection. Also, the results of this section indicate a higher interaction than the ones of the previous problem because now the metamaterial has less openings than before and so the wave energy within it cannot easily transmitted. Even though the previous problem the barriers formed sharp corners to bed, they were only of length $l\theta$, but now the sharped cornered side of the barriers extend uniformly in the y-direction. Moreover, it can be seen again that for smaller incident angles there is a slightly higher interaction, but now the difference looks smaller due to higher barriers.

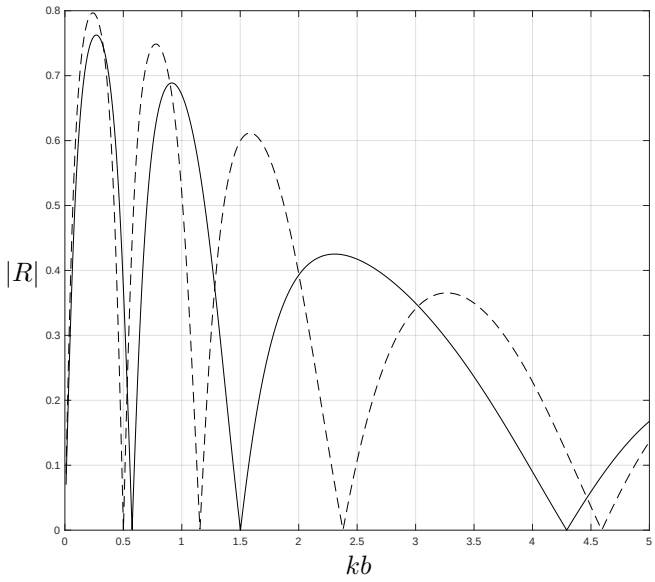

Figure 3.8: Variation of $|R|$ with kb, for $d/h = 0.1$, $c/h = 0.7$, $b/h = 1$ and $\theta = 0$, for incident directions $\theta_0 = 60°$ (full) and $\theta_0 = 30°$ (dashed).

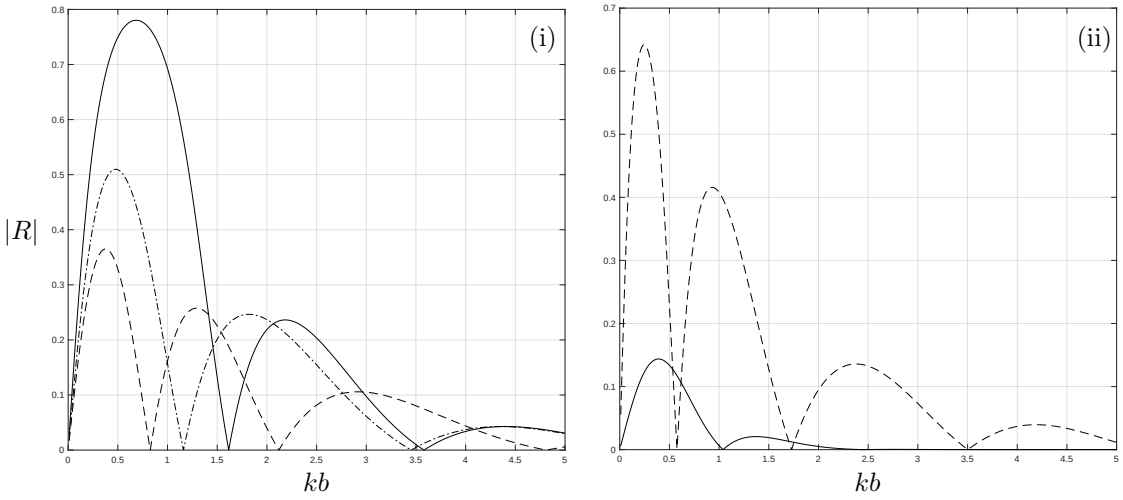

Figure 3.9: $|R|$ against kb for $\theta = 0$. The parameters are (i) $(\theta_0, d/h, b/h) = (45°, 0.3, 1)$ for $c/h = 2$ (full), 1 (chained), 0.5 (dashed) and (ii) $(\theta_0, c/h, b/h) = (0°, 1, 0.5)$ for $d/h = 0.7$ (full), 0.2 (dashed).

Next, the same type of curves ($|R|$ against kb) are shown in figure 3.9(i) to see how they are affected by c/h. The gap between the barriers and the free surface covers the top 30% of the fluid. The full line curve corresponds to "buried" (in the sea bed) barriers at a level twice the fluid's depth. The chained curve corresponds to barriers sitting on the bed while the dashed curve corresponds to barriers sitting on a step that occupies the lower 50% of the fluid. Therefore, the interaction increases with c/h as this parameter controls the height of the barriers.

Now figure 3.9(ii) shows how the metamaterial structure affects a normally incident wave ($\theta_0 = 0°$). The thin barriers ($\theta = 0$) now sit on the bed ($c/h = 1$) and the width of the structure is the same as the fluid's depth ($2b/h = 1$). For the full line curve, the barriers cover the lower 30% of the depth in the case of the dashed line curve, they cover 80%. It can be seen that in the case of higher barriers (dashed curve), the interaction is almost as large in figure 3.9(i) for $c/h = 2$. Normally, it should be expected to have more interaction in the current figure because the gap between the barriers and the free surface is smaller now (20% against 30%) and because the sliding ability of the incident wave within the barriers is weaker ($\theta_0 = 0°$ against $\theta_0 = 45°$). However the reason behind this, is that in the previous figure, the gaps between the barriers extend vertically downwards below the level of the bed i.e. $c/h > 1$.

Also, the curves of figure 3.9(ii) are invariant for any $\theta \in [0, 1]$ and $c \in (d, \infty)$ as the structure behaves like a rigid step in the case of normal incidence and thus the parameters that characterise the medium within its domain do not affect the solution. These results were compared with the analogous results of the rigid step problem and it turned out that they were identical. The technique used to solve that problem is again the Galerkin method (described in section 3.2.4), where the potential in $x < -b$ is the same and the potential in $x \in (-b, 0)$ can be sought be separating variables in $z \in (-d, 0)$ and applying the free surface condition at $z = 0$ and the no flow condition at $z = -d$. This will imply that the solution in $x \in (-b, 0)$ is again (3.2.51) but now the vertical eigenfunctions are $\hat{\psi}_n(z) = \hat{N}_n^{-1/2} \cosh\big[\mu_n(z+d)\big]$, with $\mu_n \tanh(\mu_n d) = K$ (wave dispersion relation over a constant rigid bed at $z = -d$). The normalisation factor is chosen to be $\hat{N}_n = \frac{1}{2} + \frac{\sinh(2\mu_n d)}{4\mu_n d}$ so that $\int_{-d}^{0} \hat{\psi}_n \hat{\psi}_m dz = d\delta_{nm}$. Therefore, by following the same solution method as before, then the scattering coefficient curves were found to be identical in the case of $\theta_0 = 0°$.

Next figure 3.10 shows how the reflection modulus is affected by the incident direction θ_0. Even though the figures are plotted in $\theta_0 \in (0°, 90°)$, it was shown analytically before (and verified numerically as well) that the problem is symmetric about $\theta_0 = 0°$. Thus $|R|$ is even in θ_0. Firstly, it can be verified that as $\theta_0 \to 90°$ then $|R| \to 0$ as expected from the sliding ability of the incident wave through the barriers.

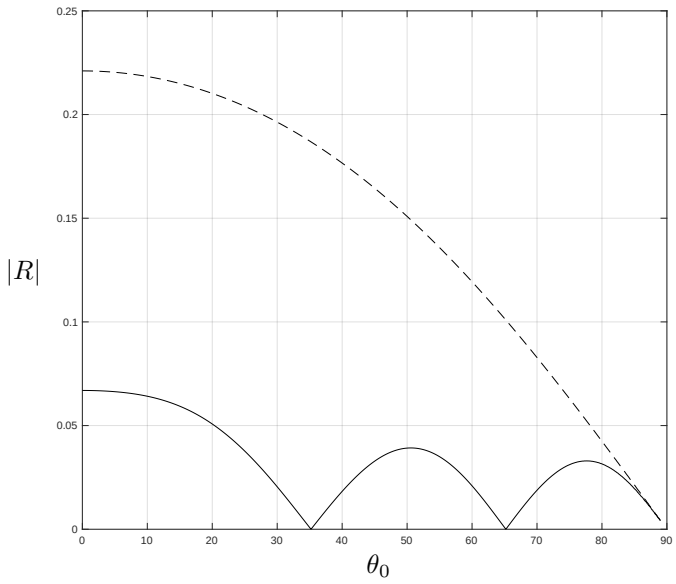

Figure 3.10: $|R|$ against θ_0, with $d/h = 0.5$, $c/h = b/h = 1$ and $\theta = 0$ for $kb = 3$ (full) and $kb = 0.2$ (dashed).

The full line curve that corresponds to a smaller incident wavelength ($kb = 3$) has a larger number of zeros than the dashed curve ($kb = 0.2$) due to the effect of the wave multiple interference.

[1] considered the same problem but in the shallow water regime, with barriers sitting on a step and oriented in the same way as here ($\delta = 90°$). But numerical comparisons between the 3D problem (full linear theory) analysed here and [1][16], will follow in section 3.3.4, where the numerics of a shallow water model introduced in this thesis are included.

Now, a surface plot of the total wave field will be demonstrated in figure 3.11(i). A long obliquely-incident wave ($kb = 0.8$ and $\theta_0 = 30°$) interacts with the high, thin barriers ($d/h = 0.1$ and $\theta = 0$) that sit on the bed ($c/h = 1$). Again the surface elevation is found from $\zeta(x, y, t) = -(\omega/g)\Im\{\phi(x, 0)e^{i\alpha y}e^{-i\omega t}\}$ and $\phi = (\phi^s + \phi^a)/2$. A similar wave behaviour with the previous problem can be seen here, as there is again a transmitted wave in $x > b$ travelling parallel to the direction of incidence and in $x < -b$ there is a doubly periodic configuration of nodes and antinodes due the interaction of the incident wave and the reflection mode. The direction of the phase speeds in $|x| < b$ were found to be $\theta_p^{(1)} \approx 11.45°$ with $\theta_p^{(2)} = -\theta_p^{(1)}$ from the symmetry of the real roots μ_n of the dispersion relation

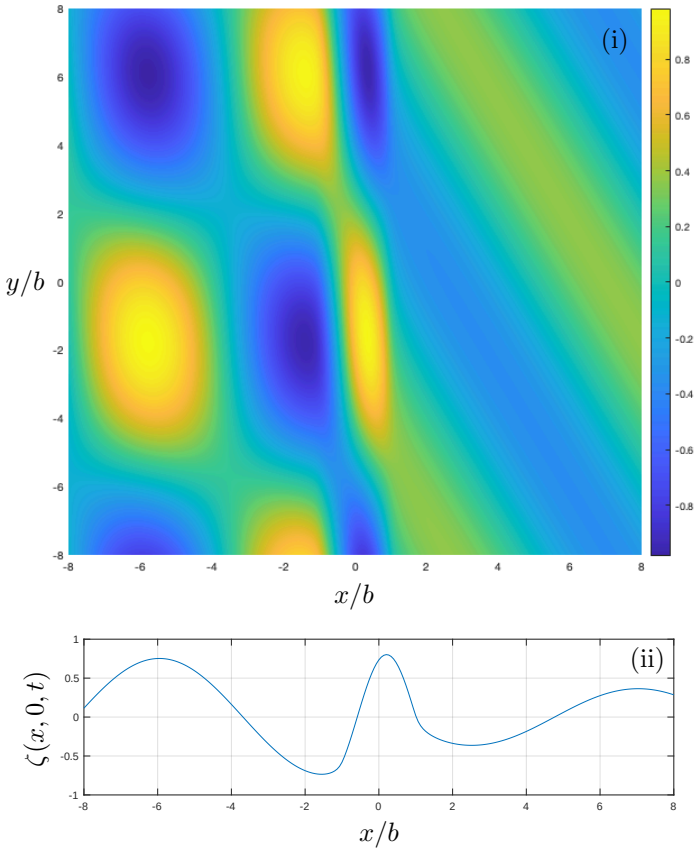

Figure 3.11: (i) Instantaneous surface elevation and (ii) wave profile at $y = 0$ for $kb = 0.8$, $\theta_0 = 30°$, $d/h = 0.1$, $c/h = b/h = 1$ and $\theta = 0$.

(3.2.48). However, the arbitrary barrier orientation of the two next problems, will allow us to direct the wave in a more straightforward way. The surface cross-section at $y = 0$ is shown in figure 3.11(ii). Again the curve is continuous and smooth at $x/b = \pm 1$ as expected from the corresponding matching conditions of $\phi^{s,a}(x, 0)$ at $x = \pm b$. The transmitted wave energy was found to be $|T|^2 \approx 42\%$ of the incident wave energy.

3.2.6 Barriers oriented at an acute angle

Finally, in this section the solution to the full linear problem of a general barrier orientation is presented (see figure 3.1). Now the geometry is not symmetric about the $x = 0$ plane and so the decomposition of the problem into even and odd parts, is not allowed as now ∂_{XX} is not invariant if x is replaced with $-x$ (see equations (3.2.1), (3.2.7)). However, the y and t dependence of the potential can be factored out of the model through $e^{i\alpha y}e^{-i\omega t}$, due to the assumption that the incident wave is time-harmonic and it is compatible with the total field in the y-direction. Therefore, due to the asymmetry of the problem, the solution into the regions $x < -b$, $|x| < b$ and $x > b$ must be considered with ϕ_1, ϕ_2 and ϕ_3 the velocity potentials in those regions respectively. Therefore, in the regions outside the metamaterial, the potentials must be solutions to (3.2.9), (3.2.10), namely

$$\begin{aligned} \phi_1(x,z) &= e^{i\beta x}\psi_0(z) + \sum_{n=0}^{\infty} a_n e^{\beta_n(x+b)}\psi_n(z) \quad \text{in } x < -b, \\ \phi_3(x,z) &= \sum_{n=0}^{\infty} \tilde{a}_n e^{-\beta_n(x-b)}\psi_n(z) \quad \text{in } x > b, \end{aligned} \tag{3.2.69}$$

using separation of variables, with β_n and ψ_n be defined in (3.2.22), $\beta_0 = -i\beta$ and $R = a_0 e^{-i\beta b}$, $T = \tilde{a}_0 e^{-i\beta b}$ for convention. Note that the y-independent potentials outside the metamaterial region are even in θ_0. However, it cannot be concluded that the scattering coefficients are θ_0-symmetric as well, as it is not known if the potential within $|x| < b$ is symmetric in θ_0 or not.

Now again the regions above and inside the metamaterial must be considered within $|x| < b$. By assuming only the time-harmonicity of the total potential, without dropping y-dependence yet, the solution in $z \in L_b$ must satisfy $\big(\partial_{XX} + \partial_{zz}\big)\phi(X,Y,z) = 0$ according to (3.2.7). Here, the (X,Y) coordinates can be found by rotating counterclockwise (x,y) by an angle δ so that X is aligned with the barrier direction, i.e. see equation (3.2.1). Therefore, by expressing this differential equation into Cartesian coordinates and then dropping y through $e^{i\alpha y}$, it yields that

$$\begin{gathered} \big(\nabla^2 - \alpha^2\big)\phi_2(x,z) = 0\ , \quad \partial_z\phi_2(x,0) = K\phi_2(x,0) \quad \text{in} \quad z \in L_g, \\ \Big[\cos^2\delta\partial_{xx} + 2i\alpha\sin\delta\cos\delta\partial_x - \alpha^2\sin^2\delta + \partial_{zz}\Big]\phi_2(x,z) = 0, \\ \partial_z\phi_2(x,-h) = 0 \quad \text{in} \quad z \in L_b, \end{gathered} \tag{3.2.70}$$

using $\partial_X = \cos\delta\partial_x + \sin\delta\partial_y$. It can also be seen that when $\delta = 0°, 90°$, then the model simplifies to the ones specified in sections 3.2.2 and 3.2.4 respectively. Seeking solutions of the form $e^{i\mu x}Z(z)$ (equivalent of separating variables with $-\mu^2$ the separation constant), then

$$\begin{aligned} Z_g''(z) &= (\alpha^2+\mu^2)Z_g(z), \quad Z_g'(0) = K Z_g(0), \\ Z_b''(z) &= (\alpha\sin\delta + \mu\cos\delta)^2 Z_b(z), \quad Z_b'(-h) = 0, \end{aligned} \tag{3.2.71}$$

where the depth functions are matched through $z = -d$ via the first two equations of (3.2.8). The solutions of these ordinary differential equations, after the application of their boundary conditions, are

$$\begin{aligned} Z_g(z) &= A_g\left[\cosh\left(z\sqrt{\alpha^2+\mu^2}\right) + \frac{K}{\sqrt{\alpha^2+\mu^2}}\sinh\left(z\sqrt{\alpha^2+\mu^2}\right)\right], \\ Z_b(z) &= A_b\cosh\Big[(\alpha\sin\delta+\mu\cos\delta)(z+h)\Big], \end{aligned} \tag{3.2.72}$$

with the dispersion relation, coming from the matching across the horizontal interface, be

$$\begin{aligned} &\gamma(1-\theta)\tanh[\gamma(h-d)]\left(\frac{K\tanh\left(d\sqrt{\alpha^2+\mu^2}\right)}{\sqrt{\alpha^2+\mu^2}} - 1\right) \\ &\qquad = \sqrt{\alpha^2+\mu^2}\tanh\left(d\sqrt{\alpha^2+\mu^2}\right) - K, \end{aligned} \tag{3.2.73}$$

where $\gamma = \alpha\sin\delta + \mu\cos\delta$.

It will be shown in Appendix A.2, that for a general acute angle δ, there will be exactly two real and non-symmetric roots (one positive and one negative). However when $\delta = 0°$, $90°$, these roots becomes symmetric as the dispersion relation becomes even (this can be seen from the μ-relations of the previous two problems). Also, at the δ endpoints, it will be shown by substituting $\mu = iy$ in the dispersion relation, that there is a symmetric infinite sequence of purely imaginary roots. But for a general $\delta \in (0°, 90°)$, if $\mu = iy$ is substituted in (3.2.73), then the dispersion relation will still have i in it due to the asymmetry of γ, suggesting the existence of complex roots. At least those complex roots will be symmetric about the real axis as if the dispersion relation is written in the form $F(\mu) = 0$, then it will satisfy $F(\overline{\mu}) = \overline{F(\mu)}$.

Those roots will be analysed in Appendix A.2. Note that the complexity of the roots is not happening at the δ endpoints as γ reduces to μ or α, making $\mu \tanh[\mu(h-d)]$ or $\alpha \tanh[\alpha(h-d)]$ real under $\mu = iy$.

Therefore at a first glance, the potential cannot be written in a semi-infinite sum over μ_n. However, if the roots of the dispersion relation are divided into two sets, say into positive and negative imaginary parts, then the solution can be written as a sum that runs from $n = 0$ to $n = \infty$ over those two sets. This allows the matching across $x = \pm b$ to be simplified as the potentials outside that region are again written in semi-infinite sums. By introducing the notation of $\mu_n^{(1)}$ to be the sequence containing the single positive real root ($n = 0$) and the complex roots with positive imaginary parts ($n \in \mathbb{N}$) and similarly $\mu_n^{(2)}$ containing the single negative real root ($n = 0$) and the complex roots with negative imaginary parts ($n \in \mathbb{N}$), then the solution within $|x| < b$ becomes

$$\begin{aligned} \phi_2(x,z) &= \sum_{n=0}^{\infty} \left[\hat{a}_n e^{i\mu_n^{(1)}(x+b)} \hat{\psi}_n^{(1)}(z) + \hat{b}_n e^{i\mu_n^{(2)}(x-b)} \hat{\psi}_n^{(2)}(z) \right], \\ \hat{\psi}_n^{(i)}(z) &= \begin{cases} \hat{D}_n^{(i)} \left(\cosh(r_n^{(i)} z) + \frac{K}{r_n^{(i)}} \sinh(r_n^{(i)} z) \right), & z \in L_g, \\ \cosh\left[\gamma_n^{(i)}(z+h) \right], & z \in L_b, \end{cases} \end{aligned} \tag{3.2.74}$$

where $r_n^{(i)} = \sqrt{\alpha^2 + {\mu_n^{(i)}}^2}$ and $\gamma_n^{(i)} = \alpha \sin\delta + \mu_n^{(i)} \cos\delta$ for $i = 1, 2$. The rescaling of the exponentials guarantees a decaying behaviour at $x = \pm b$ as n becomes large which is an efficient trick for numerical purposes (an approach taken into the previous simpler problems as well). The coefficient of the depth function over L_b was chosen as

$$\hat{D}_n^{(i)} = \frac{r_n^{(i)} \cosh\left[\gamma_n^{(i)}(h-d)\right]}{r_n^{(i)} \cosh\left(r_n^{(i)} d\right) - K \sinh\left(r_n^{(i)} d\right)}. \tag{3.2.75}$$

This can be derived by substituting $A_g = 1$ in the continuity condition of the depth functions in (3.2.72) at $z = -d$. The matching across the vertical interfaces $x = \pm b$ will be executed using the orthogonality of ψ_n as there is not a clear way on how to find the inner product associated with the orthogonality of $\hat{\psi}_n^{(i)}$. Also, here it is not obvious that the potential ϕ_2 is even in θ_0, from the asymmetry of the dispersion relation satisfied by $\mu_n^{(i)}$. However, it will be verified numerically later that the scattering coefficients are even in θ_0.

The unknown coefficients $a_n, \tilde{a}_n, \hat{a}_n, \hat{b}_n$, will be found by matching ϕ_1 and ϕ_3 with ϕ_2 across $x = \pm b$ using the pressure and normal flux conditions determined in (3.2.8). Expressing them in unrotated coordinates using $\partial_X = \cos\delta\partial_x + \sin\delta\partial_y$ and then using the fact that the y-dependence is contained in the multiplicative factor $e^{i\alpha y}$, then they become

$$\begin{aligned}
\phi(\pm b^{\pm}, z) &= \phi(\pm b^{\mp}, z), \quad \text{in} \quad z \in L_g \cup L_b, \\
\phi_x(\pm b^{\pm}, z) &= \begin{cases} \phi_x(\pm b^{\mp}, z), & z \in L_g, \\ (1-\theta)\cos\delta\Big[\cos\delta\phi_x(\pm b^{\mp}, z) + i\alpha\sin\delta\phi(\pm b^{\mp}, z)\Big], & z \in L_b, \end{cases}
\end{aligned} \tag{3.2.76}$$

where the subscripts of the potential ϕ_i (for $i = 1, 2, 3$) were removed but they can be retained depending on the evaluation of x. These four equations after been multiplied by ψ_m and integrated throughout the depth, become

$$\begin{aligned}
e^{-i\beta b}\delta_{n0} + a_n &= \sum_{m=0}^{\infty}\Big[\hat{a}_m W_{nm}^{(1)} + \hat{b}_m e^{-2i\mu_m^{(2)}b} W_{nm}^{(2)}\Big], \\
\tilde{a}_n &= \sum_{m=0}^{\infty}\Big[\hat{a}_m e^{2i\mu_m^{(1)}b} W_{nm}^{(1)} + \hat{b}_m W_{nm}^{(2)}\Big], \\
-e^{-i\beta b}\delta_{n0} + a_n &= i\sum_{m=0}^{\infty}\frac{1}{\beta_n}\Big[\mu_m^{(1)}(G_{nm}^{(1)} + (1-\theta)\cos^2\delta B_{nm}^{(1)}) + \alpha(1-\theta)\sin\delta\cos\delta B_{nm}^{(1)}\Big]\hat{a}_m \\
&+ i\sum_{m=0}^{\infty}\frac{e^{-2i\mu_m^{(2)}b}}{\beta_n}\Big[\mu_m^{(2)}(G_{nm}^{(2)} + (1-\theta)\cos^2\delta B_{nm}^{(2)}) + \alpha(1-\theta)\sin\delta\cos\delta B_{nm}^{(2)}\Big]\hat{b}_m, \\
-\tilde{a}_n &= i\sum_{m=0}^{\infty}\frac{e^{2i\mu_m^{(1)}b}}{\beta_n}\Big[\mu_m^{(1)}(G_{nm}^{(1)} + (1-\theta)\cos^2\delta B_{nm}^{(1)}) + \alpha(1-\theta)\sin\delta\cos\delta B_{nm}^{(1)}\Big]\hat{a}_m \\
&+ i\sum_{m=0}^{\infty}\frac{1}{\beta_n}\Big[\mu_m^{(2)}(G_{nm}^{(2)} + (1-\theta)\cos^2\delta B_{nm}^{(2)}) + \alpha(1-\theta)\sin\delta\cos\delta B_{nm}^{(2)}\Big]\hat{b}_m,
\end{aligned} \tag{3.2.77}$$

where $W_{nm}^{(i)}$ will be given by the complicated but explicit integral

$$W_{nm}^{(i)} \equiv \frac{1}{h}\int_{-h}^{0} \psi_n(z)\hat{\psi}_m^{(i)}(z)dz = G_{nm}^{(i)} + B_{nm}^{(i)}$$

$$\begin{aligned}
&= \frac{N_n^{-1/2}}{\left(k_n^2 - {r_m^{(i)}}^2\right)h}\left[(1-\theta)\gamma_m^{(i)}\cosh\left[k_n(h-d)\right]\sinh\left[\gamma_m^{(i)}(h-d)\right]\right] \\
&\quad -\frac{N_n^{-1/2}}{\left(k_n^2 - {r_m^{(i)}}^2\right)h}\left[k_n\sinh\left[k_n(h-d)\right]\cosh\left[\gamma_m^{(i)}(h-d)\right]\right] \\
&\quad +\frac{N_n^{-1/2}}{\left(k_n^2 - {\gamma_m^{(i)}}^2\right)h}\left[k_n\sinh\left[k_n(h-d)\right]\cosh\left[\gamma_m^{(i)}(h-d)\right]\right] \\
&\quad -\frac{N_n^{-1/2}}{\left(k_n^2 - {\gamma_m^{(i)}}^2\right)h}\left[\gamma_m^{(i)}\cosh\left[k_n(h-d)\right]\sinh\left[\gamma_m^{(i)}(h-d)\right]\right],
\end{aligned} \tag{3.2.78}$$

where $G_{nm}^{(i)}$ are the first two terms which come from integral over L_g, $B_{nm}^{(i)}$ are the last two terms which come from the integral over L_b and so $W_{nm}^{(i)}$ comes from the integral over the whole depth. Therefore, by writing (3.2.77) in vectorial form and solving it, then

$$\begin{aligned}
\hat{\mathbf{a}} &= 2e^{-i\beta b}\left[\left(\mathbf{W^{(1)}} - \mathbf{R^{(1)}}\right) - \left(\mathbf{Q^{(2)}} - \mathbf{S^{(2)}}\right)\left(\mathbf{W^{(2)}} + \mathbf{R^{(2)}}\right)^{-1}\left(\mathbf{Q^{(1)}} + \mathbf{S^{(1)}}\right)\right]^{-1}\mathbf{J}, \\
\hat{\mathbf{b}} &= 2e^{-i\beta b}\left[\left(\mathbf{Q^{(2)}} - \mathbf{S^{(2)}}\right) - \left(\mathbf{W^{(1)}} - \mathbf{R^{(1)}}\right)\left(\mathbf{Q^{(1)}} + \mathbf{S^{(1)}}\right)^{-1}\left(\mathbf{W^{(2)}} + \mathbf{R^{(2)}}\right)\right]^{-1}\mathbf{J}, \\
\mathbf{a} &= \mathbf{W^{(1)}}\hat{\mathbf{a}} + \mathbf{Q^{(2)}}\hat{\mathbf{b}} - e^{-i\beta b}\mathbf{J}, \\
\tilde{\mathbf{a}} &= \mathbf{Q^{(1)}}\hat{\mathbf{a}} + \mathbf{W^{(2)}}\hat{\mathbf{b}},
\end{aligned} \tag{3.2.79}$$

where the matrices and vectors above, are defined as

$$J_n = \delta_{n0}, \quad Q_{nm}^{(i)} = e^{-2i(-1)^i \mu_m^{(i)} b} W_{nm}^{(i)},$$
$$R_{nm}^{(i)} = \frac{i}{\beta_n}\Big[\mu_m^{(i)}(G_{nm}^{(i)} + (1-\theta)\cos^2\delta B_{nm}^{(i)}) + \alpha(1-\theta)\sin\delta\cos\delta B_{nm}^{(i)}\Big], \tag{3.2.80}$$
$$S_{nm}^{(i)} = e^{-2i(-1)^i \mu_m^{(i)} b} R_{nm}^{(i)}.$$

Therefore, the scattering coefficients of the problem can be found using just the first components of the vectors $\mathbf{a}$, $\tilde{\mathbf{a}}$, namely $R = a_0 e^{-i\beta b}$ and $T = \tilde{a}_0 e^{-i\beta b}$.

3.2.7 Numerical results

In this section, numerical results for the problem solved in section 3.2.6 are provided. The scattering coefficients convergence with respect to the single truncation parameter associated with the infinitude of the scattering coefficients (see equation (3.2.79)) is tested in table 3.3. The data shows two different cases of low frequency and high frequency for barriers covering 75% of the water depth. At lower frecuencies we expect fluid velocities to decrease less rapidly with the depth than at higher frequencies. It is therefore typical that more depth functions are needed to resolve the interaction with the submerged metamatarial for lower frequencies. However, this expected feature is not particularly shown in the table results as they show that only a few modes are required for 2 or 3 decimal place accuracy. Also, the table includes the values of $|E|$ where $E = 1 - |R|^2 - |T|^2$ and conservation of energy demands $E = 0$. It seems from the table and other computations performed in the preparation of this section, that energy conservation is automatically satisfied for normal incidence and is only used as an indicator of convergence for values $\theta_0 \neq 0$. The numerical convergence is much slower for extreme choices of parameters such as $\theta \to 1$, $d/h \to 0$ or $\delta \to 90°$. For example, for $\delta = 89°$, $kb = 2.5$, $d/h = 0.1$, $\theta = 0.9$ and $b/h = 1$, we find that $|E| = 3.8 \times 10^{-3}$ for $N = 64$ and $|E| = 2.2 \times 10^{-3}$ for $N = 128$. In the figures that follow, we choose N depending on the choice of these parameters to display accurately certain types of curves.

In figure 3.12 we examine the variation of the reflection modulus against the dimensionless wavenumber kb. Similar features of these curves can be found in the previous problems, such as the oscillatory behaviour with a non-constant period in kb, passing through the origin, decay for large wavenumbers and interaction proportional

N	$\|R\|$	$\|E\|$	$\|R\|$	$\|E\|$
4	0.162670	10^{-16}	0.139759	8.1×10^{-6}
8	0.xxx727	10^{-16}	0.xxx991	1.7×10^{-6}
16	0.xxxx43	10^{-16}	0.140059	3.5×10^{-8}
32	0.xxxxx6	10^{-15}	0.xxxx77	2.5×10^{-8}
64	0.xxxxx7	10^{-16}	0.xxxx82	2.8×10^{-9}

Table 3.3: Scattering coefficients convergence against truncation size N for two set of parameters. Namely, $(kb, \theta_0) = (0.25, 0^\circ)$ for the first two columns and $(kb, \theta_0) = (2.5, 60^\circ)$ for the last two with common variables $(d/h, \delta, b/h, \theta) = (0.25, 60^\circ, 1, 0.1)$.

to the barriers height (short barriers in figure 3.12(i) and large barriers in 3.12(ii)). The array consists of thin barriers ($\theta = 0$) and has a width twice the depth ($2b = 2h$). In figure 3.12(i), the short barriers ($d/h = 0.9$) are oriented at an angle $\delta = 60^\circ$ and the two curves represent incident angles of $\theta_0 = 45^\circ$ (full line) and $\theta_0 = 30^\circ$ (dashed line). As in the previous problems, the reflection becomes generally smaller for incident directions that are closer to the barrier orientation or in other words the sliding ability of the incident wave increases as $\theta_0 \to \delta$. A variety of geometrical cases was tested for $\theta_0 = \delta$ and the result was total transmission (or zero reflection). The increase of interaction due to the change of incident direction, is even larger in the case of high barriers (see figure 3.12(ii) where $d/h = 0.2$). Also, it was shown that as δ approached 0° and 90°, then the curves were approaching to the ones of section 3.2.3 and 3.3.5 respectively. This is because of the alignment of the roots of the corresponding dispersion relations (the path of the dispersion roots as δ varies will be shown in Appendix A.2).

Next, figure 3.13 indicates how the reflection coefficient varies with kb. In 3.13(i) a normally incident wave ($\theta_0 = 0^\circ$) interacts with the submerged barriers oriented at an angle $\delta = 45^\circ$. The dashed line corresponds to thick barriers ($\theta = 0.8$) and the full line to thinner ($\theta = 0.2$). One can see that as $\theta \to 1$, the features tend to the rigid step analogues found in the results of the previous section (maintained through normal incidence due to the particular barrier orientation i.e. $\delta = 90^\circ$).

In figure 3.13(ii) an obliquely-incident wave ($\theta_0 = -45^\circ$) now interacts with thin barriers ($\theta = 0$) of larger height ($d/h = 0.1$). Different curves correspond to different barrier orientations δ. It can be verified that as $\delta \to -\theta_0$ there is total transmission (no reflection). This is the "transparency" property shown in [11] but now it seems to hold for barriers that extend partially through the depth as well.

Moving on, the figures found in 3.14 indicate the surface plots of the free elevation $\zeta(x, y, t) = -(\omega/g)\Im\{\phi(x, 0)e^{i\alpha y}e^{-i\omega t}\}$. The barrier configuration is chosen

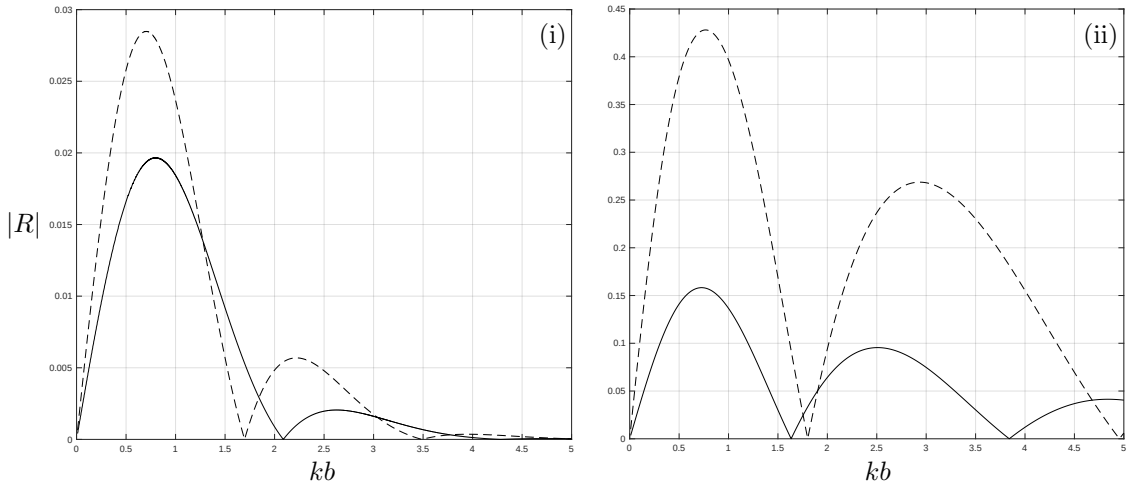

Figure 3.12: (i) $|R|$ against kb, with $\delta = 60°$, $d/h = 0.9$, $b/h = 1$ and $\theta = 0$ for $\theta_0 = 45°$ (full) and $\theta_0 = 30°$ (dashed). (ii) Same result but with $\delta = 30°$, $d/h = 0.2$, $b/h = 1$ and $\theta = 0$ for $\theta_0 = 45°$ (full) and $\theta_0 = 60°$ (dashed).

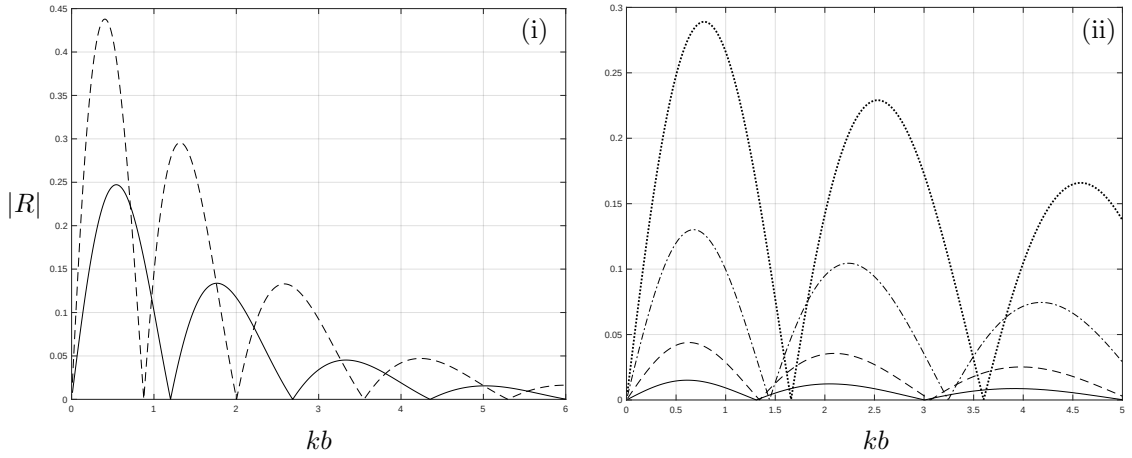

Figure 3.13: $|R|$ against kb for $b/h = 1$. In (i) the parameters are $(\theta_0, d/h, \delta) = (0°, 0.3, 45°)$ for $\theta = 0.2$ (full) and $\theta = 0.8$ (dashed) and in (ii) $(\theta_0, d/h, \theta) = (-45°, 0.1, 0)$ for $\delta = 10°$ (dotted), $\delta = 35°$ (chained), $\delta = 42°$ (dashed) and $\delta = 44°$ (full).

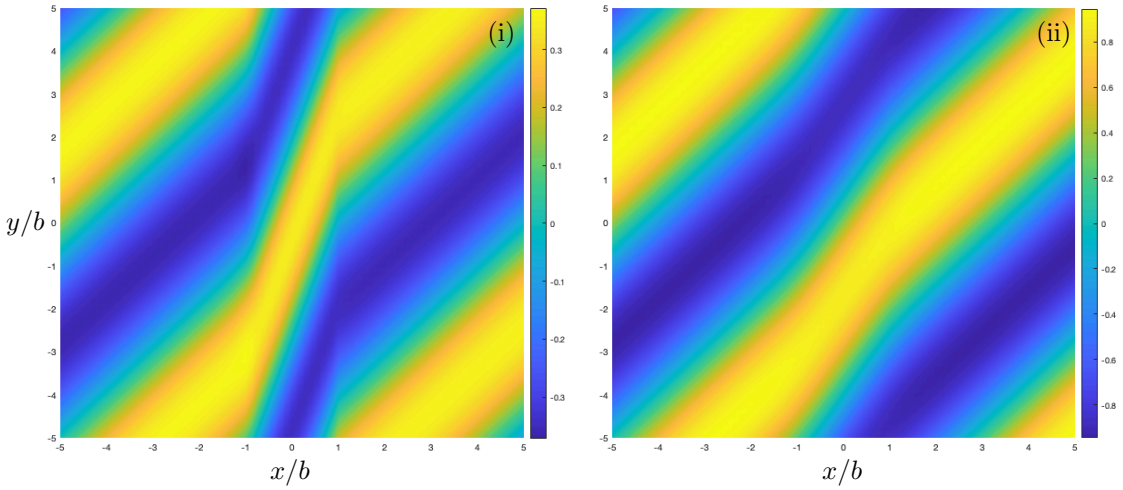

Figure 3.14: Instantaneous surface elevation for (i) $d/h = 0.02$ and (ii) $d/h = 0.5$. The common parameters are $kb = 1$, $\theta_0 = -\delta = -45°$, $b/h = 1$ and $\theta = 0$.

such that $\theta_0 = -\delta$ and $\theta = 0$. In this case it was numerically verified that $R \approx 0$ and $|T| \approx 1$ for a variety of geometrical parameters. This is the transparency property specified in [11], where the thin barriers ($\theta = 0$) were extended throughout the depth. In that paper, the vertical uniformity allowed closed-form solutions to the reflection and transmission coefficients (due to the independence from the vertical coordinate), showing the transparency property analytically. However, in the following sections when the simplification of the shallow water regime will be used (again the model will become independent of the vertical coordinate), then closed-form solutions to the scattering coefficients will be yielded, even though the barriers will extend partially though the depth. Now in the figure 3.14, the geometrical parameters are $\theta_0 = -\delta = -45°$, $b/h = 1$, $kb = 1$ and $\theta = 0$. The only difference between figure 3.14(i) and 3.14(ii), is that in the first the barriers cover the 98% of the fluid's depth, but only the 50% in the second. Figure 3.14(i) shows that this problem converges to the one with the fully-extended barriers as the surface plot looks identical with [11], Fig. 2. However, in our case the transparency property appears to hold for any barrier height and $\theta = 0$. The only thing that changes is the bending of the wave towards the barrier orientation. Therefore, the negative refraction effect that occurs always for $\theta_0 = -\delta$ and $d/h \to 0$ (as specified in [11]), seems to fade away as $d \to h$. This is expected on physical grounds as in the limit $d \to h$ the structure "disappears" and the wave is transmitted unaffected. Unfortunately here, there is no direct way to calculate a value for the wave phase speeds within $|x| < b$ of figure 3.14. In the

previous problems (sections 3.2.2 and 3.2.4) $\pm\mu_n$ was real for $n = 0$, corresponding to travelling waves of phase speed direction $\pm\arctan(\alpha/\mu_0)$, and purely imaginary for $n \in \mathbb{N}$ corresponding to evanescent modes that have no effect on the phase speed. However, in this problem, even though the roots of the dispersion relation are real for $n = 0$, they become complex for $n \in \mathbb{N}$ (lying in the complex quadrants). Therefore the calculation of the phase speeds in $|x| < b$ becomes more difficult as these waves are comprised of an infinite number of travelling waves (with a decaying part as well from the $\mu_n^{(i)}$ complexity). The rate at which the negative refraction phenomenon fades away with the barrier height, will be seen in the next sections, where the same problem is considered but under the shallow water approximation.

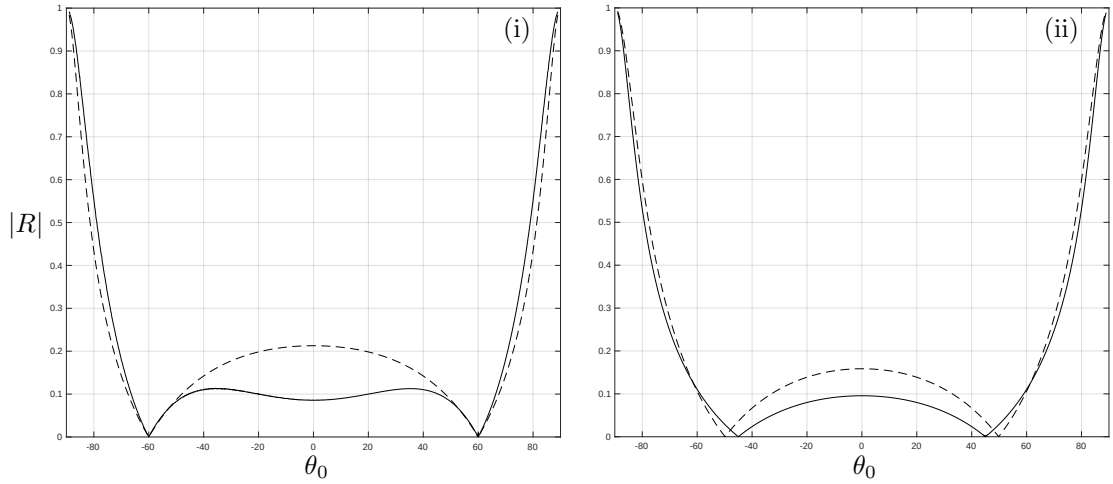

Figure 3.15: Variation of $|R|$ with θ_0. In (i) $d/h = 0.5$, $b/h = 1$, $\theta = 0$ and $\delta = 60°$ with $kb = 1$ (full) and $kb = 0.5$ (dashed) and in (ii) $kb = 0.5$, $d/h = 0.6$, $b/h = 1$ and $\delta = 45°$ with $\theta = 0$ (full) and $\theta = 0.5$ (dashed).

Moving on, the variation of $|R|$ with respect to θ_0 is shown in figure 3.15. The modulus of the scattering coefficients seems to be even in θ_0. This is a property shown analytically in [11] for $d \to 0$ and it will be shown to hold in the shallow water regime later. Also, the figures indicate that in the limit $\theta_0 \to \pm 90°$ there is a total reflection and that in the case of thin barriers ($\theta = 0$), there are exactly two symmetric zeros at $\theta_0 = \pm\delta$ (transparency property discussed above). However as θ increases from zero, then these two roots are shifted. This happens due to the fact that as $\theta \to 1$, the metamaterial behaves like a rigid step and therefore the zeros of the reflection coefficient will be shifted.

3.3 Shallow water approximation

3.3.1 Effective medium equations

In this section, we will consider waves that are long with respect to the depth and allow the depth of the fluid and variations of the height of the plate array to vary slowly with respect to space (compared to the wavelength). Under these assumptions, a shallow water model can be developed in which depth averaging leads to a 2D governing equation in two horizontal space dimensions in which the effect of the varying depth is captured in the coefficients of the differential equation. Thus, we can consider a much broader class of problems than in the previous sections but will be restricted to long waves.

From the work of [15][77], in the absence of any structure in the fluid's domain, the linear shallow water equation for the surface elevation $\zeta(x, y, t)$ bounded below by a space-varying sea bed at $z = -h(x, y)$ under the action of gravity g is $\zeta_{tt} = g\nabla\cdot(h\nabla\zeta)$ to leading order of the small parameter $(H/L)^2$ (depth to wavelength ratio). Under this description the wave is non-dispersive and its speed is $\sqrt{gh}$. The long wave limit was assumed (wavelengths much larger than the depth) and the standard linearity assumption that the wave amplitudes are much smaller that the depth. The derivation of this equation was built upon the assumption of the small parameter $h^3/\lambda^2\eta_0 \ll 1$ (or $h^2/\lambda^2 \ll \eta_0/h \ll 1$), where λ is the wavelength and η_0 is the incident amplitude.

Recently, [78] proposed an extension to the linear shallow water equation that includes higher order terms. This equation showed that the wave speed is slowed by the gradients of the sea bed. The controlling of wave speeds in different directions, is often a requirement in the design of the metamaterials. This is the idea used also in [58][79] to show how a submerged metamaterial structure of circular shape could rotate a water wave locally by controlling speeds in different directions.

In this section, a new model that describes the wave motion in the presence of a submerged microstructure made of vertical barriers in the shallow water regime, will be derived by starting from the first principles of mass and momentum conservation of the fluid. It will turn out that at leading order, the scalar function $h(x, y)$ in the standard linear shallow water equation will be replaced by a 2×2 diagonal tensor (of rank 2) whose components will be the effective depths that the wave feels in the directions perpendicular and parallel to the barriers (from now on called the "depth tensor").

This type of equation structure has been derived in other models involving

submerged beds based on different modelling assumptions to the ones used here. For example, [1][13] presented different methods for deriving the tensorial model with effective depths in the directions parallel and perpendicular to the barriers of a structured bed in the shallow water setting. In both models, the effective depth in the direction parallel to the barriers was found to be $\langle h \rangle = \theta h^+ + (1-\theta)h^-$ with $h^+ < h^-$ be the two constant metamaterial interfaces. This is the same result that will be deduced later in this section and it is expected on physical grounds as it represents the averaged depth over the unit cell i.e. $\langle h \rangle = h^-$ when $\theta = 0$ (wave travelling parallel to thin barriers feels only the fluid's depth) and $\langle h \rangle = h^+$ when $\theta = 1$ (rigid step analogue). The result will be more general, as the effective depth in that direction will be found to be the same as the previous authors ($\theta h^+ + (1-\theta)h^-$) even if the metamaterial interfaces are space-varying i.e. located at $z = -h^{\pm}(x, y)$ where (x, y) are the horizontal space variables.

However, the difference between all models lies upon the expression of the effective depth in the direction perpendicular to the barriers. For example, [13] used shallow water theory in a standard "layered-medium" homogenisation formulation (see [67] for an elasticity analogue example) to derive a model for a structured bed with rapid fluctuations in depth. They found that the effective depth in that direction to be $\langle h^{-1} \rangle^{-1}$ which tends to h^- when $\theta \to 0$ and to h^+ when $\theta \to 1$. This will contrast the constant (in θ) value of h^+ which will be derived later in this section. However, it can be seen that the result of [13] works for widely-spaced barriers in the sense of $l/h^{\pm} \gg 1$ (where l is the barrier periodicity). This is because the standard shallow water theory assumes small bed gradients and it can only be used in the presence of discontinuous "steps" in an asymptotic sense [26] and the wide-spacing limit of the barriers ensures this happens. The assumption of closely spaced barriers or $l/h^{\pm} \ll 1$, is the main difference between our work and the work of the authors discussed above. [1] proposed a numerically-determined value for the effective depth in the perpendicular direction to the barriers, that includes both of the two limiting cases of barrier spacing. The spacing generalisation requires the effective depth expression to be an integral over the unit cell of a velocity potential associated to a simple potential flow problem. Numerical comparisons were made in that paper showing that the effective depth converges slowly to the one of [13] in the large spacing limit and to the constant value of h^+ in the small spacing limit (as derived in this section). Then, in [16], the same problem involving vertical barriers in shallow water was revisited but now new matching conditions across the vertical interfaces of the metamaterial structure were derived at a higher order in the small parameter describing the ratio of the barrier spacing and the wavelength, to match solutions between standard and structured beds.

The shallow water equation that will be used in our problem, will be derived using a multiscale homogenisation technique applied to the governing equations describing mass and momentum conservation. The small parameters will now be three, namely the fluid shallowness, the metamaterial contrast and the linearisation parameter of the ratio between amplitude and depth. As promised, the generalisation of the spatially-varying barrier height, will be assumed. The derivation is formulated using a Cartesian framework in the same manner as the problem of the previous sections, but now the fluid is bounded below by a bed which fluctuates rapidly between two surfaces described by the functions $z = -h^-(x, y)$ and an upper surface given by $z = -h^+(x, y)$ such that $h^+ \leq h^-$ for (x, y) inside the metamaterial region and $h^+ = h^-$ otherwise. The notation of $h^\pm$ is used to align this work to the work of [1].

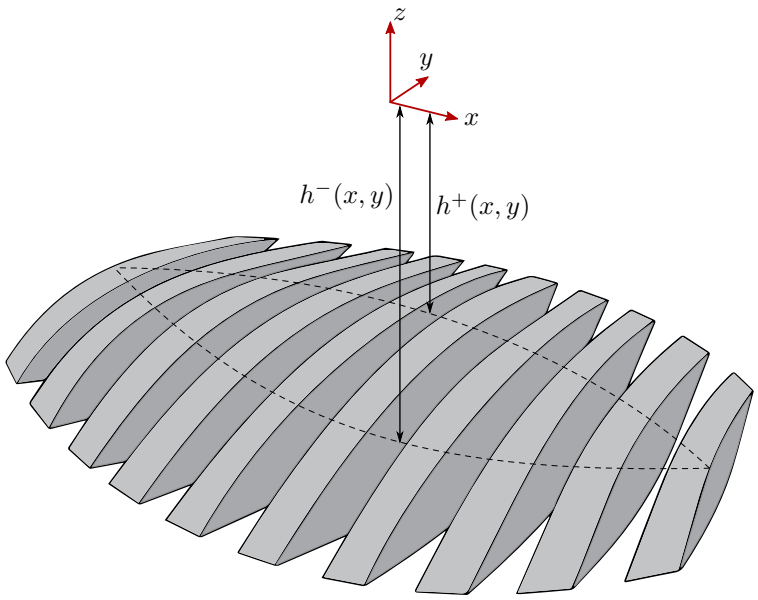

Figure 3.16: Structure made of thick barriers of periodicity l and thickness θl, with spatially varying interfaces $h^\pm(x, y)$, under the swallow water approximation.

We are interested in developing a governing equation in the region occupied by the parallel-structured bathymetry and are not yet interested in how this connects to exterior domains. We therefore align our coordinate system with the orientation of the barriers i.e., y coordinate is aligned with the barriers and we will use a rotated coordinate transformation later on when considering barriers aligned at different angles to the x and y axes.

The derivation starts from the mass and momentum conservation laws and the boundary conditions. The no flow conditions through the rigid interfaces of each barrier should now be $w + \nabla h^+ \cdot \mathbf{u} = 0$ on the top of each barrier, $w + \nabla h^- \cdot \mathbf{u} = 0$ at the bed between the gaps and $u = 0$ on the vertical faces of each barrier (where $\mathbf{u} = (u, v)$ are the horizontal components of the fluid's velocity). Now there are four lengthscales in the problem: (i) L is a characteristic horizontal lengthscale either representing the underlying wavelength or the scale over which macroscopic changes to the fluid depth occur; (ii) H is a characteristic depth of fluid; (iii) l is the lengthscale of the structured bed; (iv) a is the wave amplitude. The following three dimensionless quantities from these parameters are formed as

$$\mu = H/L, \quad \epsilon = l/L, \quad \delta = a/H, \tag{3.3.1}$$

which represent shallowness, microstructure contrast and wave-linearisation respectively. Each one is supposed to be small and the theory is demanded to work in the limit $\delta \to 0^\circ$ (i.e. in the linearised regime) independently of the size of ϵ and μ. We further assume that the barriers are closely spaced when compared to the shallow depth of the fluid (namely $\epsilon \ll \mu$). This underlying assumption of closely spaced barriers is the main difference between our model and the models of [1][13]. The parameters of microstructure contrast and shallowness are coupled together through $\epsilon = \mathcal{O}(\mu^2)$ and this relation is required for generating theory to second order.

In the definition of dimensionless variables, two distinct lengthscales in the x-direction must be taken into account. Therefore,

$$\begin{gathered} x = lX' + Lx', \quad y = Ly', \quad z = Hz', \quad t = \frac{L}{\sqrt{gH}}t', \\ \mathbf{u} = \frac{a\sqrt{gH}}{H}\mathbf{u}', \quad w = \frac{a\sqrt{gH}}{L}w', \quad p = \rho g H p', \quad \zeta = a\zeta', \quad h = Hh', \end{gathered} \tag{3.3.2}$$

where the vertical velocity scale was set to be a/T, where T is the time scale and the horizontal velocity scales were found from the continuity equation (mass conservation). Under the transformation above, the mass, momentum and surface equations

read

$$
\begin{gathered}
u'_{X'} + \epsilon\Big(\nabla' \cdot \mathbf{u}' + w'_{z'}\Big) = 0, \\
p'_{X'} + \epsilon\Big(p'_{x'} + \delta u'_{t'}\Big) = 0, \quad p'_{y'} + \delta v'_{t'} = 0, \quad p'_{z'} + 1 + \delta\mu^2 w'_{t'} = 0, \\
w' = \zeta'_{t'}, \quad p' = p'_{atm} \ \text{ on } \ z' = 0,
\end{gathered}
\tag{3.3.3}
$$

where the higher order of δ in the momentum and surface equation was neglected to be consistent with the linearisation process and as δ is assumed to be significantly smaller than any power of ϵ under consideration. Also, here the differential operator over the macroscale horizontal coordinates is $\nabla' = (\partial_{x'}, \partial_{y'})$. The set of conditions on the fixed submerged bed must be abbreviated to $(\mathbf{u}', w') \cdot \hat{\mathbf{n}} = 0$, where $\hat{\mathbf{n}}$ is the unit normal to the bed.

From now on, the primes are dropped from the dimensionless variables for simplicity and the unknowns are expanded as

$$
\begin{gathered}
\mathbf{u} \approx \mathbf{u}^{(0)} + \epsilon\mathbf{u}^{(1)} + \ldots, \quad w \approx w^{(0)} + \epsilon w^{(1)} + \ldots, \\
p \approx \tilde{p}^{(0)} + \delta\big(p^{(0)} + \epsilon p^{(1)} + \ldots\big), \quad \zeta \approx \zeta^{(0)} + \epsilon\zeta^{(1)} + \ldots,
\end{gathered}
\tag{3.3.4}
$$

where all the superscripted velocity and pressure terms depend on (x, y, z, t, X) and all the elevation terms, depends only on (x, y, t, X). This is predominantly a multiple-scales expansion in the contrast parameter ϵ, although the expansion is mixed with that used in the derivation of the linearised shallow water equation [15]. Then the equations in (3.3.3) become

$$
u^{(0)}_X + \epsilon\Big(u^{(1)}_X + \nabla \cdot \mathbf{u}^{(0)} + w^{(0)}_z\Big) = 0, \tag{3.3.5}
$$

$$
\tilde{p}^{(0)}_X + \delta p^{(0)}_X + \epsilon\Big(\tilde{p}^{(0)}_x + \delta\big(p^{(1)}_X + p^{(0)}_x + u^{(0)}_t\big)\Big) = 0, \tag{3.3.6}
$$

$$
\tilde{p}^{(0)}_y + \delta\big(p^{(0)}_y + v^{(0)}_t\big) + \epsilon\delta\big(p^{(1)}_y + v^{(1)}_t\big) = 0, \tag{3.3.7}
$$

$$
\tilde{p}^{(0)}_z + 1 + \delta p^{(0)}_z + \epsilon\delta\big(p^{(1)}_z + w^{(0)}_t\big) = 0, \tag{3.3.8}
$$

$$w^{(0)} + \epsilon w^{(1)} = \zeta_t^{(0)} + \epsilon \zeta_t^{(1)} \quad \text{on} \quad z = 0, \tag{3.3.9}$$

$$\tilde{p}^{(0)} - p_{atm} + \delta\big(\zeta^{(0)}\tilde{p}_z^{(0)} + p^{(0)}\big) + \epsilon\delta\big(\zeta^{(1)}\tilde{p}_z^{(0)} + p^{(1)}\big) = 0 \quad \text{on} \quad z = 0. \tag{3.3.10}$$

Also, the no flow conditions though the rigid boundaries of the structured bathymetry must be imposed to the problem. Namely,

$$0 = \begin{cases} w^{(n)} + \mathbf{u}^{(n)} \cdot \nabla h^+, & 0 < X < \theta, \ z = -h^+, \\ w^{(n)} + \mathbf{u}^{(n)} \cdot \nabla h^-, & \theta < X < 1, \ z = -h^-, \\ u^{(n)}, & X = \theta, 1, \ -h^- < z < -h^+, \end{cases} \tag{3.3.11}$$

for $n = 0, 1, 2, ...$, standing for $\mathcal{O}(\epsilon^n)$.

From now on, powers of ϵ and δ of the equations (3.3.5) to (3.3.11) will be compared. Also, if for example a superscripted expansion function is known to be independent of some variable, then the sum of all the other functions included in the same equation and order, must be independent of that variable as well. This idea will be applied throughout this derivation. Therefore, starting from $\mathcal{O}(\epsilon^0\delta^0)$, then equation (3.3.5) implies that $u^{(0)}$ is independent of X throughout the depth and the third equation of (3.3.11) imply that

$$u^{(0)} \equiv \begin{cases} u^{(0)}(x, y, z, t), & -h^+ < z < 0, \\ 0, & -h^- < z < -h^+, \end{cases} \tag{3.3.12}$$

while equations (3.3.6) to (3.3.10) give

$$\tilde{p}^{(0)}(z) = p_{atm} - z, \tag{3.3.13}$$

which is just the background hydrostatic pressure in the fluid. Since $\mathbf{u}^{(0)}$ is now discontinuous at $z = -h^+$, then the continuity of velocity normal to this surface requires that

$$\big[w^{(0)} + \mathbf{u}^{(0)} \cdot \nabla h^+\big]_{z=-h^+ + 0^+} = \big[w^{(0)} + v^{(0)} h_y^+\big]_{z=-h^+ - 0^+}, \tag{3.3.14}$$

by using (3.3.12).

One may ask if there is an additional contribution near the boundary $z = -h^+$ due to the local flow detailed around the top face of the barrier. To see that this effect is negligible at leading order, a multiple scales method to the vertical coordinate near the boundary must be taken into account using matched asymptotic expansions to the inner and outer regions. This is a technique used to derive matching conditions near sharp-ends boundaries. For example, in [16], a similar procedure was followed to derive matching conditions across the vertical interface of a rectangular shaped metamaterial. This is essentially the same procedure, but the inner and outer regions are in the vertical coordinate instead of the horizontal. Forgetting for now the analysis from (3.3.2) until the last equation, the solution of the flow in the inner region can be found by introducing a small scale to the vertical variation near the boundary $z = -h^+$. That is to set $z = -h^+ + \epsilon H z'$ in (3.3.2) instead of just $z = Hz'$ and leave the x, y, t scales as they were. Next, using this transformation of coordinates in the mass conservation law and the x and z component of the momentum conservation law, then

$$u_X + w_z + \epsilon(u_x + v_y) = 0, \quad p_X + \epsilon(p_x + \delta u_t) = 0, \quad p_z + \epsilon = 0, \tag{3.3.15}$$

by non-dimensionalising all the variables in the same fashion as in (3.3.3), removing the dashes and neglecting orders of ϵ^2. Introducing ϵ expansions to all variables according to (3.3.4) the last two equations at $\mathcal{O}(\epsilon^0)$ imply that $\tilde{p}^{(0)} \equiv \tilde{p}^{(0)}(x, y, t)$ in the inner region. Using the fact that the inner expansion of the outer pressure (call it $\tilde{P}^{(0)}$) must match $\tilde{p}^{(0)}(x, y, t)$ to leading order, then

$$\lim_{z\to 0^+} \tilde{P}^{(0)} = \lim_{z\to\infty} \tilde{p}^{(0)}(x, y, t) = \lim_{z\to-\infty} \tilde{p}^{(0)}(x, y, t) = \lim_{z\to 0^-} \tilde{P}^{(0)}, \tag{3.3.16}$$

which imply the continuity of pressure across the metamaterial boundary. A similar idea can be used also in full linear theory to show the same result. Since the pressure is proportional to the velocity potential under the assumptions of full linear theory, then the continuity of ϕ across metamaterial boundaries can be imposed as happened back in (3.2.8).

Continuing on the leading order $\mathcal{O}(\epsilon^0)$ of mass conservation in (3.3.15), gives $\nabla \cdot \mathbf{U}^{(0)} = 0$ where now $\nabla = (\partial_X, \partial_z)$ and $\mathbf{U}^{(0)} = (u^{(0)}, w^{(0)})$. Integrating it over the unit cell of the inner region, namely Ω^* which is comprised of the regions

$(X,z)\in(0,1)\times(0,z^*)$ and $(X,z)\in(\theta,1)\times(-z^*,0)$, then

$$0=\int\limits_{\Omega^*}\nabla\cdot\mathbf{U}^{(0)}dV=\int\limits_{\partial\Omega^*}\mathbf{U}^{(0)}\cdot\hat{\mathbf{n}}dS=\int\limits_0^{z^*}\left(u^{(0)}\Big|_{X=1}-u^{(0)}\Big|_{X=0}\right)dz \\ -\int\limits_0^1 w^{(0)}\Big|_{z=z^*}dX+\int\limits_\theta^1 w^{(0)}\Big|_{z=-z^*}dX, \tag{3.3.17}$$

where here the divergence theorem was used supported with no flow conditions across the rigid boundaries $X\in(0,\theta)$, $z=0$ and $z\in(-z^*,0)$, $X=\theta$, 1. The first term of the right-hand side can be neglected after making the standard assumption of X periodicity to all variables. Thus, the result is the balance of the local vertical flux across the boundary. Therefore, by matching the inner expansions of the outer flux to the outer expansions of the inner flux, then

$$\int\limits_0^1\left[w^{(0)}+\mathbf{u}^{(0)}\cdot\nabla h^+\right]_{z=-h^++0^+}dX=\lim_{z^*\to\infty}\int\limits_0^1 w^{(0)}\Big|_{z=z^*}dX \\ =\lim_{z^*\to\infty}\int\limits_\theta^1 w^{(0)}\Big|_{z=-z^*}dX=\int\limits_\theta^1\left[w^{(0)}+v^{(0)}h_y^+\right]_{z=-h^+-0^+}dX, \tag{3.3.18}$$

which results to the integrated version of (3.3.14). It will be seen later that eventually this equation will be integrated in over the cell. Therefore, the equations (3.3.15) to (3.3.18) are giving a verification of equation (3.3.14) and so they can be ignored from now on.

Proceeding to $\mathcal{O}(\epsilon^0\delta^1)$, the equations (3.3.6), (3.3.8) imply that $\tilde{p}^{(0)}$ is independent of z and X. Then the equations (3.3.10), (3.3.13), will give

$$p^{(0)}(x,y,t)=\zeta^{(0)}(x,y,t), \tag{3.3.19}$$

which imply the X-independence of $\zeta^{(0)}$. Using the last equation, then (3.3.7) corre-

sponds to

$$v_t^{(0)}(x,y,t) = -\zeta_y^{(0)}(x,y,t), \tag{3.3.20}$$

which imply that $v^{(0)}$ is independent of X. Additionally, since $v^{(0)}$ is independent of z from the equation above, then (3.3.14) is transformed to

$$\left[w^{(0)}\right]_{-h^+-0^+}^{-h^++0^+} = -\left[u^{(0)}h_x^+\right]_{z=-h^++0^+} \quad \text{in} \quad X \in (\theta,1). \tag{3.3.21}$$

Moving on to $\mathcal{O}(\epsilon^1\delta^0)$, then equation (3.3.5) gives

$$\nabla \cdot \mathbf{u}^{(0)} + w_z^{(0)} = -u_X^{(1)}, \tag{3.3.22}$$

while continuing to $\mathcal{O}(\epsilon^1\delta^1)$ of (3.3.6), using (3.3.19), then

$$u_t^{(0)} + \zeta_x^{(0)} = -p_X^{(1)}. \tag{3.3.23}$$

The two terms of the left-hand side are independent of X from (3.3.12) and (3.3.19) respectively. Thus by integrating the equation above with respect to $X \in (0,1)$, then the left-hand side will remain invariant and on the right-hand side the fundamental theorem of calculus can be applied to give a contribution that is proportional to l (after returning to original coordinates). This is due to the assumption that all higher order variables (for example the ones that are superscripted by (1)) are periodic in X with a period of order ϵ. The fact that the periodicity of higher order variables in the microscale is small, is a standard assumption to multiscale expansions for homogenisation purposes [67]. Therefore, equation (3.3.23) will imply that

$$u_t^{(0)}(x,y,t) = -\zeta_x^{(0)}(x,y,t), \tag{3.3.24}$$

which imply the z-independence of $u^{(0)}$. Integrating (3.3.22) over a single cell, then

$$\int_0^1 \int_{-h^+}^0 \Big(\nabla \cdot \mathbf{u}^{(0)} + w_z^{(0)}\Big) dz dX + \int_\theta^1 \int_{-h^-}^{-h^+} \Big(v_y^{(0)} + w_z^{(0)}\Big) dz dX = 0, \tag{3.3.25}$$

after using (3.3.12) and neglecting the $u_X^{(1)}$ term from both integrands. The reason for neglecting $u_X^{(1)}$ in the first integral is from the fact that higher order variables are assumed to have X-periodicity of order ϵ (same reason for why $p_X^{(1)}$ is neglected from (3.3.23)) while the reason it is neglected from the second integral is by applying the fundamental theorem of calculus on X and make use of the no flow conditions through the barriers. Next, using the z, X independence of $u^{(0)}$, $v^{(0)}$ from (3.3.24) and (3.3.20) respectively and applying the fundamental theorem of calculus on $w_z^{(0)}$ in the first integral with $w^{(0)} = \zeta_t^{(0)}$ on $z = 0$ from the $\mathcal{O}(\epsilon^0)$ of (3.3.9), then

$$\zeta_t^{(0)} + h^+ u_x^{(0)} + \overline{h} v_y^{(0)} - \int_0^1 w^{(0)}\big|_{z=-h^+ + 0^+} dX + \int_\theta^1 \int_{-h^-}^{-h^+} w_z^{(0)} dz dX = 0, \tag{3.3.26}$$

where $\overline{h} = \theta h^+ + (1-\theta) h^-$ denotes the averaged depth over the single cell. Now, by dichotomising the first integral about $X = \theta$, then applying again the fundamental theorem of calculus in the second integral with $w^{(0)} = -h_y^- v^{(0)}$ on $z = -h^-$ from $\mathcal{O}(\epsilon^0)$ of the second equation of (3.3.11) using (3.3.12) and combining the integrals over $(1, \theta)$, then

$$\zeta_t^{(0)} + h^+ u_x^{(0)} + \overline{h} v_y^{(0)} + (1-\theta) h_y^- v^{(0)} - \int_0^\theta w^{(0)}\Big|_{z=-h^+ + 0^+} dX - \int_\theta^1 \big[w^{(0)}\big]_{-h^+ - 0}^{-h^+ + 0^+} dX = 0, \tag{3.3.27}$$

using the X-independence of $v^{(0)}$ again. Next, the first integral (including the minus sign) is identical to $\theta h_x^+ u^{(0)} + \theta h_y^+ v^{(0)}$ using the $\mathcal{O}(\epsilon^0)$ of the first equation of (3.3.11) and the z, X of $u^{(0)}$, $v^{(0)}$. Similarly, the second integral (including the minus sign) is $(1-\theta) h_x^+ u^{(0)}$ using (3.3.21) and the fact that $u^{(0)}$ is independent of z, X again.

Therefore in matrix form the equation reads

$$\zeta_t^{(0)} + \nabla \cdot \Big(\mathbf{h}\mathbf{u}^{(0)} \Big) = 0 \quad \text{where} \quad \mathbf{h} = \text{diag}\{h^+, \overline{h}\}. \tag{3.3.28}$$

Now by combing the leading order momentum equations (3.3.24), (3.3.20) in a vectorial form and then

$$\mathbf{u}_t^{(0)} + \nabla \zeta^{(0)} = \mathbf{0}. \tag{3.3.29}$$

Elimination of $\mathbf{u}^{(0)}$ between (3.3.28) and (3.3.29) gives $\zeta_{tt}^{(0)} = \nabla \cdot \Big(\mathbf{h} \nabla \zeta^{(0)} \Big)$. But $\zeta^{(0)}$ can be replaced by ζ as they are the same to leading order by neglecting $O(\epsilon)$. Also, this governing equation for ζ is written in the dimensionless dashed variables. Therefore by returning to the original Cartesian coordinates through (3.3.2), then

$$\zeta_{tt} = g \nabla \cdot \Big(\mathbf{h} \nabla \zeta \Big), \tag{3.3.30}$$

where $\zeta(x, y, t)$ is the surface elevation to the actual physical problem. The equation (3.3.30) is an extension to the standard shallow water equation $\zeta_{tt} = g\nabla \cdot (h \nabla \zeta)$, describing again the surface elevation $\zeta(x, y, t)$ of a fluid bounded below by the bed $z = -h(x, y)$. This can be seen by taking $h^{\pm} \to h$ (setting both metamaterial interfaces at the fluid's depth level), then $\mathbf{h} \to h\mathbf{I}$ using $\overline{h} \to h$ (where $\mathbf{I}$ is the 2×2 identity matrix) which transforms the metamaterial shallow water equation (3.3.30), to the standard one (matrix $\mathbf{h}$ replaced by the scalar h).

Now in the presence of a metamaterial made of closely spaced barriers, the scalar $h(x, y)$ becomes a $2{\times}2$ diagonal tensor, with elements the effective depths which an incident wave feels by travelling in the directions perpendicular and parallel to the barriers respectively. This can be seen from the fact that if the wave was travelling only in the x-direction, then the equation would read $\zeta_{tt} = g\partial_x \big(h^+ \zeta_x \big)$ which coincides with the standard 1D shallow water equation for an effective depth h^+. Similarly, if the wave was travelling only in the y-direction then the equation would be $\zeta_{tt} = g\partial_y \big(\overline{h} \zeta_y \big)$, which describes the same thing. This is essentially the equation discussed in [80], but now derived using asymptotic multiscale expansions.

3.3.2 Solution to the scattering problem

Although the new, linear shallow water model works for spatially varying interfaces describing the alternating bed in the metamaterial region, now for the problem of this section they are assumed to be constant. Therefore, the modified shallow water equation derived in the previous section, can be used for propagation of long waves over a flat bed and a submerged metamaterial made of identical, thick barriers to consider the same scattering problems that were treated with full linear theory in previous sections. Also, in this problem, a similar generalisation as in section 3.2.4 can be made, namely let the metamaterial sit on a rigid step on $z = -h^-$. Thus, the constant alternating beds in the metamaterial region are $z = -h^+, -h^-$ with $h^+ < h^- < h$, where h is the constant depth outside the metamaterial region.

However, in section 3.2.4, the lower metamaterial interface was allowed to be below the depth level (this case of the problem was referred to "buried" barriers). However here, the case of $h^+ < h < h^-$ is not allowed as in some geometrical cases the metamaterial scatters modes whose phase speeds are not associated with the expected ones, namely two modes travelling in opposite directions above the structure. The recent paper of [81] includes a wider range of results which include scattering by structured beds in which h^- is larger than h ("buried" metamaterial). This produces some interesting results, but the focus here is on comparing with the earlier work in this thesis in which h^- is not greater than h and involves scattering over finite width ridges. Therefore in the shallow water problem described in this section, only the $h^+ < h^- < h$ case is considered.

A plane-crested incident wave of unit amplitude propagates from $-\infty$ with wavenumber k in a direction $\theta_0 \in [-90°, 90°]$ with the x-axis and is partially reflected and transmitted by the structure of arbitrarily oriented barriers. The governing equation in $|x| > b$ is the standard shallow water equation over a flat bed at $z = -h$, namely $\zeta_{tt} = g\nabla \cdot (h\nabla\zeta)$.

In $|x| < b$, an arbitrary orientation to the barriers is allowed. Therefore, using the (X, Y) coordinates found in (3.2.1), then X and Y are parallel and perpendicular to the rotated barriers (by an angle δ), respectively. Thus, the governing equation over the metamaterial region $|x| < b$ is $\hat{\zeta}_{tt} = g\hat{\nabla}\cdot(\mathbf{h}\hat{\nabla}\hat{\zeta})$ from (3.3.30), where $\hat{\zeta}$ is the elevation expressed in (X, Y) and therefore $\hat{\nabla} = (\partial_X, \partial_Y)$. Thus, in Cartesian coordinates is $\zeta_{tt} = g\nabla\cdot\left(\mathbf{R}^{-1}\mathbf{h}\mathbf{R}\nabla\zeta\right)$, using $\hat{\nabla} = \mathbf{R}\nabla$ (chain rule), where $\mathbf{R}$ is the conventional rotation matrix defined in (3.2.1). In the equation above the identity $\left(\mathbf{R}\nabla\right)\cdot\mathbf{f} = \nabla\cdot\left(\mathbf{R}^{-1}\mathbf{f}\right)$ for any $\mathbf{f}$ was implemented, given that the inverse of the rotation matrix is its transpose. Note that since the tilted coordinate system looks like the one in figure 3.1 (but in the shallow water regime and the metamaterial sits on a rigid step), then the shallow water depth tensor is chosen to be $\mathbf{h} = \mathrm{diag}\{\overline{h}, h^+\}$, so

that its first element represent the effective depth in the direction parallel to barriers and the second in the direction perpendicular to barriers. Here the averaged depth in the unit cell will be $\overline{h} = \theta h^+ + (1-\theta)h^-$. Also, now the domain of δ can be $[-90°, 90°]$, as under shallow water approximation, there are no vertical eigenfunctions to match. Therefore, the three different barrier orientations considered in the previous section (full linear theory) can be combined to a single case due to the fact that the shallow water model is independent of the vertical coordinate.

Assuming the time harmonicity of the incident wave and the global y-variation compatibility of the total field with the incident wave due to the constant cross-sectional geometry of the problem (as the metamaterial acts as an effective homogenised medium), then y and t can be factored out from the solution as $\zeta(x,y,t) = \Re\{\eta(x)e^{i\alpha y}e^{-i\omega t}\}$ for ω be the incident angular frequency and $\alpha = k\sin\theta_0$ be the wavenumber in the y-direction. The incident wave is given by $\zeta_{inc}(x,y,t) = \Re\{\eta_{inc}(x)e^{i\alpha y}e^{-i\omega t}\}$ with $\eta_{inc}(x) = e^{i\beta x}$ for $\beta = k\cos\theta_0$. After this simplification the governing equation for the scattering modes outside the metamaterial region, becomes

$$\eta''(x) = -\beta^2\eta(x) \quad \text{in} \quad |x| > b, \tag{3.3.31}$$

using that $K \equiv \omega^2/g = k^2h$ from the dispersion relation and the shallow water approximation. Note that this equation is satisfied by the incident wave as well.

Now in the region $|x| < b$, the effective equation that describes the surface elevation over a metamaterial consist of arbitrarily oriented barriers, namely $\zeta_{tt} = g\nabla\cdot\left(\mathbf{R}^{-1}\mathbf{h}\mathbf{R}\nabla\zeta\right)$, becomes

$$H_1\eta''(x) + 2i\tilde{H}\eta'(x) + \Big(K - \alpha^2 H_2\Big)\eta(x) = 0 \quad \text{in} \quad |x| < b, \tag{3.3.32}$$

for $H_1 = h^+\sin^2\delta + \overline{h}\cos^2\delta$, $H_2 = h^+\cos^2\delta + \overline{h}\sin^2\delta$ and $\tilde{H} = \alpha(1-\theta)(h^- - h^+)\sin\delta\cos\delta$ by using the surface field proportionality to $e^{i\alpha y}e^{-i\omega t}$. By seeking solutions $\eta(x) \sim e^{i\mu x}$ in (3.3.32), then μ will satisfy a quadratic equation whose explicit solutions are given by

$$\mu_{1,2} = \frac{-\tilde{H} \pm \sqrt{\tilde{H}^2 + H_1(k^2h - \alpha^2 H_2)}}{H_1}, \tag{3.3.33}$$

using that $K = k^2 h$ again. Note that the bracket term inside the square root is positive due to the fact that $\alpha^2 H_2 < k^2 H_2 < k^2(h\cos^2\delta + h\sin^2\delta) = k^2 h$ as $\overline{h}$ lies somewhere in between h^+ and h^- which are both smaller than h. This means that $\mu_{1,2} \in \mathbb{R}$ (positive discriminant) with the two roots having different sign as $H_1^2\mu_1\mu_2 = -H_1(k^2 h - \alpha^2 H_2) < 0$. That means they will be two waves travelling in opposite directions in the region $|x| < b$. Without the loss of generality μ_1 is chosen to be the positive root and μ_2 the negative. However the existence of two real roots (opposite in sign) is guaranteed from the fact that the lower metamaterial interface lies above the level of the exterior sea bed ($h^- < h$). It was shown in [81] that when this interface lies below the sea bed ($h^- > h$), then the nature of the roots $\mu_{1,2}$ could change i.e. two real and negative roots or two complex conjugate roots. However these cases will not be included in this thesis.

Providing to the problem the usual far field condition

$$\eta(x) \sim \begin{cases} \eta_{inc}(x) + R\eta_{inc}(-x), & x \to -\infty, \\ T\eta_{inc}(x), & x \to \infty, \end{cases} \tag{3.3.34}$$

where R and T are the reflection and transmission coefficients, then the solutions of (3.3.31), (3.3.32) will be

$$\begin{aligned} \eta_1(x) &= e^{i\beta x} + Re^{-i\beta x}, \quad x < -b, \\ \eta_2(x) &= Ae^{i\mu_1 x} + Be^{i\mu_2 x}, \quad |x| < b, \\ \eta_3(x) &= Te^{i\beta x}, \quad x > b, \end{aligned} \tag{3.3.35}$$

where η_1, η_2 and η_3 describe the total surface elevation. Note that if $h^+ < h < h^-$ was assumed (instead of $h^+ < h^- < h$), then there would be cases for which μ_1 and μ_2 could be complex [81].

According to [26], the elevation and mass flux must be matched across straight depth discontinuities at leading order. Normally in the presence of straight depth discontinuities, matching conditions of higher order must be imposed. However, [26] showed that the higher order matching conditions applied to the scattering over a step of conventional bathymetry changes the phase but not the modulus of the scattering coefficients. Also, in the work of [16] the metamaterial matching conditions to leading and higher order in $\epsilon = \omega\sqrt{l/g}$ were derived using a formal

asymptotic matching process of an inner and outer region of the metamaterial interface. However, the higher order contribution of these conditions can be neglected as the governing equation (3.3.30) is also of leading order. Therefore, the elevation matching translates to

$$\eta_1(-b) = \eta_2(-b), \quad \eta_2(b) = \eta_3(b). \tag{3.3.36}$$

Now flux expressions for outside and within the structure must be introduced. In the derivation of the standard shallow water equation bounded by a slow-varying bed, at some point the horizontal components of the momentum equation will give $\mathbf{u}_t = -g\nabla\zeta$. Thus, by denoting $\mathbf{q}$ to be the velocity flux, then by multiplying both sides by h, then the flux in the absence of submerged obstacles is given by $\mathbf{q}_t = -gh\nabla\zeta$. Now for deriving an expression for the velocity flux within the metamaterial region, equation (3.3.29) is considered. First approximating each variable by its zeroth order term and then returning to the original Cartesian coordinates, then the result is again $\mathbf{u}_t = -g\nabla\zeta$. But before multiplying this equation with $\mathbf{h}$ to get the velocity flux expression within the metamaterial region, first the barrier orientation should be considered. Thus the velocity flux expression over the submerged structure becomes $\hat{\mathbf{q}}_t = -g\mathbf{h}\hat{\nabla}\hat{\zeta}$, with $\hat{\mathbf{q}} = \mathbf{R}\mathbf{q}$ and $\hat{\nabla}\hat{\zeta} = \mathbf{R}\nabla\zeta$ where again $\mathbf{R}$ is the rotation matrix used to derive equation (3.3.32). Therefore, the flux expression for generally oriented barriers in Cartesian coordinates is $\mathbf{q}_t = -g\mathbf{R}^{-1}\mathbf{h}\mathbf{R}\nabla\zeta$ where the matrix product can be calculated trivially. Thus, by taking the flux expressions in the two regions, factoring out the y and t dependence through $e^{i\alpha y}e^{-i\omega t}$ and matching their x-components across the interfaces $x = \pm b$, then

$$h\eta_1'(-b) = H_1\eta_2'(-b) + i\tilde{H}\eta_2(-b), \quad h\eta_3'(b) = H_1\eta_2'(b) + i\tilde{H}\eta_2(b). \tag{3.3.37}$$

Now equations (3.3.36) and (3.3.37) give a 4×4 linear system for R, T, A, B. Their

formulas are complicated but explicit and they are found to be

$$\begin{aligned}
A &= e^{-i\beta b}e^{i\mu_2 b}\frac{2\beta h\gamma_-^{(2)}}{\gamma_+^{(1)}\gamma_-^{(2)}e^{-i(\mu_1-\mu_2)b}-\gamma_-^{(1)}\gamma_+^{(2)}e^{i(\mu_1-\mu_2)b}},\\
B &= -e^{-i\beta b}e^{i\mu_1 b}\frac{2\beta h\gamma_-^{(1)}}{\gamma_+^{(1)}\gamma_-^{(2)}e^{-i(\mu_1-\mu_2)b}-\gamma_-^{(1)}\gamma_+^{(2)}e^{i(\mu_1-\mu_2)b}},\\
R &= -ie^{-2i\beta b}\frac{2\gamma_-^{(1)}\gamma_-^{(2)}\sin[(\mu_1-\mu_2)b]}{\gamma_+^{(1)}\gamma_-^{(2)}e^{-i(\mu_1-\mu_2)b}-\gamma_-^{(1)}\gamma_+^{(2)}e^{i(\mu_1-\mu_2)b}},\\
T &= e^{-2i\beta b}e^{i(\mu_1+\mu_2)b}\frac{2\beta hH_1(\mu_1-\mu_2)}{\gamma_+^{(1)}\gamma_-^{(2)}e^{-i(\mu_1-\mu_2)b}-\gamma_-^{(1)}\gamma_+^{(2)}e^{i(\mu_1-\mu_2)b}},
\end{aligned} \tag{3.3.38}$$

where $\gamma_\pm^{(i)} = \beta h \pm (\tilde{H} + \mu_i H_1)$ for $i = 1, 2$. It is easier to derive the expressions above if $\eta_2(\pm b)$ in (3.3.37) is written in terms of η_1 and η_3 from (3.3.36). The formulas for the amplitudes A abnd B will be used in the numerical results section to produce surface plots for $\zeta(x, y, t)$. The advantage of the scattering coefficients in the shallow water regime is that they are always in closed-form. Therefore, a variety of scattering properties such as energy conservation, transparency, negative refraction etc. will now be shown analytically. Similar properties were shown analytically in [11], where the closed-form solutions came from the extension of the barriers throughout the depth (instead of the shallow water limit). However here, the expressions are more complicated and the proof of the scattering properties require some more complicated algebra.

Starting from the proof of energy conservation i.e. $|R|^2 + |T|^2 = 1$, then

$$|R|^2 + |T|^2 = \frac{4\left(\gamma_-^{(1)}\gamma_-^{(2)}\right)^2 \sin^2\left[(\mu_1-\mu_2)b\right] + 4\beta^2h^2H_1^2(\mu_1-\mu_2)^2}{\left|\gamma_+^{(1)}\gamma_-^{(2)}e^{-i(\mu_1-\mu_2)b}-\gamma_-^{(1)}\gamma_+^{(2)}e^{i(\mu_1-\mu_2)b}\right|^2} \tag{3.3.39}$$

and then, it will be proven that the denominator of this expression, equals the nu-

merator. Therefore, using the identity $|z_1+z_2|^2=|z_1|^2+|z_2|^2+2\Re\{z_1\overline{z_2}\}$, then

$$\begin{aligned}
&\left|\gamma_+^{(1)}\gamma_-^{(2)}e^{-i(\mu_1-\mu_2)b}-\gamma_-^{(1)}\gamma_+^{(2)}e^{i(\mu_1-\mu_2)b}\right|^2\\
&=\left(\gamma_+^{(1)}\gamma_-^{(2)}\right)^2+\left(\gamma_-^{(1)}\gamma_+^{(2)}\right)^2-2\gamma_+^{(1)}\gamma_+^{(2)}\gamma_-^{(1)}\gamma_-^{(2)}\cos\left[2(\mu_1-\mu_2)b\right]\\
&=4\gamma_+^{(1)}\gamma_+^{(2)}\gamma_-^{(1)}\gamma_-^{(2)}\sin^2\left[(\mu_1-\mu_2)b\right]+\left(\gamma_+^{(1)}\gamma_-^{(2)}-\gamma_-^{(1)}\gamma_+^{(2)}\right)^2,
\end{aligned}\tag{3.3.40}$$

by applying the cosine double angle formula. Now one may use the $\gamma_\pm^{(i)}$ definitions to prove the straightforward result $\gamma_+^{(1)}\gamma_-^{(2)}-\gamma_-^{(1)}\gamma_+^{(2)}=2\beta hH_1(\mu_1-\mu_2)$ and the more demanding formula $\gamma_+^{(1)}\gamma_+^{(2)}=\beta^2h^2-\tilde{H}^2+\mu_1\mu_2H_1^2=\gamma_-^{(1)}\gamma_-^{(2)}$. The latter can be derived by expanding the products into 9 terms and group the $\mu_1+\mu_2$ terms together, so that $\mu_1+\mu_2=-2\tilde{H}/H_1$ is used from (3.3.33). These two formulas prove that the result in (3.3.40) is identical to the numerator of (3.3.39), verifying the conservation of energy analytically i.e. $|R|^2+|T|^2=1$. Using the two formulas discussed here, from now on the scattering coefficients expressions used will be

$$\begin{aligned}
R&=-ie^{-2i\beta b}\frac{2\gamma_+^{(1)}\gamma_+^{(2)}\sin[(\mu_1-\mu_2)b]}{\gamma_+^{(1)}\gamma_-^{(2)}e^{-i(\mu_1-\mu_2)b}-\gamma_-^{(1)}\gamma_+^{(2)}e^{i(\mu_1-\mu_2)b}},\\
T&=e^{-2i\beta b}e^{-2i\tilde{H}b/H_1}\frac{2\beta hH_1(\mu_1-\mu_2)}{\gamma_+^{(1)}\gamma_-^{(2)}e^{-i(\mu_1-\mu_2)b}-\gamma_-^{(1)}\gamma_+^{(2)}e^{i(\mu_1-\mu_2)b}}.
\end{aligned}\tag{3.3.41}$$

The next property that will be shown, is the incident and barrier symmetry, in the sense that R, $|T|$, $|A|$ and $|B|$ are even in both θ_0 and δ. Starting from

$$\begin{aligned}
\gamma_\pm^{(i)}=\beta h\pm\left(\tilde{H}+\mu_iH_1\right)&=\beta h\pm(-1)^{i+1}\sqrt{\tilde{H}^2+H_1\left(k^2h-\alpha^2H_2\right)},\\
\mu_1-\mu_2&=\frac{2\sqrt{\tilde{H}^2+H_1\left(k^2h-\alpha^2H_2\right)}}{H_1},
\end{aligned}\tag{3.3.42}$$

and using that H_1, H_2 are independent of θ_0, then it can be seen that the two expressions above are even in both θ_0 and δ. This implies that R is symmetric in θ_0

and δ. However, when θ_0 is replaced by $-\theta_0$ or δ by $-\delta$, then T, A and B change only by a phase. Therefore $|T|$, $|A|$ and $|B|$ are even in θ_0 and δ as well. The θ_0 symmetry is a property shared with the modulus of scattering coefficients of the full linear theory problems defined in section 3.2. However, for a general angle δ, it was difficult to show analytically the θ_0 symmetry but it was verified numerically. But in the special cases of $\delta = 0°, 90°$, the symmetry could be shown analytically. Now in this section, even when δ is arbitrary, the shallow water approximation seems to simplify the problem at a level where the θ_0 symmetry can be shown as well.

Now we consider a special geometrical case that gives rise to the "transparency" property. Inspired from [11], it was shown that if the barriers were thin, started from the bed and extended throughout the depth (no shallow water assumed), then there was a total transmission if the barriers were parallel to the incident direction or the symmetric about $\theta_0 = 0°$ direction. Therefore, it will be proven now that the same result holds for barriers that extend partially throughout the depth in shallow water. The geometrical assumptions are

$$\theta = 0, \quad h^- = h, \quad \theta_0 = \pm\delta, \tag{3.3.43}$$

meaning that the barriers are assumed to be thin and they sit on the bed instead of an extra step. The incident direction is chosen such that $\theta_0 = \delta$ represents a wave that travels parallel to the barriers orientation and $\theta_0 = -\delta$ represents the same wave but its direction is reflected about the x-axis.

The geometrical assumptions above, imply that $\alpha = \pm k \sin\delta$, $\beta = k\cos\delta$, $\overline{h} = h$, $H_1 = h^+ \sin^2\delta + h\cos^2\delta$, $H_2 = h^+\cos^2\delta + h\sin^2\delta$ and $\tilde{H} = \pm k(h - h^+)\sin^2\delta\cos\delta$ after some simple algebraic manipulation. The discriminant of the polynomial satisfied by $\mu_{1,2}$ (the term which is inside the square root of (3.3.33)), will simplify to $\tilde{H}^2 + H_1(k^2 h - \alpha^2 H_2) = \beta^2 h^2$. Thus, the final simplifications are $\mu_1 - \mu_2 = 2\beta h/H_1$, $\gamma_+^{(1)} = \gamma_-^{(2)} = 2\beta h$ and $\gamma_-^{(1)} = \gamma_+^{(2)} = 0$ from the definitions of $\gamma_\pm^{(i)}$ found after the equation (3.3.38).

Using all those simplified formulas derived above, then it can be easily proven that $R = B = 0$ and

$$\begin{aligned} T &= \exp\left[\frac{2i\beta b}{H_1}\Big(h \mp (h - h^+)\sin^2\delta - h^+\sin^2\delta - h\cos^2\delta\Big)\right], \\ A &= \exp\left[\frac{i\beta b}{H_1}\Big(h \mp (h - h^+)\sin^2\delta - h^+\sin^2\delta - h\cos^2\delta\Big)\right], \end{aligned} \tag{3.3.44}$$

where the $\mp$ sign corresponds to the θ_0 cases found in (3.3.43). Therefore, it can be seen that when the incident direction is aligned with the barriers (that is $\theta_0 = \delta$ or take the minus sign of the transmission formula above), the result is $T = A = 1$ which is what was expected on physical grounds - the incident wave slides through the barriers unaffected. However when the incident direction is flipped about the x-axis (that is $\theta_0 = -\delta$ or take the plus sign of the transmission formula above), the result is $T = \exp\left[4ikb(h - h^+)\sin^2\delta\cos\delta/H_1\right]$ and $A = \exp\left[2ikb(h - h^+)\sin^2\delta\cos\delta/H_1\right]$ which imply that $|T| = |A| = 1$. Also, from these last expressions of T and A one could see that when the barrier height tends to zero ($h^+ \to h$), then $T = A = 1$. This is the transparency property proved in [11]. Actually it can be seen when the barriers extend throughout the fluid's depth ($h^+ \to 0$), then $T = \exp(4ikL\sin^2\delta)$, where $L = b\sec\delta$ is the half-length of the barriers.

In order to show certain refraction phenomena in $|x| < b$, we need define the group velocity as

$$\mathbf{c}_g^{(i)} = \left(\frac{\partial\omega}{\partial\mu_i}, \frac{\partial\omega}{\partial\alpha}\right), \tag{3.3.45}$$

for $i = 1, 2$ standing for the two travelling waves ($e^{i\mu_i x}$). Here the angular frequency can be found from $\omega = \sqrt{Kg}$, where K can be expressed in terms of μ_i and α by rearranging equation (3.3.33) as $K = \alpha^2 H_2 + \mu_i\big(\mu_i H_1 + 2\tilde{H}\big)$. Therefore, the partial derivatives can be calculated using the chain rule as

$$\mathbf{c}_g^{(i)} = \left(\frac{g}{K}\right)^{1/2}\Big(\mu_i H_1 + \tilde{H}, \alpha H_2 + \mu_i(1-\theta)(h^- - h^+)\sin\delta\cos\delta\Big). \tag{3.3.46}$$

The direction of the vector above coincides with the direction of energy propagation. This angle, call it $\theta_g^{(i)}$ for $i = 1, 2$, which gives important information about refraction within the metamaterial region, is not always the same as the wave phase speed $\theta_p^{(i)} = \arctan(\alpha/\mu_i)$. Also, it can be verified from (3.3.33) that the x-component of $\theta_g^{(1)}$ is positive and the one of $\theta_g^{(2)}$ is negative as expected (even though for sunken barriers is not always true - see [81]).

Therefore, by calculating the directions of energy propagation for the two waves within the region $|x| < b$ from the equation above, we have that

$$\theta_g^{(i)} = \arctan\left(\frac{\alpha H_2 + \mu_i(1-\theta)\big(h^- - h^+\big)\sin\delta\cos\delta}{\mu_i H_1 + \tilde{H}}\right), \tag{3.3.47}$$

where the first property can be verified easily, namely the independence of $\theta_g^{(i)}$ from k and b. Firstly, all the variables specified above are independent of b clearly. Also, since the numerator and denominator of the fraction above is linearly proportional to k (from μ_i and $\tilde{H}$), then $\theta_g^{(i)}$ is shown to be independent of k and b. Therefore the direction of energy propagation within the structural region depend only on the incident direction θ_0, the barriers orientation and thickness (δ and θ respectively), the flat depth outside the structural region (h) and the two metamaterial interfaces ($h^{\pm}$).

Next, a special case of negative refraction will be shown. Considering again, the geometrical case of (3.3.43) and using the "transparency" property shown above then only $\theta_g^{(1)}$ should be calculated as the amplitude of the second mode was found to be zero. The geometrical assumptions of this special case, simplify the parameters as discussed after equation (3.3.43). Therefore,

$$\begin{aligned}\theta_g^{(1)} &= \arctan\left(\frac{-H_1H_2k\sin\delta + (h-h^+)(\beta h - \tilde{H})\sin\delta\cos\delta}{\beta h H_1}\right)\\ &= \arctan\left(\frac{h^2\sin\delta\cos^2\delta - hh^+\sin\delta(1+\cos^2\delta)}{hH_1\cos\delta}\right)\\ &= \arctan\left(\frac{(h-h^+)\sin\delta\cos^2\delta - h^+\sin\delta}{\cos\delta(h^+\sin^2\delta + h\cos^2\delta)}\right),\end{aligned} \tag{3.3.48}$$

where in the first step, the geometrical simplifications were made and the numerator and denominator were multiplied by H_1. In the second step the numerator and denominator were divided by k and a long algebraic simplification was carried out. In the last step the numerator and denominator were divided by h. The trivial limit $h^+ \to h$ is verified as it gives $\theta_g^{(1)} \to \arctan(-h\sin\delta/h\cos\delta) = -\delta = \theta_0$ which implies that as the barrier height becomes small (when compared to the depth), the direction of energy propagation in $|x| < b$ is aligned with the incident direction of the wave. Now by taking the limit $h^+ \to 0$, then it can be shown that $\theta_g^{(1)} \to \arctan(h\sin\delta/h\cos\delta) = \delta$. This property suggests that for thin barriers that extend through the whole depth, the wave energy direction is aligned with the barrier orientation and thus the metamaterial acts as an all-frequency negative refraction medium [11].

3.3.3 Alternative effective depth tensor representation

In this subsection, an alternative representation of the diagonal depth tensor within the metamaterial region, will be derived. Here instead of starting from first principles, a hybrid method involving ideas combining full linear wave theory and shallow water theory will be considered.

Here, we consider the equations that hold within $|x| < b$ for the problem solved in section 3.2.4. The alternating beds are located at $z = -h^+$ and $z = -h^-$ with $0 < h^+ < h^-$ to have the same notation with the previous section. After finding the effective depths in the direction parallel and perpendicular to the barriers, then the barriers can be tilted at any angle and the effect upon the governing equation will be to multiply from each side the depth tensor with a rotation matrix, as happened in the previous section. Now the velocity potential from full linear theory (shallow water assumption not used yet) will satisfy the Laplacian equation $\nabla^2\Phi = 0$ in $L_g = (-h^+, 0)$ and the reduced Laplacian equation $\big(\partial_{yy} + \partial_{zz}\big)\Phi = 0$ in $L_b = (-h^-, -h^+)$ as the barriers are aligned with the y-axis and no x-variation is allowed into narrow channels. Now we consider a time-harmonic incident wave of wavenumber k and angular frequency ω. The idea now is to solve the dispersion relation for wave propagation over the structured bed under full linear theory for two different wave directions: parallel and perpendicular to the ridges. With the wavenumbers in those directions, one could infer equivalent "effective depths" of section 3.3.1 through a dispersion relation and use these instead of h^+ and $\overline{h}$ in the shallow water model. Writing the wavenumber as $k^2 = k_\parallel^2 + k_\perp^2$, with $k_\parallel$, $k_\perp$ be the components of the wavenumber in the directions parallel and perpendicular to the barriers, then the total potential can be expressed as $\Phi(x, y, z, t) = \Re\{\phi(x, z)e^{ik_\parallel y}e^{-i\omega t}\}$ under the usual assumption of y and t variation compatibility with the incident wave. Note that because of the special barrier orientation, the actual incident wavenumbers in x, y directions ($\beta = k\cos\theta_0$ and $\alpha = k\sin\theta_0$ in the notation of the previous sections) coincide with $k_\perp$, $k_\parallel$. Under these simplifications the model becomes

$$\begin{aligned} \big(\nabla^2 - k_\parallel^2\big)\phi_g(x, z) &= 0, \quad z \in L_g, \\ \big(\partial_{zz} - k_\parallel^2\big)\phi_b(x, z) &= 0, \quad z \in L_b. \end{aligned} \tag{3.3.49}$$

Seeking solutions of separable form as $e^{ik_\perp x} Z_{g,b}(z)$, then

$$\begin{aligned} Z_g''(z) = k^2 Z_g(z), \quad Z_g'(0) = K Z_g(0), \\ Z_b''(z) = k_\parallel^2 Z_b(z), \quad Z_b'(-h^-) = 0, \end{aligned} \tag{3.3.50}$$

where $K = \omega^2/g$ and using that $k^2 = k_\perp^2 + k_\parallel^2$. The particular solutions of (3.3.50) are

$$\begin{aligned} Z_g(z) = A_g \Big[\cosh(kz) + \frac{K}{k} \sinh(kz) \Big], \\ Z_b(z) = A_b \cosh\big[k_\parallel (z + h^-)\big]. \end{aligned} \tag{3.3.51}$$

By applying the continuity of pressure and normal flux at the top interface i.e. $Z_g(-h^+) = Z_b(-h^+)$ and $Z_g'(-h^+) = (1-\theta) Z_b'(-h^+)$, then the dispersion relation coming from the vanishing determinant of the linear (A_g, A_b) system will be the same as in section 3.2.4, namely

$$(1-\theta) k_\parallel \tanh\big[k_\parallel (h^- - h^+)\big] = \frac{K - k \tanh(kh^+)}{k - K \tanh(kh^+)} k. \tag{3.3.52}$$

Now this is where the hybrid nature of this method will be used. According to the shallow water model over a metamaterial specified in (3.3.30), the existence of effective depths in the directions perpendicular and parallel to the barriers, is assumed. Those depths are included in the diagonal tensor $\mathbf{h} = \mathrm{diag}\{h_\perp, h_\parallel\}$ with $h_\perp$ be the effective depth in the x-direction (perpendicular to the barriers) and $h_\parallel$ be the effective depth in the y-direction (parallel to the barriers). To find an expression for $h_\perp$, the assumption $k_\parallel = 0$ and (and so $k = k_\perp$) in the dispersion relation (3.3.52) can be used. This gives

$$K = k \tanh(kh^+), \tag{3.3.53}$$

which suggests that $h_\perp = h^+$ from the standard water dispersion relation.

Similarly, to get the effective depth for a wave travelling in the y-direction, $k_\perp = 0$ (and so $k = k_\parallel$) can be assumed in the same equation to get

$$(1-\theta) \tanh\big[k_\parallel (h^- - h^+)\big] = \frac{K - k_\parallel \tanh(k_\parallel h^+)}{k_\parallel - K \tanh(k_\parallel h^+)}. \tag{3.3.54}$$

One can see that there are no explicit solutions to the wavenumber $k_\parallel$. However, the location of the roots is known as this dispersion relation is identical to (3.2.31) (up to some trivial rearrangement) but with the renamed variables $h \to h^-$ and $d \to h^+$. There are two real and symmetric roots and a sequence of purely imaginary ones, but because in the shallow water regime there are no depth eigenfunction expansions (depth is always averaged out of the equation), then the only root of interest is the positive real one. This root (call it $k_\parallel \in \mathbb{R}_{>0}$) can be found computationally using the bisection method and using the dispersion relation $k_\parallel \tanh(k_\parallel h_\parallel) = K$, then the effective depth in the direction parallel to the barriers can be found to be

$$h_\parallel = \frac{1}{k_\parallel} \tanh^{-1}\left(\frac{K}{k_\parallel}\right). \tag{3.3.55}$$

Therefore a slightly different model to the one of subsection 3.3.1 has been derived, namely

$$\zeta_{tt} = g\nabla \cdot \big(\mathbf{h}\nabla\zeta\big), \quad \text{with} \quad \mathbf{h} = \text{diag}\{h^+, h_\parallel\}, \tag{3.3.56}$$

with $h_\parallel$ found from the equations (3.3.54) and (3.3.55). The only difference is that the averaged depth $\overline{h}$ is replaced $h_\parallel$. Therefore, R and T can be found from (3.3.41) with $H_{1,2}$ and $\tilde{H}$ affected by the averaged depth $\overline{h}$ replacement.

Now, the useful inequality $h_\parallel \leq \overline{h}$ (where the equality holds only for $\theta = 0, 1$) will be derived. This result will prove that there are again two modes travelling in opposite directions within the metamaterial. The proof starts by substituting $K = k_\parallel \tanh(k_\parallel h_\parallel)$ from (3.3.55) into (3.3.54) and use the hyperbolic tangent of difference formula, to get

$$\tanh\big[k_\parallel(h_\parallel - h^+)\big] = (1-\theta)\tanh\big[k_\parallel(h^- - h^+)\big]. \tag{3.3.57}$$

From this equality, one can see that $h_\parallel = h^-$ for $\theta = 0$ and $h_\parallel = h^+$ for $\theta = 1$ (using that the hyperbolic tangent is a bijective function). Note that by definition, $\overline{h}$ gets the same values with $h_\parallel$ at the endpoints of θ. Now for a general $\theta \in (0, 1)$, the

previous equality gives rise to the useful inequality

$$0 < \tanh\left[k_{\parallel}(h_{\parallel} - h^{+})\right] < \tanh\left[k_{\parallel}(h^{-} - h^{+})\right]. \tag{3.3.58}$$

The middle term is positive as the right-hand side of (3.3.57) was positive. Therefore from the triple inequality one can see that $h^{+} < h_{\parallel} < h^{-}$ for $\theta \in (0,1)$, by using again the increasing behaviour of the hyperbolic tangent. Using the upper bound of $h_{\parallel}$, then $\alpha^2 H_2 < k^2(h^{+}\cos^2\delta + h_{\parallel}\sin^2\delta) \leq k^2(h^{+}\cos^2\delta + h^{-}\sin^2\delta) < k^2 h$ as the alternating depths of the structure are both smaller than the actual depth of the fluid. This inequality proves that $\mu_{1,2}$ from (3.3.33) are real and opposite in sign which on physical grounds means that there are two waves travelling in opposite directions within $|x| < b$.

Although $h_{\parallel}$ and $\overline{h}$ have the same bounds at the same θ values (endpoints), it can be also be proved that $h_{\parallel}$ is always smaller than $\overline{h}$ for any $\theta \in (0,1)$. The proof starts from the inequality $\tanh(ax) > a\tanh(x)$ for any $a \in (0,1)$ and $x > 0$ which can be proved by using $f'(x) > g'(x)$ for $x > 0$ and $f(0) = g(0)$ for f, g be the left and right-hand side of the inequality. Then by substituting $a = (1-\theta) \in (0,1)$ and $x = k_{\parallel}(h^{-} - h^{+}) > 0$, the following inequality yields

$$\tanh\left[(1-\theta)k_{\parallel}(h^{-} - h^{+})\right] > (1-\theta)\tanh\left[k_{\parallel}(h^{-} - h^{+})\right]. \tag{3.3.59}$$

Using that $\overline{h} - h^{+} = (1-\theta)(h^{-} - h^{+})$ (by definition) in the left-hand side and (3.3.57) in the right-hand side, then (3.3.59) becomes

$$\tanh\left[k_{\parallel}(\overline{h} - h^{+})\right] > \tanh\left[k_{\parallel}(h_{\parallel} - h^{+})\right]. \tag{3.3.60}$$

Again from the increasing behaviour of the hyperbolic tangent then the final result follows as

$$h_{\parallel} \leq \overline{h}, \quad \forall\theta \in [0,1], \tag{3.3.61}$$

with the equality holding at the θ-endpoints, namely $h_{\parallel} = \overline{h} = h^{-}$ for $\theta = 0$ and $h_{\parallel} = \overline{h} = h^{+}$ for $\theta = 1$.

Also, since the effective depth of this model is found to depend on the wavenumber $k_{\parallel}$, it will now be shown that in the long wave limit, $h_{\parallel} = \overline{h}$. First it

is worth noting that if k becomes small, then so does $k_\parallel$ as they are related through $k^2 = k_\parallel^2 + k_\perp^2$. Therefore by approximating the hyperbolic tangents of equation (3.3.54) by their small arguments, then

$$(1-\theta)k_\parallel(h^- - h^+) = \frac{K - k_\parallel^2 h^+}{k_\parallel(1 - Kh^+)}. \tag{3.3.62}$$

Using that $\overline{h} - h^+ = (1-\theta)(h^- - h^+)$ (by definition) and $K = k_\parallel \tanh(k_\parallel h_\parallel) \approx k_\parallel^2 h_\parallel$ from (3.3.55), then the equation above can be rearranged to

$$\frac{h_\parallel - h^+}{\overline{h} - h^+} = 1 - k_\parallel^2 h_\parallel h^+ \approx 1, \tag{3.3.63}$$

which implies that $h_\parallel = \overline{h}$ in the long wave limit.

3.3.4 Numerical results

In this section, numerical results for the scattering problem introduced in section 3.3.1 will be demonstrated using the two different solutions of sections 3.3.2 and 3.3.3. The two models over the metamaterial region, have the same equation structure, namely the first can be found from (3.3.32) with $H_1 = h^+ \sin^2\delta + \overline{h}\cos^2\delta$, $H_2 = h^+\cos^2\delta + \overline{h}\sin^2\delta$ and $\tilde{H} = \alpha(\overline{h} - h^+)\sin\delta\cos\delta$ and the second from the same equation but with $\overline{h}$ replaced by $h_\parallel$ from (3.3.55). From now on, these models will be referred to SW1 and SW2 respectively.

First, a comparison between the SW1 and SW2 models is made in figure 3.17(i) by plotting the ratio $h_\parallel/\overline{h}$ against the thickness parameter θ. Note that $h_\parallel$ requires a value of k. The geometrical parameters (in dimensionless form) of the two curves are $(kh, h^+/h, h^-/h) = (0.6, 0.4, 0.8)$ (full line) and $(kh, h^+/h, h^-/h) = (0.2, 0.1, 0.9)$ (dashed line). It can be verified that $h_\parallel \leq \overline{h}$ with the equality hold only at $\theta = 0, 1$ (as shown analytically in the previous section). It will be verified later that the difference between these two effective depths is significantly small in the long wave limit.

Now in figure 3.17(ii), different effective depths from different authors are plotted (in dimensional form with $h^+ = 0.4$ and $h^- = 1.4$). [1] and [13] considered the

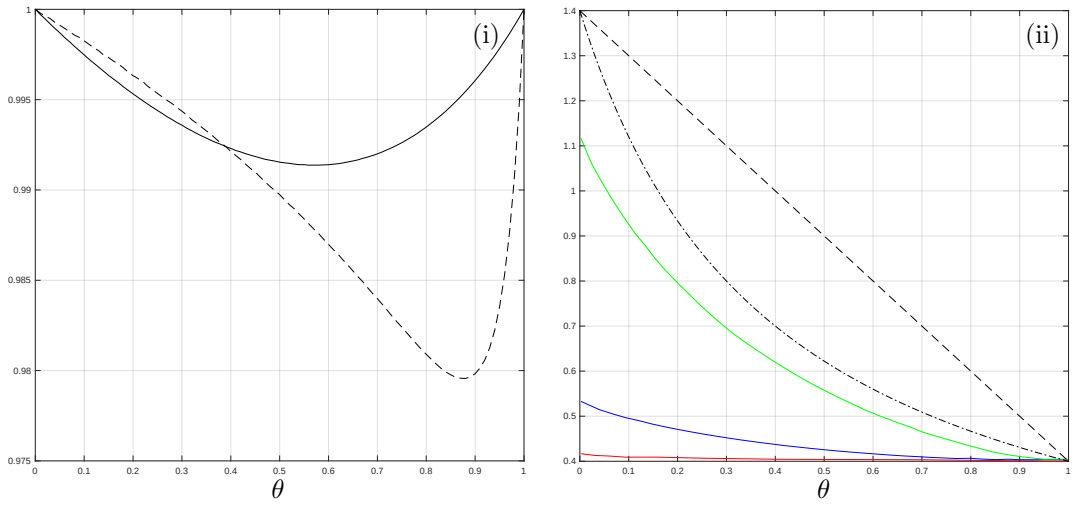

Figure 3.17: (i) $h_{\|}/\overline{h}$ against θ for $(kh, h^+/h, h^-/h) = (0.6, 0.4, 0.8)$ (full) and $(kh, h^+/h, h^-/h) = (0.2, 0.1, 0.9)$ (dashed). (ii) $\overline{h}$ (dashed) and $\langle h^{-1}\rangle^{-1}$ (chained) for $h^+ = 0.4$ and $h^- = 1.4$. The coloured curves are the effective depths found from [1] for $l/h^- = 0.04$ (red), $l/h^- = 0.4$ (blue), $l/h^- = 4$ (green).

scattering by a bed with barriers in the shallow water regime and they have derived the same structure of equation as in section 3.3.1, using different assumptions and methods. They determined the effective depth tensor as $\mathbf{h} = \text{diag}\{h_1, h_2\}$ and both authors found that $h_2 = \overline{h} = \theta h^+ + (1-\theta)h^-$ which coincides with the one used in our model (SW1). This common effective depth is demonstrated from the dashed curve of figure 3.17(ii) and it can be seen that it is linear in θ as expected from its closed-form expression. The difference between the models discussed above, lies upon the definition of h_1. The modelling assumption of [13] resulted in $h_1 = \langle h^{-1}\rangle^{-1}$ for $\langle f\rangle \equiv \theta f^+ + (1-\theta)f^-$ which is represented by the chained curve of figure 3.17(ii). This effective depth tends to h^- as $\theta \to 0$ and to h^+ as $\theta \to 1$, in contrast to the constant value $h_1 = h^+$ found in the previous sections. However the model of [13] is expected to work for widely-spaced barriers ($l/h^- \gg 1$) as in the homogenisation method used, there was no extra dimensionless small variable taken into account apart from $H/L \ll 1$ (as happened with $\epsilon = l/L$ found in equation (3.3.1)). The numerically-determined value of [1], which covers the two limiting cases (closely and widely spaced barriers), is shown in figure 3.17(ii) by the coloured curves (each colour represent different spacing). This value was determined based on the shallow water assumptions and by solving a potential flow problem in a fundamental cell which

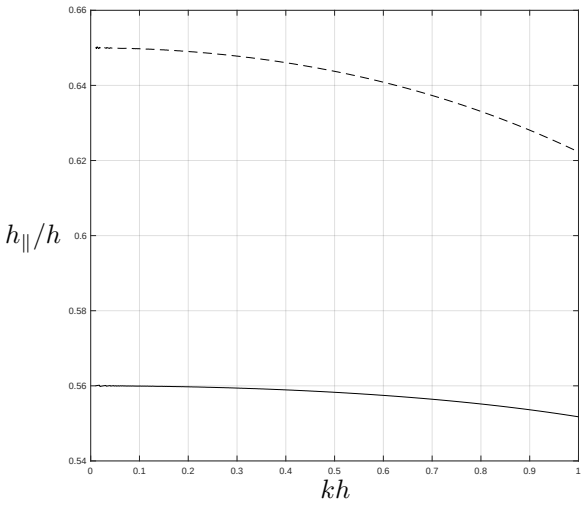

Figure 3.18: $h_\parallel/h$ against kh for parameters $(\theta, h^+/h, h^-/h) = (0.1, 0.2, 0.6)$ (full) and $(\theta, h^+/h, h^-/h) = (0.5, 0.4, 0.9)$ (dashed).

resulted from their homogenisation, without making any assumptions of the size of l/h^-. In their paper the details to determine the value of h_1 numerically are provided and in their Fig. 8(a) a comparison between their model and the one of [13], is provided (identical to the curves plotted here). Evidently, it can be seen from figure 3.17(ii), that in the wide-spacing limit their model approaches the value of $\langle h^{-1}\rangle^{-1}$ [13] and as l/h^- decreases their results converge to the constant value $h_1 = h^+$, which is a result from our effective shallow water models (SW1 & SW2). As highlighted from [1], it is the closely-spaced limit that gives rise to the largest difference between h_1 and h_2 and therefore the greatest anisotropy in propagating wave speeds (which is required for many metamaterial properties as discussed in Chapter 1, such as negative refraction, wave bending, cloaking etc.).

Next in figure 3.18, the kh-variation of the dimensionless effective depth of SW2, namely $h_\parallel/h$, is presented. The analogue SW1 curve ($\overline{h}/h$) was not plotted as it is known to be constant in kh and according to the geometrical parameters chosen in figure 3.18 it turns out that $\overline{h}/h = 0.56$ for the full line analogue and $\overline{h}/h = 0.65$ for the dashed curve. It can be verified numerically that the two models coincide in the limit $kh \to 0$ (long wave limit) as shown analytically in the previous section.

Moving on to figure 3.19, the full linear model represented by the full line (depth-dependent) of section 3.2.6 is compared with the shallow water models SW1 and SW2 (dashed and chained line respectively) with barriers sitting on the bed

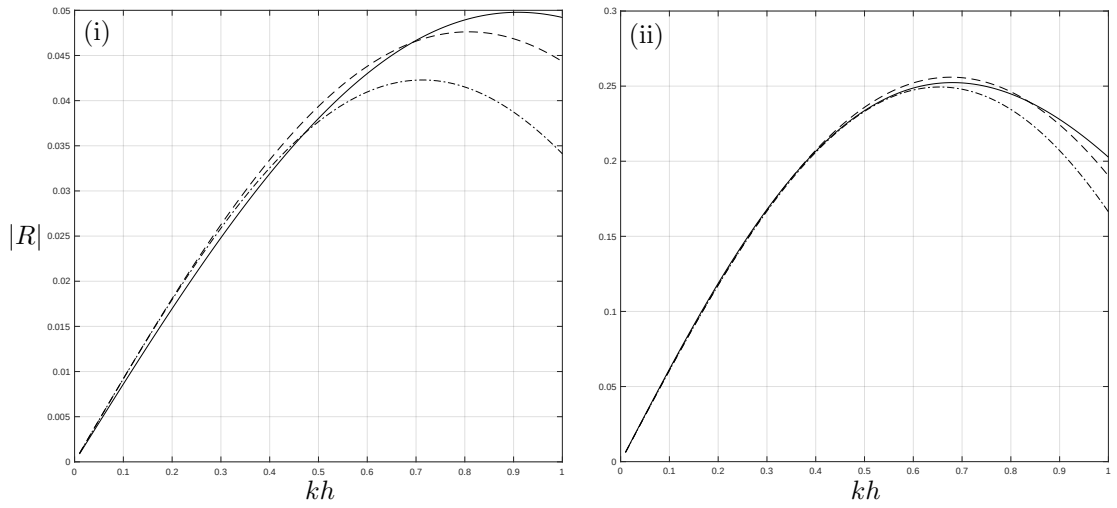

Figure 3.19: $|R|$ against kh using full linear theory (full), SW1 (dashed) and SW2 (chained). The geometrical parameters are (i) $(\delta, \theta_0, \theta, h^+/h, b/h) = (30°, 45°, 0.3, 0.5, 1)$ and (ii) $(\delta, \theta_0, \theta, h^+/h, b/h) = (45°, 60°, 0.1, 0.2, 1)$.

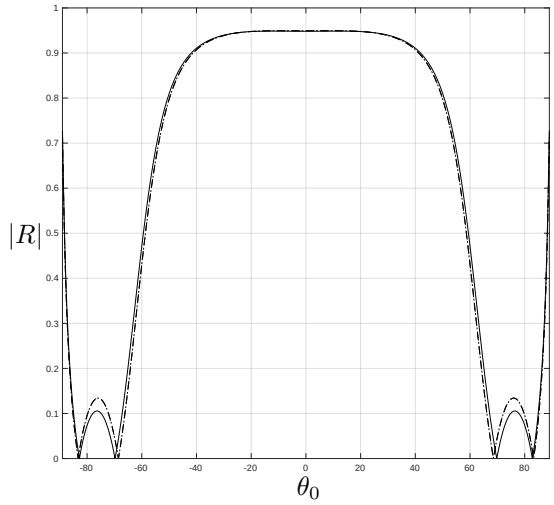

Figure 3.20: $|R|$ against θ_0 for $kh = 0.07$, $\delta = 0°$, $h^+/h = 0.025$, $h^-/h = 0.5$, $b/h = 9.1$, $\theta = 0.1$ using full linear theory of section 3.2.4 (full), SW1 (dashed) and SW2 (chained).

($h^-/h = 1$ to be comparable with the 3D model). The reflection modulus is plotted against kh for two different geometries. In both figures the behaviour of all the curves has the typical features discussed in all the previous numerical results of this chapter (oscillatory curves with non-constant kh period, passing through the origin, decay for large kh, interaction depend on barrier height etc.). The most interesting feature of the figures above, is that there is a good agreement between the three curves as $kh \to 0$ (shallow water limit). This provides us with evidence that SW1 and SW2 are good models as the full linear problem converge to them in the long wave limit. The shallow water curves of figure 3.19(i) start to diverge from each other for a smaller kh if compared to figure 3.19(ii). This is because in figure 3.19(ii) the thickness parameter was chosen to be $\theta = 0.1$ (instead of $\theta = 0.3$ from figure (i)) which is closer to the endpoint $\theta = 0$ at which it is known that SW1 and SW2 are exactly the same. So the hybrid method of SW2 does not seem to provide any extra accuracy here.

Continuing with the comparison of the three models, the reflection modulus against the incident angle θ_0 is plotted in figure 3.20 with the full line presenting the 3D model of section 3.2.4 and the dashed and chained curves present SW1 and SW2 respectively for $\delta = 90^\circ$ to be comparable with the full lined curve. Note that this particular barrier orientation of the 3D problem, allows the two metamaterial interfaces to take any value in $0 < h^+ < h^-, h$, but in the shallow water problem the restriction of $0 < h^+ < h^- < h$ is implemented to allow us to prove certain features of the solution. Therefore, in this numerical comparison, the particular geometry of $0 < h^+ < h^- < h$, will be considered.

The choice of geometrical parameters of figure 3.20 was made in a way to compare directly these curves with the ones of [16], Fig. 11(a)(ii), where they considered a long wave ($kh = 0.07$) interacting with thick barriers ($\theta = 0.1$) parallel to the y-axis ($\delta = 90^\circ$) that sit on a step ($h^-/h = 0.5$) and extend almost all the way up to the free surface ($h^+/h = 0.025$). First, there is a good agreement between the 3 curves as $kh = 0.07$ is reasonably small and it was verified above that SW2 converges to SW1 in that limit. Also, there are two roots in $\theta_0 \in (0^\circ, 90^\circ)$, namely at 69.8 and 82.8 for the 3D problem and 68.5 and 83.2 for the shallow water problems. The analogue result of [16], had two zeros as well but comparing the position of those zeros with ours, it can be seen that here the zeros are shifted to the right when compared to their Fig. 11(a)(ii) at leading order. The reason behind this might be the difference in the asymptotic relation between the two small parameters that they use, namely $\epsilon = \omega\sqrt{l/g} \ll 1$ with $\omega\sqrt{h/g} = \mathcal{O}(\epsilon)$ which suggests that the barrier spacing is of the same order of magnitude with the depth. This assumption is different than the one used in section 3.3.1 where the parameters are related as

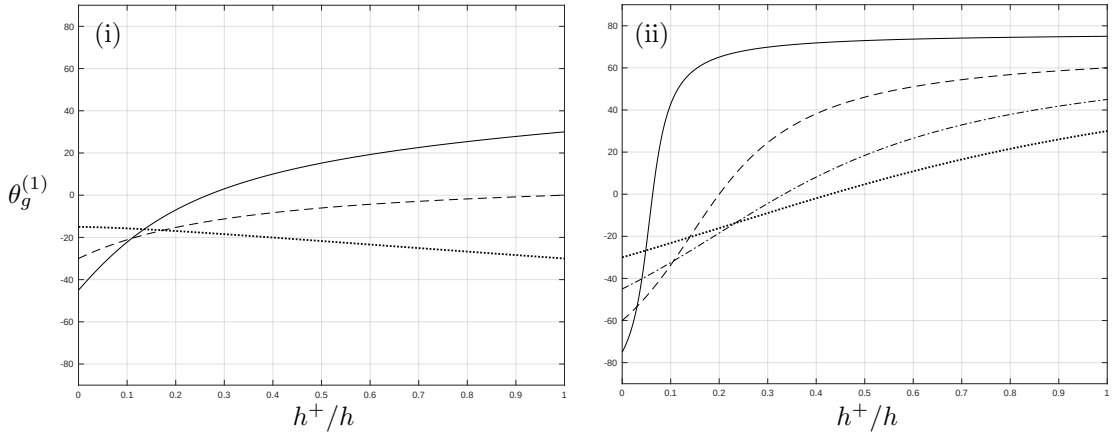

Figure 3.21: $\theta_g^{(1)}$ against h^+/h with $h^- = h$. (i) $\theta = 0.7$ for $(\theta_0, \delta) = (30°, -45°)$ (full), $(\theta_0, \delta) = (0°, -30°)$ (dashed) and $(\theta_0, \delta) = (-30°, -15°)$ (dotted). (ii) Special case of $\theta = 0$, $\theta_0 = -\delta$ with $\theta_0 = 30°$ (dotted), $\theta_0 = 45°$ (chained), $\theta_0 = 60°$ (dashed) and $\theta_0 = 75°$ (full).

$\mu = H/L$ and $\epsilon = l/L$ with $\epsilon = \mathcal{O}(\mu^2)$.

Next, the variation of the direction of energy propagation in degrees, $\theta_g^{(1)}$, with respect to the gap ratio h^+/h is demonstrated in the figures of 3.21. The common features of these plots is that the value of $\theta_g^{(1)}$ is always lying between the values of θ_0 and δ and $\theta_g^{(1)} \to \theta_0$ when $h^+ \to h$, as expected from the theory and on physical grounds. Also, in figure 3.21(ii) it can be verified that $\theta_g^{(1)} \to \delta$ for $h^+ \to 0$ as shown in section 3.3.2. The remarkable result is that the same property holds for non-zero thickness θ as shown in 3.21(i), even though was not shown analytically.

In figure 3.22 the direction of energy propagation is plotted against the incident direction θ_0 for thin barriers ($\theta = 0$) that are rotated at an angle $\delta = -45°$. The barriers sit on the bed ($h^- = h$) and we plot curves for different gap ratio (h^+/h). It can be verified that $\theta_g^{(1)} \to \theta_0$ in the limit $h^+/h \to 1$ as the structure disappears and there is no scattering (presented in the plot by the straight line $\theta_g^{(1)} = \theta_0$). Also, as h^+/h decreases the metamaterial structure extends throughout the depth and the curves tend to the constant value $\theta_g^{(1)} = -45°$ (in θ_0) coinciding with the limiting case considered in [11]. For $\theta_0 = -45°$, we get $\theta_g^{(1)} = -45°$ which means that the incident wave passes uninterrupted between the thin barriers for all h^+/h. Negative refraction occurs when $\theta_g^{(1)}$ and θ_0 have different signs and so it can be verified that

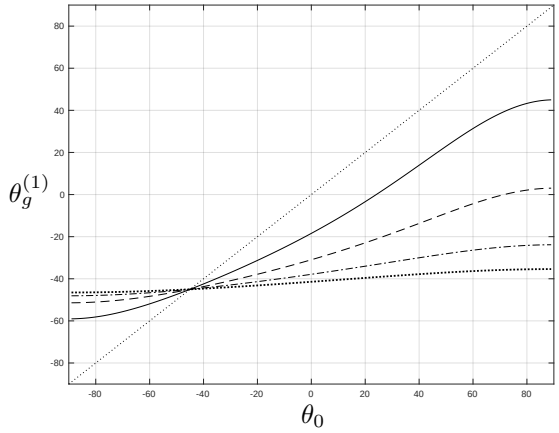

Figure 3.22: $\theta_g^{(1)}$ against θ_0 for $\theta = 0$, $h^- = h$ and $\delta = -45°$ with $h^+/h = 1/2$ (full), $h^+/h = 1/4$ (dashed), $h^+/h = 1/8$ (chained) and $h^+/h = 1/16$ (dotted).

this phenomenon occurs for $h^+/h < 1/4$ (approximately) and for all $\theta_0 > 0°$.

Next, the free surface plots and their cross-sections at $y = 0$, are demonstrated in figures 3.23 and 3.24, for the special case of $\theta_0 = -\delta$, $h^- = h$ and $\theta = 0$. The elevation is found from the piecewise definition of the free surface (3.3.35) through $\zeta(x, y, t) = \Re\{\eta(x)e^{i\alpha y}e^{-i\omega t}\}$ and the reflection and transmission found in (3.3.38). In figure 3.23, it can be verified that there is a single travelling wave in $|x| < b$ travelling at a direction parallel to the barriers. These features agree with the analytical proof of the transparency property (thin barriers sitting on the flat bed with $\theta_0 = -\delta$ produce $R = B = 0$ and $|T| = |A| = 1$ from (3.3.44)) and verify the negative refraction property discussed after (3.3.48) for high barriers (since $h^+/h = 0.01$). In figure 3.23, the direction of the energy propagation and the direction of the phase speed in $|x| < b$ was found to be $\theta_g^{(1)} \approx 43.84°$ and $\theta_p^{(1)} \approx -18.66°$ respectively. This is a verification to the negative refraction case specified in (3.3.48) since $\theta_g^{(1)} \approx \delta$. However, the direction of the phase speed has a different sign than the direction of the energy propagation. In contrast with the surface plots of the problem solved using non-shallow assumptions (problem of section 3.2.6), here there is a gradient discontinuity at $x = \pm b$. This is expected from the flux matching conditions supplied with the shallow water model. In the 3D problem, the possible gradient discontinuities of the velocity potential where located only in $z \in L_b$, but at the surface the matching conditions implied the smoothness of the potential (and therefore the free surface).

In figure 3.24, again there is a single scattering mode in the metamaterial

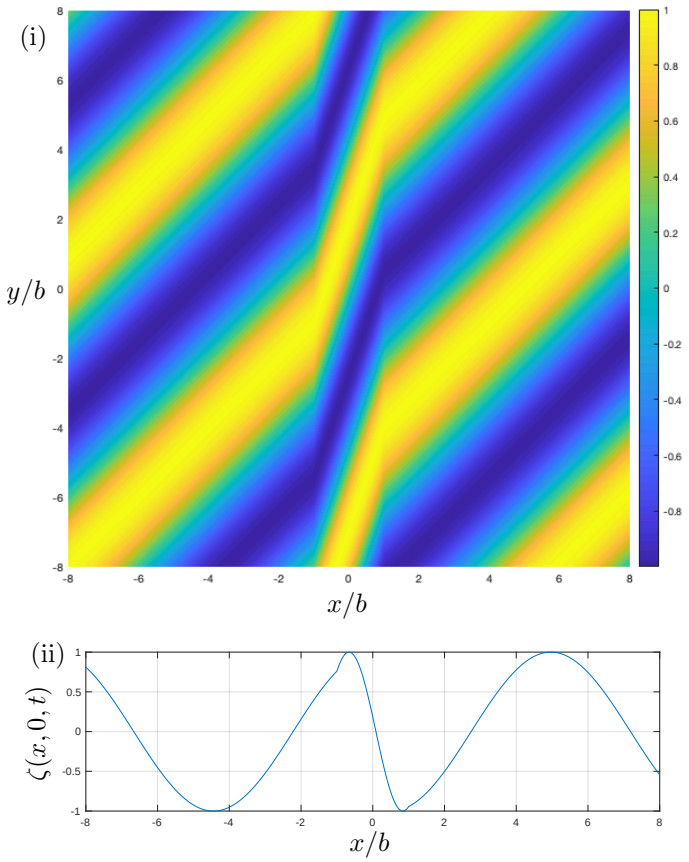

Figure 3.23: (i) Instantaneous surface elevation and (ii) wave profile at $y = 0$, for $kh = 1$, $\theta_0 = -\delta = -45°$, $\theta = 0$, $h^+/h = 0.01$ and $h^-/h = b/h = 1$.

region (as expected from the special geometrical case), but now it travels at a direction almost parallel to the incident wave. This is because now the barriers are relatively short ($h^+/h = 0.5$) and it is known from the analysis of section 3.3.2 that the negative refraction effect is fading away with the decrease of the structural height (and after a point, negative refraction becomes "positive"). Here, the direction of the energy propagation and the direction of the phase speed in $|x| < b$ was found to be $\theta_g^{(1)} \approx -18.43°$ and $\theta_p^{(1)} \approx -30.96°$ respectively. This indicates "positive" refraction as $\theta_g^{(1)}$ and θ_0 have the same sign.

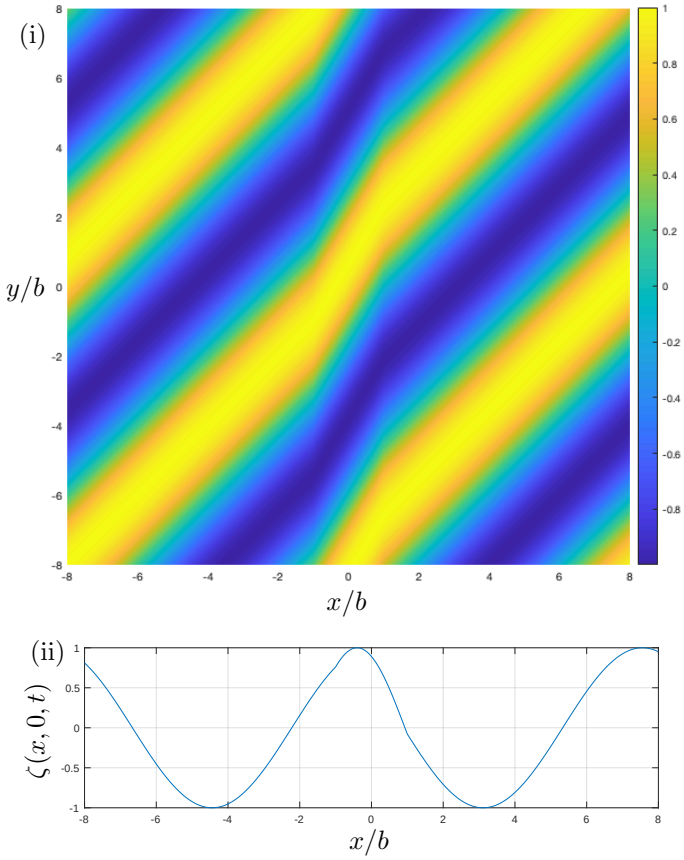

Figure 3.24: (i) Instantaneous surface elevation and (ii) wave profile at $y = 0$, for $kh = 1$, $\theta_0 = -\delta = -45°$, $\theta = 0$, $h^+/h = 0.5$ and $h^-/h = b/h = 1$.

Chapter 4

Wave interaction with a microstructured metamaterial wall

4.1 Introduction

This chapter investigates the scattering properties of a microstructured wall that consists of a periodic sequence of barrier configurations which have a triangular shape and they are uniform in the vertical coordinate. Each triangle is comprised of a closely-spaced array of thin plates with narrow channels between them (see figure 4.1). The goal is to find ways control the transmission and/or the wave energy absorption.

The most common device that produces acoustic absorption in a waveguide is the Helmholtz resonator. This device consists of a chamber attached to the waveguide via a narrow channel. The geometrical parameters of the device control the resonant frequencies and therefore the interaction between the propagating waves and the device becomes significant close to these frequencies [82]. High-efficiency absorbers can be achieved by connecting multiple resonators of different resonant frequencies to extend the absorption over a broadband region of frequencies [10], creating the analogous phenomenon of "rainbow trapping" from electromagnetics [83].

Rainbow trapping effects in the context of acoustics can be achieved also through micro-resonators in two or three dimensions. For example, [84] produced this effect through a metamaterial "carpet" made of thin grooves, allowing spectral control of acoustic waves. However, the problem of discrete micro-channels is hard to solve by exact analytical methods and typically its numerical solution can be obtained using finite element method [85]. But by taking advantage of the small channel width (with respect to other field variables) and using homogenisation theory, then the microstructured metamaterial wall can be replaced by an effective medium. For the scales of operation that are being conceived of the spacing between elements in the array are small enough that it is likely that acoustic damping effects cannot be neglected. This is a similar description of the one of [21], where they considered a normally-incident acoustic wave travelling within a waveguide on which a cavity was attached. The cavity was made of narrow channels perpendicular to the waveguide, where the field in the cavity was damped.

The derivation of a model that includes damping in the case of water and acoustic waves, will be included in the next two sections, following established theory of other authors. Then, the solution to the problem will be sought using Fourier analysis (or separation of variables) and the theory will be supported with numerical results.

Starting from the description of our problem, the metamaterial wall that consists of a periodic sequence of barrier configurations will have a triangle shape of hypotenuse L. Each triangle is made of closely spaced thick barriers of small periodicity l and thickness θl (where $\theta \in (0,1)$ is the filling fraction), that are parallel to one of the two adjacent sides. The adjacent sides are closed such that the only way for the wave to enter or leave the configuration, is the openings between the barriers through the hypotenuse. Cartesian coordinates (x, y) are chosen such that the hypotenuse of the first triangle is aligned with $y = 0$ and $x \in (0, L)$. Without the loss of generality, the orientation of the barriers is set to make an acute angle $\delta \in (0^\circ, 90^\circ)$ with the positive y-axis. Now in contrast to the previous metamaterial problems, the coordinate that is aligned with the barrier orientation is called Y (instead of X) and it can be found by rotating y towards x by an angle δ. Then, copies of the first triangle are placed next to each other to create an infinite periodic sequence that forms the metamaterial wall. The hypotenuse of the n^{th} triangle is set to be aligned with $y = 0$ and $x \in ((n-1)L, nL)$.

The lack of dependence of the geometry on the vertical coordinate makes the problem applicable to various types of waves. In this thesis only the water and acoustic wave case are considered. In the water waves context, the vertical coordinate z is chosen such that, $z = 0$ is aligned with the undisturbed free surface of the sea. In

the case of sound waves, we are considering a 2D acoustic problem which is uniform in the vertical coordinate (plane wave aligned with the z-axis). The solution method to both problems is identical. An incident wave of wavenumber k, propagates from $y \to -\infty$ and makes an angle $\theta_0 \in (-90°, 90°)$ with the positive y-axis. The wave enters the homogenised medium through $y = 0$, then travels along the narrow ducts, reflected through the closed adjacent side of the triangles and eventually reflected back into $y < 0$.

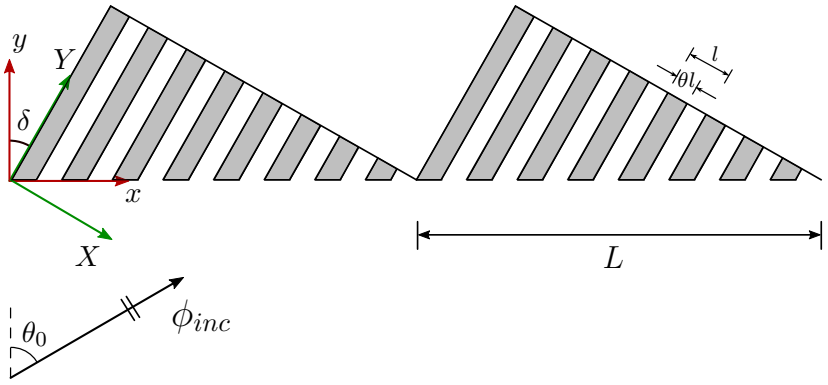

Figure 4.1: Geometry of the metamaterial wall made of a periodic sequence of triangular barrier configurations. The incident wave ϕ_{inc} interacts with the metawall and then it is reflected back into $y < 0$.

In that case of water waves, the z-dependence of the velocity potential can be factored out through $\cosh[k(z+h)]$, so that there is no flow through the constant bed at $z = -h$ and the surface condition is satisfied (using the water dispersion relation $k\tanh(kh) = \omega^2/g$ for ω be the incident angular frequency and g be the gravity constant). Therefore, writing the velocity potential as $\Phi(x, y, z, t) = \Re\{\phi(x, y)\cosh[k(z+h)]e^{-i\omega t}\}$, then the Laplace's equation reduces to the Helmholtz equation, namely

$$\big(\nabla^2 + k^2\big)\phi(x, y) = 0 \quad \text{in} \quad y < 0, \tag{4.1.1}$$

with the surface and bed conditions been satisfied (in the case of water waves). The Helmholtz equation is satisfied by the acoustic wave as well for $k = \omega/c_0$ where c_0 is the isentropic speed of sound [27]. Also, a far-field condition must be included to the problem i.e., the potential is required to be bounded at $y \to -\infty$. Next, since there is a plane wave incident on a periodic geometry, some periodic conditions to the problem arise. The change in phase of the incident wave as we move from a point

(x, y) to $(x + L, y)$ is $e^{i\alpha_0 L}$ and therefore the resulting potential must also be subject to the same change in phase across a period in x. Therefore, the far field condition and the two "periodic" boundary conditions (coming from Bloch-Floquet Theory) that must be imposed to the problem are

$$\lim_{y\to-\infty} |\phi(x,y)| < \infty,\ \phi(x+L,y) = e^{i\alpha_0 L}\phi(x,y),\ \phi_x(x+L,y) = e^{i\alpha_0 L}\phi_x(x,y), \quad (4.1.2)$$

for all $x \in \mathbb{R}$ and with $\alpha_0 = k\sin\theta_0$ be the incident wavenumber in the x-direction. Finally, homogeneous matching conditions of the potential and the normal flux through $y = 0$ must be introduced. The analogue of (3.2.76) in this problem is

$$\phi(x,0) = \hat{\phi}(x\cos\delta, x\sin\delta), \quad \phi_y(x,0) = (1-\theta)\cos\delta\hat{\phi}_Y(x\cos\delta, x\sin\delta), \qquad (4.1.3)$$

after a geometrical inspection close to the metamaterial boundary.

4.2 Linear damping within the metamaterial wall

4.2.1 Effective equations in the water waves context

In this section we derive the damped effective equation within the arrays in the case of water waves. For example in [22], a number of ways are identified that modelled this phenomenon. For example in the first, it is assumed that a small porous medium is added on top of an inviscid water such that $z \in (-d, 0)$ covers the porous layer and $z \in (-h, -d)$ the inviscid domain, with $d \ll \lambda$ (incident wavelength). Then the slow viscous-dominated flow within that porous medium will obey the vertical component of the Darcy's Law, namely $w(x, y, t) = -\kappa[p_z(x, y, z, t) + \rho g]/\mu$ [23]. Here w is the vertical velocity which is independent of z as $d \ll \lambda$, κ is the permeability (in m^2), μ is the dynamic viscosity and ρ is the density of the porous layer. Integrating in z using that $w = \zeta_t$ and $p = p_{atm}$ on $z = \zeta$, then $p = p_{atm} + \rho g(\zeta - z) - \mu z\zeta_t/\kappa$ by neglecting products of motion terms. Matching this pressure across $z = -d$, with the pressure in $z \in (-h, -d)$, namely $p = p_{atm} - \rho\Phi_t - \rho g z$, and then eliminating ζ using that $\Phi_z(x, y, -d, t) = \beta\zeta_t(x, y, t)$ for some dimensionless blockage coefficient $0 < \beta \leq 1$

(represents the fractional area of the medium occupied by pores in a horizontal cross-section), it follows that $\phi_z = \tilde{K}\phi$ on $z = 0$ for $\tilde{K} = K\beta/(1 - i\omega\mu d/\rho g\kappa)$ after assuming time harmonicity through $e^{-i\omega t}$. Normally the condition should be applied on $z = -d$, but due to $d \ll \lambda$ it can be evaluated on $z = 0$.

Also, in [24], a periodic array of buoys on the surface that work as wave energy extractors, affect the surface condition in a similar way. Using multiscale homogenisation theory with the small parameter be the ratio between the buoys separation and the depth, then the modified wavenumber in the surface condition results to $\tilde{K} = K(1 + i\omega(f - 1)c)/(1 - i\omega c)$ after assuming time harmonic motion. Here $f = \pi a^2/d^2$ with a be the radius of each buoy and d is the separation from their centres and therefore $f \in (0, \pi/4)$ to guarantee that the buoys do not overlap. Also $c = \lambda/\rho g\pi a^2$, with ρ be the water density and λ be a constant coefficient such that $-\lambda\zeta_t$ represents a linear load force on the surface that models the buoys as energy extraction devices.

The final setting, which is closer to the geometry of our problem, is the one solved by [25] and [26] (Section 9, Exercise 9.2). They showed that the effect of the dynamic viscosity μ due to the fluid interaction with the a narrow channel of height h and width d_p, shifts the wavenumber $k \in \mathbb{R}_{>0}$ to

$$k' = k(1 + i\epsilon) \text{ for } \epsilon = \frac{1}{d_p}\sqrt{\frac{2\mu}{\rho\omega}}\left(\frac{kd_p + \sinh(2kh)}{2kh + \sinh(2kh)}\right), \tag{4.2.1}$$

provided that ϵ is small and ω is the angular frequency of the wave.

Following the homogenisation method of section 3.2.1, the Helmholtz equation (4.1.1) becomes $\big(\partial_{YY} + k^2\big)\hat{\phi}(X, Y) = 0$ (reduced Helmholtz equation) at leading order of the small ratio of the barrier spacing and width. Here, $\hat{\phi}$ is the potential within the triangular metamaterial arrays and (X, Y) is the rotated orthogonal coordinates as shown in figure 4.1, related to (x, y) through $X = x\cos\delta - y\sin\delta$ and $Y = x\sin\delta + y\cos\delta$. Adopting ideas from the previous paragraphs, we characterise the damping effects that occur within the metamaterial wall by shifting the wavenumber in the reduced Helmholtz equation by a small imaginary part. So the effective medium equations within the metamaterial arrays become

$$\big(\partial_{YY} + \hat{k}^2\big)\hat{\phi}(X, Y) = 0, \quad \hat{\phi}_Y(X, L\sin\delta) = 0, \tag{4.2.2}$$

where $\hat{k} = k + k_i$ $(0 \leq k_i \ll k)$ with its real part giving information about the frequency of the wave and the imaginary part about the damping. The second equation is the homogeneous no flux condition at the end of narrow channel.

4.2.2 Effective equations in the sound waves context

The key ingredients to derive the acoustic equation is to start from the two dimensional mass and momentum conservation laws found in (2.1.5), (2.1.10) (with $\mathbf{f} = \mathbf{0}$ assuming that gravity has no effect on the wave) and write the three dependent variables as small fluctuations about an equilibrium i.e. $\rho = \rho_0 + \rho'$, $p = p_0 + p'$, $\mathbf{u} = \mathbf{u}'$. Another equation is needed to get the same number of equations and unknowns. Namely, $\frac{\partial p}{\partial \rho} = c_0^2$ where c_0 is the isentropic speed of sound [27]. The general solution is $p = c_0^2\rho + const.$ and in the equilibrium state (switching off p' and ρ') it becomes $p_0 = c_0^2\rho_0 + const.$ By eliminating the integration constant, the three equations become

$$\frac{\partial \rho'}{\partial t} + \rho_0 \nabla \cdot \mathbf{u}' = 0, \quad \rho_0 \frac{\partial \mathbf{u}'}{\partial t} = -\nabla p' + \frac{1}{3}\mu \nabla\Big(\nabla \cdot \mathbf{u}'\Big) + \mu \nabla^2 \mathbf{u}', \quad p' = c_0^2 \rho'. \tag{4.2.3}$$

Note that in the case of $\mu = 0$, then through elimination it turns out that all the variables (ρ', p' and Φ' - the velocity potential i.e. $\mathbf{u}' = \nabla\Phi'$) satisfy $\big(\partial_{tt} - c_0^2\nabla^2\big)\Phi' = 0$ which results to the Helmholtz equation $\big(\nabla^2 + k^2\big)\phi' = 0$ for $k = \omega/c_0$ by assuming time harmonic motion with angular frequency ω.

However by adding viscosity, then an expression for the tangential shearing stress near a wall must be derived. This can be found by solving the Stokes boundary layer problem [28] in the presence of a wall at $y = 0$ and a fluid in $y < 0$ oscillating in the direction parallel to the wall. Writing the velocity as $\mathbf{u}'(y,t) = u'(y,t)\hat{\mathbf{x}}$, then the two components of the second equation in (4.2.3), give

$$-i\omega\rho_0 u'(y) = -p'_x + \mu u'_{yy}(y), \quad 0 = -p'_y, \tag{4.2.4}$$

by assuming time harmonic motion. The second equation implies that the pressure must be only a function of x and since in the first equation all the other terms apart from the pressure are independent of x, then it follows that p'_x is a constant. This constant can be found using that $p'_x = \frac{\partial p'_\infty}{\partial x} = i\omega\rho_0 u'_\infty$, where the terms with the

subscripted infinity symbol means that the function is evaluated far from the wall ($y \to -\infty$). In the first equality the fact that p'_x is constant was used, while in the second equality was found from the first equation of (4.2.4) using that far from the wall the viscous effects are negligible. Substituting back $p'_x = i\omega\rho_0 u'_\infty$ into the first equation of (4.2.4), then an ordinary differential equation for the velocity arises. The particular solution of that differential equation can be found easily as

$$u'(y) = u'_\infty \left[1 - \exp\left(\frac{1-i}{\delta_V} y\right)\right] \quad \text{for} \quad \delta_V = \left(\frac{2\mu}{\rho_0 \omega}\right)^{1/2}, \tag{4.2.5}$$

using that $u'(0) = 0$ (no flow through the wall) and $u' \to u'_\infty$ as $y \to -\infty$. Also, δ_V is defined to be the viscous boundary layer length [27]. Therefore, the tangential shearing stress near the wall is

$$S \equiv \mu \frac{\partial u'}{\partial y}\Big|_{y=0} = -\mu u'_\infty \frac{1-i}{\delta_V}. \tag{4.2.6}$$

Now using this stress expression, the problem of the narrow duct should be considered (two walls at $y = 0$ and $y = -a$). Using the leading order result (in a homogenisation under a small gap assumption) of (3.2.7), that the wave within two closely spaced barriers tends to move only in the direction parallel to barriers orientation, the velocity field can be written as $\mathbf{u}'(x, y, t) = u'(x, y, t)\hat{\mathbf{x}}$ (acoustic waves are independent of z as gravity effects are negligible). Substituting this velocity into the first component of the second equation of (4.2.3) then it follows that

$$-i\omega\rho_0 u' = -p'_x + \frac{L_p}{A} S', \tag{4.2.7}$$

where L_p and A are the cross-sectional perimeter and area of the narrow duct and S' can be found from (4.2.6) by replacing u'_∞ with u' (method also found in [27]). Note that that the pressure can be writen in terms of the velocity using the first and third equations of (4.2.3) in the frequency domain i.e. $-i\omega\rho' + \rho_0 u'_x = 0$ and $p' = c_0^2 \rho'$. Thus, after a considerable algebra, the velocity is found to satisfy the

modified Helmholtz equation $\left(\partial_{xx} + \hat{k}^2\right)u' = 0$ with

$$\hat{k}^2 = k^2\left(1 + \frac{L_p}{2A}(1+i)\delta_V\right), \tag{4.2.8}$$

using that $k = \omega/c_0$. One can see that the fraction $L_p\delta_V/2A = (1+a/h)\delta_V/a$ is small since $\delta_V \ll a$, where a is the barrier separation. Therefore, by taking the square root of (4.2.8) and expanding $\sqrt{1+x} \approx 1 + x/2$ for small x, then

$$\hat{k} = k\left(1 + \frac{L_p}{4A}(1+i)\delta_V\right). \tag{4.2.9}$$

This expression of the modified wavenumber should be used in (4.2.2), as the barriers are confined to be parallel in the Y direction.

4.3 Solution to the problem

The aim of the problem is to find the general solution of the potential in the regions $y < 0$ and $y > 0$ and then apply the matching conditions across $y = 0$. Note that because of the periodicity of the geometry (see figure 4.1), the problem need only be solved only in a single strip $x \in (0, L)$. The solution in $0 < x < L$ can be extended to $x < 0$ and $x > L$ using the periodicity conditions found in (4.1.2).

Therefore the effective equations in $(x, y) \in (0, L) \times \mathbb{R}_{<0}$ are (4.1.1), (4.1.2) with the periodic conditions now be applied on the x-endpoints of the strip, namely $\phi(L, y) = e^{i\alpha_0 L}\phi(0, y)$ and same for ϕ_x. The effective equations that needed to be solved within the single barrier configuration are the equations found in (4.2.2). At the end the two potentials must be matched using the two conditions found in (4.1.3) for $x \in (0, L)$.

The unit amplitude incident wave is chosen to be $\phi_{inc}(x, y) = e^{i\alpha_0 x}e^{i\beta_0 y}$ for $\alpha_0 = k\sin\theta_0$ and $\beta_0 = k\cos\theta_0$ so that it satisfies the Helmholtz equation (4.1.1) and the far-field condition specified in (4.1.2). Then, the response field (or reflected modes) can be found separately and added to the incident wave to get the total potential field. Thus, separating variables in $\left(\nabla^2 + k^2\right)\phi_{res}(x, y) = 0$ as $\phi_{res} \sim$

$e^{i\alpha x}Y(y)$ (with ϕ_{res} be the response field and α be the separation constant), then

$$Y''(y) = -\beta^2 Y(y) \quad \text{for} \quad \beta = \sqrt{k^2 - \alpha^2}. \tag{4.3.1}$$

Note that α, can be found by applying the periodic boundary conditions found in (4.1.2) into $e^{i\alpha x}Y(y)$. Both of these conditions result to $e^{i\alpha L} = e^{i\alpha_0 L}$, which gives $\alpha \equiv \alpha_n = \alpha_0 + 2n\pi/L$ for all $n \in \mathbb{Z}$. Therefore the solution for the response field becomes

$$\begin{aligned} \phi_{res}(x,y) &= \sum_{n=-\infty}^{\infty} e^{i\alpha_n x}\Big(a_n e^{-i\beta_n y} + b_n e^{i\beta_n y}\Big), \\ \alpha_n &= \alpha_0 + \frac{2n\pi}{L}, \quad \beta_n = \sqrt{k^2 - \alpha_n^2}. \end{aligned} \tag{4.3.2}$$

It remains to make sure that the far-field condition is satisfied and the scattering wave travels in the correct direction (negative y-direction). To do that, first note that depending on the integer value of n, β_n is either a positive real or a purely imaginary number with a positive imaginary part. Let $\mathcal{S}$ be the subset of the integers that makes $\beta_n \in \mathbb{R}_{>0}$ for all $n \in \mathcal{S}$. Consequently β_n will be purely imaginary for all $n \notin \mathcal{S}$. Therefore the $b_n e^{i\beta_n y}$ term of the sum in (4.3.2) represents either a wave that travels in the positive y-direction or a non-decaying wave at $y \to -\infty$. Since the scattering potential must be either a wave travelling in the negative y-direction or a decaying wave in the far-field, then $b_n = 0$ for $n \in \mathbb{Z}$. Therefore, the total potential is represented by

$$\phi(x,y) = e^{i\alpha_0 x}e^{i\beta_0 y} + \sum_{n=-\infty}^{\infty} a_n e^{i\alpha_n x}e^{-i\beta_n y}, \quad y < 0. \tag{4.3.3}$$

Note that the expressions of α_n and β_n that were defined in (4.3.2) were chosen such that when $n = 0$, they actually coincide with the incident wavenumbers in the x and y directions i.e. $\alpha_0 = k\sin\theta_0$ and $\beta_0 = k\sin\theta_0$. Also it would be useful to identify the elements of $\mathcal{S}$, as the number and direction of reflective modes could be determined by that. The $e^{i\alpha_n x}$ term of the sum is the change of phase over the "periodic" variable x and therefore the $e^{-i\beta_n y}$ term really indicates if the wave is travelling or decaying. It remains to find the elements of $\mathcal{S}$ which are all the $n \in \mathbb{Z}$ that make β_n real or equivalently $\alpha_n^2 < k^2$. After some algebraic inequality manipulation, it turns out that

$-kL(1+\sin\theta_0)/2\pi < n < kL(1-\sin\theta_0)/2\pi$ which suggests that the set of indices that correspond to travelling waves is defined to be

$$\mathcal{S} = \{-r, ..., s\} \quad \text{with} \quad r = \left\lfloor \frac{kL}{2\pi}(1+\sin\theta_0) \right\rfloor, \quad s = \left\lfloor \frac{kL}{2\pi}(1-\sin\theta_0) \right\rfloor, \tag{4.3.4}$$

where $\lfloor\cdot\rfloor$ indicate the floor function that gives the largest integer which is smallest than its argument. From now on $\mathcal{S}$ will be referred to the scattering set. It can be seen that $r,\ s \in \mathbb{N}_0$ for all possible geometries (thus $0 \in \mathcal{S}$ always) and when $\theta_0 > 0°$, then $r \geq s$ and vice versa. The equality $r = s$ is guaranteed for normal incidence ($\theta_0 = 0°$). Also the direction of the reflected modes can be found through the relation $k\sin\theta_n = \alpha_n$ for all $n \in \mathcal{S}$ with α_n defined in (4.3.2). The reflected angle $\theta_n \in (-90°, 90°)$ is formed by the negative y-axis and the reflected wave where the positive direction is measured counterclockwise from the negative y-axis.

Proceeding to the solution inside the triangular homogenised medium, the wave must satisfy the differential equation found in (4.2.2) whose general solution is

$$\hat{\phi}(X,Y) = \hat{A}_1(X)e^{i\hat{k}Y} + \hat{A}_2(X)e^{-i\hat{k}Y}, \tag{4.3.5}$$

with $\hat{k} \in \mathbb{C}$ found in (4.2.9) in the case of acoustic waves and $\hat{k} = k + ik_i$ in the case of water waves with k_i defined in (**??**). Applying the no flux condition at the end of the narrow channels at $Y = L\sin\delta$, then one of the unknown coefficient X-functions can be eliminated, for example $\hat{A}_2(X) = \hat{A}_1(X)e^{2i\hat{k}L\sin\delta}$. Substituting this back to (4.3.5), then after some algebraic manipulation it follows that

$$\hat{\phi}(X,Y) = \hat{A}(X)\cos[\hat{k}(L\sin\delta - Y)], \tag{4.3.6}$$

for $\hat{A}(X)$ be an unknown function to be found.

Now the matching conditions in (4.1.3) should be applied into (4.3.3) and

(4.3.6) to get a linear system for a_n and $\hat{a}_n$, namely

$$\begin{aligned} e^{i\alpha_0 x} + \sum_{m=-\infty}^{\infty} a_m e^{i\alpha_m x} &= \hat{a}(x)\cos[\hat{k}(L-x)\sin\delta], \\ i\beta_0 e^{i\alpha_0 x} - i\sum_{m=-\infty}^{\infty} a_m\beta_m e^{i\alpha_m x} &= \hat{a}(x)(1-\theta)\hat{k}\cos\delta\sin[\hat{k}(L-x)\sin\delta], \end{aligned} \tag{4.3.7}$$

where $\hat{a}(x) = \hat{A}(x\cos\delta)$.

Since, the potential in $y < 0$ is written as a sum over some unknown Fourier coefficients then it would be ideal if the right-hand sides of the previous equations were written in a similar form, so that the matching procedure would be simpler. To do that, first it can verified that $e^{i\alpha_n x}$ spans the space of complex differentiable functions in $(0, L)$, since they are eigenfunctions of a Sturm–Liouville problem. They also satisfy the orthogonality relation

$$\int_0^L e^{i\alpha_n x}\overline{e^{i\alpha_m x}}dx = \int_0^L e^{2i(n-m)\pi x/L}dx = L\delta_{nm}. \tag{4.3.8}$$

Therefore any complex function can be written as a sum over that basis. In our case, after expanding $\hat{a}(x)$, the matching conditions above become

$$\begin{aligned} e^{i\alpha_0 x} + \sum_{m=-\infty}^{\infty} a_m e^{i\alpha_m x} &= \cos[\hat{k}(L-x)\sin\delta]\sum_{m=-\infty}^{\infty}\hat{a}_m e^{i\alpha_m x}, \\ i\beta_0 e^{i\alpha_0 x} - i\sum_{m=-\infty}^{\infty} a_m\beta_m e^{i\alpha_m x} &= (1-\theta)\hat{k}\cos\delta\sin[\hat{k}(L-x)\sin\delta]\sum_{m=-\infty}^{\infty}\hat{a}_m e^{i\alpha_m x}. \end{aligned} \tag{4.3.9}$$

Next, the orthogonality relation in (4.3.8) must be used, so that the sums of the left-hand sides are removed to get a system for a_n and $\hat{a}_n$. Thus, by multiplying the

equations by $e^{-i\alpha_n x}$ and integrate in $x \in (0, L)$, the system in vectorial form becomes

$$\mathbf{J} + \mathbf{a} = \mathbf{A}\hat{\mathbf{a}},\ -\mathbf{J} + \mathbf{a} = \mathbf{B}\hat{\mathbf{a}} \text{ for } J_n = \delta_{n0},\ A_{nm} = \frac{1}{2i}\Big[T_{nm}(\delta) + T_{nm}(-\delta)\Big],$$
$$B_{nm} = \frac{(1-\theta)\hat{k}\cos\delta}{2i\beta_n}\Big[T_{nm}(\delta) - T_{nm}(-\delta)\Big] \text{ with } T_{nm}(\delta) = \frac{1 - e^{i\hat{k}L\sin\delta}}{2(m-n)\pi - \hat{k}L\sin\delta}, \tag{4.3.10}$$

where $T_{nm}(\pm\delta)$ comes from the integrals in $(0, L)$ over the product of the eigenfunctions and certain trigonometric functions. Also, one can see from the second vectorial equation above, that in the limit $\theta \to 1$ it follows that $B_{nm} = 0$ and thus the scattering coefficients are found analytically as $a_n = \delta_{n0}$. This is expected on physical grounds as in the presence of a rigid wall at $y = 0$, there should be a single reflected mode in the θ_0 direction (measured counterclockwise from the negative y-axis to the direction of the reflected wave) according to the law of reflection. Elimination between the unknown coefficients of (4.3.10), results to

$$\hat{\mathbf{a}} = 2(\mathbf{A} - \mathbf{B})^{-1}\mathbf{J},\ \ \mathbf{a} = \Big(2\mathbf{A}(\mathbf{A} - \mathbf{B})^{-1} - \mathbf{I}\Big)\mathbf{J}, \tag{4.3.11}$$

where $\mathbf{I}$ is the identity matrix.

Now an analytical solution to this problem, will be introduced. First the length of the longest channel of the triangular barrier configuration is set to be a half wavelength (that is $L\sin\delta = \lambda/2$ or $kL\sin\delta = \pi$), and the direction of incidence is aligned with the barriers ($\theta_0 = \delta \in (0°, 90°)$). The features of this geometry result to $\alpha_{-1} = -\alpha_0$ and $\beta_{-1} = \beta_0$ after a simple algebraic manipulation. Then, by assuming that the barriers are thin ($\theta = 0$) and no thermoviscous effects inside the metamaterial wall occur ($\hat{k} = k$), then $a_n = \delta_{n,-1}$ is a closed-form solution to the problem. To prove this, then the wave field (4.3.3) in $y < 0$ and (4.3.6) inside the metamaterial, must be simplified under these geometrical assumptions. Thus,

$$\phi(x, y) = 2\cos(\alpha_0 x + \beta_0 y) \ \text{ and } \ \hat{\phi}(X, Y) = -\hat{A}(X)\cos(kY), \tag{4.3.12}$$

after using the guessed solution of a_n in $y < 0$ combined with the values α_{-1}, β_{-1} in terms of the incident wavenumbers in x and y directions. In the triangular region, the

inviscid assumption was used with the fact that $\cos(\pi - kY) = -\cos(kY)$. Note that the unknown coefficients within the metamaterial are written compactly in terms of the function $\hat{A}(X)$ instead of the infinite sum.

Applying the matching conditions (4.1.3) into the simplified potentials above, then the system of equations become

$$\begin{aligned} 2\cos(\alpha_0 x) &= -\hat{a}(x)\cos(kx\sin\delta), \\ -2\beta_0\sin(\alpha_0 x) &= \hat{a}(x)k\cos\delta\sin(kx\sin\delta), \end{aligned} \tag{4.3.13}$$

where after the cancellations of the x-dependent trigonometric functions, both equations independently result to $\hat{a}(x) = -2$. Therefore, $a_n = \delta_{n,-1}$ must be a solution.

Now it will be shown that the single non-zero amplitude $a_{-1} = 1$, correspond to a scattering mode that travels in the direction opposite to the incident wave. First to show that this particular mode corresponds to a travelling wave, then it must be verified that $r \geq 1$ so that $-1 \in \mathcal{S}$ (the scattering set). Let us assume the contrary, namely $r = 0$ as it is known that $r \in \mathbb{N}_0$. Then by using the geometrical feature $kL\sin\delta = \pi$, it follows that

$$0 = r = \left\lfloor \frac{kL}{2\pi} + \frac{1}{2} \right\rfloor, \tag{4.3.14}$$

which implies that the term inside the floor function must be in $(0, 1)$ (zero is excluded as $kL > 0$). Therefore by starting from

$$0 < \frac{kL}{2\pi} + \frac{1}{2} < 1, \tag{4.3.15}$$

subtracting a half from each side, multiply by $2\sin\delta$ and making use of $kL\sin\delta = \pi$, then the result is $1 < \sin\delta$ which is of course a contradiction. Therefore r must be greater or equal to 1 and so a_{-1} corresponds to the amplitude of a travelling wave. Its direction θ_{-1} can be calculated from the equation $k\sin\theta_{-1} = \alpha_{-1}$. By substituting $\alpha_{-1} = -\alpha_0$ which was found above, then the equation becomes $\sin\theta_{-1} = \sin(-\theta_0)$ whose solution is $\theta_{-1} = -\theta_0$ as $\theta_{-1} \in (-90°, 90°)$. This implies that there is a single scattering mode (with non-zero amplitude) that travels directly opposite to the incident wave.

4.4 Expression for the normalised output energy

In this section, an expression for the normalised output energy will be calculated. First, the strip $x \in (0, L)$ and $y < 0$ is defined to be V^- and the triangular configuration above to be V^+. The integral counterclockwise contour that characterise the boundary of V^- is comprised by four line segments, namely C_i for $i \in \{1, 2, 3, 4\}$, starting from the right vertical (C_1), then upper horizontal (C_2), then left vertical (C_3) and finally lower horizontal (C_4).

Beginning by defining the time-averaged energy flux through a boundary S [26], we have that

$$-\frac{\omega\rho}{2}\Im\int_S \phi\overline{\phi}_n dS, \tag{4.4.1}$$

where $\phi_n = \hat{\mathbf{n}} \cdot \nabla\phi$ with $\hat{\mathbf{n}}$ be the unit normal pointing out of the boundary S. If this quantity is divided by $\omega\rho\beta_0 L/2$, we get the normalised absorption coefficient

$$\eta \equiv -\frac{1}{\beta_0 L}\Im\int_{C_2} \phi\overline{\phi}_n dS, \tag{4.4.2}$$

where C_2 is the metamaterial boundary. Now it remains to calculate the surface integral. First a useful formula is proved by using the divergence theorem, namely

$$\Im\int_{\partial V^-} \phi\overline{\phi}_n dS = \Im\int_{V^-} \Big(\phi\nabla^2\overline{\phi} + |\nabla\phi|^2\Big) dV = \Im\int_{V^-} \Big(|\nabla\phi|^2 - k^2|\phi|\Big) dV = 0, \tag{4.4.3}$$

since $\nabla^2\phi = -k^2\phi$ in V^-. Therefore, the equation above suggests that the sum of the imaginary part of the four contributions C_i vanishes. However the sum of the vertical contributions results in

$$\left(\int_{C_1} + \int_{C_3}\right)\phi\overline{\phi}_n dS = \int_{-\infty}^{0} \phi(L, y)\overline{\phi}_x(L, y)dy + \int_{0}^{-\infty} \phi(0, y)\overline{\phi}_x(0, y)dy = 0, \tag{4.4.4}$$

where here the periodic conditions (4.1.2) coming from Bloch-Floquet theory are

used. Therefore, the surface integral over C_2 (in (4.4.2)) is minus the surface integral over C_4. Thus it remains to calculate the C_4 contribution as

$$\Im \int_{C_4} \phi \overline{\phi}_n dS = \lim_{y \to -\infty} \Im \int_0^L \phi(x,y) \overline{\phi}_y(x,y) dx. \tag{4.4.5}$$

Next, the product of ϕ and $\overline{\phi}_y$ in the far-field will give

$$\begin{gathered} \phi(x,y)\overline{\phi}_y(x,y) \sim -i\beta_0 + ie^{i\alpha_0 x}e^{i\beta_0 y}{\sum_n}' \beta_n \overline{a}_n e^{-i\alpha_n x}e^{i\beta_n y} \\ -i\beta_0 e^{-i\alpha_0 x}e^{-i\beta_0 y}{\sum_n}' a_n e^{i\alpha_n x}e^{-i\beta_n y} + i{\sum_{n,m}}' \beta_m a_n \overline{a}_m e^{i\alpha_n x}e^{-i\alpha_m x}e^{-i\beta_n y}e^{i\beta_m y}, \end{gathered} \tag{4.4.6}$$

as $y \to -\infty$. The dashed sums run over $\mathcal{S}$ only as for integers not in $\mathcal{S}$, $e^{-i\beta_n y}$ represent a decaying wave. The scattering set $\mathcal{S}$ is defined in (4.3.4). Next, by integrating the previous result in $x \in (0, L)$ and making use of (4.3.8), then

$$\int_0^L \phi(x,y)\overline{\phi}_y(x,y)dx \sim -i\beta_0 L + iL{\sum_n}' \beta_n |a_n|^2 + 2\beta_0 L \Im\{a_0 e^{-2i\beta_0 y}\}, \tag{4.4.7}$$

which when it is substituted into (4.4.5), it results in the normalised absorption coefficient

$$\eta = 1 - \sum_{n=-r}^{s} \frac{\beta_n}{\beta_0} |a_n|^2. \tag{4.4.8}$$

Since when $\eta = 0$ energy is conserved (no absorption) and when $\eta = 1$ we have total absorption, then the sum in (4.4.8) represents the normalised output energy (that is the ratio between the energy though the metamaterial opening and incident wave energy). We call this

$$\mathcal{E} \equiv 1 - \eta = \sum_{n=-r}^{s} \frac{\beta_n}{\beta_0} |a_n|^2. \tag{4.4.9}$$

This formula will be used in the numerical results to show how the energy losses vary over a number of geometrical parameters and what influence do they have on the scattering coefficients. The energy will be conserved when $\mathcal{E} = 1$ and for $\mathcal{E} = 0$ the incident wave will be totally absorbed by the metamaterial wall.

This formula can easily be used to verify the energy conservation of the problem with the special geometrical configuration that is described by the wave field in (4.3.12). Using the fact that in this case $r \geq 1$ (proven by contradiction in the previous section), $a_n = \delta_{n,-1}$ and $\beta_{-1} = \beta_0$, then according to the formula above, the output energy can be found to be $\mathcal{E} = 1$, which is expected on physical grounds as damping was assumed to be zero in that case.

4.5 Numerical results

In this section, computational results of the problem above will be illustrated through truncation of the system solution (4.3.11). The truncation parameter is defined to be N and the truncated vectors include $2N + 1$ components i.e., from $-N$ to N. The scattering coefficients can be found from the components of the vector $\mathbf{a}$ while the normalised output energy across the metamaterial wall boundary ($y = 0$) is $\mathcal{E}$ from(4.4.9).

From now on the "amount" of damping will be included in the parameter k_i from $\hat{k} = k + ik_i$. One may question that this is not the complex wavenumber form specified in (4.2.9) for the acoustic problem. However, using that the viscous boundary layer length δ_V is small when compared to the width of the channels then one could calculate that $L_p\delta_V/2A \approx \delta_V/a \ll 1$ (where L_p, A and a is the perimeter, area and width of the channel respectively) in the large wall height limit (when compared to the other field variables). Thus, using the small viscous boundary layer limit, one could see that the description $\hat{k} = k + ik_i$ for small $k_i \ll k$, fits the description of (4.2.9). At this point it will be seen why the classic linear model that describes the problem, needed to include a damping coefficient.

Starting from figure 4.2, note that $|a_0|$ was plotted for all kL as it is known that for all wavenumbers it represents the fundamental reflected wave i.e. $0 \in \mathcal{S}$ always. A common feature of such plots is that $|a_0| \to 1$ as $kL \to 0$. It is expected on physical grounds that $|a_0| \to 1$ in the limit $kL \to 0$ as when the incident wavelength becomes large with respect to the size of the arrays, the wave would not "feel" any obstacles. However $|a_{-1}|$, was plotted only for values greater than $kL \approx 3.68$, which is the value where the particular index of the mode become an element of $\mathcal{S}$ i.e. the

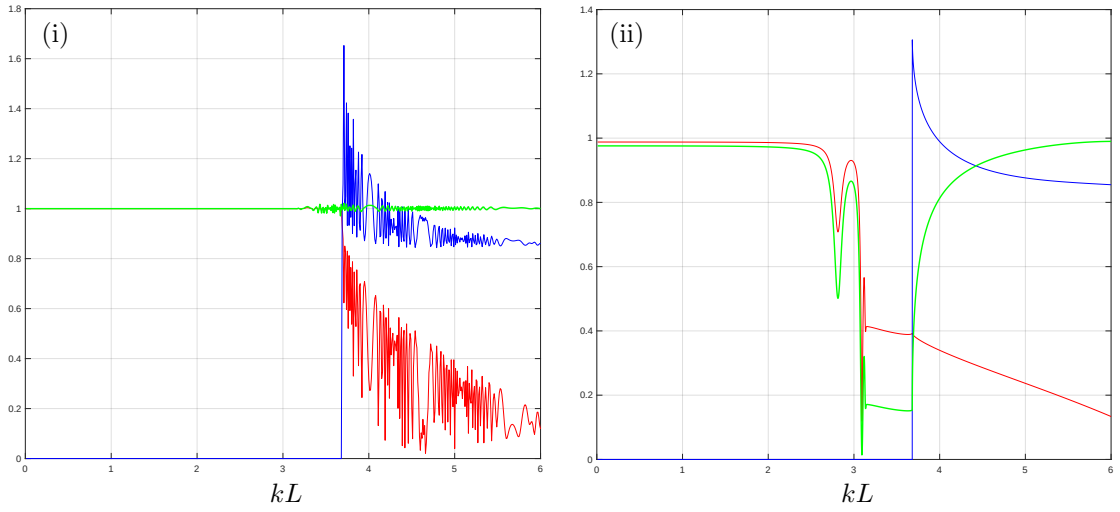

Figure 4.2: Modulus of the scattering coefficients $|a_0|$ (red), $|a_{-1}|$ (blue) and normalised output energy $\mathcal{E}$ (green) against the dimensionless wavenumber kL, for $(N, \theta_0, \delta, \theta) = (2^{10}, 45°, 30°, 0)$. In figure (i) $k_i L = 0$ and in figure (ii) $k_i L = 10^{-2}$.

value at which r is switched from 0 to 1. The next reflected wave would appear when s is switched from 0 to 1 (for $|a_1|$) and when r is switched from 1 to 2 (for $|a_{-2}|$). This happens for the values $kL \approx 21.45$ and $kL \approx 7.36$ respectively which are outside the plotting region.

In figure 4.2(i), the curves converge up to a particular value of kL which corresponds to the longest microchannel in the array that becomes "resonant". Because there is a continuum of microchannel lengths for all values of kL above this point, then the existence of a resonant microchannel in the array is guaranteed. The solution fails to converge with increasing N for any of these values of kL. This lack of convergence is manifested by the numerically noisy lines in figure 4.2(i) and persist after the second reflected wave is cut on. This is because the mathematical model is based on homogenisation of the microstructure and this requires there to be a clear separation of scales. However, when there is resonance at one discrete location in the microstructure array then, by definition, is a local effect and not a macroscale behaviour. So the fundamental problem is that homogenisation fails when there is resonance. The introduction of damping, which is a reasonable addition, removed the local effect and ensures that the variation of the field variable is everywhere on a macroscale. This is verified in figure 4.2(ii) where the same parameters as in figure 4.2(i) were used but a small additional damping was introduced.

k_iL	10^0	10^{-1}	10^{-2}	10^{-3}	0
N	2^3	2^7	2^9	2^{12}	∞

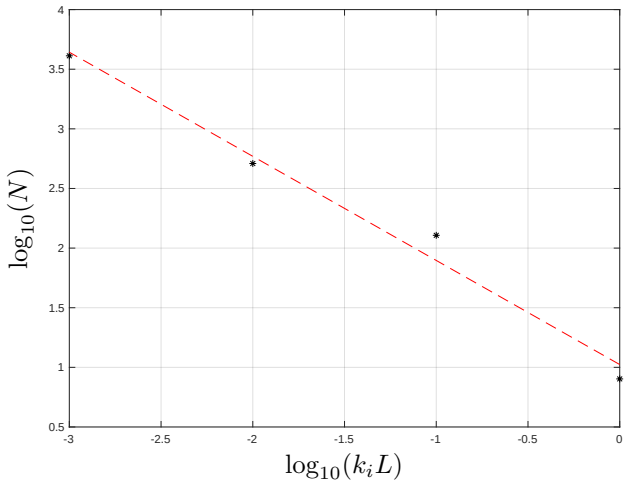

Table 4.1: The table indicates the truncation parameter N needed for convergent results for each k_iL. In the figure below, the line of best fit for the pairs $(\log_{10}(k_iL), \log_{10}(N))$ from the table, is plotted.

Also, it was noticed that as k_iL was chosen to be smaller, a larger value of N was needed to get convergence. Therefore, by plotting the reflection coefficients for a variety of geometries, the optimal N was found by graph inspection for each value of k_iL. Table 4.1 shows the number of modes needed to get convergence for each k_iL. When damping coefficient was zero there was no truncation that could give stable results (and that is the reason behind $N \to \infty$). This table suggests that there might be a power law between the two parameters, namely $N = (k_iL)^p$. The exponent p can be found by taking logarithms as $p = \log_{10}(N)/\log_{10}(k_iL)$. In the figure under the table 4.1, $\log_{10}(N)$ was plotted against $\log_{10}(k_iL)$ from the table's data and thus the gradient of the line of best fit gives an approximate value for the exponent p. This exponent was found to be $p = -0.873$ and its negative value verifies that $N = (k_iL)^p$ tends to infinity as k_iL approaches zero. Therefore, since this power law between N and k_iL was tested in many geometrical cases, then from now on N will be chosen according to the table above.

Next in figure 4.3, the normalised output energy is plotted against kL. Note that the value of N was chosen according to the damping parameter k_iL from the table 4.1. In the first figure, the plates are thin ($\theta = 0$) and in the second they are thick ($\theta = 0.5$). In both plots, there is a wide range of frequencies over which

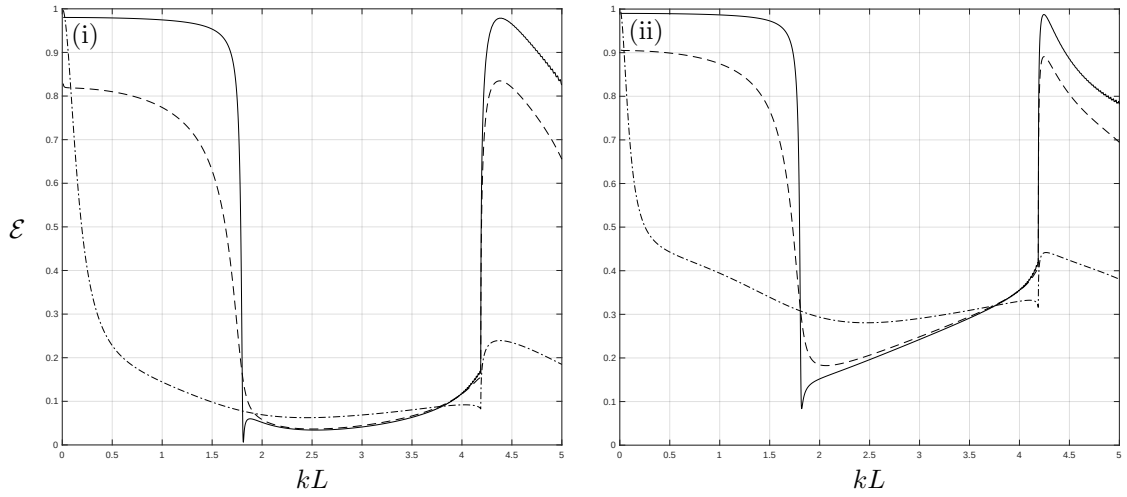

Figure 4.3: Normalised output energy $\mathcal{E}$ against kL for $(k_iL, N) = (10^{-2}, 2^9)$ (full line), $(k_iL, N) = (10^{-1}, 2^7)$ (dashed line), $(k_iL, N) = (10^0, 2^3)$ (chained line). The parameters are $(\theta_0, \delta) = (30°, 60°)$ and for figure (i) $\theta = 0$ and for figure (ii) $\theta = 0.5$.

a high proportion of the incident wave energy is absorbed by the wall, more so in the case of thin barriers. This frequency region ends at $kL = 4\pi/3 \approx 4.19$ or at the value for which r turns from 0 to 1 according to the geometrical parameters. When this happens, a new scattering mode is added and increases the normalised output energy, but just before that point the single mode seems to have a "weak" effect on energy. Before this value it can be verified that $r = s = 0$. Also, it can be seen that as θ increases, the normalised output energy increases as well since the metamaterial array tends to be a rigid wall at $y = 0$. The normalised output energy is generally dropped with the increase of the damping parameter, as expected on physical grounds.

Now the variation of the scattering coefficients with respect to the incident direction θ_0, can be seen in figure 4.4. Again N was chosen accordingly with the value of k_iL i.e. $(k_iL, N) = (10^{-2}, 2^9)$. Also, the modulus of the fundamental mode $|a_0|$ (red curve) seems to be even in θ_0. This was verified numerically for many test cases, but not analytically. Again, there is a wide region of direction of incidence for which a high percentage of the incident wave energy is absorbed by the wall i.e. roughly $\theta_0 \in (-60°, 34°)$. The approximate values $\pm 34°$ are where another modes (blue and magenta curves representing $|a_{-1}|$ and $|a_1|$ respectively) are switched on (when r and s turn from 0 to 1) and contribute to the increase of the normalised

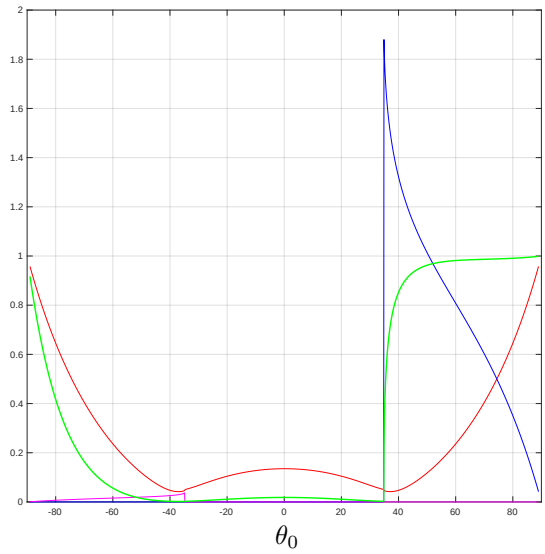

Figure 4.4: Modulus of the scattering coefficients $|a_0|$ (red), $|a_1|$ (magenta), $|a_{-1}|$ (blue) and normalised output energy $\mathcal{E}$ (green) against θ_0, for parameters $(N, kL, k_iL, \delta, \theta) = (512, 4, 10^{-2}, 45°, 0)$.

output energy. Near the endpoints of this interval, the $|a_0|$ mode is weak enough to say that for angles within $(-60°, 34°)$, the metamaterial acts as an absorption wall. Also, it can be verified that there are no other scattering modes apart from $|a_0|$, $|a_{-1}|$ and $|a_1|$ as from the simple algebra discussed above, $0 \leq r, s \leq \lfloor kL/\pi \rfloor = 1$.

Next, the free surface elevation of a water wave is plotted by considering the formula $\zeta(x, y, t) = -(\omega/g)\Im\{\phi(x, y)e^{-i\omega t}\}$ (neglecting the hyperbolic cosine term) in figure 4.5(i) and in figure 4.5(ii) its $y = 0$ cross-section (wave profile at the metamaterial boundary). Note that the surface is plotted only in the single strip $x \in (0, L)$, but all the other strips can be plotted through the periodic boundary conditions found in (4.1.2). The surface at $y = 0$ is continuous but with the gradient discontinuity. This is expected as the flux matching conditions are not the same as matching the gradient of ϕ and the local distortion in the gradient at the matching boundary is a local effect which is not resolved at the level of the modelling used here. Also, the colour variation in $y < 0$ seem to be small compared to the one in $y > 0$. This is because typically there are microchannels in which resonance occurs and the wave amplitude in there becomes extremely large when compared with the other field variables. From now on the surface of water waves will be plotted only in $y < 0$ (scattering region), as this is our only region of interest because a far-field

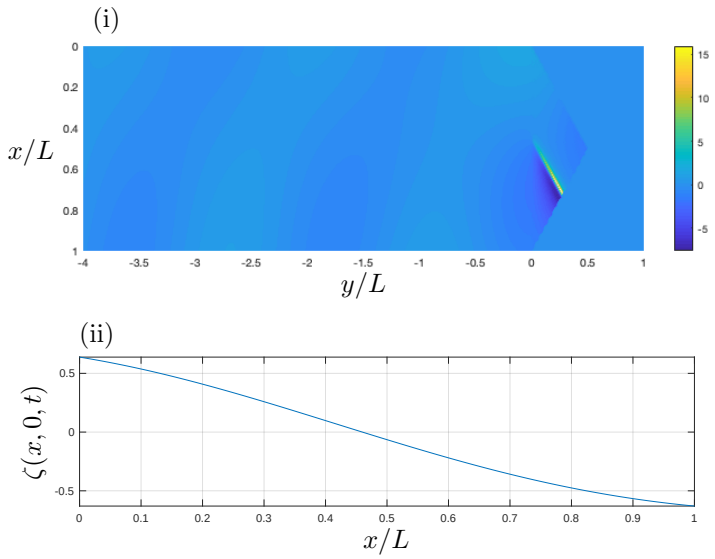

Figure 4.5: (i) Instantaneous surface elevation of a water wave for the set of geometrical parameters $(N, kL, k_iL, \theta_0, \delta, \theta) = (2^7, 4, 10^{-1}, 30°, 45°, 0.5)$ and (ii) its profile at the metamaterial boundary $y = 0$.

observer in $y < 0$, will only see what comes out from the microstructured wall.

Now the same surface is plotted for $(kL, \theta_0, \theta) = (2\pi/\sqrt{3}, 60°, 0)$ in figure 4.6. The amplitudes within the metamaterial ($y > 0$), were found to be huge at a level for which the colour variation in $y < 0$ was indistinguishable to the eye. Therefore, the surface is plotted only in $y < 0$ for the reasons explained above. The difference between figures 4.6(i) and 4.6(ii) is that in the first $(N, k_iL, \delta) = (2^9, 10^{-2}, 30°)$ and in the second $(N, k_iL, \delta) = (2^{12}, 10^{-3}, 60°)$. The truncation parameter N was chosen accordingly from the value of k_iL (see table 4.1 above).

In figure 4.6(i), it can be observed that there is a pattern of nodes and antinodes. This effect is expected as there are reflected modes travelling in different directions from the incident wave. However, in figure 4.6(ii) the barrier orientation is aligned with the incident direction i.e. $\delta = \theta_0 = 60°$. Also, it can be easily verified that $kL \sin\delta = \pi$ and since the barriers are thin ($\theta = 0$), then the figure represents the approximate effect of the special case solution found in (4.3.12). The analytical solution required $k_iL = 0$, but the numerical computations required a non-zero damping parameter to converge. Here the lack of convergence in the special case of $k_iL = 0$ is related to truncation of infinite systems of equations. Although we confirmed analytically that for an infinite system of equations there is an exact

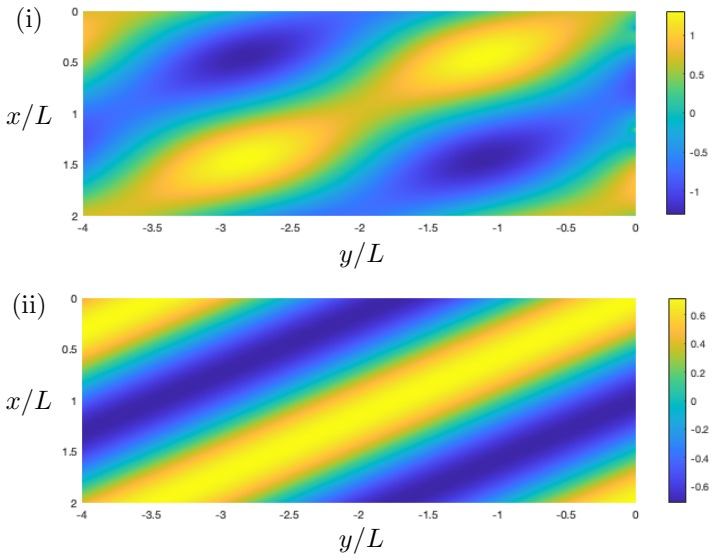

Figure 4.6: Instantaneous surface elevation for $(kL, \theta_0, \theta) = (2\pi/\sqrt{3}, 60^\circ, 0)$ with (i) $(N, k_iL, \delta) = (2^9, 10^{-2}, 30^\circ)$ and (ii) $(N, k_iL, \delta) = (2^{12}, 10^{-3}, 60^\circ)$.

solution (the one we anticipate), numerically once the infinite system of equations is truncated we cannot get the exact solution. This is a strange result because one normally expects truncation to be well behaved. However, it is never guaranteed that it gives a convergent result. Thus, we picked a significantly small value of the damping parameter ($k_iL = 10^{-3}$) at the cost of choosing a large truncation ($N = 2^{12}$). One could easily verify from the analysis of the problem found in the previous sections, that $r = 1$ and $s = 0$ according to the geometrical parameters. Therefore there are two reflected modes as $\mathcal{S} = \{-1, 0\}$. It can also be checked that $\theta_{-1} = -60^\circ = -\theta_0$ which implies that the $|a_{-1}|$ mode travels opposite the incident wave. But it is expected that $a_n = \delta_{n,-1}$ will not be a solution to the problem because $k_iL \neq 0$. However, in the limit $k_iL \to 0$, we get the expected result by choosing the appropriate truncation N. This is the reason why the node-antinode pattern is not observed in the second figure. Thus, for this particular geometrical configuration, the metamaterial wall violates the reflection law in the eyes of a far-field observer in $y < 0$.

Chapter 5

Wave scattering by cracks on floating ice sheets

5.1 Introduction

From this point onward, the second type of problems explored in this thesis will be considered. Two thin semi-infinite ice sheets float on the surface of an inviscid fluid of finite constant depth and they are separated by a crack of finite length and uniform width. An obliquely-incident wave in one of the two ice sheets, propagates from the far-field with a direction towards the crack. Therefore, the fluid within the crack region acts a scattering mechanism to the problem.

Cartesian coordinates (x, y, z) are chosen such that $z = 0$ coincides with the midplane of the two semi-infinite floating ice sheets of small thickness d (with repsect to the incident wavelength and fluid depth). The fluid is bounded below by a rigid, flat bed at $z = -h$ and the ice sheet separation distance is $2a$. Therefore, the ice sheets cover the region $|x| > a$, $-\infty < y < \infty$. Using the Archimedes Principle, it can be verified that in the presence of the static ice sheets the fluid surface is displaced at $z = \delta - d/2$, where $\delta = (\rho_i/\rho_w)d$ (where $\rho_i/\rho_w \approx 0.9$ is the ice to water density ratio). Also, E and ν are defined to be the Young's modulus and the Poisson ratio of the ice sheets (material parameters). An obliquely-incident flexural wave

propagates from $x \to \infty$ towards the crack region $|x| < a$, at an angle θ_0 with the negative x-axis and an angular frequency ω. The value of the depth h will vary between 20m and 160m (so not shallow water but not necessarily infinite depth) and the thickness d about 0.5-2m. The crack width $2a$ can take any positive value and this is the main parameter we want to explore.

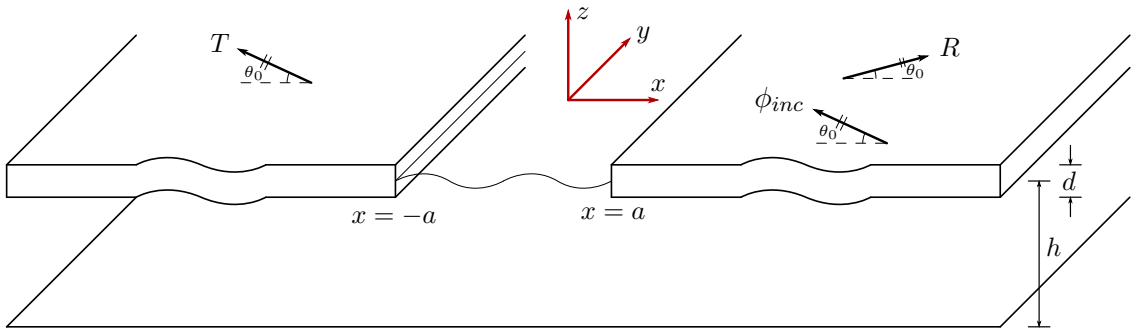

Figure 5.1: Two thin semi-infinite floating ice sheets of thickness d, separated by a distance $2a$ in a fluid of depth h. The incident wave ϕ_{inc} of angular frequency ω and direction θ_0 is scattered by the crack creating reflection and transmission (R, T).

Taking advantage of the constant depth (geometry is uniform in y) and the time harmonicity of the incident wave, then the fluid's velocity potential can be written in the form

$$\Phi(x, y, z, t) = \Re\{\phi(x, z)e^{i\alpha_0 y}e^{-i\omega t}\}, \tag{5.1.1}$$

where $\alpha_0 = k_0 \sin\theta_0$, with k_0 be the incident wavenumber and ω is the incident angular frequency. Therefore the fluid's continuity equation (2.2.1) and the no flow condition through the bed (2.2.2) are

$$\left(\nabla^2 - \alpha_0^2\right)\phi(x, z) = 0, \quad -\infty < x < \infty, \ -h < z < 0, \tag{5.1.2}$$

$$\phi_z(x, -h) = 0, \quad -\infty < x < \infty. \tag{5.1.3}$$

The combined kinematic and dynamical fluid's surface conditions over the gap and

the ice-covered sea [38] are

$$\phi_z(x,0) = K\phi(x,0), \quad |x| < a, \tag{5.1.4}$$

$$\mathcal{L}\phi \equiv \left\{ \Big[\beta\big(\partial_{xx} - \alpha_0^2\big)^2 + 1 - K\delta\Big]\partial_z - K \right\}\phi(x,0) = 0, \quad |x| > a, \tag{5.1.5}$$

where $K = \omega^2/g$ with g be the gravitational acceleration and the ice sheet parameter β is now defined by $\beta = Ed^3/12\rho_w g(1-\nu^2)$.

Since the incident wave of the problem comes from $|x| \gg a$, then by separating variables in the velocity potential below the ice sheets (in equation (5.1.2)), then it follows that

$$\phi(x,z) \sim e^{\pm i\beta_n x}\cosh[k_n(z+h)], \quad \beta_n^2 + \alpha_0^2 = k_n^2, \tag{5.1.6}$$

where $-k_n^2$ is the separation constant and using the no flow condition (5.1.3) at the bed. Then, by substituting this ϕ expression into the surface condition between the fluid and the floating ice sheet, then the following dispersion relation for the wavenumbers k_n rises. Namely,

$$\Delta(k_n) \equiv \big(\beta k_n^4 + 1 - K\delta\big)k_n\tanh(k_n h) - K = 0, \tag{5.1.7}$$

the roots of which represent the possible wavenumbers of flexural waves travelling in a thin floating ice sheet. This dispersion relation has two symmetric real roots ($\pm k_0$ for $k_0 > 0$), an infinite sequence of symmetric purely imaginary roots ($\pm k_n$ for $n \in \mathbb{N}$ with $\Im\{k_n\} > 0$) and four complex roots - one in each quadrant of the complex plane [71]. The four complex roots are related to each other from the two symmetries of the function $\Delta(z)$ defined above. Since the dispersion function satisfies $\Delta(-z) = \Delta(z)$ and $\Delta(\overline{z}) = \overline{\Delta(z)}$, then the four roots are called $\pm k_{-1}$ and $\pm k_{-2}$ where $\Re\{k_{-1}\}$, $\Im\{k_{-1}\} > 0$ and $k_{-2} = -\overline{k_{-1}}$. Also, the complex root of the first quadrant satisfies $\Im\{k_{-1}\} > \Re\{k_{-1}\}$ which gives important information when calculating it numerically [39]. A listing of MatLab codes to compute k_{-1} is included in [86]. It can be seen that when the ice thickness tends to zero ($d \to 0$), then the equation above becomes $k_n\tanh(k_n h) = K$ which is what was expected as this is the

standard water dispersion relation for a wave travelling in a fluid of constant depth in the absence of ice sheets.

Now at the straight edge of a semi-infinite plate (see figure 5.1) some boundary conditions must be imposed, namely at the free edges of an elastic plate must be free of bending and moments and vertical shear forces [38][87]. This translates to

$$\Big(\partial_{xx} - \nu\alpha_0^2\Big)\phi_z(\pm a^{\pm}, 0) = 0, \quad \Big(\partial_{xxx} - (2-\nu)\alpha_0^2\partial_x\Big)\phi_z(\pm a^{\pm}, 0) = 0. \tag{5.1.8}$$

The problem is supported with a far-field condition (usually called the radiation condition) which is

$$\phi(x,z) \sim \begin{cases} \phi_{inc}(x,z) + R\phi_{inc}(-x,z), & x \to \infty, \\ T\phi_{inc}(x,z), & x \to -\infty, \end{cases} \tag{5.1.9}$$

where $\phi_{inc}(x,z) = e^{-i\beta_0 x}\cosh[k_0(z+h)]$ for $\beta_0 = k_0\cos\theta_0$, is the incident wave that arrives from $x = \infty$ that satisfy (5.1.2), (5.1.3) and R and T are the complex-valued reflection and transmission coefficients of the scattering problem (see figure 5.1).

5.2 Scattering using inviscid theory

5.2.1 Ice crack of finite width

In this section, the problem formulated in section 5.1 will be solved using Fourier cosine and sine transforms to the scattering part of the wave, similar to the approach taken in [41]. One of the problems that he considered, was the trapped waves in an open water lead between two ice sheets in infinite depth. In the problem analysed in this section, the incident flexural wave interacts with the fluid in the crack. The assumption of finite depth can be used as an advantage to convert certain integrals into infinite sums over the ice sheet dispersion relation roots (which are easier to be evaluated numerically). This will be discussed in greater detail later in this section.

First, it can be seen that the geometry of the problem is symmetric about

the $x = 0$ plane. Therefore, similar to the first problems solved in Chapter 3, the problem can be decomposed into symmetric and antisymmetric parts which can be solved only in $x > 0$ as

$$(\nabla^2 - \alpha_0^2)\phi^{s,a}(x,z) = 0, \tag{5.2.1}$$

$$\phi_z^{s,a}(x,-h) = 0, \tag{5.2.2}$$

$$\big(\partial_z - K\big)\phi^{s,a}(x,0) = H(x-a)\bigg(K\delta - \beta\big(\partial_{xx} - \alpha_0^2\big)^2\bigg)\phi_z^{s,a}(x,0), \tag{5.2.3}$$

$$\phi_x^s(0,z) = 0, \quad \phi^a(0,z) = 0, \tag{5.2.4}$$

$$\begin{aligned} \mathcal{B}\phi_z^{s,a}(a^+,0) &\equiv \Big(\partial_{xx} - \nu\alpha_0^2\Big)\phi_z^{s,a}(a^+,0) = 0, \\ \mathcal{S}\phi_z^{s,a}(a^+,0) &\equiv \Big(\partial_{xxx} - (2-\nu)\alpha_0^2\partial_x\Big)\phi_z^{s,a}(a^+,0) = 0, \end{aligned} \tag{5.2.5}$$

where H is the Heaviside function that gives 1 for positive arguments and 0 for negative. The first three equations can easily be verified as their x derivatives are of even order (zeroth, second and fourth). The third equation is the continuous surface condition to guarantee that the potential satisfies the free surface condition in the fluid region $x \in (0,a)$ and the surface condition between the fluid and the elastic sheet in $x \in (a,\infty)$ (see equation (5.1.5)). The fourth equation is the conditions that needed to be satisfied in order for ϕ^s, ϕ^a being even and odd respectively. The conditions for the free edge at $x = a^+$ are specified in the fifth equation. The differential operators $\mathcal{B}$ and $\mathcal{S}$ stand for the bending moment and the shear stress respectively. Also, separate far field conditions at $x \to \infty$ for the symmetric and antisymmetric problems must be introduced. It can be seen that if

$$\phi^{s,a}(x,z) \sim \frac{1}{2}\Big(e^{-i\beta_0 x} + R^{s,a}e^{i\beta_0 x}\Big)\cosh\big[k_0(z+h)\big] \quad \text{as} \quad x \to \infty, \tag{5.2.6}$$

is chosen then the far field condition (5.1.9) is satisfied provided that

$$R = \frac{R^s + R^a}{2}, \quad T = \frac{R^s - R^a}{2}. \tag{5.2.7}$$

Since the solution method involves the Fourier cosine and sine transform

for the scattering part the algebra can be simplified by choosing the incident waves in a way to satisfy the conditions at $x = 0$, namely

$$\begin{aligned} \phi^s_{inc}(x,z) &= \cos(\beta_0 x)\cosh\big[k_0(z+h)\big], \\ \phi^a_{inc}(x,z) &= -i\sin(\beta_0 x)\cosh\big[k_0(z+h)\big]. \end{aligned} \tag{5.2.8}$$

It can be easily verified that those incident waves satisfy equations (5.2.1), (5.2.2), (5.2.4) and (5.2.3) in $x > a$ from the dispersion relation (5.1.7).

The symmetric solution starts by introducing the Fourier cosine transform for the scattering part of the velocity potential as

$$\tilde{\phi}^s(\xi,z) \equiv \int_0^\infty \Big[\phi^s(x,z) - \phi^s_{inc}(x,z)\Big]\cos(\xi x)dx. \tag{5.2.9}$$

The reason why the incident wave is removed from the transform, is to make sure that the integrand is outgoing as $x \to \infty$ and this is important for imposing the radiation condition as it determines the path of the integration contour in the inverse transform. Under the (5.2.9) transformation, equations (5.2.1), (5.2.2) and (5.2.3) become

$$\Big(\partial_{zz} - k^2(\xi)\Big)\tilde{\phi}^s(\xi,z) = 0, \tag{5.2.10}$$

$$\tilde{\phi}^s_z(\xi,-h) = 0, \tag{5.2.11}$$

$$\big(\partial_z - K\big)\int_0^\infty \phi^s(x,0)\cos(\xi x)dx = \int_a^\infty \left\{\left(K\delta - \beta\big(\partial_{xx} - \alpha_0^2\big)^2\right)\phi^s_z(x,0)\right\}\cos(\xi x)dx, \tag{5.2.12}$$

in $0 < \xi < \infty$, where $k^2(\xi) = \xi^2 + \alpha_0^2$. Successively integrating by parts the right-hand

side of (5.2.12) and using the edge conditions (5.2.5), then

$$\begin{aligned}\Big(\beta k^4+1-K\delta\Big)\int_0^\infty \phi_z^s(x,0)\cos(\xi x)dx - K\int_0^\infty \phi^s(x,0)\cos(\xi x)dx\\ =(\beta k^4-K\delta)\int_0^a \phi_z^s(x,0)\cos(\xi x)dx - P^s f_1^s(\xi)-Q^s f_2^s(\xi),\end{aligned}\tag{5.2.13}$$

after expressing the integral over (a,∞) as the difference between the integrals over $(0,\infty)$ and $(0,a)$. Also, in the equation above the following quantities are defined as $P^s=\phi_{xz}^s(a^+,0)$, $Q^s=\phi_z^s(a^+,0)$ and

$$f_1^s(\xi)\equiv\beta\big(\xi^2+\nu\alpha_0^2\big)\cos(a\xi),\quad f_2^s(\xi)\equiv\beta\big(\xi^3+(2-\nu)\alpha_0^2\xi\big)\sin(a\xi).\tag{5.2.14}$$

Now using the fact that $\phi_{inc}^s(x,z)$ satisfies (5.2.3) in $x>a$, multiplying it by $\cos(\xi x)$ and integrating in $x\in(0,\infty)$, then

$$\begin{aligned}0=\int_0^\infty\left\{\left(\beta\Big(\partial_{xx}-\alpha_0^2\Big)^2+1-K\delta\right)\frac{\partial\phi_{inc}^s}{\partial z}(x,0)-K\phi_{inc}^s(x,0)\right\}\cos(\xi x)dx\\ =\Big(\beta k^4+1-K\delta\Big)\int_0^\infty\frac{\partial\phi_{inc}^s}{\partial z}(x,0)\cos(\xi x)dx-K\int_0^\infty\phi_{inc}^s(x,0)\cos(\xi x)dx,\end{aligned}\tag{5.2.15}$$

where the second equality came by integration by parts. Using the vanishing right-hand side of (5.2.15) into (5.2.13), then

$$\begin{aligned}\big(\beta k^4+1-K\delta\big)\tilde\phi_z^s(\xi,0)-K\tilde\phi^s(\xi,0)\\ =(\beta k^4-K\delta)\int_0^a\phi_z^s(x,0)\cos(\xi x)dx-P^sf_1^s(\xi)-Q^sf_2^s(\xi),\end{aligned}\tag{5.2.16}$$

which is the surface condition for the symmetric potential in the Fourier space. Therefore the governing equation in the Fourier space (5.2.10), gives the general solution $\tilde{\phi}^s(\xi,z) = \tilde{A}^s(\xi)\cosh[k(z+h)]$ (using the no flow condition at the bed), where $\tilde{A}^s(\xi)$ can be found from (5.2.16). Therefore, by inverting the transform it follows that

$$\begin{aligned}\phi^s(x,z) = \phi^s_{inc}(x,z) + \frac{2}{\pi}\int\!\!\!\!\!\!\diagup_0^\infty \frac{\cosh[k(z+h)]}{\Delta(k)\cosh(kh)}\Big\{ - P^s f_1^s(\xi) - Q^s f_2^s(\xi) \\ +\big(\beta k^4 - K\delta\big)\int_0^a \phi^s_z(t,0)\cos(\xi t)dt\Big\}\cos(\xi x)d\xi,\end{aligned} \tag{5.2.17}$$

where the ξ-integral symbol, means that contour avoids the integrand pole β_0 from below in order that the radiation condition is satisfied.

This solution satisfies all conditions specified above. It remains to find the unknown parameters P^s and Q^s. A coupled 2×2 system between those unknown will arise if the xz and z partial derivatives of (5.2.17) (evaluated at the edge $x = a^+$, $z = 0$) are taken into account. First, the solution of the potential is differentiated with respect to z and evaluated at $z = 0$ to give

$$\begin{aligned}k_0\cos(\beta_0 x)\sinh(k_0 h) - P^s F_1^s(x) - Q^s F_2^s(x) \\ +\frac{2}{\pi}\int\!\!\!\!\!\!\diagup_0^\infty \frac{K - k\tanh(kh)}{\Delta(k)}\cos(\xi x)\int_0^a \phi^s_z(t,0)\cos(\xi t)dtd\xi = \begin{cases}\phi^s_z(x,0), & x > a,\\ 0, & 0 < x < a,\end{cases}\end{aligned} \tag{5.2.18}$$

after making use of the equation

$$\int_0^\infty \cos(\xi x)\cos(\xi t)d\xi = \frac{\pi}{2}\delta(x-t). \tag{5.2.19}$$

The equation above can be derived by calculating the Fourier cosine transform of

$\delta(x-t)$ as $\cos(\xi t)$ (assuming that $t>0$) and then inverting the transform. Also,

$$F_i^s(x) \equiv \frac{2}{\pi} \int\!\!\!\!\!\!\diagup_0^\infty \frac{k\tanh(kh)}{\Delta(k)} f_i^s(\xi)\cos(\xi x)d\xi \quad \text{for} \quad i=1,2, \tag{5.2.20}$$

was used in equation (5.2.18) which was derived after making use of the dispersion relation on the integral term that is proportional to $(\beta k^4 - K\delta)$.

Now, the linear system for P^s and Q^s can be created by substituting $x=a^+$ into the equation above and its x-derivative. Namely,

$$\begin{aligned}
P^s F_1^s(a^+) + Q^s\Big[1+F_2^s(a^+)\Big] - \mathcal{K}^s\phi_z^s &= k_0\cos(\beta_0 a)\sinh(k_0 h),\\
P^s\Big[1+F_1^{s'}(a^+)\Big] + Q^s F_2^{s'}(a^+) + \mathcal{K}^{s'}\phi_z^s &= -k_0\beta_0\sin(\beta_0 a)\sinh(k_0 h),\\
\mathcal{K}^s\phi_z^s &\equiv \frac{2}{\pi}\int\!\!\!\!\!\!\diagup_0^\infty \frac{K-k\tanh(kh)}{\Delta(k)}\cos(a\xi)\int_0^a \phi_z^s(t,0)\cos(\xi t)dtd\xi,\\
\mathcal{K}^{s'}\phi_z^s &\equiv \frac{2}{\pi}\int\!\!\!\!\!\!\diagup_0^\infty \frac{K-k\tanh(kh)}{\Delta(k)}\xi\sin(a\xi)\int_0^a \phi_z^s(t,0)\cos(\xi t)dtd\xi.
\end{aligned} \tag{5.2.21}$$

Therefore the system can be solved once the vertical velocity $\phi_z^s(x,0)$ in the region of the crack $0<x<a$ is found. Thus, the choice of

$$\phi_z^s(x,0) \equiv \frac{\pi}{2}\big[P^s R_1^s(x) + Q^s R_2^s(x) - k_0\sinh(k_0 h)R_3^s(x)\big], \quad 0<x<a, \tag{5.2.22}$$

is made, for some unknown functions $R_1^s(x)$, $R_2^s(x)$ and $R_3^s(x)$ that satisfy

$$\int\!\!\!\!\!\!\diagup_0^\infty \frac{K-k\tanh(kh)}{\Delta(k)}\cos(\xi x)\int_0^a R_i^s(t)\cos(\xi t)dtd\xi = \begin{cases} F_i^s(x), & i=1,2,\\ \cos(\beta_0 x), & i=3, \end{cases} \tag{5.2.23}$$

to guarantee that equation (5.2.18) is satisfied in $0 < x < a$. It remains to solve the three integral equations satisfied by $R_i^s(t)$ $(i = 1, 2, 3)$ in (5.2.23).

The vertical velocity of the fluid surface in the crack, can be approximated by the orthogonal family of Legendre polynomials. The reason behind this choice, is that Legendre polynomials have no particular weighting associated with the end points of the intervals. Also under this choice, certain integrals can be evaluated in closed form. This choice was also used in [36], where a floating rigid plate of finite width was interacting with the fluid surface surrounding it. Therefore is appropriate to expand

$$R_i^s(t) \approx \sum_{m=0}^{N} b_{2m}^{(i)} (-1)^m P_{2m}\left(\frac{t}{a}\right), \tag{5.2.24}$$

where P_{2m} are the even Legendre polynomials (to guarantee that the condition at $x = 0$ is satisfied) and $b_{2m}^{(i)}$ are the unknown expansion coefficients to be found. Here N is a truncation parameter typically proportional to the ratio a/d, because as the gap between the ice sheets increases (with respect to the ice thickness), then more polynomial terms are needed to characterise the fluid surface motion (more wavelengths will fit in the crack region). This is the Galerkin method discussed in (3.2.60). Substituting the expansion (5.2.24) into the integral equation of R_i^s, then

$$\begin{gathered}
\sum_{m=0}^{N} M_{2n,2m}^{s} b_{2m}^{(i)} = f_{2n}^{(i)} \quad \text{for} \quad M_{2n,2m}^{s} = a \int_0^\infty \frac{K - k\tanh(kh)}{\Delta(k)} j_{2n}(a\xi) j_{2m}(a\xi) d\xi, \\
f_{2n}^{(i)} = \frac{2}{\pi} \int_0^\infty \frac{k\tanh(kh)}{\Delta(k)} f_i^s(\xi) j_{2n}(a\xi) d\xi \text{ for } i = 1, 2 \text{ and } f_{2n}^{(3)} = j_{2n}(\beta_0 a),
\end{gathered} \tag{5.2.25}$$

where $j_{2m}(z)$ are the spherical Bessel function of even order, using the useful formula $(-1)^m \int_0^a P_{2m}(t/a)\cos(\xi t)dt = a j_{2m}(a\xi)$ found from [76], pg. 38(4). Note that the x-dependence was removed from (5.2.23), by multiplying it with $\frac{1}{a}(-1)^n P_{2n}(x/a)$ and integrating it in $x \in (0, a)$. That is essentially the application of the Galerkin method, where the solution error due to truncation is assumed to be orthogonal to the space of functions described by the expansion basis. Therefore, the equation (5.2.25) is basically a linear system of N equations for N unknowns i.e. the coefficients $b_{2m}^{(i)}$. Finally, using the expansion (5.2.24) into the 2×2 system for P^s, Q^s found in (5.2.21), after taking the expansion coefficients to be $\mathbf{b}_s^{(i)} = \mathbf{M}_s^{-1}\mathbf{f}_s^{(i)}$ (in vectorial

form), then

$$\begin{aligned}
&\begin{pmatrix} F_1^s(a^+) - \mathbf{K}_s^T\mathbf{M}_s^{-1}\mathbf{f}_s^{(1)} & 1 + F_2^s(a^+) - \mathbf{K}_s^T\mathbf{M}_s^{-1}\mathbf{f}_s^{(2)} \\ 1 + F_1^{s'}(a^+) + \mathbf{K'}_s^T\mathbf{M}_s^{-1}\mathbf{f}_s^{(1)} & F_2^{s'}(a^+) + \mathbf{K'}_s^T\mathbf{M}_s^{-1}\mathbf{f}_s^{(2)} \end{pmatrix} \begin{pmatrix} P^s \\ Q^s \end{pmatrix} \\
&\qquad = k_0 \sinh(k_0 h) \begin{pmatrix} \cos(\beta_0 a) - \mathbf{K}_s^T\mathbf{M}_s^{-1}\mathbf{f}_s^{(3)} \\ \mathbf{K'}_s^T\mathbf{M}_s^{-1}\mathbf{f}_s^{(3)} - \beta_0 \sin(\beta_0 a) \end{pmatrix}, \\
&\qquad K_{2n}^s \equiv a \int_0^\infty \frac{K - k\tanh(kh)}{\Delta(k)} \cos(a\xi) j_{2n}(a\xi) d\xi, \\
&\qquad K_{2n}^{s'} \equiv a \int_0^\infty \frac{K - k\tanh(kh)}{\Delta(k)} \xi \sin(a\xi) j_{2n}(a\xi) d\xi.
\end{aligned} \tag{5.2.26}$$

Now the formula for the reflection coefficient R^s must be derived by sending $x \to \infty$ in (5.2.17) using the far-field condition (5.2.6) and the incident wave definition (5.2.8). By writing the vertical fluid velocity in the crack as a linear combination of $R_i^s(t)$ from (5.2.22) and using the (5.2.24) expansion, then

$$\begin{aligned}
&\frac{1}{2}(R^s - 1) e^{i\beta_0 x} \cosh[k_0(z+h)] \\
&= -\frac{2}{\pi} \int_0^\infty \frac{\cosh[k(z+h)]}{\Delta(k)\cosh(kh)} \left[P^s f_1^s(\xi) + Q^s f_2^s(\xi)\right] \cos(\xi x) d\xi \\
&+ a \sum_{m=0}^N \left(P^s b_{2m}^{(1)} + Q^s b_{2m}^{(2)}\right) \int_0^\infty \frac{\cosh[k(z+h)]}{\Delta(k)\cosh(kh)} (\beta k^4 - K\delta) j_{2m}(a\xi) \cos(\xi x) d\xi \\
&- a k_0 \sinh(k_0 h) \sum_{m=0}^N b_{2m}^{(3)} \int_0^\infty \frac{\cosh[k(z+h)]}{\Delta(k)\cosh(kh)} (\beta k^4 - K\delta) j_{2m}(a\xi) \cos(\xi x) d\xi.
\end{aligned} \tag{5.2.27}$$

Now using the advantage of finite depth, a method that transforms the semi-infinite integrals into sums over the residues of the integrand poles, will follow. It can be seen that the poles of the integrands are $\pm\beta_n$ for $n \geq -2$. Note that the roots $\pm\beta_n$ are scattered to the complex plane in the same fashion as $\pm k_n$ due to the

relation between them, i.e. $k_n^2 = \beta_n^2 + \alpha_0^2$. Therefore, $\beta_0 \in \mathbb{R}_{>0}$, β_n for $n \in \mathbb{N}$ are purely imaginary with $\Im\{\beta_n\} > 0$ and β_{-1} lie in the first quadrant with $\beta_{-2} = -\overline{\beta_{-1}}$ in the second. In the case of infinite depth, the purely imaginary roots get infinitely close to each other as the purely imaginary roots tend to $\pm in\pi/h$ as $n \to \pm\infty$ [39]. Therefore, this method is applicable only in finite depth as is the only case where the sum over the dispersion roots makes sense because the roots are discrete (at a finite distance from each other) and not as in continuous line (branch cut). This method will be used also in Appendix C.1, to transform all the integrals used to find P^s, Q^s in (5.2.25), (5.2.26), into sums over the dispersion roots.

The method starts by using the fact that the integrands are always even. Therefore, they can be expressed as half of the infinite integrals, avoiding the negative real pole $-\beta_0$ from above and the positive real pole β_0 from below (as before) to satisfy the radiation condition. The second step will be to express a part of the integrands, in terms of decaying functions in the upper and lower half complex planes (typically trigonometric functions in terms of complex exponentials and in some cases spherical Bessel functions in terms of spherical Hankel functions). The third step will be to write the integral as an integral over the closed semicircular loop that covers the upper or lower complex plane (this will give the sum over the residues from the Cauchy's residue theorem), minus the contribution at infinity which it will turn out to be zero always. For example, by considering an arbitrary even function $f(\xi)$, with $f(\xi)e^{ia\xi}$ decaying on the boundary of a semicircular contour of radius $R \gg 1$ that covers the upper half complex plane, then

$$\int\!\!\!\!\!\!\diagup_0^\infty \frac{f(\xi)}{\Delta(k)}\cos(a\xi)d\xi = \frac{1}{4}\int\!\!\!\!\!\!\diagup_{-\infty}^{\infty} \frac{f(\xi)}{\Delta(k)}e^{ia\xi}d\xi + \frac{1}{4}\int\!\!\!\!\!\!\diagup_{-\infty}^{\infty} \frac{f(\xi)}{\Delta(k)}e^{-ia\xi}d\xi = i\pi\sum_{r=-2}^{\infty}\frac{k_r f(\beta_r)}{\beta_r\Delta'(k_r)}e^{i\beta_r a}, \tag{5.2.28}$$

where the dashed integral symbol means the β_0 pole is avoided from below and the $-\beta_0$ from above. In the equation above, the first infinite integral was decomposed into the upper half plane (considering β_n poles), the second to the lower (considering $-\beta_n$ poles) and the even behaviour of the integrand was implemented to combine the two infinite sums. Also, the chain rule $\frac{d}{d\xi}\big[\Delta(k)\big] = \frac{\xi}{k}\Delta'(k)$ was used. Applying this trick to the expression of (5.2.27), some infinite sums over the dispersion roots will emerge (summed over $r \geq -2$). Since all the summation terms are proportional to $e^{i\beta_r x}$ and $x \gg a$, then all the $r \neq 0$ terms will be vanished since $\Im\{\beta_r\} > 0$ and $x \to \infty$. So by retaining only the $r = 0$ term of the infinite sum and using

$\mathbf{b}_s^{(i)} = \mathbf{M}_s^{-1}\mathbf{f}_s^{(i)}$ (in vectorial form), then

$$R^s = 1 + \frac{2ik_0}{\beta_0\Delta'(k_0)\cosh(k_0h)}\Bigg\{P^s\Big[\pi a(\beta k_0^4 - K\delta)\mathbf{j}_s^T\mathbf{M}_s^{-1}\mathbf{f}_s^{(1)} - 2f_1^s(\beta_0)\Big]$$

$$+Q^s\Big[\pi a(\beta k_0^4 - K\delta)\mathbf{j}_s^T\mathbf{M}_s^{-1}\mathbf{f}_s^{(2)} - 2f_2^s(\beta_0)\Big] - \pi a(\beta k_0^4 - K\delta)k_0\sinh(k_0h)\mathbf{j}_s^T\mathbf{M}_s^{-1}\mathbf{f}_s^{(3)}\Bigg\}, \tag{5.2.29}$$

where $\Big[\mathbf{j}_s\Big]_m = j_{2m}(\beta_0 a)$, using that $j_{2m}(a\xi)e^{i\xi x} \sim \sin(a\xi)e^{i\xi x}/\xi$ (times a multiplicative constant that depends on m) decays in the upper half plane as $x > a$ from [75], equation (9.2.1).

Now to find an expression for the antisymmetric scattering coefficient R^a, the same process that starts from (5.2.9) and ends at (5.2.29) must be followed. The Fourier sine transform for the scattering part of the velocity potential is

$$\tilde{\phi}^a(\xi, z) \equiv \int_0^\infty \Big[\phi^a(x,z) - \phi^a_{inc}(x,z)\Big]\sin(\xi x)dx. \tag{5.2.30}$$

Under this transformation, the continuity equation (5.2.10) and the no flow condition (5.2.11) is satisfied by $\tilde{\phi}^a(\xi, z)$. However, the integrated version of the surface condition (5.2.3), becomes

$$\big(\partial_z - K\big)\int_0^\infty \phi^a(x,0)\sin(\xi x)dx = \int_a^\infty \Big\{\Big(K\delta - \beta\big(\partial_{xx} - \alpha_0^2\big)^2\Big)\phi^a_z(x,0)\Big\}\sin(\xi x)dx, \tag{5.2.31}$$

in $0 < \xi < \infty$. Through integration by parts and application of zero bending moment and shear stress at the edge (equation (5.2.5)), the analogue equation for

the antisymmetric modes becomes

$$\begin{aligned}
&\Big(\beta k^4+1-K\delta\Big)\int_0^\infty \phi_z^a(x,0)\sin(\xi x)dx - K\int_0^\infty \phi^a(x,0)\sin(\xi x)dx\\
&\quad=(\beta k^4-K\delta)\int_0^a \phi_z^a(x,0)\sin(\xi x)dx - P^a f_1^a(\xi)+Q^a f_2^a(\xi),\\
&\text{for}\quad f_1^a(\xi)\equiv\beta\big(\xi^2+\nu\alpha_0^2\big)\sin(a\xi),\quad f_2^a(\xi)\equiv\beta\big(\xi^3+(2-\nu)\alpha_0^2\xi\big)\cos(a\xi),
\end{aligned}\tag{5.2.32}$$

and $P^a=\phi_{xz}^a(a^+,0)$, $Q^a=\phi_z^a(a^+,0)$. Now using again that $\phi_{inc}^a(x,z)$ satisfies (5.2.3) in $x>a$, multiplying this condition by $\sin(\xi x)$ and integrating in $x\in(0,\infty)$, then

$$\begin{aligned}
0&=\int_0^\infty\left\{\left(\beta\Big(\partial_{xx}-\alpha_0^2\Big)^2+1-K\delta\right)\frac{\partial\phi_{inc}^a}{\partial z}(x,0)-K\phi_{inc}^a(x,0)\right\}\sin(\xi x)dx\\
&=\Big(\beta k^4+1-K\delta\Big)\int_0^\infty\frac{\partial\phi_{inc}^a}{\partial z}(x,0)\sin(\xi x)dx-K\int_0^\infty\phi_{inc}^a(x,0)\sin(\xi x)dx,
\end{aligned}\tag{5.2.33}$$

where the second equality came by integration by parts. Therefore, by combining the last two equations, then

$$\begin{aligned}
&\big(\beta k^4+1-K\delta\big)\tilde\phi_z^a(\xi,0)-K\tilde\phi^a(\xi,0)\\
&=(\beta k^4-K\delta)\int_0^a\phi_z^a(x,0)\sin(\xi x)dx-P^af_1^a(\xi)+Q^af_2^s(\xi),
\end{aligned}\tag{5.2.34}$$

which is the surface condition for the antisymmetric potential in the Fourier space. The antisymmetric potential in the Fourier space can be calculated from the continuity equation and the no flow condition at the bed as $\tilde\phi^a(\xi,z)=\tilde A^a(\xi)\cosh[k(z+h)]$,

where $\tilde{A}^a(\xi)$ can be found from (5.2.34). Inversion of the transform results to

$$\phi^a(x,z) = \phi^a_{inc}(x,z) + \frac{2}{\pi} \int\limits_0^\infty \frac{\cosh[k(z+h)]}{\Delta(k)\cosh(kh)} \Big\{ - P^a f_1^a(\xi) + Q^a f_2^a(\xi) \\ + \big(\beta k^4 - K\delta\big) \int\limits_0^a \phi_z^a(t,0)\sin(\xi t)dt \Big\} \sin(\xi x)d\xi. \tag{5.2.35}$$

Proceeding to the 2×2 system for P^a and Q^a, the equation is differentiated with respect to z and evaluated at $z=0$, to give

$$-ik_0 \sin(\beta_0 x)\sinh(k_0 h) - P^a F_1^a(x) + Q^a F_2^a(x) \\ + \frac{2}{\pi} \int\limits_0^\infty \frac{K - k\tanh(kh)}{\Delta(k)} \sin(\xi x) \int\limits_0^a \phi_z^a(t,0)\sin(\xi t)dtd\xi = \begin{cases} \phi_z^a(x,0), & x > a, \\ 0, & 0 < x < a, \end{cases} \tag{5.2.36}$$

after making use of the equation

$$\int\limits_0^\infty \sin(\xi x)\sin(\xi t)d\xi = \frac{\pi}{2}\delta(x-t). \tag{5.2.37}$$

The equation above can be derived by calculating the Fourier sine transform of $\delta(x-t)$ as $\sin(\xi t)$ (assuming that $t>0$) and then inverting the transform. Also

$$F_i^a(x) \equiv \frac{2}{\pi} \int\limits_0^\infty \frac{k\tanh(kh)}{\Delta(k)} f_i^a(\xi)\sin(\xi x)d\xi \quad \text{for} \quad i=1,2, \tag{5.2.38}$$

was used in equation (5.2.36) above.

The analogue linear system for P^a and Q^a is created again by substituting

$x = a^+$ into the equation above and its x-derivative. Namely,

$$
\begin{aligned}
P^a F_1^a(a^+) + Q^a\Big[1 - F_2^a(a^+)\Big] - \mathcal{K}^a\phi_z^a &= -ik_0\sin(\beta_0 a)\sinh(k_0 h),\\
P^a\Big[1 + F_1^{a'}(a^+)\Big] - Q^a F_2^{a'}(a^+) - \mathcal{K}^{a'}\phi_z^a &= -ik_0\beta_0\cos(\beta_0 a)\sinh(k_0 h),\\
\mathcal{K}^a\phi_z^a &\equiv \frac{2}{\pi}\int\!\!\!\!\!\!\diagup_0^\infty \frac{K - k\tanh(kh)}{\Delta(k)}\sin(a\xi)\int_0^a \phi_z^a(t,0)\sin(\xi t)dtd\xi,\\
\mathcal{K}^{a'}\phi_z^a &\equiv \frac{2}{\pi}\int\!\!\!\!\!\!\diagup_0^\infty \frac{K - k\tanh(kh)}{\Delta(k)}\xi\cos(a\xi)\int_0^a \phi_z^a(t,0)\sin(\xi t)dtd\xi.
\end{aligned}
\tag{5.2.39}
$$

The fluid surface vertical velocity $\phi_z^a(x,0)$ in the region of the crack is chosen to be

$$
\phi_z^a(x,0) \equiv \frac{\pi}{2}\big[P^a R_1^a(x) - Q^a R_2^a(x) + ik_0\sinh(k_0 h)R_3^a(x)\big],\quad 0 < x < a, \tag{5.2.40}
$$

for some unknown functions $R_1^a(x)$, $R_2^a(x)$ and $R_3^a(x)$ that satisfy

$$
\int\!\!\!\!\!\!\diagup_0^\infty \frac{K - k\tanh(kh)}{\Delta(k)}\sin(\xi x)\int_0^a R_i^a(t)\sin(\xi t)dtd\xi = \begin{cases} F_i^a(x), & i = 1,2,\\ \sin(\beta_0 x), & i = 3,\end{cases} \tag{5.2.41}
$$

so that the surface equation in the crack is satisfied. In the equation above, if the unknown surface functions are expanded in the basis of $R_i^a(t) \approx \sum_{m=0}^{N} b_{2m+1}^{(i)}(-1)^m P_{2m+1}(t/a)$

(where P_{2m+1} are the odd Legendre polynomials), then

$$\begin{gathered}
\sum_{m=0}^{N} M^a_{2n+1,2m+1} b^{(i)}_{2m+1} = f^{(i)}_{2n+1}, \\
\text{for} \quad M^a_{2n+1,2m+1} = a \int_0^\infty \frac{K - k\tanh(kh)}{\Delta(k)} j_{2n+1}(a\xi) j_{2m+1}(a\xi) d\xi, \\
f^{(i)}_{2n+1} = \frac{2}{\pi} \int_0^\infty \frac{k\tanh(kh)}{\Delta(k)} f^a_i(\xi) j_{2n+1}(a\xi) d\xi \text{ for } i = 1,2 \text{ and } f^{(3)}_{2n+1} = j_{2n+1}(\beta_0 a),
\end{gathered} \tag{5.2.42}$$

where $j_{2m+1}(z)$ are the spherical Bessel function of odd order, using the useful formula $(-1)^m \int_0^a P_{2m+1}(t/a)\sin(\xi t)dt = a j_{2m+1}(a\xi)$ found from [76], pg. 94(4). Similarly to the symmetric problem, the x-dependence was removed from (5.2.41), by multiplying it with $\frac{1}{a}(-1)^n P_{2n+1}(x/a)$ and integrating it in $x \in (0,a)$. Using $\mathbf{b}^{(i)}_a = \mathbf{M}^{-1}_a \mathbf{f}^{(i)}_a$ in vectorial form, then equations (5.2.39) become

$$\begin{gathered}
\begin{pmatrix} F^a_1(a^+) - \mathbf{K}^T_a \mathbf{M}^{-1}_a \mathbf{f}^{(1)}_a & 1 - F^a_2(a^+) + \mathbf{K}^T_a \mathbf{M}^{-1}_a \mathbf{f}^{(2)}_a \\ 1 + F^{a'}_1(a^+) - \mathbf{K}'^T_a \mathbf{M}^{-1}_a \mathbf{f}^{(1)}_a & \mathbf{K}'^T_a \mathbf{M}^{-1}_a \mathbf{f}^{(2)}_a - F^{a'}_2(a^+) \end{pmatrix} \begin{pmatrix} P^a \\ Q^a \end{pmatrix} \\
= ik_0 \sinh(k_0 h) \begin{pmatrix} \mathbf{K}^T_a \mathbf{M}^{-1}_a \mathbf{f}^{(3)}_a - \sin(\beta_0 a) \\ \mathbf{K}'^T_a \mathbf{M}^{-1}_a \mathbf{f}^{(3)}_a - \beta_0 \cos(\beta_0 a) \end{pmatrix} \quad \text{for} \\
K^a_{2n+1} \equiv a \int_0^\infty \frac{K - k\tanh(kh)}{\Delta(k)} \sin(a\xi) j_{2n+1}(a\xi) d\xi, \\
K^{a'}_{2n+1} \equiv a \int_0^\infty \frac{K - k\tanh(kh)}{\Delta(k)} \xi \cos(a\xi) j_{2n+1}(a\xi) d\xi.
\end{gathered} \tag{5.2.43}$$

Next, the equation (5.2.35) as $x \to \infty$ is considered to get an expression for R^a. The far-field condition (5.2.6) and the incident wave definition (5.2.8) must be implemented as well as the vertical velocity expansion in the crack (equation

(5.2.40)) to give

$$\begin{aligned}
&\frac{1}{2}(R^a+1)e^{i\beta_0 x}\cosh[k_0(z+h)]\\
&=-\frac{2}{\pi}\int_0^\infty \frac{\cosh[k(z+h)]}{\Delta(k)\cosh(kh)}\left[P^a f_1^a(\xi)-Q^a f_2^a(\xi)\right]\sin(\xi x)d\xi\\
&+a\sum_{m=0}^{N}\left(P^a b_{2m+1}^{(1)}-Q^a b_{2m+1}^{(2)}\right)\int_0^\infty \frac{\cosh[k(z+h)]}{\Delta(k)\cosh(kh)}(\beta k^4-K\delta)j_{2m+1}(a\xi)\sin(\xi x)d\xi\\
&+ik_0 a\sinh(k_0 h)\sum_{m=0}^{N} b_{2m+1}^{(3)}\int_0^\infty \frac{\cosh[k(z+h)]}{\Delta(k)\cosh(kh)}(\beta k^4-K\delta)j_{2m+1}(a\xi)\sin(\xi x)d\xi.
\end{aligned} \tag{5.2.44}$$

Proceeding to the final calculation for R^a by expressing the integrals in the infinite domain (due to even integrands), writing $\sin(\xi x)$ in terms of complex exponentials and applying the Cauchy's residue theorem in the upper and lower half plane accordingly (as in the symmetric case), then

$$\begin{aligned}
R^a=-1+\frac{2k_0}{\beta_0\Delta'(k_0)\cosh(k_0h)}\Bigg\{&P^a\left[\pi a(\beta k_0^4-K\delta)\mathbf{j}_a^T\mathbf{M}_a^{-1}\mathbf{f}_a^{(1)}-2f_1^a(\beta_0)\right]\\
-Q^a\Big[\pi a(\beta k_0^4-K\delta)\mathbf{j}_a^T\mathbf{M}_a^{-1}\mathbf{f}_a^{(2)}-2f_2^a(\beta_0)\Big]&+i\pi a(\beta k_0^4-K\delta)k_0\sinh(k_0h)\mathbf{j}_a^T\mathbf{M}_a^{-1}\mathbf{f}_a^{(3)}\Bigg\},
\end{aligned} \tag{5.2.45}$$

where $\left[\mathbf{j}_a\right]_m = j_{2m+1}(\beta_0 a)$, using that $j_{2m+1}(a\xi)e^{i\xi x}\sim\cos(a\xi)e^{i\xi x}/\xi$ (times a multiplicative constant that depends on m) decays in the upper half plane as $x>a$, from [75], equation (9.2.1). In this calculation, also the fact that j_{2m+1} is odd was taken into account to combine the two infinite sums (upper and lower half planes) into one and only the $r=0$ term survives from that sum as $\Im\{\beta_r\}>0$ for $r\neq 0$.

Note that in the symmetric and antisymmetric problems there is no transmission but only reflection. Therefore, the conservation of energy is translated into $|R^{s,a}|=1$, which can be used as a checkpoint in the numerical results. Note that the scattering coefficients to the physical problem can be found in terms of $R^{s,a}$ from (5.2.7) and using that $|R^{s,a}|=1$ then it can be verified that the energy conservation $|R|^2+|T|^2=1$ is satisfied.

5.2.2 Approximation for small crack width

Over the years, it was noticed that when the gap between the ice sheets is narrow, then the problem admits a closed-form solution. For example, [42] and [43] showed that such expressions can be maintained using a Green's function approach at infinite depth. In the case of finite depth [44] adopted the Wiener-Hopf technique and [46] using two approaches: the Green's function and an eigenfunction expansion method.

In this thesis, the approach of maintaining a closed-form solution for a small crack will be to expand the vertical velocity of the fluid surface in the crack as a single term approximation. This is appropriate as if you expand a function $f(x)$ over $0 < x < a$ and a is "small" then, by Taylor expansion $f(x) \approx f(0) + xf'(0) + \mathcal{O}(x^2)$ whose symmetric part is $f^s(x) = f(0) + \mathcal{O}(x^2)$. But since $x^2 < a^2$ and a is small then $f^s(x) = f(0)$ which is a constant. The antisymmetric part of the expansion $f^a(x) = xf'(0) + \mathcal{O}(x^3)$ and its leading order is $f^a(x) = xf'(0)$ which is a constant times x. Physically this means that a short segment of a curve is approximately a straight line (or $Ax + B$). Thus, we truncate the $R_i^{s,a}(t)$ expansions at $N = 0$ or use $\phi_z^s(x, 0) = C^s$ and $\phi_z^a(x, 0) = C^a x/a$ in $0 < x < a \ll d$ for C^s, C^a constants, instead of equations (5.2.22) and (5.2.40). This suggest that the dimension of all the vectors and matrices could be dropped to 1 as the products of the form $\mathbf{K}^T\mathbf{M}^{-1}\mathbf{f}^{(i)}$ will be equivalent to a scalar product that looks like $K_0 f_0^{(i)}/M_{0,0}$ at leading order of $\mathcal{O}(a^0)$.

Also, all the definitions involved in the remaining equations, are approximated at leading order in a. However, by doing that, in some cases the convergent integrals could become divergent. For example, if within a convergent integral the terms tend to $\xi^{-2}\sin(a\xi)$ as $\xi \to \infty$, then if the trigonometric function is approximated by $a\xi$ (to leading order), then the integrand is asymptotic to ξ^{-1} which is divergent. Therefore, before approximating any function inside integrals, first the dispersion relation must be used to guarantee that even after the approximation, the integral is still convergent.

Normally, one could start by approximating the integrals of the 2×2 linear systems for $P^{s,a}$ and $Q^{s,a}$ in (5.2.26) and (5.2.43). Starting from the integrals of the symmetric case, by approximating $\sin(a\xi) \approx a\xi$, $\cos(a\xi) \approx 1$, $j_{2n}(a\xi) \approx \delta_{n0}$, then it can be proved that at leading order $F_1^s(a^+) \approx f_0^{(1)}$, $F_2^s(a^+), F_2^{s'}(a^+) \approx 0$, $F_1^{s\prime}(a^+) \approx -1$, $K_0^s \approx M_{0,0}^s$, $K_0^{s'}/M_{0,0}^s \sim \mathcal{O}(a)$ and $f_0^{(2)}, f_0^{(3)} \approx 1$ by using the dispersion relation where appropriate (the application of this trick can be found in Appendix C.1). Using this information, one could see by direct substitution that the system in (5.2.26) has no unique solutions as all the matrix elements and the right-hand side become zero. The same happens in the antisymmteric system of (5.2.43) as $F_1^a(a^+), F_1^{a'}(a^+) \approx 0$, $F_2^{a'} \approx 1$, $K_1^a f_1^{(i)}/M_{1,1}^a \sim \mathcal{O}(a)$, $K_1^{a'} f_1^{(1)}/M_{1,1}^a \approx 1$,

$K_1^{a'} f_1^{(2)}/M_{1,1}^a \approx F_2^{a'}(a^+)$, $K_1^a f_1^{(3)}/M_{1,1}^a \approx \beta_0 a$ and $K_1^{a'} f_1^{(3)}/M_{1,1}^a \approx \beta_0$. Therefore, the closed-form solution will be derived using a slightly different approach.

Starting from symmetric problem, the edge conditions $\mathcal{B}\phi_z^s(a^+,0)=0$ and $\mathcal{S}\phi_z^s(a^+,0)=0$ are applied to the right-hand side of the surface condition (5.2.18) in $x>a$. These two equations result to

$$\begin{aligned}&\begin{pmatrix}\mathcal{C}^s R_1^s + \mathcal{B}F_1^s(a^+) & \mathcal{C}^s R_2^s + \mathcal{B}F_2^s(a^+)\\ \mathcal{C}^{s'} R_1^s - \mathcal{S}F_1^s(a^+) & \mathcal{C}^{s'} R_2^s - \mathcal{S}F_2^s(a^+)\end{pmatrix}\begin{pmatrix}P^s\\ Q^s\end{pmatrix}\\ &= k_0\sinh(k_0h)\begin{pmatrix}\mathcal{C}^s R_3^s - (\beta_0^2+\nu\alpha_0^2)\cos(\beta_0 a)\\ \mathcal{C}^{s'} R_3^s - (\beta_0^3+(2-\nu)\alpha_0^2\beta_0)\sin(\beta_0 a)\end{pmatrix},\end{aligned} \tag{5.2.46}$$

after expanding the vertical velocity of the fluid surface in $0<x<a$ from (5.2.22) and the following integrals are used

$$\begin{aligned}\mathcal{C}^s R_i^s &\equiv \int_0^\infty \frac{K-k\tanh(kh)}{\Delta(k)}(\xi^2+\nu\alpha_0^2)\cos(a\xi)\int_0^a R_i^s(t)\cos(\xi t)dtd\xi,\\ \mathcal{C}^{s'} R_i^s &\equiv \int_0^\infty \frac{K-k\tanh(kh)}{\Delta(k)}(\xi^3+(2-\nu)\alpha_0^2\xi)\sin(a\xi)\int_0^a R_i^s(t)\cos(\xi t)dtd\xi,\end{aligned} \tag{5.2.47}$$

with $R_i^s(t)$ satisfy (5.2.23) to guarantee that the surface condition in the crack is satisfied.

Now by making a single term approximation (small crack assumption) to

R_i^s from (5.2.24) using $b_0^{(i)} = f_0^{(i)}/M_{0,0}^s$, then the system above becomes

$$\begin{aligned}
&\begin{pmatrix} (c_0^s f_0^{(1)}/M_{0,0}^s) + \mathcal{B}F_1^s(a^+) & (c_0^s f_0^{(2)}/M_{0,0}^s) + \mathcal{B}F_2^s(a^+) \\ (c_0^{s'} f_0^{(1)}/M_{0,0}^s) - \mathcal{S}F_1^s(a^+) & (c_0^{s'} f_0^{(2)}/M_{0,0}^s) - \mathcal{S}F_2^s(a^+) \end{pmatrix} \begin{pmatrix} P^s \\ Q^s \end{pmatrix} \\
&= k_0 \sinh(k_0 h) \begin{pmatrix} (c_0^s f_0^{(3)}/M_{0,0}^s) - (\beta_0^2 + \nu\alpha_0^2)\cos(\beta_0 a) \\ (c_0^{s'} f_0^{(3)}/M_{0,0}^s) - (\beta_0^3 + (2-\nu)\alpha_0^2\beta_0)\sin(\beta_0 a) \end{pmatrix}, \\
&c_0^s \equiv a \int_0^\infty \frac{K - k\tanh(kh)}{\Delta(k)} (\xi^2 + \nu\alpha_0^2)\cos(a\xi) j_0(a\xi) d\xi, \\
&c_0^{s'} \equiv a \int_0^\infty \frac{K - k\tanh(kh)}{\Delta(k)} (\xi^3 + (2-\nu)\alpha_0^2\xi)\sin(a\xi) j_0(a\xi) d\xi.
\end{aligned} \tag{5.2.48}$$

Note that some of the integrals above become divergent in the small a limit and therefore the dispersion relation should be used appropriately before approximating the trigonometric and Bessel functions. Starting from $\mathcal{B}F_1^s(a^+)$ and $\mathcal{S}F_1^s(a^+)$, then all the derivatives are considered as

$$\begin{aligned}
F_1^s(a^+) &= \frac{2}{\pi} \int_0^\infty \frac{\beta k \tanh(kh)}{\Delta(k)} (\xi^2 + \nu\alpha_0^2)\cos^2(a\xi) d\xi, \\
F_1^{s'}(a^+) &= -1 + \frac{1}{\pi} \int_0^\infty \frac{\big[\beta\alpha_0^2(\alpha_0^2 + (2-\nu)\xi^2) + 1 - K\delta\big] k\tanh(kh) - K}{\xi\Delta(k)} \sin(2a\xi) d\xi, \\
F_1^{s''}(a^+) &= \frac{2}{\pi} \int_0^\infty \frac{\big[\beta\alpha_0^2(\alpha_0^2 + (2-\nu)\xi^2) + 1 - K\delta\big] k\tanh(kh) - K}{\Delta(k)} \cos^2(a\xi) d\xi, \\
F_1^{s'''}(a^+) &= -\frac{1}{\pi} \int_0^\infty \frac{\big[\beta(2\nu-3)\alpha_0^4 + 1 - K\delta\big] k\tanh(kh) - K}{\Delta(k)} \xi\sin(2a\xi) d\xi \\
&-(2-\nu)\alpha_0^2 + \frac{(2-\nu)\alpha_0^2}{\pi} \int_0^\infty \frac{\big(\beta\alpha_0^4 + 1 - K\delta\big) k\tanh(kh) - K}{\xi\Delta(k)} \sin(2a\xi) d\xi,
\end{aligned} \tag{5.2.49}$$

where the second equation was maintained using (C.1.3) and the fourth by using

$$\begin{aligned}\frac{\big[\beta\alpha_0^2(\alpha_0^2+(2-\nu)\xi^2)+1-K\delta\big]k\tanh(kh)-K}{\Delta(k)} &= \frac{(2-\nu)\alpha_0^2}{\xi^2}\\ +\frac{\big[\beta(2\nu-3)\alpha_0^4+1-K\delta\big]k\tanh(kh)-K}{\Delta(k)}&\\ -(2-\nu)\alpha_0^2\frac{\big(\beta\alpha_0^4+1-K\delta\big)k\tanh(kh)-K}{\xi^2\Delta(k)}&.\end{aligned} \tag{5.2.50}$$

The advantage with this kind of formulas is that ν can be relabelled with any other function of ν as the only dependence on the Poisson ratio in the dispersion relation, is β. Also in the derivatives of F_1^s above, the formulas

$$\begin{aligned}\int_0^\infty \frac{\sin(A\xi)\cos(B\xi)}{\xi}d\xi &= \frac{\pi}{4}\Big[\operatorname{sgn}(A+B)+\operatorname{sgn}(A-B)\Big],\\ \int_0^\infty \frac{\sin^2(A\xi)}{\xi^2}d\xi &= \frac{\pi}{2}|A|,\end{aligned} \tag{5.2.51}$$

were used. Therefore by approximating $\sin(2a\xi)\approx 2a\xi$ and $\cos(a\xi)\approx 1$ to the expressions above, then it can be verified that

$$\mathcal{B}F_1^s(a^+)\approx\frac{2}{\pi}\int_0^\infty \frac{\big[\beta\alpha_0^2(1-\nu)\big(2\xi^2+(1+\nu)\alpha_0^2\big)+1-K\delta\big]k\tanh(kh)-K}{\Delta(k)}d\xi, \tag{5.2.52}$$

and $\mathcal{S}F_1^s(a^+)\approx 0$ by neglecting $\mathcal{O}(a)$. Proceeding onto the expressions for $\mathcal{B}F_2^s(a^+)$

and $\mathcal{S}F_2^s(a^+)$, the higher derivatives of F_2^s are calculated as follows.

$$
\begin{aligned}
F_2^s(a^+) &= -\frac{1}{\pi}\int_0^\infty \frac{\big[\beta\alpha_0^2(\alpha_0^2+\nu\xi^2)+1-K\delta\big]k\tanh(kh)-K}{\xi\Delta(k)}\sin(2a\xi)d\xi,\\
F_2^{s'}(a^+) &= \nu\alpha_0^2 a+\frac{2}{\pi}\int_0^\infty \frac{\big[\beta(1-2\nu)\alpha_0^4+1-K\delta\big]k\tanh(kh)-K}{\Delta(k)}\sin^2(a\xi)d\xi\\
&\quad -\frac{2\nu\alpha_0^2}{\pi}\int_0^\infty \frac{\big(\beta\alpha_0^4+1-K\delta\big)k\tanh(kh)-K}{\xi^2\Delta(k)}\sin^2(a\xi)d\xi,\\
F_2^{s''}(a^+) &= \frac{1}{\pi}\int_0^\infty \frac{\big[\beta(1-2\nu)\alpha_0^4+1-K\delta\big]k\tanh(kh)-K}{\Delta(k)}\xi\sin(2a\xi)d\xi\\
&\quad -\frac{\nu\alpha_0^2}{\pi}\int_0^\infty \frac{\big(\beta\alpha_0^4+1-K\delta\big)k\tanh(kh)-K}{\xi\Delta(k)}\sin(2a\xi)d\xi,\\
F_2^{s'''}(a^+) &= \frac{2\nu\alpha_0^2}{\pi}\int_0^\infty \frac{\big(\beta\alpha_0^4+1-K\delta\big)k\tanh(kh)-K}{\xi^2\Delta(k)}\sin^2(a\xi)d\xi\\
&\quad +\frac{K}{\beta}\left[\frac{1}{\alpha_0\tanh(\alpha_0 h)}-\frac{2}{\pi}\int_0^\infty \frac{\beta\alpha_0^2(\alpha_0^2+2\xi^2)k\tanh(kh)-K}{\xi^2 k\tanh(kh)\Delta(k)}\sin^2(a\xi)d\xi\right]\\
&\quad -\frac{\beta(1-2\nu)\alpha_0^4+1-K\delta}{\beta}\left[a-\frac{2}{\pi}\int_0^\infty \frac{\beta\alpha_0^2(\alpha_0^2+2\xi^2)k\tanh(kh)-K}{\xi^2\Delta(k)}\sin^2(a\xi)d\xi\right],
\end{aligned}
\tag{5.2.53}
$$

where the first equation was maintained using (C.1.3), the second by (5.2.50) and the fourth by

$$
\frac{\xi^2 k\tanh(kh)}{\Delta(k)} = \frac{1}{\beta\xi^2}-\frac{\beta\alpha_0^2(\alpha_0^2+2\xi^2)k\tanh(kh)-K}{\beta\xi^2\Delta(k)}. \tag{5.2.54}
$$

Also in the $F_2^{s'''}$ formula above, the Cauchy's residue theorem was used to get the (non-integral) terms that are proportional to β^{-1} by expressing $\sin(a\xi)$ in terms of complex exponentials and considering the new pole at $\xi = 0$. Therefore, it can be seen that at leading order $\mathcal{B}F_2^s(a^+), \mathcal{S}F_2^s(a^+) \approx 0$ by neglecting $\mathcal{O}(a)$.

Proceeding to the integrals found in equations (5.2.25) (for $n = m = 0$) and

(5.2.48), it follows that

$$
\begin{aligned}
M_{0,0}^{s} &\approx a \int_0^{\infty} \frac{K - k\tanh(kh)}{\Delta(k)} d\xi \equiv a M_{0,0}^{s^*}, \\
f_0^{(1)} &\approx \frac{2\beta}{\pi} \int_0^{\infty} \frac{k\tanh(kh)}{\Delta(k)} (\xi^2 + \nu\alpha_0^2) d\xi, \;\; f_0^{(2)} \approx 1, \;\; f_0^{(3)} \approx 1, \\
c_0^{s} &\approx a \int_0^{\infty} \frac{K - k\tanh(kh)}{\Delta(k)} (\xi^2 + \nu\alpha_0^2) d\xi \equiv a c_0^{s^*}, \quad c_0^{s'} \approx \pi \frac{\alpha_0 a \tanh(\alpha_0 h) - K}{2\beta\alpha_0 \tanh(\alpha_0 h)},
\end{aligned}
\tag{5.2.55}
$$

where the approximations $\cos(a\xi), j_0(a\xi) \approx 1$ and $\sin(a\xi) \approx a\xi$ were used. Also for the $f_0^{(2)}$ expression, equation (C.1.3) was used and for the last expression above, the following identity was implemented.

$$
\begin{aligned}
\frac{\beta\xi^3\big(K - k\tanh(kh)\big)}{\Delta(k)} &= \frac{K}{\xi k \tanh(kh)} - \frac{1}{\xi} \\
+ \frac{K + k\tanh(kh)}{\xi k \tanh(kh)\Delta(k)} &\left\{ 1 - \big[\beta\alpha_0^2(\alpha_0^2 + 2\xi^2) + 1 - K\delta\big] k\tanh(kh) \right\}.
\end{aligned}
\tag{5.2.56}
$$

Then, using the simplified integrals found in equations (5.2.52) and (5.2.68) the 2×2 system of (5.2.48) transforms to

$$
\begin{aligned}
&\begin{pmatrix} c_0^{s^*} f_0^{(1)} + M_{0,0}^{s^*} \mathcal{B} F_1^{s}(a^+) & c_0^{s^*} \\ c_0^{s'} f_0^{(1)} & c_0^{s'} \end{pmatrix} \begin{pmatrix} P^s \\ Q^s \end{pmatrix} \\
&= k_0 \sinh(k_0 h) \begin{pmatrix} c_0^{s^*} - M_{0,0}^{s^*}(\beta_0^2 + \nu\alpha_0^2) \\ c_0^{s'} - \beta_0 a M_{0,0}^{s}(\beta_0^3 + (2-\nu)\alpha_0^2\beta_0) \end{pmatrix}.
\end{aligned}
\tag{5.2.57}
$$

By neglecting the term that is proportional to $aM_{0,0}^{s} \sim \mathcal{O}(a^2)$, then $c_0^{s'}$ can be cancelled from the second equation. Then by solving analytically the system by

inversion the 2×2 matrix, the result is

$$\begin{pmatrix} P^s \\ Q^s \end{pmatrix} = \frac{k_0 \sinh(k_0 h)}{\mathcal{B}F_1^s(a^+)} \begin{pmatrix} -(\beta_0^2 + \nu\alpha_0^2) \\ \mathcal{B}F_1^s(a^+) + (\beta_0^2 + \nu\alpha_0^2) f_0^{(1)} \end{pmatrix}, \tag{5.2.58}$$

which is a closed-form solution for P^s and Q^s which is much simpler than the solutions when the separation distance between the ice sheets is finite.

Now, the simplified expression for the reflection coefficient R^s from (5.2.29) will be calculated using the P^s and Q^s formulas from (5.2.58). Approximating $j_{2m}(\beta_0 a) \approx \delta_{m0}$ in the R^s expression, $\cos(\beta_0 a) \approx 1$ and $\sin(\beta_0 a) \approx \beta_0 a$ in $f_i^s(\beta_0)$ from (5.2.14) then

$$R^s = 1 + \frac{4i\beta k_0^2 \tanh(k_0 h)}{\beta_0 \Delta'(k_0) \mathcal{B}F_1^s(a^+)} \Big(\beta_0^2 + \nu\alpha_0^2\Big)^2, \tag{5.2.59}$$

by using the simplified integrals of equation (5.2.68). This is a much simpler formula than the one of the previous section (crack of finite length) as it requires only the calculation of the single integral $\mathcal{B}F_1^s(a^+)$ instead of $N^2 + 4N + 4$ where N is the number of modes required to characterise the surface expansion within the crack (N^2 from the single integral matrix, $4N$ from the four integral vectors and 4 from the four scalar integrals). Also, the simple expression of R^s in (5.2.59) will be proven to satisfy the energy conservation relation $|R^s|^2 = 1$ analytically. Using the formula for the modulus of the sum, then

$$|R^s|^2 = 1 + \frac{8\beta\big(\beta_0^2 + \nu\alpha_0^2\big)^2 k_0^2 \tanh(k_0 h)}{\beta_0 \Delta'(k_0) |\mathcal{B}F_1^s(a^+)|^2} \left[\Im\Big\{ \mathcal{B}F_1^s(a^+) \Big\} + \frac{2\beta k_0^2 \tanh(k_0 h)}{\beta_0 \Delta'(k_0)} \big(\beta_0^2 + \nu\alpha_0^2\big)^2 \right], \tag{5.2.60}$$

using $\Re\{i/z\} = \Im\{z\}/|z|^2$ and $\Delta'(k_0) \in \mathbb{R}$. Therefore, it remains to prove that the square bracket is zero. According to (C.1.1), the only imaginary contribution of $\mathcal{B}F_1^s(a^+)$ is half the contribution of the integrand's residue at $\xi = \beta_0$. This translates

to

$$\Im\Big\{\mathcal{B}F_1^s(a^+)\Big\} = \frac{2k_0}{\beta_0}\frac{\big[\beta\alpha_0^2(1-\nu)\Big(2\beta_0^2+(1+\nu)\alpha_0^2\Big)+1-K\delta\big]k_0\tanh(k_0h)-K}{\Delta'(k_0)}$$
$$= -\frac{2\beta k_0^2\tanh(k_0h)}{\beta_0\Delta'(k_0)}\big(\beta_0^2+\nu\alpha_0^2\big)^2, \tag{5.2.61}$$

by expanding the terms of the numerator and using $K=(\beta k_0^4+1-K\delta)k_0\tanh(k_0h)$ from the dispersion relation. In conclusion, this result proves that the energy is conserved analytically through $|R^s|^2=1$. Therefore, R^s can be found from (5.2.59), where the $\mathcal{B}F_1^s(a^+)$ integral can be converted into an infinite sum through the Cauchy's residue theorem, by writing the integral in the infinite domain (even integrand) and decomposing the contour in the upper half complex plane. Thus,

$$\mathcal{B}F_1^s(a^+) = 2i\sum_{r=-2}^{\infty} k_r\frac{\big[\beta\alpha_0^2(1-\nu)\big(2\beta_r^2+(1+\nu)\alpha_0^2\big)+1-K\delta\big]k_r\tanh(k_rh)-K}{\beta_r\Delta'(k_r)}. \tag{5.2.62}$$

Now the same procedure will be followed for the derivation of the closed-form solution of R^a. Starting by applying the antisymmetric conditions $\mathcal{B}\phi_z^a(a^+,0)=0$ and $\mathcal{S}\phi_z^a(a^+,0)=0$ (zero bending moment and zero shear stress at the edge of the ice sheet) into (5.2.36) in $x>a$, then the system for P^a and Q^a becomes

$$\begin{pmatrix}\mathcal{C}^aR_1^a+\mathcal{B}F_1^a(a^+) & -\mathcal{C}^aR_2^a-\mathcal{B}F_2^a(a^+)\\ \mathcal{C}^{a'}R_1^a+\mathcal{S}F_1^a(a^+) & -\mathcal{C}^{a'}R_2^a-\mathcal{S}F_2^a(a^+)\end{pmatrix}\begin{pmatrix}P^a\\Q^a\end{pmatrix}$$
$$= ik_0\sinh(k_0h)\begin{pmatrix}(\beta_0^2+\nu\alpha_0^2)\sin(\beta_0a)-\mathcal{C}^aR_3^a\\(\beta_0^3+(2-\nu)\alpha_0^2\beta_0)\cos(\beta_0a)-\mathcal{C}^{a'}R_3^a\end{pmatrix},$$
$$\mathcal{C}^aR_i^a \equiv \int_0^{\infty}\frac{K-k\tanh(kh)}{\Delta(k)}(\xi^2+\nu\alpha_0^2)\sin(a\xi)\int_0^a R_i^a(t)\sin(\xi t)dtd\xi, \tag{5.2.63}$$
$$\mathcal{C}^{a'}R_i^a \equiv \int_0^{\infty}\frac{K-k\tanh(kh)}{\Delta(k)}(\xi^3+(2-\nu)\alpha_0^2\xi)\cos(a\xi)\int_0^a R_i^a(t)\sin(\xi t)dtd\xi,$$

after expanding the vertical velocity of the fluid surface in the crack from (5.2.40),

with $R_i^a(t)$ satisfy (5.2.41) to guarantee that the surface condition in $0 < x < a$ is satisfied. Next, by making a single term approximation to $R_i^a(t) \approx b_1^{(i)} P_1(t/a)$ using $b_1^{(i)} = f_1^{(i)}/M_{1,1}^a$ from (5.2.42), then the P^a, Q^a system becomes

$$\begin{aligned}
&\begin{pmatrix} (c_1^a f_1^{(1)}/M_{1,1}^a) + \mathcal{B}F_1^a(a^+) & -(c_1^a f_1^{(2)}/M_{1,1}^a) - \mathcal{B}F_2^a(a^+) \\ (c_1^{a'} f_1^{(1)}/M_{1,1}^a) + \mathcal{S}F_1^a(a^+) & -(c_1^{a'} f_1^{(2)}/M_{1,1}^a) - \mathcal{S}F_2^a(a^+) \end{pmatrix} \begin{pmatrix} P^a \\ Q^a \end{pmatrix} \\
&= ik_0 \sinh(k_0 h) \begin{pmatrix} (\beta_0^2 + \nu\alpha_0^2)\sin(\beta_0 a) - (c_1^a f_1^{(3)}/M_{1,1}^a) \\ (\beta_0^3 + (2-\nu)\alpha_0^2\beta_0)\cos(\beta_0 a) - (c_1^{a'} f_1^{(3)}/M_{1,1}^a) \end{pmatrix}, \\
&\qquad c_1^a \equiv a \int_0^\infty \frac{K - k\tanh(kh)}{\Delta(k)} (\xi^2 + \nu\alpha_0^2)\sin(a\xi) j_1(a\xi) d\xi, \\
&\qquad c_1^{a'} \equiv a \int_0^\infty \frac{K - k\tanh(kh)}{\Delta(k)} (\xi^3 + (2-\nu)\alpha_0^2\xi)\cos(a\xi) j_1(a\xi) d\xi.
\end{aligned} \tag{5.2.64}$$

Now, the integral expressions should be derived by making sure that they converge through the dispersion relation. Starting from $\mathcal{B}F_1^a(a^+)$ and $\mathcal{S}F_1^a(a^+)$, then all the derivatives are considered as

$$\begin{aligned}
F_1^a(a^+) &= a - \frac{2}{\pi}\int_0^\infty \frac{\big[\beta\alpha_0^2(\alpha_0^2 + (2-\nu)\xi^2) + 1 - K\delta\big]k\tanh(kh) - K}{\xi^2\Delta(k)} \sin^2(a\xi) d\xi, \\
F_1^{a'}(a^+) &= -\frac{1}{\pi}\int_0^\infty \frac{\big[\beta\alpha_0^2(\alpha_0^2 + (2-\nu)\xi^2) + 1 - K\delta\big]k\tanh(kh) - K}{\xi\Delta(k)} \sin(2a\xi) d\xi, \\
F_1^{a''}(a^+) &= \nu\alpha_0^2 a + \frac{2}{\pi}\int_0^\infty \frac{\big[\beta(2\nu-3)\alpha_0^4 + 1 - K\delta\big]k\tanh(kh) - K}{\Delta(k)} \sin^2(a\xi) d\xi \\
&\quad - \frac{2\nu\alpha_0^2}{\pi}\int_0^\infty \frac{\big(\beta\alpha_0^4 + 1 - K\delta\big)k\tanh(kh) - K}{\xi^2\Delta(k)} \sin^2(a\xi) d\xi, \\
F_1^{a'''}(a^+) &= \frac{1}{\pi}\int_0^\infty \frac{\big[\beta(2\nu-3)\alpha_0^4 + 1 - K\delta\big]k\tanh(kh) - K}{\Delta(k)} \xi\sin(2a\xi) d\xi \\
&\quad - \frac{\nu\alpha_0^2}{\pi}\int_0^\infty \frac{\big(\beta\alpha_0^4 + 1 - K\delta\big)k\tanh(kh) - K}{\xi\Delta(k)} \sin(2a\xi) d\xi,
\end{aligned} \tag{5.2.65}$$

where in the first and third expressions, equations (C.1.3) and (5.2.50) for $\nu \to (2-\nu)$

were used respectively. Also, similar identities as in the symmetric case were used where appropriate. By neglecting $\mathcal{O}(a)$, then it can be shown that $\mathcal{B}F_1^a(a^+) \approx 0$ and $\mathcal{S}F_1^a(a^+) \approx 0$. Moving on to the higher derivatives of F_2^a, then

$$\begin{aligned}
F_2^a(a^+) &= 1 - \frac{1}{\pi}\int_0^\infty \frac{\big[\beta\alpha_0^2(\alpha_0^2+\nu\xi^2)+1-K\delta\big]k\tanh(kh)-K}{\xi\Delta(k)}\sin(2a\xi)d\xi,\\
F_2^{a'}(a^+) &= -\frac{2}{\pi}\int_0^\infty \frac{\big[\beta\alpha_0^2(\alpha_0^2+\nu\xi^2)+1-K\delta\big]k\tanh(kh)-K}{\Delta(k)}\cos^2(a\xi)d\xi,\\
F_2^{a''}(a^+) &= \nu\alpha_0^2 + \frac{1}{\pi}\int_0^\infty \frac{\big[\beta(1-2\nu)\alpha_0^4+1-K\delta\big]k\tanh(kh)-K}{\Delta(k)}\xi\sin(2a\xi)d\xi\\
&\quad -\frac{\nu\alpha_0^2}{\pi}\int_0^\infty \frac{\big(\beta\alpha_0^4+1-K\delta\big)k\tanh(kh)-K}{\xi\Delta(k)}\sin(2a\xi)d\xi,\\
F_2^{a'''}(a^+) &= \frac{2}{\pi}\int_0^\infty \frac{\big[\beta(1-2\nu)\alpha_0^4+1-K\delta\big]k\tanh(kh)-K}{\Delta(k)}\xi^2\cos^2(a\xi)d\xi\\
&\quad -\frac{2\nu\alpha_0^2}{\pi}\int_0^\infty \frac{\big(\beta\alpha_0^4+1-K\delta\big)k\tanh(kh)-K}{\Delta(k)}\cos^2(a\xi)d\xi,
\end{aligned} \tag{5.2.66}$$

where the same equations as in (5.2.65) were used. Now by retaining only the leading order (neglect $\mathcal{O}(a)$) then $\mathcal{B}F_2^a(a^+) \approx 0$ and

$$\begin{aligned}
\mathcal{S}F_2^a(a^+) &\approx \frac{4\alpha_0^2(1-\nu)}{\pi}\int_0^\infty \frac{\big(\beta\alpha_0^4+1-K\delta\big)k\tanh(kh)-K}{\Delta(k)}d\xi\\
&\quad +\frac{2}{\pi}\int_0^\infty \frac{\big[\beta\alpha_0^4(1-\nu^2)+1-K\delta\big]k\tanh(kh)-K}{\Delta(k)}\xi^2 d\xi.
\end{aligned} \tag{5.2.67}$$

Proceeding to the remaining integrals found in (5.2.25) (for $n = m = 0$) and (5.2.64), then by approximating $j_1(a\xi) \approx a\xi/3$ and use the dispersion relation

where appropriate, it follows that

$$M_{1,1}^a \approx \frac{a^3}{9}\int_0^\infty \frac{K-k\tanh(kh)}{\Delta(k)}\xi^2 d\xi \equiv a^3 M_{1,1}^{a^*}, \quad f_1^{(1)} \approx \frac{a}{3},$$

$$f_1^{(2)} \approx -\frac{2a}{3\pi}\int_0^\infty \frac{\left[\beta\alpha_0^2(\alpha_0^2+\nu\xi^2)+1-K\delta\right]k\tanh(kh)-K}{\Delta(k)}d\xi \equiv a f_1^{(2)^*},$$

$$f_1^{(3)} \approx \frac{\beta_0 a}{3}, \quad c_1^a \approx \frac{\pi a^2}{6\beta}\frac{K-\alpha_0\tanh(\alpha_0 h)}{\alpha_0\tanh(\alpha_0 h)} \equiv a^2 c_1^{a^*},$$

$$c_1^{a'} \approx \frac{(2-\nu)\alpha_0^2 a^2}{3}\int_0^\infty \frac{K-k\tanh(kh)}{\Delta(k)}\xi^2 d\xi$$

$$+\frac{a^2}{3\beta}\int_0^\infty \Big[K+k\tanh(kh)\Big]\frac{1-\left[\beta\alpha_0^2(\alpha_0^2+2\xi^2)+1-K\delta\right]k\tanh(kh)}{k\tanh(kh)\Delta(k)}d\xi \equiv a^2 c_1^{a'^*}. \tag{5.2.68}$$

For the $f_1^{(1)}$ and $f_1^{(2)}$ expressions, equation (C.1.3) was used. Also the useful identities

$$\int_0^\infty \frac{\sin(a\xi)}{\xi}d\xi = \frac{\pi}{2} \quad \text{and} \quad \int_0^\infty \frac{\cos(a\xi)j_1(a\xi)}{\xi}d\xi = 0, \tag{5.2.69}$$

which were derived by applying the Cauchy's Residue theorem after expanding $\cos(a\xi)$, were used. In the last two expressions, equation (5.2.56) was used with

$$\int_0^\infty \frac{\sin(a\xi)j_1(a\xi)}{\xi^2}d\xi = \frac{\pi a}{6} \quad \text{and} \quad \int_0^\infty \frac{\cos(a\xi)j_1(a\xi)}{\xi k\tanh(kh)}d\xi = 0. \tag{5.2.70}$$

Note that if the P^a and Q^a equations found in (5.2.64), were multiplied by $M_{1,1}^a$, then a^3 will be the minimum power of a coming from the $M_{1,1}^a \mathcal{S}F_2^a(a^+)$ term. Also using that a^2 is the minimum power of a in c_1^a and $c_1^{a'}$, then in the $f_1^{(i)}$ expansions, $\mathcal{O}(a^2)$ were neglected. Therefore after a considerable algebra similar to the one of the symmetric case, the closed-form solutions for P^a, Q^a and R^a are found

from (5.2.64) and (5.2.45), as

$$\begin{gathered}\begin{pmatrix}P^a\\Q^a\end{pmatrix}=-\frac{ik_0\sinh(k_0h)}{\mathcal{S}F_2^a(a^+)}\begin{pmatrix}\beta_0\mathcal{S}F_2^a(a^+)+3\big(\beta_0^3+(2-\nu)\alpha_0^2\beta_0\big)f_1^{(2)^*}\\ \beta_0^3+(2-\nu)\alpha_0^2\beta_0\end{pmatrix},\\ R^a=-1-\frac{4i\beta k_0^2\tanh(k_0h)}{\beta_0\Delta'(k_0)\mathcal{S}F_2^a(a^+)}\Big(\beta_0^3+(2-\nu)\alpha_0^2\beta_0\Big)^2,\end{gathered}\tag{5.2.71}$$

Again the closed-form solution of R^a requires only the calculation of a single integral. The energy conservation $|R^a|^2=1$ will be analytically proven in the antisymmetric case as well. Again by using the formula for the modulus of the sum, then

$$|R^a|^2=1+\frac{8\beta\Gamma_0^2k_0^2\tanh(k_0h)}{\beta_0\Delta'(k_0)|\mathcal{S}F_2^a(a^+)|^2}\left[\Im\Big\{\mathcal{S}F_2^a(a^+)\Big\}+\frac{2\beta k_0^2\tanh(k_0h)}{\beta_0\Delta'(k_0)}\Gamma_0^2\right],\tag{5.2.72}$$

for $\Gamma_0=\beta_0^3+(2-\nu)\alpha_0^2\beta_0$. If the square bracket is proven to be zero, then the energy conservation will be proved. Using that the only imaginary contribution of $\mathcal{S}F_2^a(a^+)$ is half the contribution of the integrand's residue at $\xi=\beta_0$, then

$$\begin{aligned}\Im\Big\{\mathcal{S}F_2^a(a^+)\Big\}&=\frac{2k_0}{\beta_0\Delta'(k_0)}\Bigg[2\alpha_0^2(1-\nu)\Big\{\big(\beta\alpha_0^4+1-K\delta\big)k_0\tanh(k_0h)-K\Big\}\\&+\beta_0^2\Big\{\big(\beta\alpha_0^4(1-\nu^2)+1-K\delta\big)k_0\tanh(k_0h)-K\Big\}\Bigg]=-\frac{2\beta k_0^2\tanh(k_0h)}{\beta_0\Delta'(k_0)}\Gamma_0^2,\end{aligned}\tag{5.2.73}$$

by simplifying terms in the numerator and using K from the dispersion relation. Therefore, the energy is again conserved analytically through $|R^a|^2=1$. Using that $|R^{s,a}|=1$, then the energy to the actual problem is conserved as $|R|^2+|T|^2=1$ from (5.2.7). Therefore, R^a will be calculated numerically from (5.2.71) and the $\mathcal{S}F_2^a(a^+)$ integral can be turned into an infinite sum through the Cauchy's residue theorem

again, namely,

$$\begin{aligned}\mathcal{S}F_2^a(a^+) = 4i\alpha_0^2(1-\nu)\sum_{r=-2}^{\infty} k_r \frac{\big(\beta\alpha_0^4 + 1 - K\delta\big)k_r\tanh(k_r h) - K}{\beta_r \Delta'(k_r)} \\ +2i\sum_{r=-2}^{\infty} k_r\beta_r \frac{\big[\beta\alpha_0^4(1-\nu^2) + 1 - K\delta\big]k_r\tanh(k_r h) - K}{\Delta'(k_r)}.\end{aligned} \tag{5.2.74}$$

Many authors have solved a "zero gap" problem since it is mathematically convenient. Note that from the asymptotic analysis in the $a/d \ll 1$ regime above, one could retain higher orders in a (meaning the solution will depend explicitly on a) and then show that the "zero gap" limit is a good approximation to a small gap.

There is a variety of reasons why the higher order solution is not included in this thesis. First, the huge simplification allowed by the $\mathcal{O}(a)$ negligence (calculation of only two integrals) did not happen by its retainment as we still had to calculate nine integrals in the symmetric problem and nine in the antisymmetric ($N^2 + 4N + 4$ for $N = 1$). This complicated algebra produced a computationally expensive numerical code that did not have any significant impact on the results.

The theory above shows analytically that by starting with a gap of finite width and taking the limit $a/d \to 0$, then the solution converge to the "zero gap" problem solved by many authors. Actually, the leading order expressions of $R^{s,a}$ found in (5.2.59) and (5.2.71) are identical to the ones of [46] who solved the "zero gap" problem using a much different method (Green's function approach). This is a remarkable result. However, it is not very obvious to see that the solutions are identical, since the notation is different (written in non-dimensionalised language as well) and the far field conditions (and therefore the reflection and transmission coefficients) were chosen differently than the ones used here.

5.2.3 Numerical results for the inviscid problems

In this section, numerical results for the sections 5.2.1 and 5.2.2 are presented. From now on, we choose the typical physical parameters for such ice-water problems as $E = 5\text{GPa}$, $\nu = 0.3$, $g = 9.81\text{ms}^{-2}$, $\rho_i = 922.5\text{kgm}^{-3}$, $\rho_w = 1025\text{kgm}^{-3}$, to get $\beta/d^4 = 45536/d$ and $\delta/d = 0.9$ [42]. Therefore, the ice thickness d (which is always measured in meters) is left as a parameter that we can vary.

First, we show in 5.2 how the dispersion relation root k_{-1} varies in the

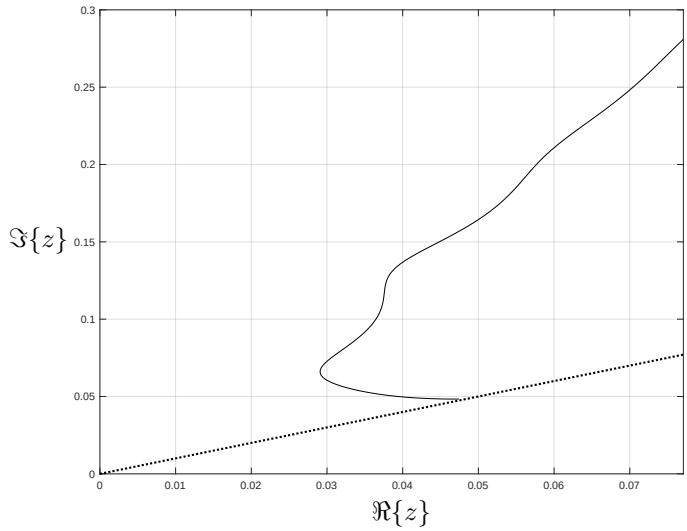

Figure 5.2: Path of k_{-1} root as k_0 varies from 0.01 to 0.3 for $(d, h) = (1, 40)$. The dotted line represents $\arg(z) = \pi/4$.

complex plane by shifting the incident wavenumber k_0. Note that the remaining complex roots are not plotted as they can be found from k_{-1} by the symmetry in the real and imaginary axes of the dispersion relation. Also, it can be verified that the root lies always in the first quadrant with $\Im\{k_{-1}\} > \Re\{k_{-1}\}$ (as dotted line represents $\arg(z) = \pi/4$). It can be verified that for small wavenumbers k_0, the root k_{-1} lies near $\arg(z) = \pi/4$. Starting from the dispersion relation for small k_0 one can get the approximate value $K \approx k_0^2 h$ by neglecting $\mathcal{O}(k_0^4)$. Substituting this value back in the dispersion relation for k_{-1} and neglecting $\mathcal{O}(k_0^2)$, then one could easily derive that $\beta k_{-1}^4 + 1 \approx 0$, which results to $k_{-1} \approx \beta^{-1/4} e^{i\pi/4}$ (using that k_{-1} must lie in the first quadrant). As all the simulations start from a small k_0, then $\beta^{-1/4} e^{i\pi/4}$ is a good initial guess for capturing the k_{-1} root accurately and the by shifting k_0 in small increments the initial guess can be taken from the previous iterations.

Moving on to the solution of section 5.2.1, one can see that there are two truncation parameters. The first is N_m which represents the number of modes taken to describe the free surface in the gap $x \in (-a, a)$ (actually is $2N_m$ Legendre polynomial modes as the problem is divided into symmetric and antisymmetric parts) and the second truncation parameter is the one for calculating the infinite integrals (N_i) or infinite sums (N_r). From now on the summation method will be used with $N_r = 1024$ as it is a much more computationally inexpensive technique than calcu-

a/d	2^{-10}	2^{-7}	2^{-5}	2^{-3}	2^{-1}	2^{0}	2^{1}	2^{2}	2^{3}	2^{4}
N_m	1	1	1	1	1	2	2	4	8	8

Table 5.1: Table showing number of modes N_m needed to get convergence (7 decimal places) for certain values of a/d. The results come from a variety of geometrical cases.

lating infinite integrals, to get the same level of accuracy (7 decimal places). The infinite sums are split into a sum over the k_{-2}, k_{-1}, k_0 roots and a truncated infinite sum over the imaginary root sequence k_n ($n \in \mathbb{N}$), so that a simplification of functions at purely imaginary evaluations is made for numerical stability. Depending on the gap size, a suitable N_m must be chosen to characterise the fluctuations of the free surface. A variety of geometrical cases was tested (reflection and transmission coefficients against wavenumber $k_0 d$) and the optimal N_m for each gap size a/d was found (see table 5.1).

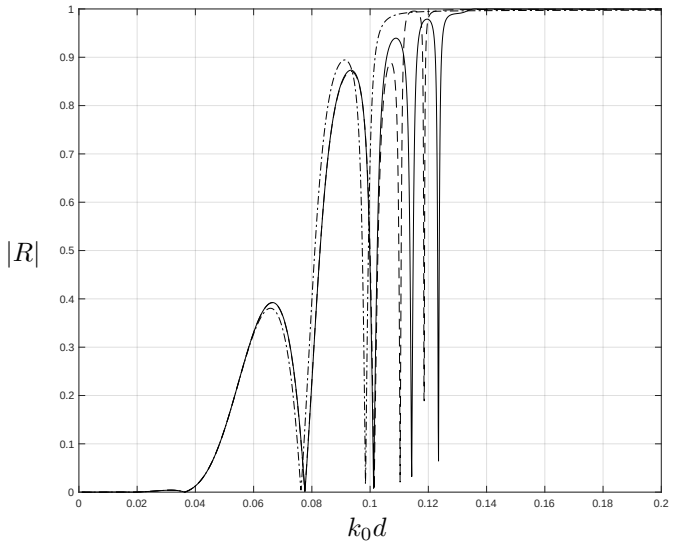

Figure 5.3: $|R|$ against $k_0 d$ for $(d, h/d, a/d, \theta_0) = (1, 40, 4, 45°)$ and number of modes $N_m = 1$ (chained), 2 (dashed), 4 (full).

An example of that is figure 5.3, where the reflection modulus $|R|$ is plotted against $k_0 d$ for gap size $a/d = 4$. One can see that as N_m increases, the number of spikes increases as well, but then at some point the curves converge. Some spikes do not touch the axis as larger resolution is required (this is a typical feature [40]). For example, if the gap is small ($a/d \leq 0.5$) then $N_m = 1$ is enough but for larger

gaps more modes are required. The values of N_m stated in the table 5.1, are the ones needed to get to the convergence of 7 decimal places for each a/d. Also, energy was accurately conserved at 8 decimal places, so there will be no need to plot both scattering coefficients as they are linked though $|R|^2 + |T|^2 = 1$. The typical features of total transmission for long waves (obstacle invisibility) and total reflection for short waves are verified as well.

Now a comparison with [40] will follow. They plotted their results on a different axis due to the way in which they chose to non-dimensionalise their problem from the outset. In order to make this conversion we need to plot $|R|$ against $\beta^{1/8}\sqrt{K}$ and take $h/d = a/d = (\beta^{1/4}/d)\pi/3$. The number of modes $N_m = 8$ is the optimal from the table above, as $a/d = (\beta^{1/4}/d)\pi/3 \approx 15.3$ for $d = 1$. The oblique incidence of $\theta_0 = 60^\circ$ makes the curve in figure 5.4 to look like their figure 2(d), even though their solution method is different (the residue calculus technique).

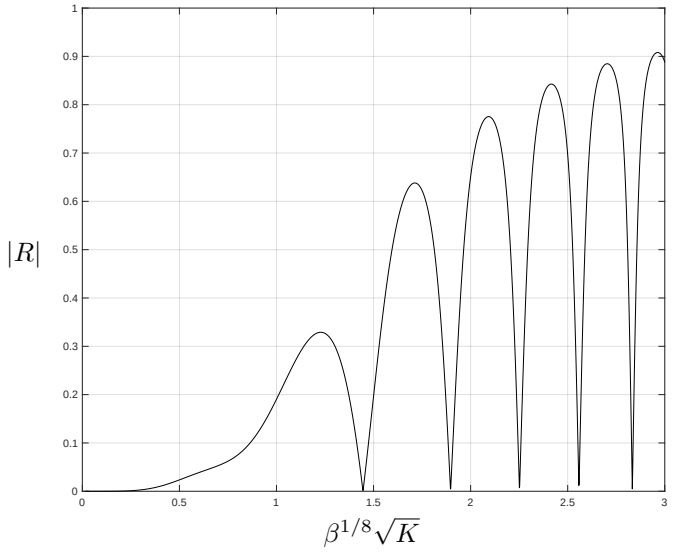

Figure 5.4: $|R|$ against $\beta^{1/8}\sqrt{K}$ for parameters $(N_m, d, \theta_0) = (8, 1, 60^\circ)$ and $h/d = a/d = (\beta^{1/4}/d)\pi/3$.

Now a comparison between the solutions of section 5.2.1 and 5.2.2 will be made by plotting $|R|$ curves against $k_0 d$ for a decreasing sequence of gap sizes (figure 5.5). Only one mode is taken ($N_m = 1$) as it can be verified from the table 5.1 that is enough for $a/d < 1$ and the rest variables were chosen to be $h/d = 30$, $\theta_0 = 30^\circ$ and a smaller ice thickness of $d = 0.69462$ to produce the value of $\beta/d^4 \approx 65555$. The typical behaviour of the solution in the long and short wave limit happens in all cases

(total transmission and reflection respectively). The "finite gap" curves converge to the small crack approximation solution (5.2.59), (5.2.71) (which is identical to the "zero gap" solution of [46] in the limit $a/d \to 0$). As the gap size decreases, the spikes are shifted to the right. However, even though the small crack approximation comes from taking the limit $a/d \to 0$ in the "finite gap" problem the numerical results converge to each other very gradually with a/d for larger $k_0 d$. Nevertheless, we developed a method which only needs one term in the symmetric and antisymmetric solution when a/d is small but not zero. So, this is numerically efficient compared to [40] who need to increase the number of terms in their numerical scheme as a/d tends to zero. Comparisons between the approximated solution of the previous section and the work of other authors will follow later. The solution of the small crack approximation satisfies energy conservation again as expected from the previous section ($|R^{s,a}| = 1$ analytically).

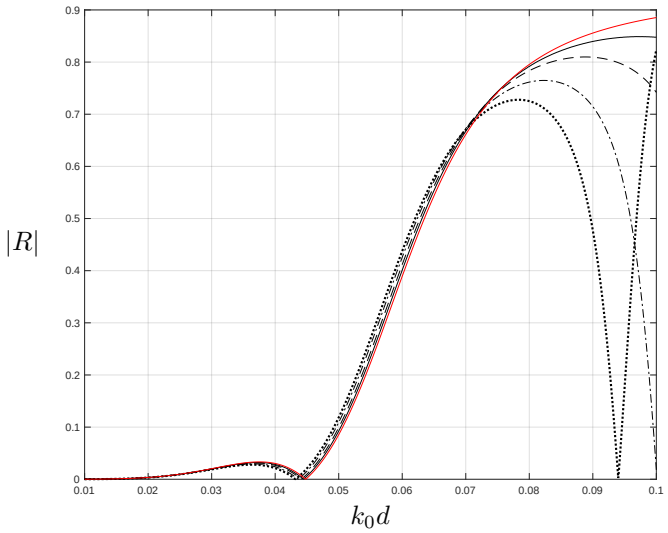

Figure 5.5: $|R|$ against $k_0 d$ with $(N_m, d, h/d, \theta_0) = (1, 0.69462, 30, 30°)$ for $a/d = 0.9$ (dotted), 0.7 (chained), 0.4 (dashed), 0.2 (full) and small crack approximation (red).

Moving on to the last two figures, one can see the variation of $|R|$ with the incident wave period in 5.6(i) and the variation of $|T|$ with the incident direction θ_0 in 5.6(ii). In the first, we see an analogue (normally incident) plot of [42] which is verified three years later by [46]. However, [42] used infinite depth and [46] finite and larger than the one used here ($h/d = 80$ for all ice thicknesses). But it is clear from 5.6(i) that $h/d = 40$ is sufficient to replicate infinite depth to a good degree of

accuracy (by graphical inspection). Note that $h = 40d$ corresponds to $h = 20$, 40, 80 for $d = 0.5$, 1, 2.

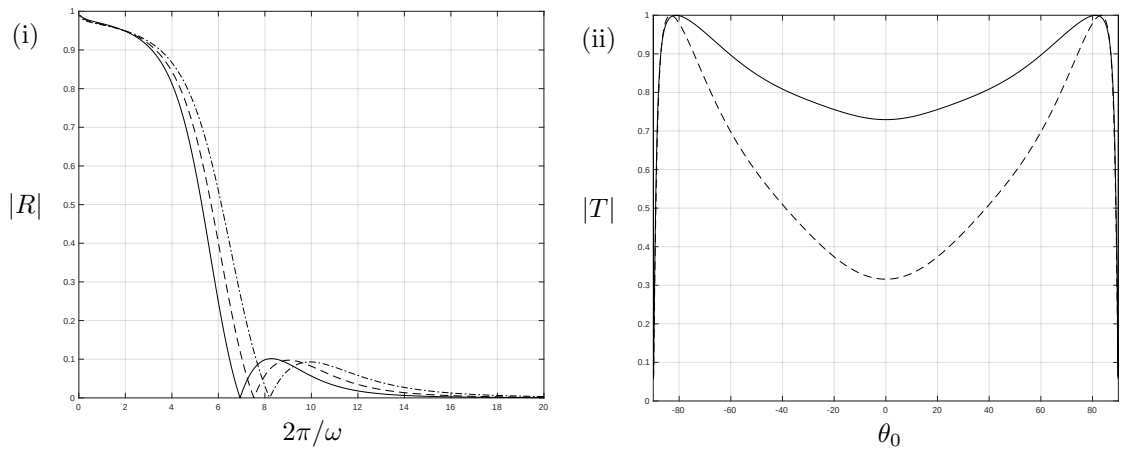

Figure 5.6: (i) $|R|$ against wave period for ice thicknesses $d = 0.5$ (chained), 1 (dashed), 2 (full) and (ii) $|T|$ against θ_0 with $d = 1$ and $k_0 d = 0.1168$ (dashed), 0.0736 (full). The common variables are $\beta/d^4 = 45536/d$ and $h/d = 40$.

Next for figure 5.6(ii), the $k_0 d$ values were chosen in a way to produce a wave period of 2 and 5 which are the ones used by [43] (extension of [42] to oblique incidence). The remarkable result in figure 5.6(ii), shows that the solution analysed here matches theirs even though their solution technique is much different (Green's function method). The solution is always even in θ_0 as expected from physical grounds. This can also be verified from the theory as all α_0 dependence comes only in even powers (inside sums or within β_r). Also, the crack has a minimal effect on long waves as when $k_0 d \to 0$, $|T| \to 1$. This phenomenon was verified again by [46]. Overall, the results of this section are well known as these two problems (crack of finite and small width) were solved in the past by many authors with different methods.

5.3 Small crack filled with viscous fluid

5.3.1 New ice conditions for normal incidence

In this section, two semi-infinite elastic ice sheets of density ρ_i and thickness d are separated by a small distance $2a \ll d$. They float on top of the free surface of an incompressible and irrotational fluid of density ρ_w of finite depth. Cartesian coordinates are employed such that $x = \pm a$ are aligned with the vertical faces of the static ice sheets and $z = 0$ is aligned with their lower horizontal interfaces. The interface $z = 0$ now does not coincide with the one of the problem defined in section 5.1 i.e. midplane of the ice sheet. However due to the linearisation assumption $d \ll \lambda_0$, at the end all conditions will be evaluated on the same level as before. The flat sea bed is located at $z = -h$. The fluid within $|x| < a$ and $z > 0$ is assumed to have a non-zero viscosity μ and some density ρ. The Reynolds number for the flow in the crack is $\mathrm{Re} = \rho U l/\mu$, where U is the characteristic velocity, l is the lengthscale associated with the ice sheets spacing, μ is the dynamic viscosity and ρ is the viscous fluid density. Using $U = A\omega = 2\pi A/T$ where A and T are the wave amplitude and period with $A \sim \mathcal{O}(1\mathrm{m})$, $T \sim \mathcal{O}(10\mathrm{s})$, $\mu/\rho \sim \mathcal{O}(10^{-2}\mathrm{m}^2\mathrm{s}^{-1})$ and $l \sim \mathcal{O}(10^{-1}\mathrm{m})$, then $\mathrm{Re} \sim \mathcal{O}(1)$. The order of magnitude of μ/ρ was estimated from laboratory and field data to characterise the viscosity of a grease ice cover and a frazil-pancake ice field [2][54].

A normally incident flexural wave ($\theta_0 = 0^\circ$ and now the problem is two-dimensional) of wavenumber k_0, propagates from $x \to \infty$ towards the small crack. The propagating wave in $x > a$, sets in motion the viscous fluid within the crack and consequently causes scattering modes to the ice sheets. If the ice floes were at rest, then from the Archimedean principle their vertical faces would be wetted in the domain of $z \in (0, \delta)$ for $\delta = (\rho_i/\rho_w)d$. However, when the fluid surface is set into motion the surface elevation $\zeta(x,t)$ can be approximated by its average in x, i.e. $\overline{\zeta}(t) \approx \frac{1}{2a}\int_{-a}^{a}\zeta(x,t)dx$. This simplification is based on the one term approximation of the previous section which assumes that the vertical fluid velocity within a narrow crack, is comprised only by a constant term (symmetric) and a term proportional to x (antisymmetric). The antisymmetric term vanishes under integration over the symmetric interval $(-a, a)$. The same can be assumed for the surface elevation due to their linear relation (2.2.7). The vertical faces of the ice sheets have velocities $U^{\pm}$ and angular velocities $\Omega^{\pm}$ about their midpoints and they are assumed to be small in the sense $\Omega^{\pm}, U^{\pm}/d \ll \omega$ (where ω is the angular frequency of the fluid motion).

The small crack assumption $2a \ll d$, allows the application of lubrication

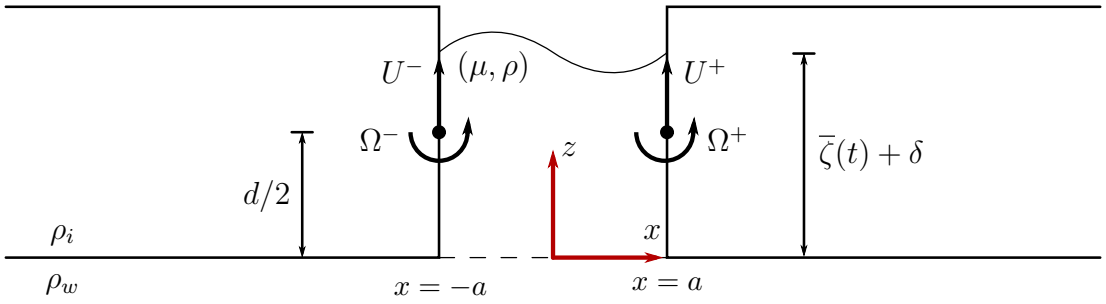

Figure 5.7: Geometric configuration of the thin, elastic, floating ice sheets separated by a small crack filled with a fluid of dynamic viscosity μ.

theory in $z > 0$ and the resulting equations are just the Stokes equations for a slow viscous flow under a rescaling of coordinates to bring out the contrast in lengthscales, as there is in the gap [56][88]. Namely,

$$\frac{\partial p}{\partial x} = 0, \quad \frac{\partial p}{\partial z} + \rho g = \mu \frac{\partial^2 w}{\partial x^2}, \tag{5.3.1}$$

where $w(x, z, t)$ is the vertical component of the fluid velocity $\mathbf{u}(x, z, t) = u\hat{\mathbf{x}} + w\hat{\mathbf{z}}$ and p is the pressure. The equations above are the two component of the momentum equation at leading order of a small parameter associated with the ratio a/d.

Moving back to the problem specified in figure 5.7, then it can be seen that the velocity of the vertical faces of the ice sheets at $x = \pm a$ is

$$\mathbf{U}^{\pm}_{vf}(z, t) = -\left(z - \frac{d}{2}\right)\Omega^{\pm}(t)\hat{\mathbf{x}} + U^{\pm}(t)\hat{\mathbf{z}}. \tag{5.3.2}$$

Solving the second equation of (5.3.1) by applying the no-slip conditions of the vertical walls, $\left[\mathbf{u}(\pm a, z, t) - \mathbf{U}^{\pm}_{vf}(z, t)\right] \cdot \hat{\mathbf{z}} = 0$, then

$$w(x, z, t) = \frac{x^2 - a^2}{2\mu}\Big[p_z(z, t) + \rho g\Big] + \frac{U^+(t) + U^-(t)}{2} + \frac{x}{a}\frac{U^+(t) - U^-(t)}{2}, \tag{5.3.3}$$

using (5.3.2) and the x independence of pressure from (5.3.1). Now by x-averaging in $(-a,a)$ the mass conservation $u_x + w_z = 0$ and then integrating in z, then

$$p_z(z,t) + \rho g = C(t) + \frac{3\mu}{2a^3}\frac{\Omega^+(t) - \Omega^-(t)}{2} z(d-z), \tag{5.3.4}$$

where $C(t)$ is a constant coming from the integration in z and after making use of $\big[\mathbf{u}(\pm a, z, t) - \mathbf{U}^{\pm}_{vf}(z,t)\big]\cdot \hat{\mathbf{x}} = 0$. Taking the average in x of equation (5.3.3), then

$$\overline{w}(z,t) = \frac{U^+(t) + U^-(t)}{2} - \frac{a^2}{3\mu}\Big[p_z(z,t) + \rho g\Big]. \tag{5.3.5}$$

Next, by writing explicitly the pressure gradient and the x-averaged vertical velocity from the last two equations by eliminating $C(t)$ (by evaluating the pressure gradient at $z = 0$), then

$$\begin{aligned} p_z(z,t) + \rho g &= \frac{3\mu}{a^2}\left[\frac{U^+(t) + U^-(t)}{2} - \overline{w}(0,t) + \frac{1}{2a}\frac{\Omega^+(t) - \Omega^-(t)}{2} z(d-z)\right], \\ \overline{w}(z,t) &= \overline{w}(0,t) - \frac{1}{2a}\frac{\Omega^+(t) - \Omega^-(t)}{2} z(d-z). \end{aligned} \tag{5.3.6}$$

Integrating the pressure gradient equation above, with respect to z in $(z, \overline{\zeta}(t) + \delta)$ using that the pressure evaluated at the upper integration limit is p_{atm}, then

$$\begin{aligned} p(z,t) = p_{atm} &+ \rho g\left[\overline{\zeta}(t) + \delta - z\right] + \frac{3\mu}{a^2}\left[\overline{w}(0,t) - \frac{U^+(t) + U^-(t)}{2}\right](\delta - z) \\ &- \frac{\mu}{4a^3}\frac{\Omega^+(t) - \Omega^-(t)}{2}\Big[\delta^2(3d - 2\delta) - z^2(3d - 2z)\Big], \end{aligned} \tag{5.3.7}$$

after neglecting products of time dependent terms. Balancing pressures at $z = 0$

using that the pressure in $z<0$ is $p(x,z,t)=p_{atm}+\rho_i g d-\rho_w\Phi_t(x,z,t)-\rho_w g z$, then

$$\begin{aligned}\rho\Phi_t(x,0,t)+\rho g\overline{\zeta}(t)+\frac{3\mu\delta}{a^2}\left(\overline{w}(0,t)-\frac{U^+(t)+U^-(t)}{2}\right)\\ -\frac{\mu\delta^2}{4a^3}(3d-2\delta)\frac{\Omega^+(t)-\Omega^-(t)}{2}=0,\end{aligned}\tag{5.3.8}$$

after using that the fluid density at the interface $z=0$ is ρ. The x-averaged elevation $\overline{\zeta}(t)$ above, can be eliminated by taking a time derivative and making use the x-averaged version of the linear surface condition (2.2.7), namely $\overline{\zeta}_t(t)=\overline{w}\big(\overline{\zeta}(t)+\delta,t\big)\approx\overline{w}(0,t)-\frac{1}{2a}\frac{\Omega^+(t)-\Omega^-(t)}{2}\delta(d-\delta)$ by neglecting again products of motion terms. Therefore, the condition across the viscous fluid interface becomes

$$\begin{aligned}\rho\Phi_{tt}(x,0,t)+\rho g\left(\overline{w}(0,t)-\frac{1}{2a}\frac{\Omega^+(t)-\Omega^-(t)}{2}\delta(d-\delta)\right)\\ +\frac{3\mu\delta}{a^2}\left[\overline{w}(0,t)-\frac{U^+(t)+U^-(t)}{2}\right]_t-\frac{\mu\delta^2}{4a^3}(3d-2\delta)\left[\frac{\Omega^+(t)-\Omega^-(t)}{2}\right]_t=0.\end{aligned}\tag{5.3.9}$$

Now an expression for the fluid vertical velocity at $z=0$ will be given. Normally, the fluid vertical velocity on the surface is of the form $Ax+B$ after using the single term approximation from the previous section. But due to the linearisation condition $d\ll\lambda_0$, then the same approximation can be used in the fluid vertical velocity at $z=0$. Therefore, $\Phi_z(x,0,t)$ is chosen to be

$$\Phi_z(x,0,t)=\overline{w}(0,t)+\frac{x}{a}\frac{U^+(t)-U^-(t)}{2}.\tag{5.3.10}$$

This guess suggests that the flow through the small crack at $z=0$, can be written as a sum of a plug flow and a shear flow. The plug flow $\overline{w}(0,t)$ was chosen such that the equation above is satisfied under x-averaging. The antisymmetric term in the right-hand side of the equation above (term proportional to x), is chosen such that when the vertical faces are synchronised (in the case of $U^+(t)=U^-(t)$), the shear flow contribution vanishes. Therefore, by eliminating $\overline{w}(0,t)$ from (5.3.9) using

(5.3.10), then

$$\begin{aligned} K\phi(x,0) &= (1-3i\tau)\phi_z(x,0) - (1-3i\tau)\frac{x}{a}\frac{U^+-U^-}{2} \\ &+3i\tau\frac{U^++U^-}{2} - \frac{\delta}{2a}\Big[d-\delta-\frac{i\tau}{2}(3d-2\delta)\Big]\frac{\Omega^+-\Omega^-}{2}, \end{aligned} \tag{5.3.11}$$

for $K=\omega^2/g$, $\tau=\mu\delta\omega/\rho g a^2$ after writing the condition in the frequency domain through $\Phi(x,z,t)=\Re\{\phi(x,z)e^{-i\omega t}\}$. Note that now $U^\pm$ and $\Omega^\pm$ are independent of time. Also, when the viscosity is switched off (setting $\mu=0$), the condition becomes $\big(\partial_z-K\big)\phi(x,0)=\frac{x}{a}\frac{U^+-U^-}{2}+\frac{\delta}{2a}(d-\delta)\frac{\Omega^+-\Omega^-}{2}$, where the left-hand side includes the usual linear terms from inviscid theory. The right-hand side express the sum of a flux term (which has zero average over the crack) and a term coming from the rotation of the vertical faces of the ice sheets. This condition is based on the assumption that the pressures and fluxes are matched at the interface between the viscous and inviscid flows. Although this is a fair assumption, one should have a local solution in the vicinity of the matching region in which the matching conditions should be derived precisely.

The analogue conditions for the bending moments and shearing stresses at the edges of the ice floes found in equation (5.1.8), will be affected as well. First $\alpha_0=0$ should be used in their left-hand sides (as the propagating wave is normally incident) and their right-hand sides will no longer be zero due to the moments and stresses exerted from the viscous fluid onto the vertical faces of the ice sheets. The formulas of these exerted moments and stresses should be calculated separately.

Back in the time domain, $\theta^\pm(t)$ are defined to be the angles between the rotated vertical faces of the ice sheets (at $x=\pm a$) and the z-axis (measured counterclockwise). The unit normal vectors to the rotated faces pointing onto each ice sheet, are found to be $\hat{\mathbf{n}}^\pm=\pm\big[\cos\theta^\pm(t),0,\sin\theta^\pm(t)\big]$ in the (x,y,z) coordinates, where y is the coordinate perpendicular to both x and z. Then the vertical faces moment vector $\mathbf{M}^\pm(t)=\big[M_x^\pm(t),M_y^\pm(t),M_z^\pm(t)\big]$ (where the components represent the bending moments in all directions), is defined to be

$$\mathbf{M}^\pm(t)=\int\limits_{z_0^\pm(t)}^{\zeta(\pm a,t)+\delta}\mathbf{r}^\pm(z,t)\times\Big[\tilde{\boldsymbol{\sigma}}(\pm a,z,t)\hat{\mathbf{n}}^\pm(t)\Big]dz, \tag{5.3.12}$$

where the stress tensor is defined as $\tilde{\boldsymbol{\sigma}} = -\tilde{p}\mathbf{I} + \mu\big[(\nabla\mathbf{u}) + (\nabla\mathbf{u})^T\big]$ with $\mathbf{I}$ be the 3×3 identity matrix and $\mathbf{u} = u\hat{\mathbf{x}} + w\hat{\mathbf{z}}$ be the viscous fluid velocity. Here $\tilde{p}$ is the non-hydrostatic pressure of the viscous fluid (includes only dynamical terms or small motion terms) given by $\tilde{p}(z,t) = p(z,t) - p_{atm} - \rho g(\delta - z)$ with p defined in (5.3.7). Note that $\tilde{p}$ is independent of x from lubrication theory. The integration region is the wetted surface of the vertical faces (with $z_0^{\pm}$ be the moving lower corners) and $\mathbf{r}^{\pm}$ is the relative position of any point on the vertical faces from the pivot which can be found by rotating the vector $\big(0,0,z-d/2\big)^T$ counterclockwise by an angle $\theta^{\pm}(t)$.

Namely,

$$\mathbf{r}^{\pm}(z,t) = \begin{pmatrix} \cos\theta^{\pm} & 0 & -\sin\theta^{\pm} \\ 0 & 1 & 0 \\ \sin\theta^{\pm} & 0 & \cos\theta^{\pm} \end{pmatrix} \begin{pmatrix} 0 \\ 0 \\ z-\frac{d}{2} \end{pmatrix} = \Big(z-\frac{d}{2}\Big) \begin{pmatrix} -\sin\theta^{\pm} \\ 0 \\ \cos\theta^{\pm} \end{pmatrix}. \tag{5.3.13}$$

Using the result above, then the integrant of (5.3.12) becomes

$$\begin{gathered} \mathbf{r}^{\pm}(z,t) \times \Big[\tilde{\boldsymbol{\sigma}}(x,z,t)\hat{\mathbf{n}}^{\pm}(t)\Big] = \\ \pm\Big(z-\frac{d}{2}\Big)\Big[-\tilde{p}(z,t) + 2\mu\Big(u_x\cos^2\theta^{\pm} + w_z\sin^2\theta^{\pm} + (u_z+w_x)\sin\theta^{\pm}\cos\theta^{\pm}\Big)\Big]\hat{\mathbf{y}}, \end{gathered} \tag{5.3.14}$$

after a considerable algebra. The next step is to evaluate it at $x = \pm a$. First one could see that $u_x(\pm a,z,t) = w_z(\pm a,z,t) = 0$ from (5.3.3) and the mass conservation law. Using again the equation (5.3.3) with the pressure gradient from (5.3.6), then

$$\begin{aligned} w_x(\pm a,z,t) = \pm\frac{3}{a}\Bigg[\frac{U^+(t)+U^-(t)}{2} - \overline{w}(0,t) + \frac{1}{2a}z(d-z)\frac{\Omega^+(t)-\Omega^-(t)}{2}\Bigg] \\ + \frac{1}{a}\frac{U^+(t)-U^-(t)}{2}, \end{aligned} \tag{5.3.15}$$

which can be seen that is proportional to time dependent terms only. Since w_x from equation (5.3.14) is proportional to $\sin\theta^{\pm}\cos\theta^{\pm} \approx \theta^{\pm}$ (using that $|\theta^{\pm}| \ll 1$), then its contribution at the boundaries $x = \pm a$ can be neglected (product of motion terms). Also one could see that $u_z(\pm a,z,t) = -\Omega^{\pm}(t)$ straight from the boundary condition $\big[\mathbf{u}(\pm a,z,t) - \mathbf{U}_{vf}^{\pm}(z,t)\big]\cdot\hat{\mathbf{x}} = 0$. Alternatively one could find a general solution for

u by integrating the mass conservation law with respect to x. Then by applying the same boundary condition to find the particular solution of u and by taking a z-derivative, the same result yields i.e. $u_z(\pm a, z, t) = -\Omega^{\pm}(t)$. Now since u_z is proportional to motion terms only on the boundaries $x = \pm a$, then its contibution can be neglected (as it is multiplied by $\sin\theta^{\pm}\cos\theta^{\pm} \approx \theta^{\pm}$ again).

Using the results above in the moment vector defined in (5.3.12), then it can be seen that $M_x^{\pm} = M_z^{\pm} = 0$, with

$$M_y^{\pm}(t) \approx \mp \int_0^{\delta} \tilde{p}(z,t)\left(z - \frac{d}{2}\right)dz, \tag{5.3.16}$$

where the time dependent terms in the integration limits were neglected due to the dynamic behaviour of $\tilde{p}$ (products of motion terms are assumed to be small). It is known from intuition that if a positive pressure is applied on the lower halves of the vertical faces then M_y^+ should be positive and M_y^- negative. This is compatible with the result found in the previous equation. But if $M_y^+ > 0$, then $D\zeta_{xx}(a^+, t) > 0$ from the local plate curvature at the edge, where D is the flexural rigidity. Similarly if $M_y^- < 0$, then $D\zeta_{xx}(-a^-, t) > 0$ (as $D\zeta_{xx}$ represents the local moment on the ice sheet). So by balancing moments carefully at each vertical face, then

$$\pm\, D\zeta_{xx}(\pm a^{\pm}, t) = M_y^{\pm}(t) = \mp \int_0^{\delta} \tilde{p}(z,t)\left(z - \frac{d}{2}\right)dz, \tag{5.3.17}$$

and by evaluating the non-hydrostatic pressure $\tilde{p}$ with p defined in (5.3.7), then

$$\begin{aligned} D\zeta_{xx}(\pm a^{\pm}, t) = -\int_0^{\delta} \tilde{p}(z,t)\left(z - \frac{d}{2}\right)dz &= \frac{\rho g \delta}{2}(d-\delta)\overline{\zeta}(t) \\ &+ \frac{\mu\delta^2}{4a^2}(3d - 2\delta)\Big[\overline{w}(0,t) - \frac{U^+(t) + U^-(t)}{2}\Big] \\ &- \frac{\mu\delta^3}{40a^3}(10d^2 - 15\delta d + 6\delta^2)\frac{\Omega^+(t) - \Omega^-(t)}{2}. \end{aligned} \tag{5.3.18}$$

Note that by taking a time derivative of the equation above, the left-hand side becomes $D\Phi_{xxz}(\pm a^{\pm}, 0, t)$ from the linearised surface condition. Also, $\overline{\zeta}_t$ should be eliminated in the same way as in (5.3.9). Therefore the moment balance equation above, written in the frequency domain due to the assumption of time harmonicity of the incident wave, becomes

$$\begin{aligned}\beta\phi_{xxz}(\pm a^{\pm}, 0) = \frac{\delta}{2}\Big[d - \delta - \frac{i\tau}{2}(3d - 2\delta)\Big]\overline{w}(0) + \frac{i\delta\tau}{4}(3d - 2\delta)\frac{U^+ + U^-}{2} \\ -\frac{\delta^2}{4a}\Big[(d-\delta)^2 - \frac{i\tau}{10}(10d^2 - 15\delta d + 6\delta^2)\Big]\frac{\Omega^+ - \Omega^-}{2}.\end{aligned} \tag{5.3.19}$$

Moving into the calculation of the shear stress exerted from the viscous fluid on the vertical faces of the ice sheets, then the following formula is considered

$$S^{\pm}(t) = -\mathbf{z}^T \int_{z_0^{\pm}(t)}^{\zeta(\pm a, t)+\delta} \tilde{\boldsymbol{\sigma}}(\pm a^{\pm}, z, t)\hat{\mathbf{n}}^{\pm}(t)dz. \tag{5.3.20}$$

After some calculations, the matrix-vectors product above becomes

$$-\mathbf{z}^T\tilde{\boldsymbol{\sigma}}(\pm a^{\pm}, z, t)\hat{\mathbf{n}}^{\pm}(t) \approx \pm\mu\Omega^{\pm}(t) \mp \mu w_x(\pm a^{\pm}, z, t), \tag{5.3.21}$$

after using that $|\theta^{\pm}| \ll 1$ and neglecting the products of motion terms. Also, $w_z(\pm a, z, t) = 0$ and $u_z(\pm a, z, t) = -\Omega^{\pm}(t)$ were used from the calculations after equation (5.3.14). One could see from equation (5.3.15) that $w_x(\pm a, z, t)$ is proportional only to motion terms. Therefore, the integration limits of (5.3.20) can be reduced to $(0, \delta)$. Thus, the shear stresses on the vertical faces are found to be

$$\begin{aligned}S^{\pm}(t) = \frac{3\mu\delta}{a}\left[\overline{w}(0,t) - \frac{U^+(t) + U^-(t)}{2}\right] - \frac{\mu\delta^2}{4a^2}(3d - 2\delta)\frac{\Omega^+(t) - \Omega^-(t)}{2} \\ \pm\mu\delta\Omega^{\pm}(t) \mp \frac{\mu\delta}{a}\frac{U^+(t) - U^-(t)}{2}.\end{aligned} \tag{5.3.22}$$

Now since the shear stress exerted by the fluid on the edges of the ice sheets is $D\frac{d}{dn}\zeta_{xx}(\pm a^{\pm},t) \equiv D\hat{\mathbf{n}}^{\pm}\cdot\nabla\zeta_{xx}(\pm a^{\pm},t) \approx \pm D\zeta_{xxx}(\pm a^{\pm},t)$ (using $|\theta^{\pm}| \ll 1$), then the stress balance becomes $\pm D\zeta_{xxx}(\pm a^{\pm},t) = S^{\pm}(t)$. Taking a time derivative of this condition to write it in terms of the velocity potential (instead of the surface elevation) then

$$\begin{aligned}\beta\phi_{xxxz}(\pm a^{\pm},0) = \pm 3ia\tau\left[\frac{U^{+}+U^{-}}{2} - \overline{w}(0)\right] \pm \frac{i\delta\tau}{4}(3d-2\delta)\frac{\Omega^{+}-\Omega^{-}}{2} \\ -ia^{2}\tau\Omega^{\pm} + ia\tau\frac{U^{+}-U^{-}}{2},\end{aligned} \tag{5.3.23}$$

in the frequency domain using the time harmonicity of the incident wave and making use of (5.3.22).

The modified surface condition over the ice-covered sea found in (5.3.11) and the moment and stress balance conditions on the ice sheet edges derived in (5.3.19) and (5.3.23) respectively, are all in terms of the new variables $U^{\pm}$, $\Omega^{\pm}$ and $\overline{w}(0)$. It will be explained in the next section how these variables will be chosen.

5.3.2 Solution to the problem

In this section, a semi-analytical solution to the scattering problem involving a small crack in an ice sheet filled with a viscous fluid is provided. Due to the limitations of the new conditions derived in the previous section, the incident wave of wavenumber k and angular frequency ω is assumed to propagate from $x \to \infty$ at normal incidence. Also the thin ice sheets float at a sea of finite depth. Therefore, the geometry of the problem is the same as the one of section 5.2.2, with the only differences be the existence of a viscous fluid within the small gap and the normal incidence of the propagated wave.

Since the geometry of the problem is symmetric by the yz-plane, then the velocity potential can be decomposed into even and odd parts. Therefore the governing equation for the potentials, the no flow condition at the bed and the conditions on the boundary $x = 0$ are

$$\nabla^{2}\phi^{s,a}(x,z) = 0, \quad \phi^{s,a}_{z}(x,-h) = 0, \quad \phi^{s}_{x}(0,z) = \phi^{a}(0,z) = 0, \tag{5.3.24}$$

according to equations (5.2.1), (5.2.2) and (5.2.4). Choosing the incident waves of each problem to be the ones defined in (5.2.8) then the far field condition is again (5.2.6) (where β_0 is replaced by k_0 as $\alpha_0 = 0$ from normal incidence) with $R^{s,a}$ found from (5.2.7). Also, the potentials must satisfy the standard condition in the region of the ice covered sea ($x > a$). Since this problem will be solved using Fourier cosine and sine transforms (for the symmetric and antisymmetric problems respectively), then the transformed version of the surface conditions (5.2.3) in $x > a$ become

$$\begin{aligned}
&\int_a^\infty \Big[\Big(\beta\partial_{xxxx} + 1 - K\delta\Big)\phi_z^s(x,0) - K\phi^s(x,0)\Big]\cos(\xi x)dx = 0,\\
&\int_a^\infty \Big[\Big(\beta\partial_{xxxx} + 1 - K\delta\Big)\phi_z^a(x,0) - K\phi^a(x,0)\Big]\sin(\xi x)dx = 0.
\end{aligned} \tag{5.3.25}$$

It remains to formulate the conditions at the surface in the gap and at the edges of the ice sheets. Note that these equations, namely (5.3.11), (5.3.19), (5.3.23), are in terms of the unknowns $U^\pm$, $\Omega^\pm$ and $\overline{w}(0)$. To eliminate them, first they must be related to the coefficients $P^{s,a} \equiv \phi_{xz}^{s,a}(a^+,0)$ and $Q^{s,a} \equiv \phi_z^{s,a}(a^+,0)$. Using that $\phi_{xz}(\pm a^\pm,0) = \Omega^\pm$ and $\phi_z(\pm a^\pm,0) = U^\pm$ by assuming the standard linearity condition (thin ice sheet) with $a \ll d$ and by writing $\phi^{s,a}$ in terms of ϕ (through the decomposition discussed above), then

$$P^s = \frac{\Omega^+ - \Omega^-}{2}, \quad Q^s = \frac{U^+ + U^-}{2}, \quad P^a = \frac{\Omega^+ + \Omega^-}{2}, \quad Q^a = \frac{U^+ - U^-}{2}. \tag{5.3.26}$$

Now starting from the integrated version of the surface condition of the symmetric potential in the "opening", it follows that

$$\begin{aligned}
&\int_0^a \Big[\phi_z^s(x,0) - K\phi^s(x,0)\Big]\cos(\xi x)dx = \Big(s_u^s C^s + s_P^s P^s + s_Q^s Q^s\Big)aj_0(a\xi),\\
&s_u^s = 3i\tau, \quad s_P^s = \frac{\delta}{2a}\left[d - \delta - \frac{i\tau}{2}(3d - 2\delta)\right], \quad s_Q^s = -3i\tau.
\end{aligned} \tag{5.3.27}$$

This condition is derived by starting from the left-hand side and writing the integral over $(0, a)$ as half the integral over $(-a, a)$ (as integrand is even). Then inside the $(-a, a)$ integral, ϕ^s can be replaced by ϕ as the odd ϕ^a gives no contribution over the symmetric integral. Thus, by substituting $\phi_z(x,0) - K\phi(x,0)$ from the "viscous" surface condition (5.3.11) and replacing ϕ with ϕ^s (for the same reason explained above) then the resulting integrand will consist of even and odd terms. Since the region of integration is symmetric, the odd terms have no contribution and the $(-a, a)$ integral over the remaining even terms can be written as twice the $(0, a)$ integral. Therefore by making use of $\phi^s_z(x,0) \approx C^s$ over the opening and equations (5.3.26) then the right-hand side yields. A similar procedure follows for the antisymmetric surface condition over the gap and the result gives

$$\int_0^a \left[\phi^a_z(x,0) - K\phi^a(x,0)\right] \sin(\xi x)dx = \left(s^a_u C^a + s^a_Q Q^a\right) a j_1(a\xi), \qquad (5.3.28)$$
$$s^a_u = 3i\tau, \quad s^a_Q = 1 - 3i\tau,$$

after using $\phi^a_z(x,0) \approx C^a x/a$ in $(0, a)$.

Proceeding to the ice sheet edge conditions for the symmetric and antisymmetric problem, the idea is to write $\beta\phi^{s,a}_{xxz}$ and $\beta\phi^{s,a}_{xxxz}$ in terms of the potential ϕ (note that depending on the number of x-derivatives the chain rule must be applied accordingly) and then making use of equations (5.3.19), (5.3.23). The only expression that needs to be written independently of the unknown variables $U^{\pm}$ and $\Omega^{\pm}$, is $\overline{w}(0)$. One can easily derive this expression by starting from equation (5.3.10) in the frequency domain, integrating it in $x \in (-a, a)$ to remove the odd parts and writing the $(-a, a)$ integral over the remaining even terms as two times the $(0, a)$ integral. Then using $\phi^s_z(x,0) \approx C^s$ in the gap, it follows that $\overline{w}(0) = C^s$. Using the ideas discussed here, then the ice sheet edge conditions for the symmetric and

antisymmetric problems, are

$$\phi^s_{xxz}(a^+,0) = e^{s,1}_u C^s + e^{s,1}_P P^s + e^{s,1}_Q Q^s, \quad \phi^s_{xxxz}(a^+,0) = e^{s,2}_u C^s + e^{s,2}_P P^s + e^{s,2}_Q Q^s,$$
$$\phi^a_{xxz}(a^+,0) = 0, \quad \phi^a_{xxxz}(a^+,0) = e^{a,2}_P P^a + e^{a,2}_Q Q^a, \quad \text{where}$$
$$e^{s,1}_u = \frac{\delta}{2\beta}\left[d-\delta-\frac{i\tau}{2}(3d-2\delta)\right], \quad e^{s,1}_P = -\frac{\delta^2}{4a\beta}\left[(d-\delta)^2-\frac{i\tau}{10}(10d^2-15\delta d+6\delta^2)\right],$$
$$e^{s,1}_Q = \frac{i\delta\tau}{4\beta}(3d-2\delta), \quad e^{s,2}_u = -\frac{3ia\tau}{\beta}, \quad e^{s,2}_P = \frac{i\tau}{\beta}\left[\frac{\delta}{4}(3d-2\delta)-a^2\right],$$
$$e^{s,2}_Q = \frac{3ia\tau}{\beta}, \quad e^{a,2}_P = -\frac{ia^2\tau}{\beta}, \quad e^{a,2}_Q = \frac{ia\tau}{\beta}. \tag{5.3.29}$$

Now the boundary value problem is fully described. Starting from the symmetric problem by defining the Fourier cosine transform (5.2.9), then the governing equation, the no flow condition at the bed and the surface condition become

$$\Big(\partial_{zz}-\xi^2\Big)\tilde{\phi}^s(\xi,z) = 0, \quad \tilde{\phi}^s_z(\xi,-h) = 0,$$
$$\int_a^\infty \left[\Big(\beta\partial_{xxxx}+1-K\delta\Big)\phi^s_z(x,0) - K\phi^s(x,0)\right]\cos(\xi x)dx = 0 \tag{5.3.30}$$
$$= \Big(\beta\xi^4+1-K\delta\Big)\int_0^\infty \frac{\partial\phi^s_{inc}}{\partial z}(x,0)\cos(\xi x)dx - K\int_0^\infty \phi^s_{inc}(x,0)\cos(\xi x)dx,$$

where in the second equality of the surface condition equation, (5.2.15) was used with $\alpha_0 = 0$ (normal incidence). Then, the left-hand side of the surface condition above is integrated by parts four times, to replace the ∂_{xxxx} by ξ^4 at the cost of adding some extra terms coming from the edge conditions (5.3.29) (and using that $P^s = \phi^s_{xz}(a^+,0)$ and $Q^s = \phi^s_z(a^+,0)$). Next by writing the (a,∞) integral of the left-hand side as the semi-infinite integral minus the $(0,a)$ integral and making use of the surface condition (5.3.27) over the gap, then the surface condition in the Fourier

space becomes

$$\begin{aligned}
&\Big(\beta\xi^4+1-K\delta\Big)\tilde{\phi}^s_z(\xi,0)-K\tilde{\phi}^s(\xi,0)=C^s f^s_0(\xi)+P^s f^s_1(\xi)+Q^s f^s_2(\xi),\\
&\text{for}\quad f^s_0(\xi)=\big(\beta\xi^4+s^s_u-K\delta\big)aj_0(a\xi)+\beta\xi e^{s,1}_u\sin(a\xi)+\beta e^{s,2}_u\cos(a\xi),\\
&\qquad f^s_1(\xi)=s^s_P aj_0(a\xi)+\beta\xi e^{s,1}_P\sin(a\xi)+\beta\big(e^{s,2}_P-\xi^2\big)\cos(a\xi),\\
&\qquad f^s_2(\xi)=s^s_Q aj_0(a\xi)+\beta\xi\big(e^{s,1}_Q-\xi^2\big)\sin(a\xi)+\beta e^{s,2}_Q\cos(a\xi).
\end{aligned}\tag{5.3.31}$$

Now the Fourier problem can be solved uniquely since the general solution of the first two equations of (5.3.30) is $\tilde{\phi}^s(\xi,z)=\tilde{A}^s(\xi)\cosh[\xi(z+h)]$ and $\tilde{A}^s(\xi)$ can be found from (5.3.31). Thus, by inverting the transform, the solution in the real space is

$$\phi^s(x,z)=\phi^s_{inc}(x,z)+\frac{2}{\pi}\int_0^\infty\frac{\cosh[\xi(z+h)]}{\Delta(\xi)\cosh(\xi h)}\Big[C^s f^s_0(\xi)+P^s f^s_1(\xi)+Q^s f^s_2(\xi)\Big]\cos(\xi x)d\xi \tag{5.3.32}$$

and by differentiating it with respect to z and set $z=0$, then

$$\begin{aligned}
&\phi^s_z(x,0)=k_0\cos(k_0x)\sinh(k_0h)+C^sF^s_0(x)+P^sF^s_1(x)+Q^sF^s_2(x),\\
&\text{for}\quad F^s_i(x)=\frac{2}{\pi}\int_0^\infty\frac{\xi\tanh(\xi h)}{\Delta(\xi)}f^s_i(\xi)\cos(\xi x)d\xi,\quad i=0,1,2.
\end{aligned}\tag{5.3.33}$$

Since the goal is to create a system for (P^s,Q^s), then C^s must be eliminated from the equation above. This will be done by multiplying with $P_0(x/a)=1$ and integrate in $x\in(0,a)$ (to remove the x-dependence), namely

$$C^s=\frac{P^s\tilde{F}^s_1+Q^s\tilde{F}^s_2+k_0j_0(k_0a)\sinh(k_0h)}{1-\tilde{F}^s_0}\ \text{for}\ \tilde{F}^s_i=\frac{2}{\pi}\int_0^\infty\frac{\xi\tanh(\xi h)}{\Delta(\xi)}f^s_i(\xi)j_0(a\xi)d\xi. \tag{5.3.34}$$

Using the equation above in (5.3.33) then the system for P^s and Q^s, can be created by

applying ∂_{xx} and ∂_{xxx} at $x = a^+$ and use (5.3.29). Thus, the linear system becomes

$$\begin{gathered}
\begin{pmatrix} \tilde{I}_0^s I_1^{s''} + \tilde{I}_1^s I_0^{s''} & \tilde{I}_0^s I_2^{s''} + \tilde{I}_2^s I_0^{s''} \\ \tilde{I}_0^s I_1^{s'''} + \tilde{I}_1^s I_0^{s'''} & \tilde{I}_0^s I_2^{s'''} + \tilde{I}_2^s I_0^{s'''} \end{pmatrix} \begin{pmatrix} P^s \\ Q^s \end{pmatrix} \\
= -k_0 \sinh(k_0 h) \begin{pmatrix} I_0^{s''} j_0(k_0 a) - \tilde{I}_0^s k_0^2 \cos(k_0 a) \\ I_0^{s'''} j_0(k_0 a) + \tilde{I}_0^s k_0^3 \sin(k_0 a) \end{pmatrix} \quad \text{where} \\
\tilde{I}_0^s = 1 - \tilde{F}_0^s, \quad \tilde{I}_i^s = \tilde{F}_i^s \quad \text{for} \quad i = 1, 2, \quad I_0^{s''} = F_0^{s''}(a^+) - e_u^{s,1}, \\
I_1^{s''} = F_1^{s''}(a^+) - e_P^{s,1}, \quad I_2^{s''} = F_2^{s''}(a^+) - e_Q^{s,1}, \quad I_0^{s'''} = F_0^{s'''}(a^+) - e_u^{s,2}, \\
I_1^{s'''} = F_1^{s'''}(a^+) - e_P^{s,2}, \quad I_2^{s'''} = F_2^{s'''}(a^+) - e_Q^{s,2},
\end{gathered} \tag{5.3.35}$$

where the nine integrals need to be written in a convergent form (like the two previous problems). The algebra here is much harder than the previous problems. Starting from the $\tilde{I}_i^s$ formulas, then

$$\begin{aligned}
\tilde{I}_0^s &= -\frac{2\beta}{\pi} e_u^{s,1} \int_0^\infty \frac{\xi^2 \tanh(\xi h)}{\Delta(\xi)} j_0(a\xi) \sin(a\xi) d\xi - \frac{2\beta}{\pi} e_u^{s,2} \int_0^\infty \frac{\xi \tanh(\xi h)}{\Delta(\xi)} j_0(a\xi) \cos(a\xi) d\xi \\
&\quad - \frac{2a}{\pi} \int_0^\infty \frac{K - (1 - s_u^s)\xi \tanh(\xi h)}{\Delta(\xi)} j_0^2(a\xi) d\xi, \\
\tilde{I}_1^s &= \frac{2\beta}{\pi} e_P^{s,2} \int_0^\infty \frac{\xi \tanh(\xi h)}{\Delta(\xi)} j_0(a\xi) \cos(a\xi) d\xi - \frac{2\beta}{\pi} \int_0^\infty \frac{\xi^3 \tanh(\xi h)}{\Delta(\xi)} j_0(a\xi) \cos(a\xi) d\xi \\
&\quad + \frac{2\beta}{\pi} e_P^{s,1} \int_0^\infty \frac{\xi^2 \tanh(\xi h)}{\Delta(\xi)} j_0(a\xi) \sin(a\xi) d\xi + \frac{2a}{\pi} s_P^s \int_0^\infty \frac{\xi \tanh(\xi h)}{\Delta(\xi)} j_0^2(a\xi) d\xi, \\
\tilde{I}_2^s &= \frac{2\beta}{\pi} e_Q^{s,1} \int_0^\infty \frac{\xi^2 \tanh(\xi h)}{\Delta(\xi)} j_0(a\xi) \sin(a\xi) d\xi - 1 + \frac{2}{\pi} \int_0^\infty \frac{E(\xi)}{\xi \Delta(\xi)} j_0(a\xi) \sin(a\xi) d\xi \\
&\quad + \frac{2\beta}{\pi} e_Q^{s,2} \int_0^\infty \frac{\xi \tanh(\xi h)}{\Delta(\xi)} j_0(a\xi) \cos(a\xi) d\xi + \frac{2a}{\pi} s_Q^s \int_0^\infty \frac{\xi \tanh(\xi h)}{\Delta(\xi)} j_0^2(a\xi) d\xi,
\end{aligned} \tag{5.3.36}$$

where $E(\xi) = (1 - K\delta)\xi \tanh(\xi h) - K$, by using the ice-covered sea dispersion relation.

Also, the formulas $\int_0^\infty j_0^2(a\xi)d\xi = \pi/2a$ and $\int_0^\infty j_0(a\xi)\sin(a\xi)/\xi d\xi = \pi/2$ were used in the integrals above. Moving on to the next set of integrals that involve the second derivatives of the functionals, then

$$
\begin{aligned}
I_0^{s''} &= -\frac{2a}{\pi}\int_0^\infty \frac{K-(1-s_u^s)\xi\tanh(\xi h)}{\Delta(\xi)}\xi^2 j_0(a\xi)\cos(a\xi)d\xi - \frac{3}{2}e_u^{s,1} \\
&+\frac{1}{\pi}e_u^{s,1}\int_0^\infty \frac{E(\xi)}{\xi\Delta(\xi)}\sin(2a\xi)d\xi - \frac{2\beta}{\pi}e_u^{s,2}\int_0^\infty \frac{\xi^3\tanh(\xi h)}{\Delta(\xi)}\cos^2(a\xi)d\xi, \\
I_1^{s''} &= -\frac{2a}{\pi}s_P^s\int_0^\infty \frac{\xi^3\tanh(\xi h)}{\Delta(\xi)}j_0(a\xi)\cos(a\xi)d\xi + \frac{1}{\pi}e_P^{s,1}\int_0^\infty \frac{E(\xi)}{\xi\Delta(\xi)}\sin(2a\xi)d\xi \\
&-\frac{3}{2}e_P^{s,1} - \frac{2\beta}{\pi}e_P^{s,2}\int_0^\infty \frac{\xi^3\tanh(\xi h)}{\Delta(\xi)}\cos^2(a\xi)d\xi - \frac{2}{\pi}\int_0^\infty \frac{E(\xi)}{\Delta(\xi)}\cos^2(a\xi)d\xi, \\
I_2^{s''} &= -\frac{2a}{\pi}s_Q^s\int_0^\infty \frac{\xi^3\tanh(\xi h)}{\Delta(\xi)}j_0(a\xi)\cos(a\xi)d\xi + \frac{1}{\pi}e_Q^{s,1}\int_0^\infty \frac{E(\xi)}{\xi\Delta(\xi)}\sin(2a\xi)d\xi \\
&-\frac{3}{2}e_Q^{s,1} - \frac{2\beta}{\pi}e_Q^{s,2}\int_0^\infty \frac{\xi^3\tanh(\xi h)}{\Delta(\xi)}\cos^2(a\xi)d\xi - \frac{1}{\pi}\int_0^\infty \frac{E(\xi)}{\Delta(\xi)}\xi\sin(2a\xi)d\xi.
\end{aligned}
\tag{5.3.37}
$$

To carry out the algebra used above, it is worth noting that before taking any derivative, first it is needed to make sure that the integral is convergent by making use of the dispersion relation. This is because after making use of the dispersion relation, then some constants (outside the integral with $\Delta(\xi)$ in its integrand) might rise from standard integrals such as $\int_0^\infty \sin(a\xi)/\xi d\xi$. These constants will disappear when taking the "next" derivative. Therefore, the strategy is to be careful every time a derivative is applied (by making sure that the integral at each step is convergent), instead of taking two derivatives from the beginning and then try to remove the divergence. Continuing to the next integrals that include the third derivatives of the

functionals, then

$$I_0^{s'''} = \frac{2a}{\beta\pi}(1-s_u^s)\int_0^\infty \frac{E(\xi)}{\xi\Delta(\xi)} j_0(a\xi)\sin(a\xi)d\xi + \frac{2aK}{\pi}\int_0^\infty \frac{\xi^3}{\Delta(\xi)} j_0(a\xi)\sin(a\xi)d\xi$$
$$-\frac{1}{\pi}e_u^{s,2}\int_0^\infty \frac{E(\xi)}{\xi\Delta(\xi)}\sin(2a\xi)d\xi - \frac{2}{\pi}e_u^{s,1}\int_0^\infty \frac{E(\xi)}{\Delta(\xi)}\sin^2(a\xi)d\xi - \frac{a}{\beta}(1-s_u^s) - \frac{1}{2}e_u^{s,2},$$
$$I_1^{s'''} = -\frac{2a}{\beta\pi}s_P^s\int_0^\infty \frac{E(\xi)}{\xi\Delta(\xi)} j_0(a\xi)\sin(a\xi)d\xi - \frac{1}{\pi}e_P^{s,2}\int_0^\infty \frac{E(\xi)}{\xi\Delta(\xi)}\sin(2a\xi)d\xi$$
$$+\frac{a}{\beta}s_P^s - \frac{1}{2}e_P^{s,2} - \frac{2}{\pi}e_P^{s,1}\int_0^\infty \frac{E(\xi)}{\Delta(\xi)}\sin^2(a\xi)d\xi + \frac{1}{\pi}\int_0^\infty \frac{E(\xi)}{\Delta(\xi)}\xi\sin(2a\xi)d\xi,$$
$$I_2^{s'''} = -\frac{2a}{\beta\pi}s_Q^s\int_0^\infty \frac{E(\xi)}{\xi\Delta(\xi)} j_0(a\xi)\sin(a\xi)d\xi - \frac{2}{\pi}e_Q^{s,1}\int_0^\infty \frac{E(\xi)}{\Delta(\xi)}\sin^2(a\xi)d\xi$$
$$+\frac{a}{\beta}s_Q^s - \frac{1}{2}e_Q^{s,2} + \frac{2}{\pi}\int_0^\infty \frac{E(\xi)}{\Delta(\xi)}\xi^2\sin^2(a\xi)d\xi - \frac{1}{\pi}e_Q^{s,2}\int_0^\infty \frac{E(\xi)}{\xi\Delta(\xi)}\sin(2a\xi)d\xi. \tag{5.3.38}$$

Now by using the nine integrals defined in the last three equations, then P^s and Q^s can be found from the linear system in (5.3.35). Later in the Appendix C.2, it will be shown how these integrals can be written as infinite sums (a numerically inexpensive method through truncation). Note that one could use the small a approximation to simplify this system and get closed-form solutions for P^s and Q^s and eventually R^s (as happened in the previous problem). The difference in this problem is that the extra nine (superscripted and subscripted) constants coming from the surface and edge conditions (5.3.27) and (5.3.29), include the dimensionless parameter τ which is proportional to a^{-2}. Therefore, it will be very hard to apply the small a approximation and neglect certain terms. Thus, this simplification will not be used and the solution to the problem will be sought through the complicated (but still explicit) formulas defined in the previous equations.

Using the known values of P^s and Q^s, then an expression for R^s can be derived by sending $x \to \infty$ in (5.3.32) and making use of the far field condition (5.2.6), the incident wave formula (5.2.8) and the C^s definition in (5.3.34). By carrying out

the same procedure used in (5.2.29), to calculate the semi-infinite integral then

$$\begin{aligned} R^s = 1 + \frac{4i}{\tilde{I}_0^s \Delta'(k_0)\cosh(k_0 h)} \Bigg\{ P^s \Big(\tilde{I}_0^s f_1^s(k_0) + \tilde{I}_1^s f_0^s(k_0) \Big) \\ + Q^s \Big(\tilde{I}_0^s f_2^s(k_0) + \tilde{I}_2^s f_0^s(k_0) \Big) + k_0 j_0(k_0 a)\sinh(k_0 h) f_0^s(k_0) \Bigg\}. \end{aligned} \tag{5.3.39}$$

It is expected that $|R^s| < 1$ for $\mu > 0$, due to energy loss. This will be verified numerically later as it is very hard to show this analytically.

Now for the antisymmetric problem, the analogue of (5.3.30) is

$$\begin{aligned} \Big(\partial_{zz} - \xi^2\Big)\tilde{\phi}^a(\xi, z) = 0, \quad \tilde{\phi}_z^a(\xi, -h) = 0, \\ \int_a^\infty \Big[\Big(\beta \partial_{xxxx} + 1 - K\delta\Big)\phi_z^a(x,0) - K\phi^a(x,0) \Big] \sin(\xi x) dx = 0 \\ = \Big(\beta\xi^4 + 1 - K\delta\Big) \int_0^\infty \frac{\partial \phi_{inc}^a}{\partial z}(x,0)\sin(\xi x)dx - K\int_0^\infty \phi_{inc}^a(x,0)\sin(\xi x)dx, \end{aligned} \tag{5.3.40}$$

by taking the Fourier sine transforms of the model equations. Carrying out the same long procedure as in the symmetric problem, the surface condition in the Fourier space becomes

$$\begin{aligned} \Big(\beta\xi^4 + 1 - K\delta\Big)\tilde{\phi}_z^a(\xi,0) - K\tilde{\phi}^a(\xi,0) = C^a f_0^a(\xi) + P^a f_1^a(\xi) + Q^a f_2^a(\xi), \\ \text{for} \quad f_0^a(\xi) = \big(\beta\xi^4 + s_u^a - K\delta\big) a j_1(a\xi), \quad f_1^a(\xi) = \beta\big(e_P^{a,2} - \xi^2\big)\sin(a\xi), \\ f_2^a(\xi) = s_Q^a a j_1(a\xi) + \beta e_Q^{a,2}\sin(a\xi) + \beta\xi^3\cos(a\xi). \end{aligned} \tag{5.3.41}$$

The general solution of the antisymmetric potential after applying the no flow condition at the bed is $\tilde{\phi}^a(\xi, z) = \tilde{A}^a(\xi)\cosh[\xi(z+h)]$, where the unknown function $\tilde{A}^a(\xi)$ can be found by using the surface equation above. Thus, by inverting the transform

the solution in the real space is given by

$$\phi^a(x,z) = \phi^a_{inc}(x,z) + \frac{2}{\pi}\int_0^\infty \frac{\cosh[\xi(z+h)]}{\Delta(\xi)\cosh(\xi h)}\Big[C^a f_0^a(\xi) + P^a f_1^a(\xi) + Q^a f_2^a(\xi)\Big]\sin(\xi x)d\xi. \tag{5.3.42}$$

Then to create a linear system for P^a and Q^a, the equation above is differentiated with respect to z and evaluated at $z = 0$, namely

$$\begin{aligned}\phi^a_z(x,0) &= -ik_0\sin(k_0x)\sinh(k_0h) + C^aF^a_0(x) + P^aF^a_1(x) + Q^aF^a_2(x),\\ \text{for}\quad F^a_i(x) &= \frac{2}{\pi}\int_0^\infty \frac{\xi\tanh(\xi h)}{\Delta(\xi)} f^a_i(\xi)\sin(\xi x)d\xi,\quad i=0,1,2.\end{aligned} \tag{5.3.43}$$

The third unknown C^a can be found from the equation above, by multiplying through x/a and then integrate with respect to $x \in (0,a)$ to remove the x-dependence. Using that $\phi^a_z(x,0) = C^a x/a$ in the opening $x \in (0,a)$, then C^a is found to be

$$C^a = \frac{P^a\tilde{F}^a_1 + Q^a\tilde{F}^a_2 - ik_0j_1(k_0a)\sinh(k_0h)}{\frac{1}{3} - \tilde{F}^a_0} \text{ for } \tilde{F}^a_i = \frac{2}{\pi}\int_0^\infty \frac{\xi\tanh(\xi h)}{\Delta(\xi)} f^a_i(\xi)j_1(a\xi)d\xi. \tag{5.3.44}$$

Creating the (P^a, Q^a) system by differentiating twice and thrice equation (5.3.43), then

$$\begin{aligned}&\begin{pmatrix}\tilde{I}^a_0 I^{a''}_1 + \tilde{I}^a_1 I^{a''}_0 & \tilde{I}^a_0 I^{a''}_2 + \tilde{I}^a_2 I^{a''}_0\\ \tilde{I}^a_0 I^{a'''}_1 + \tilde{I}^a_1 I^{a'''}_0 & \tilde{I}^a_0 I^{a'''}_2 + \tilde{I}^a_2 I^{a'''}_0\end{pmatrix}\begin{pmatrix}P^a\\ Q^a\end{pmatrix}\\ &= ik_0\sinh(k_0h)\begin{pmatrix}I^{a''}_0 j_1(k_0a) - \tilde{I}^a_0 k_0^2\sin(k_0a)\\ I^{a'''}_0 j_1(k_0a) + \tilde{I}^a_0 k_0^3\cos(k_0a)\end{pmatrix},\\ &\text{for}\quad \tilde{I}^a_0 = \frac{1}{3} - \tilde{F}^a_0,\quad \tilde{I}^a_i = \tilde{F}^a_i \quad\text{for}\quad i=1,2,\\ &I^{a''}_i = F^{a''}_i(a^+)\quad\text{for}\quad i=0,1,2,\quad I^{a'''}_0 = F^{a'''}_0(a^+),\\ &I^{a'''}_1 = F^{a'''}_1(a^+) - e^{a,2}_P,\quad I^{a'''}_2 = F^{a'''}_2(a^+) - e^{a,2}_Q,\end{aligned} \tag{5.3.45}$$

where the first three (x-averaged) integrals are calculated as

$$\begin{aligned}
\tilde{I}_0^a &= -\frac{2a}{\pi}\int_0^\infty \frac{K-(1-s_u^a)\xi\tanh(\xi h)}{\Delta(\xi)} j_1^2(a\xi)d\xi,\\
\tilde{I}_1^a &= \frac{2\beta}{\pi}\int_0^\infty \frac{\xi\tanh(\xi h)}{\Delta(\xi)}\left(e_P^{a,2}-\xi^2\right)\sin(a\xi)j_1(a\xi)d\xi,\\
\tilde{I}_2^a &= \frac{2a}{\pi}s_Q^a\int_0^\infty \frac{\xi\tanh(\xi h)}{\Delta(\xi)} j_1^2(a\xi)d\xi - \frac{2}{\pi}\int_0^\infty \frac{E(\xi)}{\xi\Delta(\xi)} j_1(a\xi)\cos(a\xi)d\xi\\
&\quad +\frac{2\beta}{\pi}e_Q^{a,2}\int_0^\infty \frac{\xi\tanh(\xi h)}{\Delta(\xi)} j_1(a\xi)\sin(a\xi)d\xi,
\end{aligned} \tag{5.3.46}$$

with the formulas $\int_0^\infty j_1^2(a\xi)d\xi = \pi/6a$ and $\int_0^\infty j_1(a\xi)\cos(a\xi)/\xi d\xi = 0$ being used. The formulas now seem to be simpler than the ones of the symmetric problem and this is due to the simpler expressions of $f_0^a(\xi)$ and $f_1^a(\xi)$ (single term formulas). The reason behind this simplification is that instead of having nine constants in the water surface and edge conditions (as in the symmetric problem), now there are only four

- see equations (5.3.28) and (5.3.29). Moving on to the next six integrals, then

$$I_0^{a''} = -\frac{2a}{\pi} \int_0^\infty \frac{K - (1 - s_u^a)\xi \tanh(\xi h)}{\Delta(\xi)} \xi^2 j_1(a\xi) \sin(a\xi) d\xi,$$

$$I_1^{a''} = -\frac{2\beta}{\pi} e_P^{a,2} \int_0^\infty \frac{\xi^3 \tanh(\xi h)}{\Delta(\xi)} \sin^2(a\xi) d\xi - \frac{2}{\pi} \int_0^\infty \frac{E(\xi)}{\Delta(\xi)} \sin^2(a\xi) d\xi,$$

$$I_2^{a''} = -\frac{2a}{\pi} s_Q^a \int_0^\infty \frac{\xi^3 \tanh(\xi h)}{\Delta(\xi)} j_1(a\xi) \sin(a\xi) d\xi + \frac{1}{\pi} \int_0^\infty \frac{E(\xi)}{\Delta(\xi)} \xi \sin(2a\xi) d\xi$$
$$- \frac{2\beta}{\pi} e_Q^{a,2} \int_0^\infty \frac{\xi^3 \tanh(\xi h)}{\Delta(\xi)} \sin^2(a\xi) d\xi,$$

$$I_0^{a'''} = -\frac{2a}{\beta\pi}(1 - s_u^a) \int_0^\infty \frac{E(\xi)}{\xi\Delta(\xi)} j_1(a\xi) \cos(a\xi) d\xi - \frac{2aK}{\pi} \int_0^\infty \frac{\xi^3}{\Delta(\xi)} j_1(a\xi) \cos(a\xi) d\xi,$$

$$I_1^{a'''} = \frac{1}{\pi} e_P^{a,2} \int_0^\infty \frac{E(\xi)}{\xi\Delta(\xi)} \sin(2a\xi) d\xi - \frac{1}{\pi} \int_0^\infty \frac{E(\xi)}{\Delta(\xi)} \xi \sin(2a\xi) d\xi - \frac{3}{2} e_P^{a,2},$$

$$I_2^{a'''} = \frac{2}{\pi} \int_0^\infty \frac{E(\xi)}{\Delta(\xi)} \xi^2 \cos^2(a\xi) d\xi + \frac{1}{\pi} e_Q^{a,2} \int_0^\infty \frac{E(\xi)}{\xi\Delta(\xi)} \sin(2a\xi) d\xi$$
$$+ \frac{2a}{\beta\pi} s_Q^a \int_0^\infty \frac{E(\xi)}{\xi\Delta(\xi)} j_1(a\xi) \cos(a\xi) d\xi - \frac{3}{2} e_Q^{a,2}. \tag{5.3.47}$$

Now all the tools needed for the calculation of P^a and Q^a from (5.3.45), are derived in the last two equations. Using their known values, the derivation of the R^a expression starts by taking $x \to \infty$ in (5.3.42) using C^a from (5.3.44). Following a

similar procedure as in the symmetric problem, then

$$R^a = -1 + \frac{4}{\tilde{I}_0^a \Delta'(k_0)\cosh(k_0 h)} \Bigg\{ P^a \Big(\tilde{I}_0^a f_1^a(k_0) + \tilde{I}_1^a f_0^a(k_0) \Big) \\ + Q^a \Big(\tilde{I}_0^a f_2^a(k_0) + \tilde{I}_2^a f_0^a(k_0) \Big) - i k_0 j_1(k_0 a) \sinh(k_0 h) f_0^a(k_0) \Bigg\}, \tag{5.3.48}$$

where again the actual scattering coefficients R and T can be found from (5.2.7) as usual. Also, the output energy after the wave-crack interaction, can be calculated through $|R|^2 + |T|^2$ which is expected to be less than one for $\mu > 0$.

5.3.3 Scattering by multiple cracks

In this section, the scattering by a sequence of small cracks filled with a viscous fluid, as the one described above, will be considered. The propagating wave will be of normal incidence to coincide with the two-dimensional theory analysed in the previous sections. The idea is to imagine that those cracks act as identical scatterers i.e., same gap length and same viscous fluid properties (such as viscosity and density).

First, it should be assumed that the adjacent cracks are far from each other in the sense that the spacings are sufficiently large with respect to the wavelength of the propagating modes within the ice-sheets. This assumption implies that only the scattering modes survive after travelling from one crack to another as the remaining modes decay exponentially by travelling away from the crack (evanescent waves). This is basically the wide-spacing approximation [89].

Next, by deriving the scattering matrix to relate adjacent amplitudes at each crack, then expressions for the reflection and transmission coefficients by a finite sequence of cracks, will be derived. Normally this calculation requires us to find the amplitudes after each gap interaction recurrently. But by assuming that the cracks are at an equal distance from their neighbouring cracks, then instead of calculating the scattering matrix to a large power, a huge algebraic simplification will be allowed through diagonalisation. Therefore, the reflection and transmission coefficients by a finite sequence of cracks will be calculated through simple expressions in terms of the numerical solutions R and T (from the single crack problem of the previous section). The resulting expressions will be similar to the ones of [52] where they

solve the same problem with no viscosity (scattering by multiple narrow cracks). Their methods were based on [49] and [90] who dealt with wave scattering problems of different setting. However, the methods used here are different from the previous ones as they do not assume energy conservation after each wave-scatterer interaction.

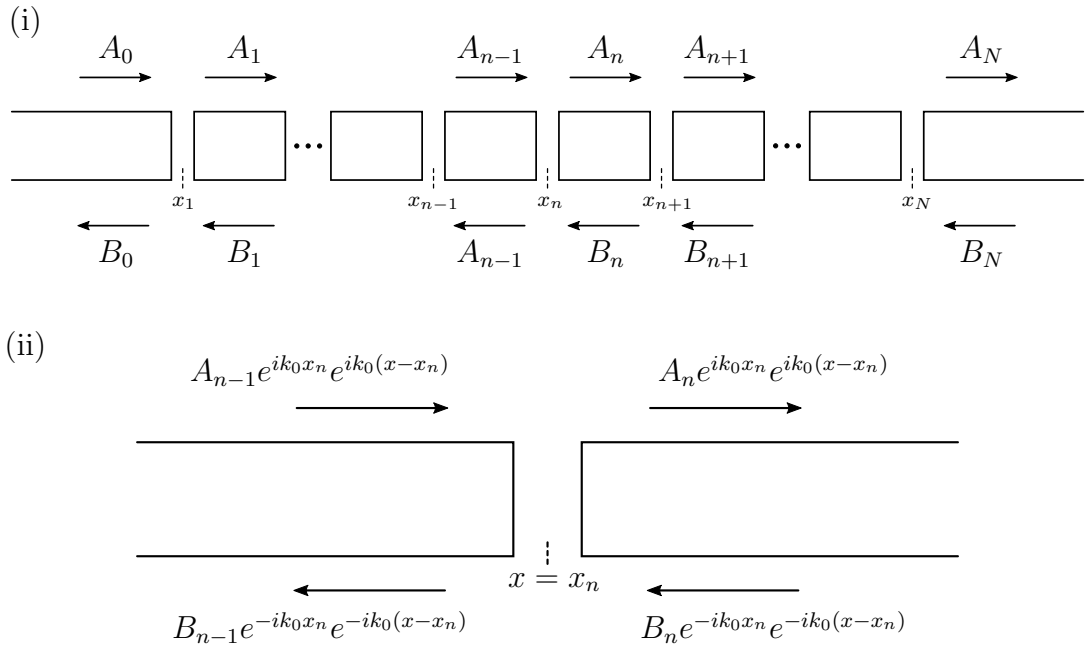

Figure 5.8: Figure (i) shows the ingoing and outgoing wave amplitudes in each ice sheet. Figure (ii) specifies the wave near a crack (no z-dependence) by assuming that the adjacent evanescent modes are negligible there (wide-spacing approximation).

The geometrical picture now is the same as the problem of the previous section, with the difference that now N cracks are placed at positions $x = x_n$ for $n = 1, ..., N$ with $x_1 < ... < x_N$ (see figure 5.8). The wide-spacing approximation is based on $2k_0a \ll k_0(x_n - x_{n-1}) \ll 1$ for $n = 2, ..., N$ so that the spacing between neighbouring cracks is much larger than the scattering wavelengths. The argument above states that the gaps are much smaller than the floes size so that, in the vicinity of a single crack, the two neighbouring ice sheets appear semi-infinite in extent allowing the use of R and T from the previous section. The ingoing (from left to right) and outgoing (from right to left) amplitudes in each ice floe are defined as A_n and B_n respectively for $n = 0, 1, ..., N$. Without the loss of generality, the incident

wave propagates from the left ($x = -\infty$) instead from the right ($x = \infty$) as in the previous section and the same scattering (reflection and transmission coefficients) is expected when it meets the first crack. Thus, it can be set that $A_0 = 1$, $B_0 = R_N$, $A_N = T_N$ and $B_N = 0$, where R_N and T_N are the reflection and transmission coefficients respectively for the scattering problem involving the N cracks.

First, the recurrence relation between the amplitudes must be stated by matching waves across cracks. By inspecting figure 5.8(ii), it follows that

$$\begin{aligned} A_n e^{ik_0 x_n} &= R\big(B_n e^{-ik_0 x_n}\big) + T\big(A_{n-1} e^{ik_0 x_n}\big), \\ B_{n-1} e^{-ik_0 x_n} &= R\big(A_{n-1} e^{ik_0 x_n}\big) + T\big(B_n e^{-ik_0 x_n}\big), \end{aligned} \tag{5.3.49}$$

as outgoing waves are the sum of reflected and transmitted waves with R and T calculated numerically from the single crack problem. Starting from the linear system above and solving for $\{A_n, B_n\}$ in terms of $\{A_{n-1}, B_{n-1}\}$, then

$$\begin{pmatrix} A_n \\ B_n \end{pmatrix} = \mathbf{P}_n \begin{pmatrix} A_{n-1} \\ B_{n-1} \end{pmatrix} \quad \text{for} \quad \mathbf{P}_n = \frac{1}{T} \begin{pmatrix} T^2 - R^2 & Re^{-2ik_0 x_n} \\ -Re^{2ik_0 x_n} & 1 \end{pmatrix}. \tag{5.3.50}$$

Substituting $n = N$ into (5.3.50) and using the amplitude matching recurrence relation, then

$$\begin{pmatrix} T_N \\ 0 \end{pmatrix} = \tilde{\mathbf{P}}_N \begin{pmatrix} 1 \\ R_N \end{pmatrix} \quad \text{where} \quad \tilde{\mathbf{P}}_N = \mathbf{P}_N \mathbf{P}_{N-1} \cdots \mathbf{P}_2 \mathbf{P}_1. \tag{5.3.51}$$

Now a simplification of the matrix $\tilde{\mathbf{P}}_N$ will be made so that its calculation is computationally inexpensive even for a large number of cracks. First, one could rewrite $\mathbf{P}_n$ from (5.3.50) as

$$\mathbf{P}_n = \begin{pmatrix} e^{-ik_0 x_n} & 0 \\ 0 & e^{ik_0 x_n} \end{pmatrix} \mathbf{Q} \begin{pmatrix} e^{ik_0 x_n} & 0 \\ 0 & e^{-ik_0 x_n} \end{pmatrix} \quad \text{for} \quad \mathbf{Q} = \frac{1}{T} \begin{pmatrix} T^2 - R^2 & R \\ -R & 1 \end{pmatrix} \tag{5.3.52}$$

and then through matrix multiplication and assuming equal spacing between the

cracks (i.e. $x_n = nb$ for $n = 1, ..., N$ with $2k_0a \ll k_0b \ll 1$), then

$$\tilde{\mathbf{P}}_N = \begin{pmatrix} e^{-ik_0Nb} & 0 \\ 0 & e^{ik_0Nb} \end{pmatrix} \tilde{\mathbf{Q}}^N \quad \text{for} \quad \tilde{\mathbf{Q}} = \mathbf{Q} \begin{pmatrix} e^{ik_0b} & 0 \\ 0 & e^{-ik_0b} \end{pmatrix}. \tag{5.3.53}$$

Note that when $N \gg 1$, the calculation of $\tilde{\mathbf{Q}}^N$ might create numerical instabilities as some of the eigenvalues of $\tilde{\mathbf{Q}}$ might be greater than one in modulus. Therefore by writing $\tilde{\mathbf{Q}} = \mathbf{X}\mathbf{\Lambda}\mathbf{X}^{-1}$ through decomposition, with $\mathbf{\Lambda} = \text{diag}\{\lambda_1, \lambda_2\}$ (where $|\lambda_1| > |\lambda_2|$ without the loss of generality) and $\mathbf{X} = \{\mathbf{v}_1, \mathbf{v}_2\}$ for $\{\lambda_i, \mathbf{v}_i\}_{i=1,2}$ be the eigenvalues and eigenvectors of $\tilde{\mathbf{Q}}$, then $\tilde{\mathbf{Q}}^N = \mathbf{X}\mathbf{\Lambda}^N\mathbf{X}^{-1}$ with $\mathbf{\Lambda}^N = \text{diag}\{\lambda_1^N, \lambda_2^N\}$. Thus,

$$\tilde{\mathbf{Q}}^N = \frac{\lambda_1^N}{\det(X)} \begin{pmatrix} X_{11}X_{22} - \mu_N X_{12}X_{21} & -(1-\mu_N)X_{11}X_{12} \\ (1-\mu_N)X_{21}X_{22} & \mu_N X_{11}X_{22} - X_{12}X_{21} \end{pmatrix} \text{ for } \mu_N = \left(\frac{\lambda_2}{\lambda_1}\right)^N, \tag{5.3.54}$$

where X_{ij} are the elements of the matrix formed by the eigenvectors of $\tilde{\mathbf{Q}}$. Also, the coefficient μ_N was chosen like that to avoid numerical instabilities when N becomes large (as $|\lambda_2| < |\lambda_1|$). Next, substituting (5.3.54) into (5.3.53), then R_N, T_N can be found from (5.3.51) as

$$R_N = \frac{(1-\mu_N)X_{21}X_{22}}{X_{12}X_{21} - \mu_N X_{11}X_{22}} \quad \text{and} \quad T_N = \frac{\lambda_2^N e^{-ik_0Nb}\big(X_{12}X_{21} - X_{11}X_{22}\big)}{X_{12}X_{21} - \mu_N X_{11}X_{22}}. \tag{5.3.55}$$

Firstly, the coefficient R_N was found by the second equation of the system (5.3.51) and then it was used in the first to get T_N. From here the output energy after the incident wave interacts with the N cracks is given by $|R_N|^2 + |T_N|^2$ and is expected to be less than one given a non-zero viscosity within the narrow cracks. This result is based on the so-called "wide spacing" approximation. In practice one often finds that this approximation works remarkably well even when the assumption of wide spacing is violated and, without any evidence for this, we shall assume this is the case here. This is because we are testing a hypothesis that the attenuation in broken ice could be attributed to viscous effects due to the differential motion of small floes of ice with narrow gaps in between.

It is expected that $T_N \to 0$ as $N \to \infty$ in the presence of a viscous fluid within the cracks. By applying the infinite crack limit, it can be seen from the

formulas above that R_N is always bounded and T_N is decaying only if $|\lambda_2| < 1$. This can be proved by calculating the characteristic polynomial of $\tilde{\mathbf{Q}}$, i.e. $\det\big(\tilde{\mathbf{Q}} - \lambda\mathbf{I}\big) = 0$. The characteristic polynomial will be of the form $\lambda^2 + A\lambda + 1 = 0$, where A is a constant depending on R, T and $e^{ik_0 b}$ and thus it can be easily verified that its roots satisfy $\lambda_1\lambda_2 = 1$. Therefore, using that $|\lambda_2| = 1/|\lambda_1|$ with $|\lambda_1| > |\lambda_2|$ (by construction), then it follows that $|\lambda_2| < 1$ (required result).

The wave attenuation is defined by how much the wave amplitude decays over a given distance. In our problem we can define this by the ratio of wave amplitudes across a distance b between two successive cracks. Thus the decaying rate for $N \gg 1$ cracks tends to

$$\left|\frac{T_N}{T_{N-1}}\right| \approx \left|\lambda_2 e^{-ik_0 b}\right| = |\lambda_2| < 1 \quad \text{as} \quad N \to \infty. \tag{5.3.56}$$

A number of authors found a different way to model the attenuation rate of a wave travelling within an ice sheet. For example, [54] simply added a small imaginary part to the wavenumber, i.e. $\hat{k} = k + ik_i$. This formula arises from the treatment of a homogeneous layer of ice which has damping mechanism built into it. Now the attenuation over a distance b (for comparison with the previous formula) is given by considering a propagating wave in the models of [54] and [55] whose imaginary parts give rise to attenuation and so

$$\big|\lambda_2\big| = \big|e^{i\hat{k}b}\big| = \big|e^{i(k+ik_i)b}\big| = e^{-k_i b} \Rightarrow k_i = -\frac{1}{b}\ln\big|\lambda_2\big| \tag{5.3.57}$$

and note that since $\big|\lambda_2\big| < 1$, then $k_i > 0$ is verified as k_i represents the exponential decay coefficient.

Now an expression for all ingoing wave amplitudes A_n will be derived so that numerical results showing the attenuation after the wave interaction at each crack, can be presented later. Substituting the $\mathbf{P}_n$ expression from (5.3.52) in (5.3.50) using the equal crack spacing $x_n = nb$, then

$$\begin{pmatrix} A_n \\ B_n \end{pmatrix} = \begin{pmatrix} e^{-ik_0 nb} & 0 \\ 0 & e^{ik_0 nb} \end{pmatrix} \tilde{\mathbf{Q}}^n \begin{pmatrix} 1 \\ R_N \end{pmatrix}, \tag{5.3.58}$$

by applying the formula recurrently and using $A_0 = 1$ and $B_0 = R_N$. Also, $\tilde{\mathbf{Q}}$ is the one defined in (5.3.53) and therefore by making the decomposition $\tilde{\mathbf{Q}} = \mathbf{X}\mathbf{\Lambda}\mathbf{X}^{-1}$, then $\tilde{\mathbf{Q}}^n$ can be calculated easily. Finally, by taking the R_N expression from (5.3.55) and after a considerable algebra, then

$$A_n = e^{-ik_0nb}\frac{\lambda_2^n X_{12}X_{21} - \tilde{\mu}X_{11}X_{22}}{X_{12}X_{21} - \mu_N X_{11}X_{22}} \quad \text{for} \quad \mu_n = \left(\frac{\lambda_2}{\lambda_1}\right)^n, \quad \tilde{\mu} = \frac{\lambda_2^N}{\lambda_1^{N-n}}, \tag{5.3.59}$$

where again the coeffiecients μ_n and $\tilde{\mu}$ were chosen like that to avoid numerical instabilities for large N. Also, it can be verified by substituting $n = 0$ and $n = N$ into the expression above that $A_0 = 1$ and $A_N = T_N$ indeed.

5.3.4 Numerical results for the viscous problem

In this section, computational results of the previous section (which is a generalisation of section 5.2.2) are presented. Here we do not always assume that $\beta/d^4 = 45536/d$, as in some cases we choose a different value of E, to compare results with the work of other authors. However, the ice to water density ratio and the truncation of dispersion roots are chosen again to be $\delta/d = \rho_i/\rho_w = 0.9$ and $N_r = 1024$ throughout this section. Also, from now on the subscript in the scattering coefficients will indicate the number of cracks e.g. $|R_8|$ means total reflection for 8 cracks. Moreover using that $\omega = \sqrt{Kg}$, then one could show that $\tau = \sigma\hat{\delta}\hat{K}^{1/2}/\hat{a}^2$ where the hatted variables are non-dimensionalised by d and $\sigma = \mu/(\rho d^{3/2}g^{1/2})$ is the dimensionless parameter that describes damping. The order of magnitude of this parameter is $\sigma \sim \mathcal{O}(10^{-3})$ according to the magnitudes described in the beginning of section 5.3.1 (given $d \sim \mathcal{O}(1m)$). However, in some cases we will choose this parameter differently to indicate certain physical phenomena or to match field data from the literature.

Starting from figure 5.9, the convergence of the viscous problem solution to the small crack approximation of section 5.2.2 is shown, by plotting $|R_1|$ against the dimensionless wavenumber k_0d for a decreasing sequence of the damping parameter σ. The curves coincide for small wavenumbers as any obstacle or scatterer (in this case the crack) has a smaller effect on long waves. Also, if the viscosity parameter increases significantly then the zero of reflection is removed (chained curve). However, the curves tend slowly to the small crack approximation curve (red) as even a small value of σ can have an effect on the solution. However the $\sigma \to 0$ limit is uniform.

Moving on to figure 5.10, a direct comparison to the work of [52] can be

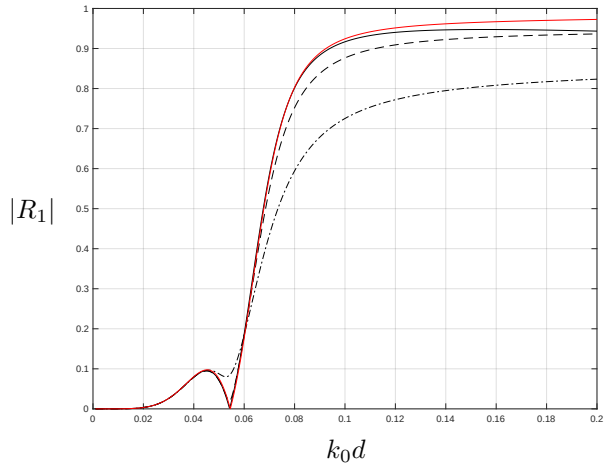

Figure 5.9: $|R_1|$ against $k_0 d$ for $(\beta/d^4, h/d, a/d) = (45536, 40, 0.1)$ and $\sigma = 0.5$ (chained), 0.1 (full), 0.01 (dashed) and small crack approximation (red).

made as they considered the scattering by multiple narrow cracks but ignoring energy losses (used inviscid theory). In figure 5.10(i), the total transmission and output energy by 2 cracks is shown. The parameters were chosen in the same way as figure 3 of the work of the authors discussed above (number of cracks, crack separation distance, ice and water parameters, water depth). The only difference here is that a viscosity parameter is added to the fluid within the cracks ($\sigma = 0.01$) and the crack width is chosen to be $a/d = 0.1$. It can be seen that the wavenumber positions of the transmission spikes do not change by adding viscosity, but the spikes diverge from 1 in the short-wave limit. Also, the output energy is less than 1 as expected.

In figure 5.10(ii), the viscous analogue of [52] figure 7(a) is plotted. The crack width is chosen to be the same as above ($a/d = 0.1$) for two different viscosity parameters. Again, the wavenumber positions of the reflection spikes do not change by adding viscosity, but the spikes diverge from 0 in the short-wave limit. The scattering coefficients in general tend to zero with the rise of viscosity. For larger viscosity (dashed) the curve is deformed at a greater degree when compared to a smaller viscosity (full) as expected.

Next, in figure 5.11(i) the transmitted amplitudes $|A_n|$ (as $|A_0| = 1$ by construction) after the interaction with each of the 80 cracks, is calculated. Each curve represents different ice thickness with the incident wavenumber chosen to be $k_0 d = 0.2$. As expected from physical grounds, the amplitude decreases exponentially after the interaction between the transmitted wave and each crack. The curves

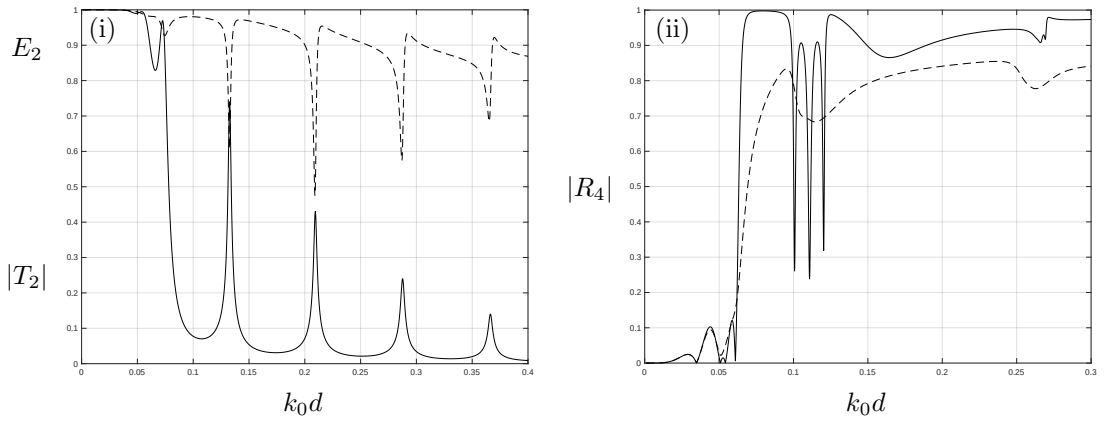

Figure 5.10: (i) $|T_2|$ (full) and energy $E_2 = |R_2|^2 + |T_2|^2$ (dashed) against k_0d for $(\sigma, b/d) = (0.01, 40)$ and (ii) $|R_4|$ against k_0d for $b/d = 20$ and $\sigma = 0.5$ (dashed), 10^{-3} (full). The common variables are $(\beta/d^4, h/d, a/d) = (45536, 40, 0.1)$.

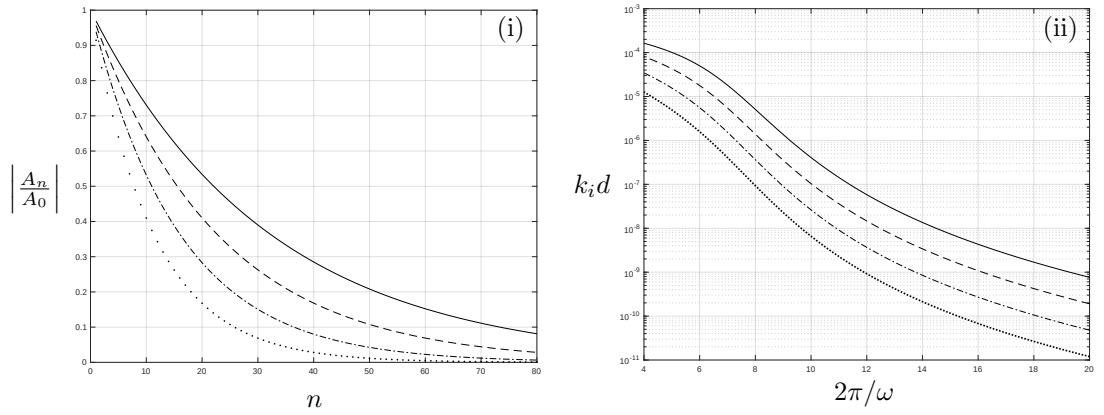

Figure 5.11: (i) $|A_n/A_0|$ against n for $k_0d = 0.2$, $\beta/d^4 = 45536/d$ with $d = 1$ (full), 0.5 (dashed), 0.25 (chained), 0.125 (dotted) and (ii) k_id against the wave period for $\beta/d^4 = 256$ (dotted), 512 (chained), 1024 (dashed), 2048 (full). The parameters are $(h/d, a/d, \sigma, b/d) = (40, 10^{-4}, 0.1, 20)$ for 80 cracks.

of $|A_n/A_0|$ coincided with $|\lambda_2|^n$, as $|\lambda_2|$ was shown to represent the decaying amplitude rate for a large number of cracks. Figure 5.11(ii) shows the variation of the exponential decay coefficient with the incident wave period for multiple values of ice material parameters. The reason behind the extreme choices of β/d^4 is to compare

results with [54] figure 8, where they achieved energy dissipation by assuming that the ice sheet is a homogeneous viscous layer model (their viscous parameters represent different characteristics than ours). They chose an ice thickness of $d = 0.5$ and water depth of $h = 100$. We chose smaller values of β/d^4 in our plot to mimic their viscoelastic model which is associated with a very small elasticity (smaller values of shear modulus G). The decaying curves have the same order of magnitude for an incident wave of period around 4 seconds with the authors discussed above. However, our curves are not completely aligned with theirs as the energy dissipation is based on a completely different assumption.

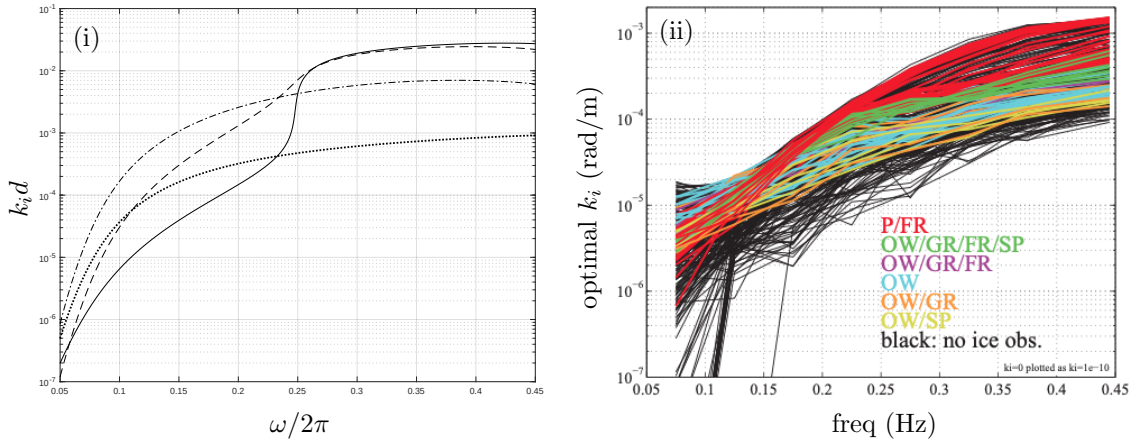

Figure 5.12: (i) $k_i d$ against frequency for $(\beta/d^4, h/d, a/d, b/d) = (45536, 40, 10^{-4}, 40)$ for 80 cracks and $\sigma = 10^{-1}$ (dotted), 10^{-2} (chained), 10^{-3} (dashed), 10^{-4} (full). (ii) Experimental result of [2] figure 10.

Moving on in figure 5.12 one can see the comparison between our solution and the experimental result of [2] figure 10. Their curves are very noisy when compared to ours, as they come from experimental measurements. But it seems that when our viscosity parameter gets larger, the curves tend to theirs as they start from 10^{-7} and end at about 10^{-3} for the same frequency range.

Now figure 5.13 shows the comparison between our solution and the result of [3] figure 2 (same as in [29]) which comes from field data. Their plot presents the log-log plot of the dissipation rate k_i and the incident angular frequency ω extracted from the experimental data median values found from the work of [91], [92], [93], [94]. Their data points seem to be aligned in the log-log plots suggesting that there is a power law $k_i \propto \omega^n$. Their exponent n varies between 1.9 and 3.6 (depending

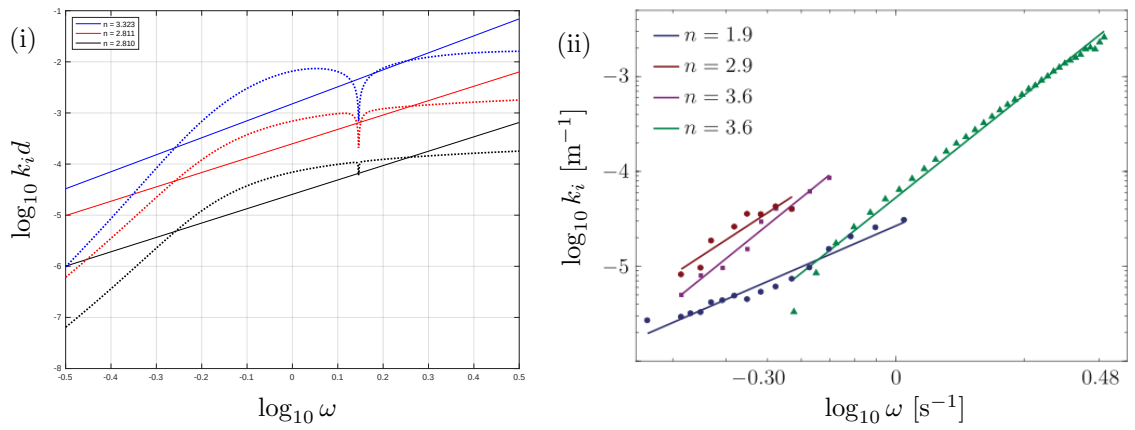

Figure 5.13: (i) $\log_{10}(k_i d)$ against $\log_{10}\omega$ for 80 cracks and $\sigma = 0.003$ (blue), 0.03 (red), 0.3 (black) with their best fits (dotted lines). The geometrical parameters are $(\beta/d^4, h/d, a/d, b/d) = (45536, 40, 10^{-4}, 40)$. (ii) Analogue result of [3] figure 2.

on the data set of each author discussed above). However, in our plot, we get a different exponent n depending on the value of viscosity. It seems that our curves do not tend to their best fits (straight lines) even though we use the best fits to compare the exponents of the power law with the literature. It looks that according to our model, that the exponent lies between 2.810 and 3.323 (approximately) as the damping parameter varies which is a good alignment with the field data of the previous authors.

Chapter 6

Conclusion

In this thesis we have considered a plethora of linear scattering problems whose solutions were semi-analytical. The results have been compared to one extent, with the work of other authors.

In Chapter 3 we considered the scattering by a submerged bottom-mounted metamaterial. By finding eigenfunction expansions we matched pressures and normal fluxes across the microstructure boundaries. However in the special case where the barriers were aligned with the longshore direction, the matching conditions along the boundaries of the metamaterial changed character. Therefore, the matching at these boundaries was done using the Galerkin method which gives approximate solutions to integral equations. Also, when the barriers were normal or parallel to the side interfaces, then the dispersion relation roots (eigenvalues) of the the depth eigenfunction over the microstructure, were lying only on the real and imaginary axis. Therefore their numerical computation was relatively easy and by calculating 1024 of them was enough to give a 7 decimal place accuracy to the solution. However, when the barriers were oriented at an angle to the side interface, the dispersion relation roots became complex (off the real and imaginary axis) and therefore their computation was more complicated. An accuracy of 4 decimal places was achieved by calculating only 64 of them. Despite that, special cases that showed negative refraction phenomena were presented and compared to the literature [11].

Then the same problem of arbitrarily oriented barriers, was considered in the shallow water regime. A new model based on first principles was derived using a multi-scaled asymptotic analysis. The simplification under this approximation,

allowed a closed-form solution to the problem, even when the lower interface of the metamaterial was not aligned with the exterior sea bed. However, we considered only the case when this lower interface is above or at the same level as the exterior sea bed since this restriction guaranteed the existence of two wave modes within the metamaterial region. If we allowed the lower metamaterial interface to be below the exterior sea bed, then there would be cases for which the modes within the structure are evanescent waves [81].

In Chapter 4, the reflection properties of a metamaterial wall were investigated. This problem was motivated by the law of reflection "violation". The numerical solution required the inclusion of a damping parameter within the narrow channel of the microstructure, to achieve accurate results. This is a reasonable assumption as the lack of convergence happened at incident frequencies close to the resonant frequency of the array. Evidently, the "metawall" acted as a broadbanded high-efficiency wave energy absorber, with the inclusion of damping.

In Chapter 5, the scattering of flexural waves by cracks on ice floes is considered. The so-called "finite gap" problem was solved in a different method than the variety of solutions found in the literature. The issue with other methods is that they require most expensive computation as the gap between the ice sheets gets smaller. However, the Fourier transform method used here works in the opposite way. Then the solution to the "small gap" problem was found by taking the appropriate limit to the solution of the "finite gap" problem. At leading order, the problem achieved a simple closed-form solution which verified to be identical to the one of [46] who solved the "zero gap" problem (using a different approach). The advantage of our method is that high order terms (in a small gap parameter) could be retained, while in the literature only leading order solutions were found. In the analysis of our problem, we derived only the leading order solution for two reasons. First, the higher order solution was much complicated as it required the calculation of more integrals and also the higher order terms did not have any significant impact on the solution.

Then the problem involving the scattering by small cracks filled with a viscous fluid is solved by deriving new ice-water conditions. This modelling assumption was used to mimic the effect of wave attenuation within ice sheets in the Arctic Ocean. Although many authors attempted to understand the energy dissipation in ice floes [91], [92], [93], [94], the natural cause of this phenomenon is still unknown. The numerical results matched, to some extent, the field measurements.

Appendix A

Roots of dispersion relations

A.1 Dispersion relation of section 3.2.2 and 3.2.4

In this part of the Appendix, the dispersion relations of (3.2.31)and (3.2.48) coming from the matching conditions across the top interface of the metamaterial, are analysed. Their roots give important information about the possible types of water waves that can travel over the metamaterial structure. First, we seek the roots of the (3.2.48) dispersion relation as its structure is simpler and it is easier to show the non-existence of complex roots. On the other hand, it is hard to show analytically (for every choice of parameters) the non-existence of complex roots of the (3.2.31) dispersion relation as it is not straightforward how to count its roots and poles on the real and imaginary axis of the complex plane. However, a computational approach on how to count them will be explained at the end of this section.

The analysis again, starts by setting $F(\mu)$ the difference between the left and right-hand side of the dispersion relation (3.2.48) and seeking its roots. However since the dependence on μ of $F(\mu)$, comes only in $\sqrt{\mu^2+\alpha^2}$, then by changing

variables from μ to $\sqrt{\mu^2-\alpha^2}$, it follows that

$$\begin{aligned} G(\mu) &\equiv F\big(\sqrt{\mu^2-\alpha^2}\big) \\ &= (1-\theta)\alpha\tanh[\alpha(c-d)]\left(\frac{K\tanh(\mu d)}{\mu}-1\right)+K-\mu\tanh(\mu d), \end{aligned} \tag{A.1.1}$$

where now $G(\mu)$ is easier to handle. The roots of $F(\mu)$ and $G(\mu)$ are called μ_n and r_n respectively and they are related through $\mu_n=\sqrt{r_n^2-\alpha^2}$. So, since μ_n represent the wavenumbers in the x-direction, then r_n represent the wavenumbers in the direction of incidence as $\mu_n^2+\alpha^2=r_n^2$.

Now for simplification purposes, the possible values which θ_0 can take, will be $(0°, 90°)$. This can be seen from the fact that if α is exchanged with $-\alpha$, then $G(\mu)$ is invariant, which implies that only the $\alpha\geq 0$ case can be considered. This can be seen by the symmetric geometry of the problem as well. Also, the case of $\alpha=0$ can be neglected as in that case the roots of $G(\mu)$ will satisfy $\mu\tanh(\mu d)=K$, which is the water wave dispersion relation over a flat bed at $z=-d$. This happens because the metamaterial behaves like a rigid step for normal incidence for reasons explained in section 3.2.4. Thus, only the case $\alpha>0$ is considered as for $\alpha=0$ the location of the roots is known from the water dispersion relation over a flat bed at $z=-d$. Also, the same argument goes for $\theta=1$ as in that case the filling fraction becomes 100% and the metamaterial becomes a rigid step again. Thus, the possible values of the filling fraction are taken to be $\theta\in[0,1)$. Also, only the special case of $c\leq h$ (metamaterial sitting on step) is considered here as for $c>h$ (barriers buried to the sea bed) a different treatment is needed. However, the methodology is the same even though we do not consider the special case of $c>h$ for the sake of simplicity of the proof.

Starting from the case $\mu\in\mathbb{R}$, the roots of $G(\mu)$ will satisfy

$$(1-\theta)\alpha\tanh[\alpha(c-d)]\left(\frac{K\tanh(\mu d)}{\mu}-1\right)=\mu\tanh(\mu d)-K, \tag{A.1.2}$$

which can represented as the points of intersection of the left and right-hand sides (call them $L(\mu)$ and $R(\mu)$ respectively). Starting from $R(\mu)$ one can see that is even with $R(0)=-K<0$. Also, it can be derived that $R'(\mu)=\tanh(\mu d)+\mu d\,\mathrm{sech}^2(\mu d)>0$ for all $\mu\in\mathbb{R}_{>0}$, $R'(0)=0$ and $R(\mu)\sim\mu$ as $\mu\to\infty$. Now for $L(\mu)$ one can see

that is even with

$$L'(\mu) = \frac{K(1-\theta)\alpha}{\mu}\tanh[\alpha(c-d)]\mathrm{sech}^2(\mu d)\left[d - \frac{\sinh(2\mu d)}{2\mu}\right] < 0, \qquad \text{(A.1.3)}$$

for all $\mu \in \mathbb{R}_{>0}$ using $\sinh x > x$ for all $x > 0$. Also it can be seen from (A.1.2) that $L(\mu)$ is finite and smooth at $\mu = 0$ which implies that $L'(0) = 0$ (as $L(\mu)$ is even). Therefore, using that $L(\mu) \sim -(1-\theta)\alpha\tanh[\alpha(c-d)] < 0$ as $\mu \to \infty$, then the plots of $R(\mu)$ and $L(\mu)$ are the ones of figure A.1. The function $L(\mu)$ intercepts the vertical axis at $L(0) = (1-\theta)(Kd-1)\alpha\tanh[\alpha(c-d)]$. Note that the horizontal

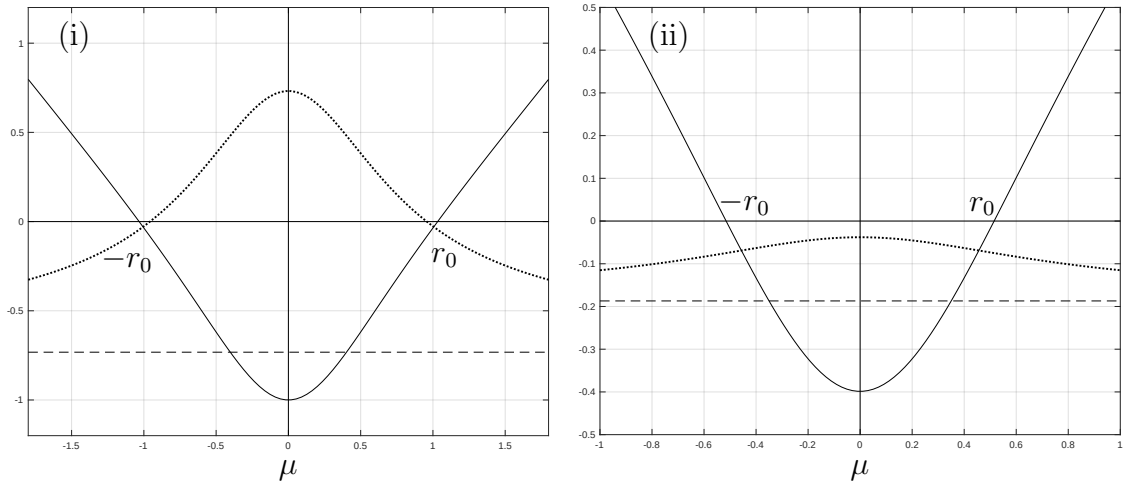

Figure A.1: $R(\mu)$ (full) and $L(\mu)$ (dotted) for $(h, c, d, \theta_0, \theta) = (8, 4, 2, 60°, 0.1)$ for (i) $k = 1$ and (ii) $k = 0.4$ (which result to a different sign of $L(0)$ or $Kd - 1$). The curves intersect at $\pm r_0$, with the horizontal asymptote (dashed) of $L(\mu)$ be located at $-(1-\theta)\alpha\tanh[\alpha(c-d)] < 0$.

asymptote of $L(\mu)$ will be always lying above the global minimiser of $R(\mu)$ as

$$(1-\theta)\alpha\tanh[\alpha(c-d)] < (1-\theta)k\tanh[k(h-d)] \leq k\tanh[k(h-d)] < k\tanh(kh) = K. \qquad \text{(A.1.4)}$$

Therefore, since the real roots of $G(\mu)$ are represented by the intersection points of $R(\mu)$ and $L(\mu)$, then $G(\mu)$ has exactly two real and opposite roots, call them $\pm r_0$

with $r_0 > 0$.

Now, it will be proved that $G(\alpha) > 0$ which implies that $r_0 > \alpha$ by the Intermediate value theorem as $G(\mu) \sim K - (1-\theta)\alpha \tanh[\alpha(c-d)] - \mu < 0$, as $\mu \to \infty$. It remains to prove that $L(\alpha) > R(\alpha)$. In the limit $\theta \to 0$, after a considerable algebra, it follows that

$$L(\alpha) - R(\alpha) = \frac{K - \alpha \tanh(\alpha c)}{1 - \tanh(\alpha c)\tanh(\alpha d)} \operatorname{sech}^2(\alpha d) > 0, \tag{A.1.5}$$

using that $\alpha \tanh(\alpha c) < k \tanh(kh) = K$. Now for $\theta = 1$, then $L(\alpha) - R(\alpha) = K - \alpha \tanh(\alpha d) > 0$ clearly as $\alpha \tanh(\alpha d) < k \tanh(kh) = K$. Therefore, since $G(\alpha)$ is a linear function of θ which is positive at $\theta = 0$ and $\theta = 1$, then is must be positive for all $\theta \in [0, 1]$. Thus, the two real roots $(\pm r_0)$ of $G(\mu)$, correspond to two real roots $(\pm\mu_0)$ of $F(\mu)$ as $\mu_0 = \sqrt{r_0^2 - \alpha^2}$ and $r_0 > \alpha$. So, within $|x| < b$, there are two travelling waves of the same wavelength travelling in opposite directions. The positive real root can be calculated computationally by looking for a sign change of $G(\mu)$ in $[\alpha, \infty]$ and then using the bisection method.

Now for the purely imaginary roots, since $\mu = 0$ is not a root, then by rearranging $\sigma G(i\sigma) = 0$ for $\sigma \in \mathbb{R}$, it follows that

$$\begin{aligned} \tan(\sigma d) = -\frac{A\sigma}{\sigma^2 + B} \quad &\text{for} \quad A = K - (1-\theta)\alpha \tanh[\alpha(c-d)] \\ &\text{and} \quad B = K(1-\theta)\alpha \tanh[\alpha(c-d)]. \end{aligned} \tag{A.1.6}$$

Clearly $B > 0$ and since $(1-\theta)\alpha \tanh[\alpha(c-d)] < k \tanh[k(h-d)] < k \tanh(kh) = K$, then $A > 0$ as well. Therefore the imaginary part of the purely imaginary dispersion roots can be represented as the common points of the curves described in the left and right-hand side of (A.1.6) (see figure A.2). The $\sigma = 0$ root must be excluded as it was introduced by the rearrangement of $\sigma G(i\sigma) = 0$. Also, the roots (common points) and poles of the plot are symmetric as $G(\mu)$ is even. The poles are located at $\tau_n = \frac{2n-1}{2d}\pi$ for $n \in \mathbb{Z}$. The sequence of the purely imaginary roots of $G(\mu)$ is called $\pm r_n = \pm i\sigma_n$ for $n \in \mathbb{N}$, with $\sigma_n \in \mathbb{R}_{>0}$ calculated computationally by bisecting the interval $(\tau_n, n\pi/d)$. Also, it can be seen graphically that $\sigma_n \to n\pi/d$ as $n \to \infty$. Therefore, after a large number of roots, they can set to be $n\pi/d$. Thus, by Taylor

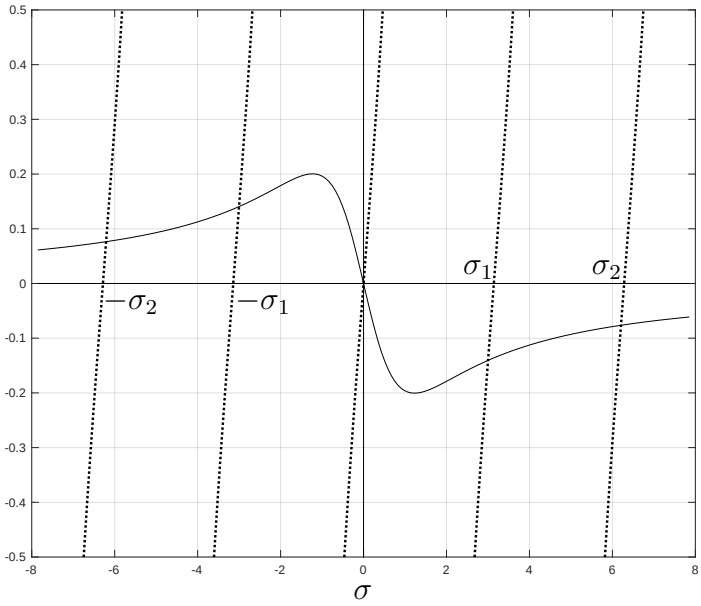

Figure A.2: $\tan(\sigma d)$ (dotted) and $-A\sigma/(\sigma^2 + B)$ (full) that intersect at $\pm\sigma_n$ for $(k, h, c, d, \theta_0, \theta) = (1.5, 4, 2, 1, 60°, 0.1)$. The vertical asymptotes of $\tan(\sigma d)$ are located at τ_n for $n \in \mathbb{Z}$ and it can be seen that $\sigma_n \to n\pi/d$ as $n \to \infty$.

expanding $\tan(\sigma d)$ about $n\pi/d$ in (A.1.6) then

$$\epsilon_n \approx \frac{An\pi}{n^2\pi^2 + (A + Bd)d}, \tag{A.1.7}$$

where $\epsilon_n = n\pi/d - \sigma_n$ is the small positive decreasing error. Using the fact that n is large the expression above can be simplified to $\epsilon_n = A/n\pi$. Thus, after the computation of about $n = \lceil \frac{A}{\pi} 10^d \rceil$ roots for $d \in \mathbb{N}$, the error becomes $\epsilon_n \approx 10^{-d}$. Also, note that the sequence $\pm r_n$ for $n \in \mathbb{N}$, which are roots of $G(\mu)$, corresponds to another sequence of purely imaginary roots of $F(\mu)$, namely $\pm\mu_n = \pm i\chi_n$ for $n \in \mathbb{N}$ and this can be seen from $\mu_n^2 + \alpha^2 = r_n^2$.

Now the non-existence of complex roots off the real and imaginary axes, will be proved. Such proofs require the application of the argument principle (see examples in [95]). This principle relates the number of roots and the number of poles of a complex function within a closed positively oriented contour. The complex

function will be the rearranged dispersion relation

$$g(\mu) = \frac{2\mu e^{\mu d}\cosh(\mu d)}{B - \mu^2 + A\mu} G(\mu) = e^{2\mu d} - \frac{\mu^2 + A\mu - B}{\mu^2 - A\mu - B}, \tag{A.1.8}$$

where A and B are defined in (A.1.6). Note that $g(\mu)$ has the same zeros as $G(\mu)$ but with the extra root at $\mu = 0$ as $G(\mu)$ was multiplied by μ. However, it does not have its $i\tau_n$ poles (for $n \in \mathbb{Z}$) as $G(\mu)$ was multiplied by $\cosh(\mu d)$. Instead, it has two poles coming from the denominator of the right-hand side of (A.1.8) which happen to be real as the discriminant of the denominator is positive.

Thus, by applying the argument principle on $g(\mu)$ in the square centred at the origin with vertices $\pm R(1 \pm i)$ for $R = \frac{4N+1}{4d}\pi$ for $N \in \mathbb{N}$ with $N \gg 1$, then

$$\tilde{c} + 2N + 1 = \frac{1}{2\pi}\Im \oint \frac{g'(\mu)}{g(\mu)} d\mu, \tag{A.1.9}$$

where $\tilde{c}$ is the number of complex roots of $g(\mu)$ off the axes (which it will be proven to be zero). In the count of the roots and poles on the left-hand side of (A.1.9) it was used that $g(\mu)$ has $2N + 3$ roots inside the square (namely $\pm r_0$, 0, $\pm r_n$ for $n = 1, 2, ..., N$) and 2 real poles as discussed in the previous paragraph.

Decomposing the integral in (A.1.9), starting from the right vertical contribution, then

$$\frac{1}{2\pi}\Im \int_{-R}^{R} \frac{g'(R+iy)}{g(R+iy)} i dy \approx \frac{1}{2\pi}\Im \int_{-R}^{R} \frac{2de^{2d(R+iy)}}{e^{2d(R+iy)} - 1} i dy \approx \frac{1}{2\pi}\Im \int_{-R}^{R} (2id) dy = 2N + \frac{1}{2}, \tag{A.1.10}$$

after some asymptotic analysis on $g(\mu)$ and $g'(\mu)$ and the evaluation of R. Similarly, for the left vertical contribution, it follows that

$$-\frac{1}{2\pi}\Im \int_{-R}^{R} \frac{g'(-R+iy)}{g(-R+iy)} i dy \approx -\frac{1}{2\pi}\Im \int_{-R}^{R} \frac{0}{0-1} i dy = 0. \tag{A.1.11}$$

Moving on the sum of the horizontal contributions, using that $\overline{g(\mu)} = g(\overline{\mu})$ and $\overline{g'(\mu)} = g'(\overline{\mu})$, then

$$-\frac{1}{2\pi}\Im\int_{-R}^{R}\frac{g'(x+iR)}{g(x+iR)}dx+\frac{1}{2\pi}\Im\int_{-R}^{R}\frac{g'(x-iR)}{g(x-iR)}dx=-\frac{1}{\pi}\Im\int_{-R}^{R}\frac{g'(x+iR)}{g(x+iR)}dx. \quad \text{(A.1.12)}$$

Now, the right-hand side of (A.1.12) is asymptotic to

$$-\frac{2d}{\pi}\Im\int_{-R}^{R}\frac{e^{2d(x+iR)}}{e^{2d(x+iR)}-1}dx\approx\frac{1}{\pi}\int_{-\infty}^{\infty}\frac{2de^{2dx}}{1+(e^{2dx})^2}dx=\frac{1}{\pi}\int_{0}^{\infty}\frac{dy}{1+y^2}=\frac{1}{2}, \quad \text{(A.1.13)}$$

using that $e^{2idR} = i$, then taking the imaginary part and using the substitution $y = e^{2dx}$. Using the four contributions from equations (A.1.10), (A.1.11), (A.1.13) to get the number of complex zeros from (A.1.9), then the result gives $\tilde{c} = 0$.

Therefore, since there are no complex roots of $g(\mu)$ off the real and imaginary axes, then the only roots of $G(\mu)$ are $\pm r_n$ for $n \in \mathbb{N}_0$. After the computation of those roots, then the actual roots of $F(\mu)$ that are important for the solution of the physical problem, can be simply found from $\pm\mu_n = \pm\sqrt{r_n^2 - \alpha^2}$.

Now, one may question why the root analysis of the dispersion relation (3.2.31) was skipped. The reason is because the non-existence of complex roots cannot be proved using the argument principle as the μ dependence inside the hyperbolic trigonometric functions, does not come in a single form, i.e. like $\sqrt{\mu^2 + \alpha^2}$ of (3.2.48).

However, it can be proved that this relation has two real and symmetric roots and in the purely imaginary case the roots can be represented as the intersection points of a graph similar to the one of A.2. Unfortunately, the n^{th} root of that plot, will not lie in a standard interval that depends on n (as happened to the previous dispersion relation). This is because there are two independent sets of asymptotes, namely $\pm\tau_n = \pm i\frac{2n-1}{2(h-d)}\pi$ and $\pm t_n = \pm i\sqrt{\left(\frac{2n-1}{2d}\pi\right)^2 + \alpha^2}$ for $n \in \mathbb{N}$. Since the roots do not lie in a single known interval then if the bisection method is applied for their calculation, it will create numerical instabilities because of the two types of asymptotes. Thus, by multiplying the dispersion relation by the two types of hyperbolic cosine functions, then those poles will be removed and the roots

will remain unchanged. After doing that then the bisection method can be used efficiently to capture all the purely imaginary roots.

Even though the roots on the axes can be calculated numerically, the non-existence of complex roots cannot be proved. This is because if the argument principle is applied on the dispersion relation (or a rearranged version of it similar to (A.1.8)) over a closed loop, then even if the integral contributions are calculated analytically, there is not straightforward way to count the roots and poles within the closed loop for any choice of geometrical parameters. However, a complicated semi-analytical proof can be maintained by counting the roots and poles computationally within the closed loop. By taking the closed loop to be the circle of radius $R = \max\{\tau_N, t_N\} + (e^{-N}/d)$ for $N \gg 1$, centred at the origin and applying the argument principle over the dispersion relation, then it was shown computationally that for all $N = 2^{10}, \ldots, 2^{13}$ there were no complex zeros off the axes.

The non-existence of complex roots of the dispersion relation of section 3.2.2 can be verified also by the next section, where it can be seen computationally that for an arbitrary barrier orientation (angle δ as defined in section 3.2.6), as δ varies from 0° to 90°, the purely imaginary roots start from the imaginary axis, then follow a path in the complex plane and eventually land on the imaginary axis again when $\delta = \pi/2$ (problem of section 3.2.4).

A.2 Dispersion relation of section 3.2.6

The roots of the dispersion relation specified in (3.2.73) will be analysed. The method starts again by defining

$$\begin{aligned} F(\mu) = \gamma(1-\theta)\tanh[\gamma(h-d)]\left(\frac{K\tanh\left(d\sqrt{\alpha^2+\mu^2}\right)}{\sqrt{\alpha^2+\mu^2}} - 1\right) \\ +K - \sqrt{\alpha^2+\mu^2}\tanh\left(d\sqrt{\alpha^2+\mu^2}\right), \end{aligned} \tag{A.2.1}$$

for $\gamma = \alpha\sin\delta + \mu\cos\delta$ and seeking its roots. First of all, it can be seen when $\delta = 0^\circ$ or $\delta = 90^\circ$, the dispersion relation coincides with the dispersion relations of sections 3.2.2 and 3.3.4 respectively. The location of the roots for those two special cases is analysed in the previous section. They have two real and symmetric roots with a symmetric sequence of purely imaginary roots. The non-existence of complex roots

off the axes is proven analytically for the case $\delta = 90^\circ$ but verified semi-analytically for $\delta = 0^\circ$. In this part of the Appendix, a new numerical verification will be produced to indicate the non-existence of complex roots off the axes for the two limiting cases of barrier orientation.

Starting from the dispersion relation (A.2.1) for a general angle $\delta \in (0^\circ, 90\circ)$, then it can be seen that for $\mu \in \mathbb{R}$ the function is real and therefore its roots can be presented graphically. Naming $L(\mu) = B(\mu)C(\mu)$ for $B(\mu) = \gamma(1-\theta)\tanh[\gamma(h-d)]$, $C(\mu) = \left[K \tanh\left(d\sqrt{\alpha^2+\mu^2}\right)/\sqrt{\alpha^2+\mu^2}\ \right] - 1$ (the left-hand side of (3.2.73)) and $R(\mu) = \sqrt{\alpha^2+\mu^2}\tanh\left(d\sqrt{\alpha^2+\mu^2}\right) - K$ (the right-hand side of the same equation), then the real roots can be represented as the points of intersection of the real functions $L(\mu)$ and $R(\mu)$. Note that for the general case of $\delta \in (0^\circ, 90^\circ)$, the roots will no longer be symmetric as the dispersion relation is not even. Therefore, the generalisation of $\alpha \in \mathbb{R}$ (not only positive as before) must be imposed again as there is no symmetry between $-\theta_0$ and θ_0. Also, the case $\theta_0 = 0^\circ$ cannot be neglected as before because it is not clear how the wave interaction will be affected.

Starting from the plot of $B(\mu)$, one may notice that the function is not even. However, using that $B(-\alpha\tan\delta) = 0$, $B(\mu) > 0$ for $\mu \in \mathbb{R} \setminus \{-\alpha\tan\delta\}$, $B'(-\alpha\tan\delta) = 0$ with $B'(\mu)$ be positive on the right of $-\alpha\tan\delta$ and negative on the left, then the plot of $B(\mu)$ can be seen from figure A.3. Also, note that $|B'(\mu)| \sim$

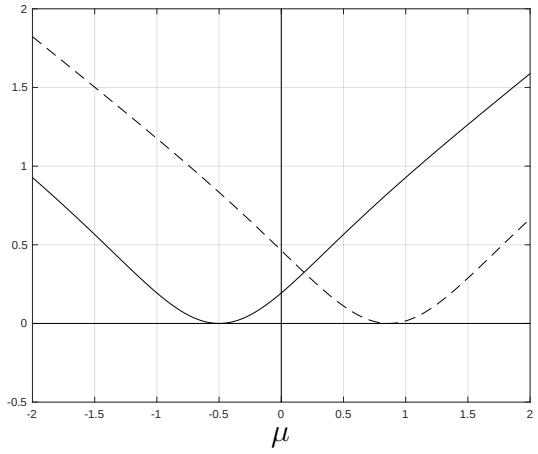

Figure A.3: $B(\mu)$ for $(k, h, d, \delta, \theta) = (1, 4, 2, 45^\circ, 0.1)$ with $\theta_0 = 30^\circ$ (full) and $\theta_0 = -60^\circ$ (dashed). The sign of the minimiser of $B(\mu)$ (namely $-\alpha\tan\delta$) depends on the sign of θ_0 since $\delta \in (0^\circ, 90^\circ$.

$(1-\theta)\cos\delta$ as $\mu \to \pm\infty$. Proceeding to the graph of $C(\mu)$ which is even, one can

prove that

$$C'(\mu) = \frac{K\mu}{q}\text{sech}^2(dq)\left[d - \frac{\sinh(2dq)}{2q}\right] < 0, \quad \forall \mu \in \mathbb{R}_{>0}, \tag{A.2.2}$$

for $q = \sqrt{\alpha^2 + \mu^2}$, using $\sinh x > x$ for all $x > 0$. Using also the facts that $C(\mu) \to -1$ as $\mu \to \infty$ and $C'(0) = 0$, then the graph of $C(\mu)$ will have the same shape as $L(\mu)$ in figure A.1. The only difference would be that the horizontal asymptote will be located at -1 with the sign of the global maximum depending on the sign of $K\tanh(\alpha d)/\alpha - 1$.

As $R(\mu)$ is even with $R(0) = \alpha\tanh(\alpha d) - K < k\tanh(kh) - K = 0$, $R'(\mu) = \mu d\text{sech}^2[d\sqrt{\alpha^2+\mu^2}] + \mu\tanh[d\sqrt{\alpha^2+\mu^2}]/\sqrt{\alpha^2+\mu^2} > 0$ for all $\mu \in \mathbb{R}_{>0}$, $R'(0) = 0$ with $R(\mu) \sim \mu$ as $\mu \to \infty$, then its shape will be the same as $R(\mu)$ in figure A.1, with the only difference be the minimum value of the function. Therefore, by combining this information with figure A.3, then the non-symmetric real roots of the dispersion relation can be represented by the intersection points of figure A.4.

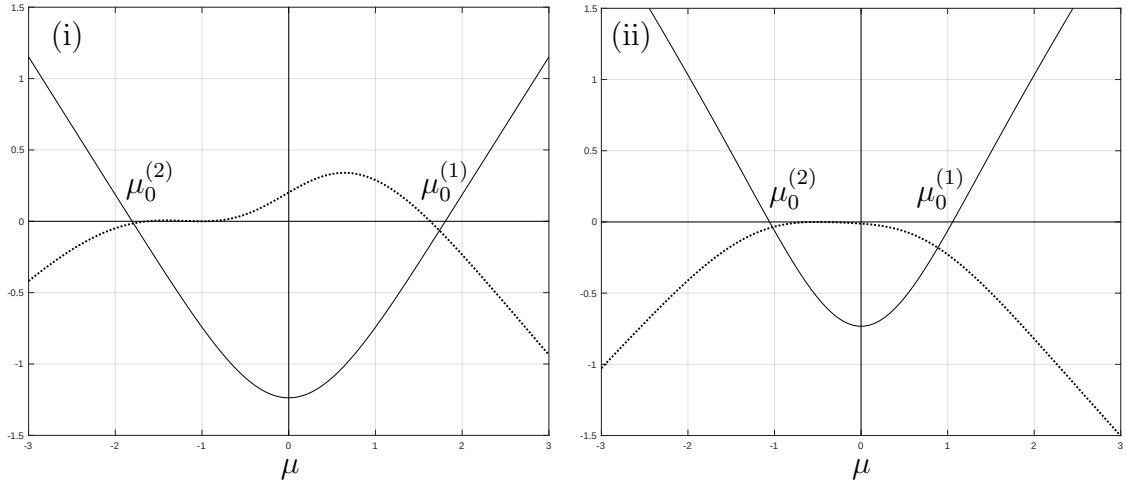

Figure A.4: $R(\mu)$ (full) and $L(\mu)$ (dotted) for $(h, d, \theta_0, \delta, \theta) = (2, 1, 30°, 45°, 0.1)$ that intersect at $\mu_0^{(i)}$ for $i = 1, 2$. The wavenumber was chosen to be $k = 2$ in (i) and $k = 1$ in (ii). These choices result to a different sign of $L(0)$ (or $C(0) = K\tanh(\alpha d)/\alpha - 1$).

For completeness, it remains to prove analytically $R(0) < L(0)$ to guarantee the existence of exactly two real solutions (one positive and one negative and

symmetry arises only when $\delta = 0°, 90°$). So, by defining

$$\begin{aligned}\Lambda &\equiv \cosh(\alpha d)\cosh[\alpha \sin\delta(h-d)]\{R(0)-L(0)\}\\ &= \frac{1+(1-\theta)\sin\delta}{2}\cosh A^{+}\big[\alpha\tanh A^{+}-K\big]\\ &+\frac{1-(1-\theta)\sin\delta}{2}\cosh A^{-}\big[\alpha\tanh A^{-}-K\big],\end{aligned} \tag{A.2.3}$$

for $A^{\pm} = \alpha[d \pm (h-d)\sin\delta]$, using the formulas for products between hyperbolic trigonometric functions. Firstly, in the case of $\alpha = 0$, one can see that $A^{\pm} = 0$ which results to $\Lambda = -K < 0$. Next, in the case of $\alpha > 0$, one can prove that $\alpha d < A^{+} < \alpha h$ and $A^{-} < \alpha d$. Using these bounds, then $\alpha\tanh A^{+} < \alpha\tanh(\alpha h) < k\tanh(kh) = K$ and $\alpha\tanh A^{-} < \alpha\tanh(\alpha d) < k\tanh(kh) = K$ which proves that $\Lambda < 0$. Finally, when $\alpha < 0$ one could prove that $A^{+} < \alpha d$ and $A^{-} > \alpha d$ which results to $A^{+} < A^{-}$. Therefore, using $\alpha\tanh A^{-} < \alpha\tanh A^{+}$ in the second term of (A.2.3) and then $\alpha\tanh A^{+} < \alpha\tanh(\alpha d) < k\tanh(kh) = K$, then it follows that again $\Lambda < 0$.

Proceeding to the next step, assuming that there are purely imaginary roots, then one would seek the solutions of $f(\xi) \equiv F(i\xi) = 0$ for $\xi \in \mathbb{R}$. Doing that, then the dispersion relation transforms to

$$\begin{aligned}f(\xi) = \Gamma(1-\theta)\tanh[\Gamma(h-d)]&\left(\frac{K\tan\left(d\sqrt{\xi^2-\alpha^2}\right)}{\sqrt{\xi^2-\alpha^2}}-1\right)\\ &+K+\sqrt{\xi^2-\alpha^2}\tan\left(d\sqrt{\xi^2-\alpha^2}\right),\end{aligned} \tag{A.2.4}$$

where $\Gamma = \alpha\sin\delta + i\xi\cos\delta$, which clearly has no real solutions in ξ because of the complex multiplicative term Γ. The complexity of the roots raised from the real differential operator $\partial_{XX}+\partial_{zz}$ (which acted on the velocity potential of the problem) that transformed into the complex operator $\cos^2\delta\partial_{xx}+2i\alpha\sin\delta\cos\delta\partial_x+\partial_{zz}-\alpha^2\sin^2\delta$ after the assumption of incident time-harmonicity and the y-compatibility of the total wave from the incident wave ($e^{i\alpha y}e^{-i\omega t}$). However, when $\delta = 0°$ and $\delta = 90°$ only, equation (A.2.4) becomes real and even, suggesting that the roots lie symmetrically on the imaginary axis. Therefore, the numerical strategy to get the those roots for a general $\delta \in (0°, 90°)$ is to use the known sequence of roots of the $\delta = 90°$ case (found in the previous section of the Appendix), then by the δ continuity of the dispersion relation, δ can be switched in small steps from 90° to the required angle and at each

iteration the roots can be found by applying 2D Newton's method on the complex plane, with initial guesses the roots of the previous iteration.

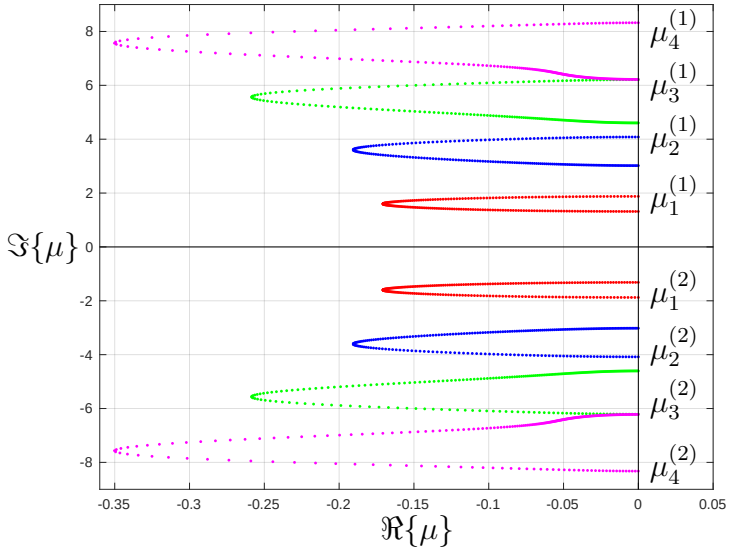

Figure A.5: Path of $\mu_n^{(i)}$ as δ varies from $90°$ to $0°$, for $i = 1, 2$ and $n = 1$ (red), $n = 2$ (blue), $n = 3$ (green) and $n = 4$ (magenta). The geometrical parameters are $k = 1$, $h = 2$, $d = 1.5$, $\theta_0 = 30°$ and $\theta = 0.1$.

The real roots are excluded from the plot as it was proven that for $\delta = 90°$ there are two real and symmetric roots and as δ decreases the symmetry breaks (but the existence of one positive and one negative root is guaranteed) and eventually when $\delta = 0°$ the symmetry on those real roots, rises again.

It can be seen from the plot that as δ decreases, the complex roots escape the imaginary axis and as δ approaches $0°$, the roots land back on the imaginary axis again. Also, the spacing between the dots in each coloured curve in A.5, shows the speed at which the roots move on the complex plane as the value of δ decreases at equal steps. One can see that the roots are symmetric about the real axis and this is because $F(\mu)$ from (A.2.1) satisfies $F(\overline{\mu}) = \overline{F(\mu)}$. The complex roots most of the times, escape the imaginary axis from the left. Despite that, there were cases when those roots escaped the imaginary axis from the right, for example when $\theta_0 < 0°$.

This can be seen by approximating $\gamma \tanh[\gamma(h-d)]$ for $0 \leq \epsilon \equiv 90 - \delta \ll 1$. Thus, by approximating $\cos\delta \approx \epsilon$ and $\sin\delta \approx 1$ and using the formula for the

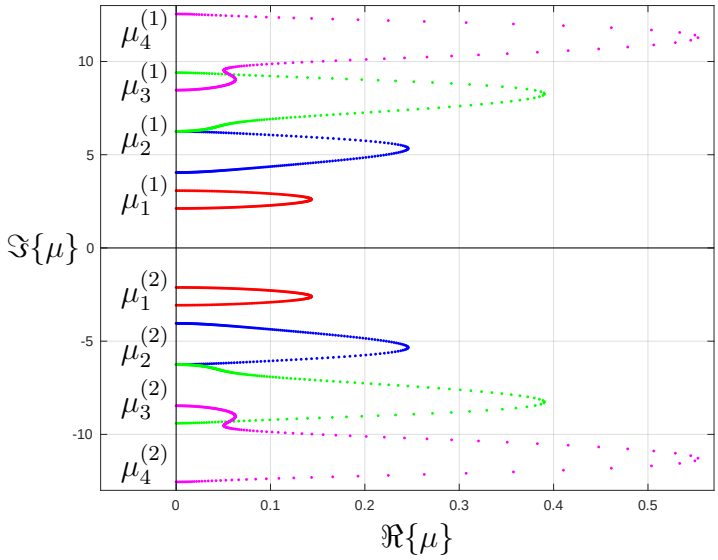

Figure A.6: Path of $\mu_n^{(i)}$ as δ varies from 90° to 0°, for $i = 1, 2$ and $n = 1$ (red), $n = 2$ (blue), $n = 3$ (green) and $n = 4$ (magenta). The geometrical parameters are $k = 0.5$, $h = 1.5$, $d = 1$, $\theta_0 = -45°$ and $\theta = 0.3$.

hyperbolic tangent of the sum then it can be proven that

$$\gamma \tanh[\gamma(h-d)] \approx \alpha \tanh[\alpha(h-d)] + \epsilon z \Big[\tanh[\alpha(h-d)] + \alpha(h-d)\mathrm{sech}^2[\alpha(h-d)] \Big], \tag{A.2.5}$$

by neglecting $\mathcal{O}(\epsilon^2)$. It can be seen that when δ is exactly 90° (or $\epsilon = 0$), then $\gamma \tanh[\gamma(h-d)] = \alpha \tanh[\alpha(h-d)]$ which is what was expected according to the previous section dispersion relation. However for a value of δ close but not equal to 90°, it can be seen that $\gamma \tanh[\gamma(h-d)]$ is shifted "linearly" by an infinitesimal distance (since the extra small term is proportional to z). Namely, $\gamma \tanh[\gamma(h-d)] \approx \alpha \tanh[\alpha(h-d)] + \epsilon z f(\alpha)$. According to (A.2.5), the sign of $f(\alpha)$ is the same as the sign of θ_0. Therefore if $\theta_0 > 0°$, then the δ-dependent part of the dispersion relation is shifted slightly on the left and when $\theta_0 < 0°$ is shifted slightly on the right.

Thus, the numerical method to capture those roots will involve only the calculation of the real roots $\mu_0^{(1)}$, $\mu_0^{(2)}$ (by bisecting the positive and negative real axis) and the complex roots $\mu_n^{(1)}$ (for $n = 1, ...N$ where N is some truncation parameter). There is no need to calculate the set of $\mu_n^{(2)}$ roots (for $n = 1, ...N$) as it can be found

directly by conjugating $\mu_n^{(1)}$.

For example, if the calculation of $|R|$ in terms of kb is needed, initially the first kb iteration is considered. In that iteration, the roots for $\delta = 90^\circ$ are calculated easily through bisection across the real and imaginary axis (as it is known from the previous section that the roots lie on the axes) and then δ is shifted down into small steps to the desired angle. In each of these steps, 2D Newton's method is applied on $F(x + iy)$ using, as initial guesses, the roots of the previous δ iteration. Therefore, recurrently the $\mu_n^{(1)}$ roots for the first kb iteration are captured. Then, in the next kb iteration, instead of the shifting δ from 90° to the desired orientation, the roots of the previous kb iteration can be used as initial guesses for applying the 2D Newton's method directly. This makes the code running much faster. The same idea can be applied for the numerical calculation of any scattering coefficient against any other geometrical parameter.

Appendix B

Eigenfunctions properties

B.1 Eigenfunction orthogonality of section 3.2.2

In this part of the Appendix, the depth eigenfunctions of (3.2.32) (which describe the z-variation of the velocity potential over the metamaterial) will be proved to be orthogonal under the inner product defined in (3.2.34). Although the problems involving this type of depth eigenfunctions are not Sturm–Liouville, it will be shown that they are orthogonal. There are many authors that showed orthogonality of depth eigenfunctions for problems that are not Sturm–Liouville involving fluid-structural interactions [96] or floating bodies over two-layer fluids [97][98].

Starting from the case of $n \neq m$, only the governing equation and boundary conditions of the eigenfunctions should be considered. Namely,

$$\begin{gathered}
\hat{\psi}_n''(z) = r_n^2 \hat{\psi}_n(z),\ \hat{\psi}_n'(0) = K\hat{\psi}_n(0) \text{ in } z \in L_g, \\
\hat{\psi}_n''(z) = \mu_n^2 \hat{\psi}_n(z),\ \hat{\psi}_n'(-h) = 0 \text{ in } z \in L_b, \\
\text{with } \hat{\psi}_n(-d^+) = \hat{\psi}_n(-d^-),\ \hat{\psi}_n'(-d^+) = (1-\theta)\hat{\psi}_n'(-d^-),
\end{gathered} \tag{B.1.1}$$

where $r_n^2 = \alpha^2 + \mu_n^2$. Using that $\mu_n \neq \mu_m$ for $n \neq m$, then

$$\begin{aligned}\Big(\mu_n^2 - \mu_m^2\Big)\langle\hat{\psi}_n, \hat{\psi}_m\rangle &= (1-\theta)\int_{-h}^{-d}\Big(\hat{\psi}_n''(z)\hat{\psi}_m(z) - \hat{\psi}_n(z)\hat{\psi}_m''(z)\Big)dz \\ &+\int_{-d}^{0}\Big[\Big(\hat{\psi}_n''(z) - \alpha^2\hat{\psi}_n(z)\Big)\hat{\psi}_m(z) - \hat{\psi}_n(z)\Big(\hat{\psi}_m''(z) - \alpha^2\hat{\psi}_m(z)\Big)\Big]dz.\end{aligned} \tag{B.1.2}$$

Note, that the first integrand (and the second integrand as they are identical after the $\hat{\psi}_n\hat{\psi}_m$ cancellation) can be written as $\big(\hat{\psi}_n'(z)\hat{\psi}_m(z) - \hat{\psi}_n(z)\hat{\psi}_m'(z)\big)'$. Applying the fundamental theorem of calculus on both integrands supported by the surface and bed conditions, then (B.1.2) is transformed into

$$\begin{aligned}\Big(\mu_n^2 - \mu_m^2\Big)\langle\hat{\psi}_n, \hat{\psi}_m\rangle &= \hat{\psi}_n(-d)\hat{\psi}_m'(-d^+) - \hat{\psi}_n'(-d^+)\hat{\psi}_m(-d) \\ &+(1-\theta)\hat{\psi}_n'(-d^-)\hat{\psi}_m(-d) - (1-\theta)\hat{\psi}_n(-d)\hat{\psi}_m'(-d^-) = 0,\end{aligned} \tag{B.1.3}$$

where the evaluations at $z = 0$ and $z = -h$ are eliminated after applying the conditions on the surface and the bed. Now that the zeroth derivative of $\hat{\psi}_n$ above is evaluated exactly at $z = -d$ (instead of the right or left side limits) as it is known that is continuous there from the first matching condition. In the last step the matching conditions at $z = -d$ were applied.

Moving on to the case of $n = m$ to verify the $\hat{N}_n$ expression specified in (3.2.33), then the inner product between $\hat{\psi}_n$ and $\hat{\psi}_m$ results to

$$\begin{aligned}\langle\hat{\psi}_n, \hat{\psi}_n\rangle = \hat{N}_n^{-1}\int_{-d}^{0}\Big(\cosh^2(r_n z) + \frac{K^2}{r_n^2}\sinh^2(r_n z) + \frac{K}{r_n}\sinh(2r_n z)\Big)dz \\ +\hat{N}_n^{-1}(1-\theta)D_n^2\int_{-h}^{-d}\cosh^2[\mu_n(z+h)]dz.\end{aligned} \tag{B.1.4}$$

Using the formulas $\sinh^2 x = \big(\cosh(2x)-1\big)/2$ and $\cosh^2 x = \big(\cosh(2x)+1\big)/2$, then after a considerable algebra the result to the integral above is found to be

$$\begin{aligned}\langle\hat{\psi}_n,\hat{\psi}_m\rangle = h\delta_{nm} \quad \text{for} \quad \hat{N}_n &= \frac{d}{h}\left[\frac{1}{2}+\frac{\sinh(2r_nd)}{4r_nd}\right]\\ -\frac{K^2d}{r_n^2h}&\left[\frac{1}{2}-\frac{\sinh(2r_nd)}{4r_nd}\right]-\frac{K}{r_n^2h}\sinh^2(r_nd)\\ +\frac{h-d}{h}&(1-\theta)D_n^2\left[\frac{1}{2}+\frac{\sinh\big(2\mu_n(h-d)\big)}{4\mu_n(h-d)}\right].\end{aligned} \tag{B.1.5}$$

B.2 Eigenfunction orthogonality of section 3.2.4

Now the orthogonality of the depth eigenfunctions in (3.2.49) over the gap between the metamaterial and the free surface will be proved. In the case of $n \neq m$, the governing equation and boundary conditions of $\hat{\psi}$ are considered. Namely,

$$\begin{gathered}\hat{\psi}_n''(z) = r_n^2\hat{\psi}_n(z),\ \hat{\psi}_n'(0) = K\hat{\psi}_n(0) \text{ in } z\in L_g,\\ \text{with } \hat{\psi}_n(-d^+) = \hat{\psi}_n(-d^-),\ \hat{\psi}_n'(-d^+) = (1-\theta)\hat{\psi}_n'(-d^-),\end{gathered} \tag{B.2.1}$$

where $r_n^2 = \alpha^2+\mu_n^2$. Starting from $n\neq m$, then

$$\begin{aligned}&\Big(\mu_n^2-\mu_m^2\Big)\int_{-d}^{0}\hat{\psi}_n(z)\hat{\psi}_m(z)dz\\ =&\int_{-d}^{0}\left[\Big(\hat{\psi}_n''(z)-\alpha^2\hat{\psi}_n(z)\Big)\hat{\psi}_m(z)-\hat{\psi}_n(z)\Big(\hat{\psi}_m''(z)-\alpha^2\hat{\psi}_m(z)\Big)\right]dz.\end{aligned} \tag{B.2.2}$$

Then after the $\hat{\psi}_n\hat{\psi}_m$ cancellation one could see that the integrand can be written as a full derivative i.e. $\big(\hat{\psi}_n'(z)\hat{\psi}_m(z)-\hat{\psi}_n(z)\hat{\psi}_m'(z)\big)'$. Thus, by applying the fundamental

theorem of calculus and making use of the surface condition, then

$$\begin{aligned}\Big(\mu_n^2-\mu_m^2\Big)\int_{-d}^{0}\hat{\psi}_n(z)\hat{\psi}_m(z)dz &= \hat{\psi}_n(-d^+)\hat{\psi}'_m(-d^+)-\hat{\psi}'_n(-d^+)\hat{\psi}_m(-d^+)\\ &= (1-\theta)\Big[\hat{\psi}_n(-d^-)\hat{\psi}'_m(-d^-)-\hat{\psi}'_n(-d^-)\hat{\psi}_m(-d^-)\Big],\end{aligned} \tag{B.2.3}$$

after the cancellation of the evaluations at $z=0$ and making use of the matching conditions at $z=-d$. Then using the definition of $\hat{\psi}_n(z)$ in L_b from (3.2.49), it will turn out that the result is zero because the only dependence of the eigenfunction in n and m comes only in the normalisation factors $\hat{N}_n^{-1/2}$, D_n and not in the hyperbolic cosine function (multiplicative coefficients can be taken outside the brackets as common factors even under differentiation). Therefore by this direct calculation, it is proved that the eigenfunctions are orthogonal.

Continuing on the case of $n=m$, then by using the $\hat{\psi}_n(z)$ expression, we get

$$\int_{-d}^{0}\hat{\psi}_n^2(z)dz=\hat{N}_n^{-1}\int_{-d}^{0}\bigg(\cosh^2(r_nz)+\frac{K^2}{r_n^2}\sinh^2(r_nz)+\frac{K}{r_n}\sinh(2r_nz)\bigg)dz. \tag{B.2.4}$$

Again by using the formulas $\sinh^2 x=\big(\cosh(2x)-1\big)/2$ and $\cosh^2 x=\big(\cosh(2x)+1\big)/2$, then after integrating the answer above is found to be d. Therefore, the orthogonality relation of $\hat{\psi}_n(z)$ becomes

$$\int_{-d}^{0}\hat{\psi}_n(z)\hat{\psi}_m(z)dz=d\delta_{nm}. \tag{B.2.5}$$

B.3 Calculation of G_{nm} and B_{nm} of section 3.2.2

In this section the integral expressions of G_{nm} and B_{nm} specified in (3.2.36) will be calculated using ideas from the previous sections. First, the integral over $\psi_n\hat{\psi}_m$ in L_g and L_b separetly, are considered. Starting from the integral over the gap L_g, then

$$\begin{aligned}\left(k_n^2 - r_m^2\right)\int_{-d}^{0}\psi_n(z)\hat{\psi}_m(z)dz &= \int_{-d}^{0}\left(\psi_n''(z)\hat{\psi}_m(z) - \psi_n(z)\hat{\psi}_m''(z)\right)dz \\ &= \int_{-d}^{0}\left(\psi_n'(z)\hat{\psi}_m(z) - \psi_n(z)\hat{\psi}_m'(z)\right)'dz.\end{aligned} \tag{B.3.1}$$

Next, by applying the fundamental theorem of calculus and making use of the surface condition at $z = 0$, then

$$\left(k_n^2 - r_m^2\right)\int_{-d}^{0}\psi_n(z)\hat{\psi}_m(z)dz = (1-\theta)\psi_n(-d)\hat{\psi}_m'(-d^-) - \psi_n'(-d)\hat{\psi}_m(-d^-), \tag{B.3.2}$$

by matching the eigenfunctions through $z = -d$. Using the solutions of ψ_n and $\hat{\psi}_m$ found in (3.2.22) and (3.2.32) respectively, then

$$\begin{aligned}G_{nm} = \frac{1}{h}\int_{-d}^{0}\psi_n(z)\hat{\psi}_m(z)dz = \Big\{&(1-\theta)\mu_m\cosh[k_n(h-d)]\sinh[\mu_m(h-d)] \\ &-k_n\sinh[k_n(h-d)]\cosh[\mu_m(h-d)]\Big\}\frac{N_n^{-1/2}\hat{N}_m^{-1/2}D_m}{\left(k_n^2 - r_m^2\right)h}.\end{aligned} \tag{B.3.3}$$

Following the same procedure as in (B.3.1), but using the multiplicative

factor $(k_n^2 - \mu_m^2)$ instead of $(k_n^2 - r_m^2)$, then

$$\left(k_n^2 - \mu_m^2\right) \int_{-h}^{-d} \psi_n(z)\hat{\psi}_m(z)dz = \psi_n'(-d)\hat{\psi}_m(-d^-) - \psi_n(-d)\hat{\psi}_m'(-d^-), \tag{B.3.4}$$

by applying the fundamental theorem of calculus again. Using the eigenfunction definitions again, then the integral over the barrier L_b, becomes

$$\begin{aligned} B_{nm} = \frac{1}{h} \int_{-d}^{0} \psi_n(z)\hat{\psi}_m(z)dz = \Big\{ & k_n \sinh[k_n(h-d)] \cosh[\mu_m(h-d)] \\ & -\mu_m \cosh[k_n(h-d)] \sinh[\mu_m(h-d)] \Big\} \frac{N_n^{-1/2} \hat{N}_m^{-1/2} D_m}{\left(k_n^2 - \mu_m^2\right)h}. \end{aligned} \tag{B.3.5}$$

Appendix C

Integral terms simplification of Chapter 5

C.1 Crack of finite width

In this part of the Appendix, the integrals needed to calculate numerically the reflection and transmission coefficients of the problem analysed in section 5.2.1, are considered. First, an explanation is given on how to compute numerically the integrals used in the linear systems (5.2.26), (5.2.43) to find $P^{s,a}$ and $Q^{s,a}$. Some of those semi-infinite integrals can be transformed into fast convergent integrals by using the ice sheet dispersion relation properly. Then using the Cauchy's residue theorem, those integrals can be evaluated as infinite sums.

All the integrals of the problem, are along the positive real line but they avoid the β_0 pole from below. Therefore, for an integrand $f(\xi)$ with a pole at β_0 the numerical integral will be calculated as follows

$$\begin{aligned} &\int\!\!\!\!\!\!-_0^\infty f(\xi)d\xi = \left(\int_0^{\beta_0-\epsilon} + \int_{\beta_0+\epsilon}^{\infty} \right) f(\xi)d\xi + i\pi \mathrm{Res}\Big[f(\xi);\xi=\beta_0\Big] \approx \\ &\approx \int_0^{\beta_0-\epsilon} \Big[f(\xi)+f(2\beta_0-\xi)\Big]d\xi + \int_{2\beta_0}^{N_i} f(\xi)d\xi + i\pi \mathrm{Res}\Big[f(\xi);\xi=\beta_0\Big], \end{aligned} \tag{C.1.1}$$

where the first line is equating an integral with a contour passing below the pole to a real Cauchy-principal value integral plus the contribution from the indentation below the pole which equates to half a residue. On the last step, the infinite integral was split into two integrals over $(\beta_0+\epsilon, 2\beta_0)$ and $(2\beta_0, \infty)$ and the substitution $\xi = 2\beta_0 - t$ was introduced in the first. The approximately equal sign came by truncating the infinite integral to $N_i \gg 1$.

Starting from the semi-infinite integrals of the symmetric problem (see equation (5.2.26)), then

$$F_1^s(a^+) = \frac{2\beta}{\pi} \int_0^\infty \frac{k \tanh(kh)}{\Delta(k)} \Big(\xi^2 + \nu\alpha_0^2\Big) \cos^2(a\xi) d\xi, \tag{C.1.2}$$

written in compact notation, instead of (C.1.1). It can be seen that this integral is convergent as its integrand is asymptotic to $\xi^{-2}\cos^2(a\xi)$ as $\xi \to \infty$. However, $F_2^s(x)$ and $F_1^{s'}(x)$ need some extra treatment to avoid divergence as their integrands are asymptotic to ξ^{-1} times some trigonometric functions as $\xi \to \infty$. Therefore using the $\Delta(k)$ definition from (5.1.7), then

$$\begin{aligned}
\frac{\beta k \tanh(kh)}{\Delta(k)} \Big(\xi^3 + (2-\nu)\alpha_0^2\xi\Big) &= \frac{1}{\xi} - \frac{\big[\beta\alpha_0^2(\alpha_0^2 + \nu\xi^2) + 1 - K\delta\big] k\tanh(kh) - K}{\xi\Delta(k)}, \\
\frac{\beta k \tanh(kh)}{\Delta(k)} \xi\Big(\xi^2 + \nu\alpha_0^2\Big) &= \frac{1}{\xi} - \frac{\big[\beta\alpha_0^2(\alpha_0^2 + (2-\nu)\xi^2) + 1 - K\delta\big] k\tanh(kh) - K}{\xi\Delta(k)},
\end{aligned} \tag{C.1.3}$$

where by making use of the identity $\int_0^\infty \frac{\sin(Ax)\cos(Bx)}{x} dx = \frac{\pi}{4}\Big[\mathrm{sgn}(A+B) + \mathrm{sgn}(A-B)\Big]$,

the expressions for the required quantities become

$$
\begin{aligned}
F_2^s(a^+) &= -\frac{1}{\pi}\int_0^\infty \frac{\big[\beta\alpha_0^2(\alpha_0^2+\nu\xi^2)+1-K\delta\big]k\tanh(kh)-K}{\xi\Delta(k)}\sin(2a\xi)d\xi,\\
F_1^{s'}(a^+) &= -1+\frac{1}{\pi}\int_0^\infty \frac{\big[\beta\alpha_0^2(\alpha_0^2+(2-\nu)\xi^2)+1-K\delta\big]k\tanh(kh)-K}{\xi\Delta(k)}\sin(2a\xi)d\xi,\\
F_2^{s'}(a^+) &= \frac{2}{\pi}\int_0^\infty \frac{\big[\beta\alpha_0^2(\alpha_0^2+\nu\xi^2)+1-K\delta\big]k\tanh(kh)-K}{\Delta(k)}\sin^2(a\xi)d\xi,
\end{aligned}
\tag{C.1.4}
$$

where the last equation can be maintained by differentiating the F_2^s with respect to x after making use of the dispersion relation. This procedure was used in [41] to improve convergence in integrals. Note that now the first two integrands go like ξ^{-3} and the last as ξ^{-2} as $\xi\to\infty$ (times a trigonometric function), which means that they converge mush faster now.

The quantities defined above are the scalar integrals needed for the problem. Proceeding to the vectors and matrices of the system (5.2.26), $M^s_{2n,2m}$ and $f^{(i)}_{2n}$ $(i=1,2,3)$ can be found from (5.2.25) and K^s_{2n} and $K^{s'}_{2n}$ from (5.2.26) in integral form. All those integrals are convergent as $j_{2n}(z)\sim\sin(z)/z$ (times a multiplicative factor that depends on n) as $z\to\infty$, so there is no need to modify them. The expressions of $f^{(i)}_{2n}$ for $i=1,2,3$ in explicit form are

$$
\begin{aligned}
f^{(1)}_{2n} &= \frac{2\beta}{\pi}\int_0^\infty \frac{k\tanh(kh)}{\Delta(k)}\big(\xi^2+\nu\alpha_0^2\big)\cos(a\xi)j_{2n}(a\xi)d\xi,\\
f^{(2)}_{2n} &= \frac{2\beta}{\pi}\int_0^\infty \frac{k\tanh(kh)}{\Delta(k)}\big(\xi^3+(2-\nu)\alpha_0^2\xi\big)\sin(a\xi)j_{2n}(a\xi)d\xi.
\end{aligned}
\tag{C.1.5}
$$

and $f^{(3)}_{2n}=j_{2n}(\beta_0 a)$.

Now, all the integrals defined above will be evaluated as infinite sums using the Cauchy's residue theorem. The procedure is very similar to the one used to calculate the R^s expression in (5.2.45). The first step is to write the semi-integrals

as half of the infinite integrals since all integrands are even. However, the $-\beta_0$ pole must be avoided from above so that the radiation condition is satisfied. Then, typically a trigonometric function of the integrand is written in terms of two complex exponentials and then the integral is split into two - one integral over a function proportional to $e^{ia\xi}$ and the other integral over a function proportional to $e^{-ia\xi}$. Next, the first integral can be written as the sum of the residues of the poles β_r (for $r \geq -2$) which lie in the upper half plane using the Cauchy's residue theorem. The contribution at infinity is zero because the integrand is asymptotic to $\xi^{-n}e^{ia\xi}$ (for some $n \in \mathbb{N}$) times a trigonometric function (possibly) evaluated at $a\xi$. For the second integral over $e^{-ia\xi}$, the same method is applied but now the contour must be over the lower half plane to guarantee the decay of $e^{-ia\xi}$ at infinity. The second sum will now be over the $-\beta_r$ ($r \geq -2$) poles but due to the even behaviour of the integrated functions, it will always turn out that the two infinite sums are identical and can be combined to one. Here, one may point out that the trigonometric functions evaluated at β_r are blowing up exponentially as $r \to \infty$. However they are balanced as they are always balanced by $e^{i\beta_r a}$ which are exponentially decaying. Therefore by applying this procedure into the convergent integral of (C.1.2), then

$$F_1^s(a^+) = i\beta \sum_{r=-2}^{\infty} \frac{k_r^2 \tanh(k_r h)}{\beta_r \Delta'(k_r)} \big(\beta_r^2 + \nu\alpha_0^2\big)\big(1 + e^{2i\beta_r a}\big), \tag{C.1.6}$$

where the last bracket came by writing $\cos(\beta_r a)e^{i\beta_r a}$ into complex exponentials for numerical stability purposes. It is known that the roots k_r (or β_r) tend to $ir\pi/h$ as $r \to \infty$ and so the terms of the sum above tend to $r^{-2}(1 + e^{-2r\pi a/h})$ which implies that the sums converge fast.

Proceeding to the integrals of (C.1.4), there are two ways to write them as infinite sums. First is to expand $\sin(2a\xi)$ in terms of complex exponentials and apply the Cauchy's residue theorem as usual. But by doing that a new pole at zero is created as now there will be two integrals over $e^{\pm 2ia\xi}/\xi$. The residue of this pole must be calculated separately from the residues of $\pm\beta_r$. Therefore the result will be a constant (coming from the residue of the pole at zero) plus an infinite sum over a fractional expression evaluated at β_r times $e^{2i\beta_r a}$. The second way, will be to use the formula $\sin(2a\xi) = 2\sin(a\xi)\cos(a\xi)$ and write only $\cos(a\xi)$ in terms of complex exponentials. The decay at infinity will be guaranteed and now there will be no creation of extra poles as it is known that $\sin(a\xi)/\xi$ has a removable singularity at $\xi = 0$. The result will be an infinite sum over the same expression as before but now

times $(1-e^{2i\beta_r a})$. By equating the two results (as they come from the same integral expression), then values for some infinite sums can be calculated [52]. However, our interest does not lie on the explicit calculation of these sums so these formulas will not be included here, but their derivation is relatively straightforward if the procedure discussed here is followed. Thus, from now on, only the first way will be used i.e. expanding $\sin(2a\xi)$ in terms of complex exponentials and treating the extra pole at zero separately. Therefore, the integrals of (C.1.4) and (C.1.5) become

$$\begin{aligned}
F_2^s(a^+) &= -\frac{1}{2} - \sum_{r=-2}^{\infty} k_r \frac{\big[\beta\alpha_0^2(\alpha_0^2+\nu\beta_r^2)+1-K\delta\big]k_r\tanh(k_r h)-K}{\beta_r^2\Delta'(k_r)} e^{2i\beta_r a},\\
F_1^{s'}(a^+) &= -\frac{1}{2} + \sum_{r=-2}^{\infty} k_r \frac{\big[\beta\alpha_0^2(\alpha_0^2+(2-\nu)\beta_r^2)+1-K\delta\big]k_r\tanh(k_r h)-K}{\beta_r^2\Delta'(k_r)} e^{2i\beta_r a},\\
F_2^{s'}(a^+) &= i\sum_{r=-2}^{\infty} k_r \frac{\big[\beta\alpha_0^2(\alpha_0^2+\nu\beta_r^2)+1-K\delta\big]k_r\tanh(k_r h)-K}{\beta_r\Delta'(k_r)} \big(1-e^{2i\beta_r a}\big),\\
f_{2n}^{(1)} &= 2i\beta\sum_{r=-2}^{\infty} \frac{k_r^2\tanh(k_r h)}{\beta_r\Delta'(k_r)} (\beta_r^2+\nu\alpha_0^2) j_{2n}(\beta_r a) e^{i\beta_r a},\\
f_{2n}^{(2)} &= 2\beta\sum_{r=-2}^{\infty} \frac{k_r^2\tanh(k_r h)}{\beta_r\Delta'(k_r)} \big(\beta_r^3+(2-\nu)\alpha_0^2\beta_r\big) j_{2n}(\beta_r a) e^{i\beta_r a},
\end{aligned} \tag{C.1.7}$$

where in the first three sums the trigonometric functions were combined with the complex exponentials. Note that all those sums converge very quickly as in the first two their terms tend to $r^{-3}(1-e^{-2r\pi a/h})$, the third to $r^{-2}(1-e^{-2r\pi a/h})$, the fourth to $r^{-2}j_{2n}(ir\pi a/h)e^{-r\pi a/h}$ and the fifth to $r^{-1}j_{2n}(ir\pi a/h)e^{-r\pi a/h}$. The convergence of the last two can be proved using the fact that $j_{2n}(ix)\sim e^x/x$ (times a multiplicative constant that depends on n) from [75], equations (9.6.3) and (9.7.1). Next, the expressions of K_{2n}^s and $K_{2n}^{s'}$ from (5.2.26) are transformed to

$$\begin{aligned}
K_{2n}^s &= i\pi a\sum_{r=-2}^{\infty} k_r \frac{K-k_r\tanh(k_r h)}{\beta_r\Delta'(k_r)} j_{2n}(\beta_r a) e^{i\beta_r a},\\
K_{2n}^{s'} &= \pi a\sum_{r=-2}^{\infty} k_r \frac{K-k_r\tanh(k_r h)}{\Delta'(k_r)} j_{2n}(\beta_r a) e^{i\beta_r a},
\end{aligned} \tag{C.1.8}$$

where again the convergence is guaranteed. It remains to write $M^s_{2n,2m}$ in summation form. First, the semi-infinite integral is written as half of the infinite integral (due to even integrand), but since its integrand is proportional to $j_{2n}(a\xi)j_{2m}(a\xi)$ (instead of trigonometric functions) then one of the spherical Bessel functions should be written as $j_{2m}(a\xi) = \left[h^{(1)}_{2m}(a\xi) + h^{(2)}_{2m}(a\xi)\right]/2$ where $h^{(p)}_{2m}(z) = j_{2m}(z) - i(-1)^p y_{2m}(z)$ is the spherical Hankel functions (or Bessel functions of third kind) and $y_{2m}(z)$ is the spherical Weber function (or Bessel function of second kind). By doing that, if the integral is divided into two integrals - one over $h^{(1)}_{2m}$ and the other over $h^{(2)}_{2m}$ - then the decay is guaranteed in the far field of upper and lower half of the complex plane respectively, as $j_{2n}(z)h^{(p)}_{2m}(z) \sim \sin(z)e^{-i(-1)^p z}/z^2$ (times a multiplicative constant that depends on n and m) as $|z| \to \infty$. But by doing that, a pole at $\xi = 0$ is created as h_{2m} is singular at the origin. So, once the integrand is written in in terms of Hankel functions then the pole at $\xi = 0$ is avoided from below (without the loss of generality) and so when the Cauchy's residue theorem is applied, the contribution of that pole will be included in the contour over the upper half plane. Also, a key feature of the matrix $M^s_{2n,2m}$ is that it is symmetric, which can be seen from its integral representation in (5.2.25). Therefore, only the $n \geq m$ elements of it should be calculated without the loss of generality, and the remaining elements above the diagonal can be copied from the elements below the diagonal. Thus by writing the integral over the whole real line, then decomposing j_{2m} in terms of Hankel functions, splitting the integral and applying the Cauchy's residue theorem, then

$$\begin{aligned} M^s_{2n,2m} &= i\pi a \sum_{r=-2}^{\infty} k_r \frac{K - k_r \tanh(k_r h)}{\beta_r \Delta'(k_r)} j_{2n}(\beta_r a) h^{(1)}_{2m}(\beta_r a) \\ &+ \frac{i\pi a}{2} \frac{K - \alpha_0 \tanh(\alpha_0 h)}{\Delta(\alpha_0)} \mathrm{Res}\Big[j_{2n}(a\xi)h^{(1)}_{2m}(a\xi); \xi = 0\Big] \text{ for } n \geq m, \end{aligned} \tag{C.1.9}$$

where the sum is the combined contribution of the $\pm\beta_r$ poles using that $h^{(2)}_{2m}(-z) = h^{(1)}_{2m}(z)$ from [75], equation (10.1.37) and the last term is the contribution of the pole at $\xi = 0$. The residue found in the equation above is calculated using the asymptotic formulas for j_{2m} and y_{2m} for small arguments from [75], equations (10.1.4) and (10.1.5) as

$$j_{2n}(z)h^{(1)}_{2m}(z) \sim \frac{z^{2(n+m)}}{(4n+1)!!(4m+1)!!} - i\frac{(4m-1)!!}{(4n+1)!!}\frac{z^{2(n-m)}}{z} \quad \text{as} \quad |z| \to 0, \tag{C.1.10}$$

where the double factorial $n!!$ is defined as the product of all integers from 1 to n that have the same parity as n. Note that normally $n, m \in \mathbb{N}_0$ and so the first term of the right-hand side above becomes $\delta_{n0}\delta_{m0}$ in the small z limit, which has no residue as it is not a pole. Now the second term is asymptotic to $-i\delta_{nm}/(4n+1)z$, since $n \geq m$ which imply that the residue of the product $j_{2n}(a\xi)h^{(1)}_{2m}(a\xi)$ at the pole at $\xi = 0$ is $-i\delta_{nm}/(4n+1)a$. Combining (C.1.9) with the information specified above, then

$$\begin{aligned} M^s_{2n,2m} = i\pi a \sum_{r=-2}^{\infty} k_r \frac{K - k_r \tanh(k_r h)}{\beta_r \Delta'(k_r)} j_{2n}(\beta_r a) h^{(1)}_{2m}(\beta_r a) \\ + \frac{\pi \delta_{nm}}{2(4n+1)} \frac{K - \alpha_0 \tanh(\alpha_0 h)}{\Delta(\alpha_0)} \text{ for } n \geq m, \end{aligned} \tag{C.1.11}$$

which converges as $j_{2n}(ix)h^{(1)}_{2m}(ix) \sim x^{-2}$ (times a multiplicative factor that depends on n and m) as $x \to \infty$ from [75], equations (9.6.3), (9.7.1), (9.6.4) and (9.7.2). This asymptotic formula can also be verified by substituting $z = ix$ into the asymptotic formula discussed after equation (C.1.8). The last equation concludes the calculations for all the quantities needed to find R^s from (5.2.29).

Proceeding to the calculation of the antisymmetric integrals, then it can be seen that $F^a_1(a^+)$ is convergent but for the integrals $F^a_2(a^+)$, $F^{a'}_1(a^+)$, $F^{a'}_2(a^+)$ equation (C.1.3) must be used. Therefore,

$$\begin{aligned} F^a_1(a^+) &= \frac{2\beta}{\pi} \int_0^{\infty} \frac{k \tanh(kh)}{\Delta(k)} \left(\xi^2 + \nu\alpha_0^2\right) \sin^2(a\xi) d\xi, \\ F^a_2(a^+) &= 1 - \frac{1}{\pi} \int_0^{\infty} \frac{\left[\beta\alpha_0^2(\alpha_0^2 + \nu\xi^2) + 1 - K\delta\right] k \tanh(kh) - K}{\xi\Delta(k)} \sin(2a\xi) d\xi, \\ F^{a'}_1(a^+) &= -\frac{1}{\pi} \int_0^{\infty} \frac{\left[\beta\alpha_0^2(\alpha_0^2 + (2-\nu)\xi^2) + 1 - K\delta\right] k \tanh(kh) - K}{\xi\Delta(k)} \sin(2a\xi) d\xi, \\ F^{a'}_2(a^+) &= -\frac{2}{\pi} \int_0^{\infty} \frac{\left[\beta\alpha_0^2(\alpha_0^2 + \nu\xi^2) + 1 - K\delta\right] k \tanh(kh) - K}{\Delta(k)} \cos^2(a\xi) d\xi, \end{aligned} \tag{C.1.12}$$

where some antisymmetric integrals can be related to the symmetric ones, namely

$F_2^a(a^+) = 1 + F_2^s(a^+)$ and $F_1^{a'}(a^+) = -1 - F_1^{s'}(a^+)$. The convergence of the integrals above is guaranteed as the integrands tend to ξ^{-n} times a trigonometric function for $n = 2, 3$ as $\xi \to \infty$.

Moving on, by considering the integrals of $M^a_{2n+1,2m+1}$, $f^{(i)}_{2n+1}$ for $i = 1, 2$ (since $f^{(3)}_{2n+1} = j_{2n+1}(\beta_0 a)$ is explicit) from (5.2.42) and K^a_{2n+1}, $K^{a'}_{2n+1}$ from (5.2.43), then it can be seen that they are convergent as $j_{2n+1}(z) \sim \cos(z)/z$ (times a multiplicative constant that depends on n) as $z \to \infty$. The integral representation of $f^{(i)}_{2n+1}$ $(i = 1, 2)$ is

$$\begin{aligned} f^{(1)}_{2n+1} &= \frac{2\beta}{\pi} \int_0^\infty \frac{k \tanh(kh)}{\Delta(k)} \left(\xi^2 + \nu\alpha_0^2\right) \sin(a\xi) j_{2n+1}(a\xi) d\xi, \\ f^{(2)}_{2n+1} &= \frac{2\beta}{\pi} \int_0^\infty \frac{k \tanh(kh)}{\Delta(k)} \left(\xi^3 + (2-\nu)\alpha_0^2 \xi\right) \cos(a\xi) j_{2n+1}(a\xi) d\xi. \end{aligned} \tag{C.1.13}$$

Now the same principles used in the symmetric integrals, will be used here as well to turn again the infinite integrals into infinite sums through the Cauchy's residue theorem. Note, that again all the integrands are even and so the integrals can be expressed over the real line in the same way as before. The first set of integrals

specified in (C.1.12) and (C.1.13) become

$$
\begin{aligned}
F_1^a(a^+) &= i\beta \sum_{r=-2}^{\infty} \frac{k_r^2 \tanh(k_r h)}{\beta_r \Delta'(k_r)} \big(\beta_r^2 + \nu\alpha_0^2\big)\big(1 - e^{2i\beta_r a}\big), \\
F_2^a(a^+) &= \frac{1}{2} - \sum_{r=-2}^{\infty} k_r \frac{\big[\beta\alpha_0^2(\alpha_0^2 + \nu\beta_r^2) + 1 - K\delta\big] k_r \tanh(k_r h) - K}{\beta_r^2 \Delta'(k_r)} e^{2i\beta_r a}, \\
F_1^{a'}(a^+) &= -\frac{1}{2} - \sum_{r=-2}^{\infty} k_r \frac{\big[\beta\alpha_0^2(\alpha_0^2 + (2-\nu)\beta_r^2) + 1 - K\delta\big] k_r \tanh(k_r h) - K}{\beta_r^2 \Delta'(k_r)} e^{2i\beta_r a}, \\
F_2^{a'}(a^+) &= -i \sum_{r=-2}^{\infty} k_r \frac{\big[\beta\alpha_0^2(\alpha_0^2 + \nu\beta_r^2) + 1 - K\delta\big] k_r \tanh(k_r h) - K}{\beta_r \Delta'(k_r)} \big(1 + e^{2i\beta_r a}\big), \\
f_{2n+1}^{(1)} &= 2\beta \sum_{r=-2}^{\infty} \frac{k_r^2 \tanh(k_r h)}{\beta_r \Delta'(k_r)} (\beta_r^2 + \nu\alpha_0^2) j_{2n+1}(\beta_r a) e^{i\beta_r a}, \\
f_{2n+1}^{(2)} &= 2i\beta \sum_{r=-2}^{\infty} \frac{k_r^2 \tanh(k_r h)}{\beta_r \Delta'(k_r)} \big(\beta_r^3 + (2-\nu)\alpha_0^2 \beta_r\big) j_{2n+1}(\beta_r a) e^{i\beta_r a},
\end{aligned}
\tag{C.1.14}
$$

where in the last two equations, the two infinite sums (one over β_r and the other over $-\beta_r$) were combined into one using the fact the j_{2n+1} is odd. Also, it can be verified that all the sums converge. The terms of the first four sums tend to $r^{-n}(1 \pm e^{-2r\pi a/h})$ for $n = 2, 3$ as $r \to \infty$ and the terms of the last two, tend to r^{-n} for $n = 2, 3$ as $j_{2n+1}(ix) \sim e^x/x$ (times a multiplicative constant that depends on n). Moving on to the next quantities specified in (5.2.43), then

$$
\begin{aligned}
K_{2n+1}^a &= \pi a \sum_{r=-2}^{\infty} k_r \frac{K - k_r \tanh(k_r h)}{\beta_r \Delta'(k_r)} j_{2n+1}(\beta_r a) e^{i\beta_r a}, \\
K_{2n+1}^{a'} &= i\pi a \sum_{r=-2}^{\infty} k_r \frac{K - k_r \tanh(k_r h)}{\Delta'(k_r)} j_{2n+1}(\beta_r a) e^{i\beta_r a}.
\end{aligned}
\tag{C.1.15}
$$

Lastly, the integral representation of the matrix $M_{2n+1,2m+1}^a$, should be considered. Again, this will be a more demanding calculation as the integral is over a product of spherical Bessel functions instead of trigonometric functions. Note that since this matrix is symmetric, then only the lower off-diagonal entries could be cal-

culated ($n \geq m$). The reason for not calculating the upper off-diagonal elements, will be explained later. First by expressing the integral over the whole real line (as integrand is even), then one of the two spherical Bessel functions is rewritten as $j_{2m+1}(z) = \left[h^{(1)}_{2m+1}(z) + h^{(2)}_{2m+1}(z)\right]/2$. By doing that, then if the integral is divided into two (one over $h^{(1)}_{2m+1}$ and the other over $h^{(2)}_{2m+1}$), then the decay is guaranteed in the upper and lower half planes respectively. However by doing that, a new pole at the origin is created from $h^{(p)}_{2m+1}$ and its contribution must be taken into account at one of the two integrals (upper half plane or for $p = 1$ without the loss of generality). Therefore,

$$\begin{aligned} M^a_{2n+1,2m+1} &= i\pi a \sum_{r=-2}^{\infty} k_r \frac{K - k_r \tanh(k_r h)}{\beta_r \Delta'(k_r)} j_{2n+1}(\beta_r a) h^{(1)}_{2m+1}(\beta_r a) \\ &+ \frac{i\pi a}{2} \frac{K - \alpha_0 \tanh(\alpha_0 h)}{\Delta(\alpha_0)} \mathrm{Res}\Big[j_{2n+1}(a\xi) h^{(1)}_{2m+1}(a\xi); \xi = 0\Big] \text{ for } n \geq m, \end{aligned} \tag{C.1.16}$$

by combing the two sums through $h^{(2)}_{2m+1}(-z) = -h^{(2)}_{2m+1}(z)$ from [75], equation (10.1.37). Now the residue specified above must be calculated using the asymptotic expansions for small arguments in the Bessel and Hankel function (see equation (C.1.10)). Therefore when $n \geq m$, it can be seen that $j_{2n+1}(z) h^{(1)}_{2m+1}(z) \sim -i\delta_{nm}/(4n+3)z$ as $|z| \to 0$. Thus, the last integral written in summation form is

$$\begin{aligned} M^a_{2n+1,2m+1} &= i\pi a \sum_{r=-2}^{\infty} k_r \frac{K - k_r \tanh(k_r h)}{\beta_r \Delta'(k_r)} j_{2n+1}(\beta_r a) h^{(1)}_{2m+1}(\beta_r a) \\ &+ \frac{\pi \delta_{nm}}{2(4n+3)} \frac{K - \alpha_0 \tanh(\alpha_0 h)}{\Delta(\alpha_0)} \text{ for } n \geq m. \end{aligned} \tag{C.1.17}$$

C.2 Small crack filled with viscous fluid

In this section, all the integrals of section 5.3.2 will be turned into infinite sums using the Cauchy's residue theorem. The viscous problem will be formulated with infinite sums as their calculation is generally more computationally inexpensive. Starting from the first three (x-averaged) integrals of the symmetric problem found in (5.3.36),

then

$$\begin{aligned}
\tilde{I}_0^s &= 1 - 2ia\sum_{r=-2}^{\infty}\frac{K-(1-s_u^s)k_r\tanh(k_rh)}{\Delta'(k_r)}j_0(k_ra)h_0^{(1)}(k_ra)\\
&-2\beta e_u^{s,1}\sum_{r=-2}^{\infty}\frac{k_r^2\tanh(k_rh)}{\Delta'(k_r)}j_0(k_ra)e^{ik_ra}-2i\beta e_u^{s,2}\sum_{r=-2}^{\infty}\frac{k_r\tanh(k_rh)}{\Delta'(k_r)}j_0(k_ra)e^{ik_ra},\\
\tilde{I}_1^s &= 2i\beta e_P^{s,2}\sum_{r=-2}^{\infty}\frac{k_r\tanh(k_rh)}{\Delta'(k_r)}j_0(k_ra)e^{ik_ra}-2i\beta\sum_{r=-2}^{\infty}\frac{k_r^3\tanh(k_rh)}{\Delta'(k_r)}j_0(k_ra)e^{ik_ra}\\
&+2\beta e_P^{s,1}\sum_{r=-2}^{\infty}\frac{k_r^2\tanh(k_rh)}{\Delta'(k_r)}j_0(k_ra)e^{ik_ra}+2ias_P^s\sum_{r=-2}^{\infty}\frac{k_r\tanh(k_rh)}{\Delta'(k_r)}j_0(k_ra)h_0^{(1)}(k_ra),\\
\tilde{I}_2^s &= 2ias_Q^s\sum_{r=-2}^{\infty}\frac{k_r\tanh(k_rh)}{\Delta'(k_r)}j_0(k_ra)h_0^{(1)}(k_ra)+2\sum_{r=-2}^{\infty}\frac{E(k_r)}{k_r\Delta'(k_r)}j_0(k_ra)e^{ik_ra}\\
&+2\beta e_Q^{s,1}\sum_{r=-2}^{\infty}\frac{k_r^2\tanh(k_rh)}{\Delta'(k_r)}j_0(k_ra)e^{ik_ra}+2i\beta e_Q^{s,2}\sum_{r=-2}^{\infty}\frac{k_r\tanh(k_rh)}{\Delta'(k_r)}j_0(k_ra)e^{ik_ra},
\end{aligned}\tag{C.2.1}$$

where the $+1$ term in $\tilde{I}_0^s$ came from the contribution of the pole at zero of the integral over $j_0(a\xi)h_0^{(1)}(a\xi)$ (when splitting the integral contour into the lower and upper half complex plane to guarantee decay at infinity). This residue can be calculated easily using the asymptotic formula (C.1.10). Moving on to the three second derivatives

and three third derivatives of functionals found in (5.3.37) and (5.3.38), then

$$
\begin{aligned}
I_0^{s''} &= -2ia\sum_{r=-2}^{\infty}\frac{K-(1-s_u^s)k_r\tanh(k_rh)}{\Delta'(k_r)}k_r^2j_0(k_ra)e^{ik_ra}-e_u^{s,1}\\
&+e_u^{s,1}\sum_{r=-2}^{\infty}\frac{E(k_r)}{k_r\Delta'(k_r)}e^{2ik_ra}-i\beta e_u^{s,2}\sum_{r=-2}^{\infty}\frac{k_r^3\tanh(k_rh)}{\Delta'(k_r)}(1+e^{2ik_ra}),\\
I_1^{s''} &= -2ias_P^s\sum_{r=-2}^{\infty}\frac{k_r^3\tanh(k_rh)}{\Delta'(k_r)}j_0(k_ra)e^{ik_ra}-i\sum_{r=-2}^{\infty}\frac{E(k_r)}{\Delta'(k_r)}(1+e^{2ik_ra})\\
&-e_P^{s,1}+e_P^{s,1}\sum_{r=-2}^{\infty}\frac{E(k_r)}{k_r\Delta'(k_r)}e^{2ik_ra}-i\beta e_P^{s,2}\sum_{r=-2}^{\infty}\frac{k_r^3\tanh(k_rh)}{\Delta'(k_r)}(1+e^{2ik_ra}),\\
I_2^{s''} &= -2ias_Q^s\sum_{r=-2}^{\infty}\frac{k_r^3\tanh(k_rh)}{\Delta'(k_r)}j_0(k_ra)e^{ik_ra}-\sum_{r=-2}^{\infty}\frac{E(k_r)}{\Delta'(k_r)}k_re^{2ik_ra}\\
&-e_Q^{s,1}+e_Q^{s,1}\sum_{r=-2}^{\infty}\frac{E(k_r)}{k_r\Delta'(k_r)}e^{2ik_ra}-i\beta e_Q^{s,2}\sum_{r=-2}^{\infty}\frac{k_r^3\tanh(k_rh)}{\Delta'(k_r)}(1+e^{2ik_ra}),\\
I_0^{s'''} &= \frac{2a}{\beta}(1-s_u^s)\sum_{r=-2}^{\infty}\frac{E(k_r)}{k_r\Delta'(k_r)}j_0(k_ra)e^{ik_ra}+2aK\sum_{r=-2}^{\infty}\frac{k_r^3}{\Delta'(k_r)}j_0(k_ra)e^{ik_ra}\\
&-e_u^{s,2}-e_u^{s,2}\sum_{r=-2}^{\infty}\frac{E(k_r)}{k_r\Delta'(k_r)}e^{2ik_ra}-ie_u^{s,1}\sum_{r=-2}^{\infty}\frac{E(k_r)}{\Delta'(k_r)}(1-e^{2ik_ra}),\\
I_1^{s'''} &= -\frac{2a}{\beta}s_P^s\sum_{r=-2}^{\infty}\frac{E(k_r)}{k_r\Delta'(k_r)}j_0(k_ra)e^{ik_ra}+\sum_{r=-2}^{\infty}\frac{E(k_r)}{\Delta'(k_r)}k_re^{2ik_ra}\\
&-e_P^{s,2}-ie_P^{s,1}\sum_{r=-2}^{\infty}\frac{E(k_r)}{\Delta'(k_r)}(1-e^{2ik_ra})-e_P^{s,2}\sum_{r=-2}^{\infty}\frac{E(k_r)}{k_r\Delta'(k_r)}e^{2ik_ra},\\
I_2^{s'''} &= -\frac{2a}{\beta}s_P^s\sum_{r=-2}^{\infty}\frac{E(k_r)}{k_r\Delta'(k_r)}j_0(k_ra)e^{ik_ra}+i\sum_{r=-2}^{\infty}\frac{E(k_r)}{\Delta'(k_r)}k_r^2(1-e^{2ik_ra})\\
&-e_Q^{s,2}-ie_Q^{s,1}\sum_{r=-2}^{\infty}\frac{E(k_r)}{\Delta'(k_r)}(1-e^{2ik_ra})-e_Q^{s,2}\sum_{r=-2}^{\infty}\frac{E(k_r)}{k_r\Delta'(k_r)}e^{2ik_ra},
\end{aligned}
\tag{C.2.2}
$$

after calculating the residue of the pole at zero in some of these integrals.

Now the nine integrals of the antisymmetric problem will be turned into infinite sums over the dispersion roots using the same principles as before. Therefore, starting from the integrals found in equations (5.3.46), (5.3.47), then

$$\tilde{I}_0^a = \frac{1}{3} - 2ia\sum_{r=-2}^{\infty}\frac{K-(1-s_u^a)k_r\tanh(k_rh)}{\Delta'(k_r)}j_1(k_ra)h_1^{(1)}(k_ra),$$

$$\tilde{I}_1^a = 2\beta\sum_{r=-2}^{\infty}\frac{k_r\tanh(k_rh)}{\Delta'(k_r)}\big(e_P^{a,2}-k_r^2\big)j_1(k_ra)e^{ik_ra},$$

$$\tilde{I}_2^a = 2ias_Q^a\sum_{r=-2}^{\infty}\frac{k_r\tanh(k_rh)}{\Delta'(k_r)}j_1(k_ra)h_1^{(1)}(k_ra)$$
$$-2i\sum_{r=-2}^{\infty}\frac{E(k_r)}{k_r\Delta'(k_r)}j_1(k_ra)e^{ik_ra}+2\beta e_Q^{a,2}\sum_{r=-2}^{\infty}\frac{k_r\tanh(k_rh)}{\Delta'(k_r)}j_1(k_ra)e^{ik_ra},$$

$$I_0^{a''} = -2a\sum_{r=-2}^{\infty}\frac{K-(1-s_u^a)k_r\tanh(k_rh)}{\Delta'(k_r)}k_r^2j_1(k_ra)e^{ik_ra},$$

$$I_1^{a''} = -i\sum_{r=-2}^{\infty}\frac{\big(\beta e_P^{a,2}k_r^2+1-K\delta\big)k_r\tanh(k_rh)-K}{\Delta'(k_r)}(1-e^{2ik_ra}),$$

$$I_2^{a''} = -2as_Q^a\sum_{r=-2}^{\infty}\frac{k_r^3\tanh(k_rh)}{\Delta'(k_r)}j_1(k_ra)e^{ik_ra}+\sum_{r=-2}^{\infty}\frac{E(k_r)}{\Delta'(k_r)}k_re^{2ik_ra}$$
$$-i\beta e_Q^{a,2}\sum_{r=-2}^{\infty}\frac{k_r^3\tanh(k_rh)}{\Delta'(k_r)}(1-e^{2ik_ra}),$$

$$I_0^{a'''} = -\frac{2ia}{\beta}(1-s_u^a)\sum_{r=-2}^{\infty}\frac{E(k_r)}{k_r\Delta'(k_r)}j_1(k_ra)e^{ik_ra}-2iaK\sum_{r=-2}^{\infty}\frac{k_r^3}{\Delta'(k_r)}j_1(k_ra)e^{ik_ra},$$

$$I_1^{a'''} = e_P^{a,2}\sum_{r=-2}^{\infty}\frac{E(k_r)}{k_r\Delta'(k_r)}e^{2ik_ra}-e_P^{a,2}-\sum_{r=-2}^{\infty}\frac{E(k_r)}{\Delta'(k_r)}k_re^{2ik_ra},$$

$$I_2^{a'''} = i\sum_{r=-2}^{\infty}\frac{E(k_r)}{\Delta'(k_r)}k_r^2(1+e^{2ik_ra})+e_Q^{a,2}\sum_{r=-2}^{\infty}\frac{E(k_r)}{k_r\Delta'(k_r)}e^{2ik_ra}$$
$$-e_Q^{a,2}+\frac{2ia}{\beta}s_Q^a\sum_{r=-2}^{\infty}\frac{E(k_r)}{k_r\Delta'(k_r)}j_1(k_ra)e^{ik_ra}. \tag{C.2.3}$$

Bibliography

[1] A. Maurel, J.-J. Marigo, P. Cobelli, P. Petitjeans, and V. Pagneux. Revisiting the anisotropy of metamaterials for water waves. *Physical Review B*, 96(13):134310, 2017.

[2] W. E. Rogers, J. Thomson, H. H. Shen, M. J. Doble, P. Wadhams, and S. Cheng. Dissipation of wind waves by pancake and frazil ice in the autumn beaufort sea. *Journal of Geophysical Research: Oceans*, 121, 10 2016.

[3] M. H. Meylan, L. G. Bennetts, J. E. M. Mosig, W. E. Rogers, M. J. Doble, and M. A. Peter. Dispersion relations, power laws, and energy loss for waves in the marginal ice zone. *Journal of Geophysical Research: Oceans*, 123, 03 2018.

[4] D. Schurig, J. J. Mock, B. J. Justice, S. A. Cummer, J. B. Pendry, A. F. Starr, and D. R. Smith. Metamaterial electromagnetic cloak at microwave frequencies. *Science*, 314(5801):977–980, 2006.

[5] T. Ergin, N. Stenger, P. Brenner, J. B. Pendry, and M. Wegener. Three-dimensional invisibility cloak at optical wavelengths. *Science*, 328(5976):337–339, 2010.

[6] M. J. A. Smith, R. C. McPhedran, C. G. Poulton, and Meylan M. H. Negative refraction and dispersion phenomena in platonic clusters. *Waves in Random and Complex Media*, 22(4):435–458, 2012.

[7] M. Farhat, S. Enoch, S. Guenneau, and A. B. Movchan. Broadband cylindrical acoustic cloak for linear surface waves in a fluid. *Physical Review letters*, 101(13):134501, 2008.

[8] J. B. Pendry. Negative refraction makes a perfect lens. *Physical Review Letters*, 85(18):3966, 2000.

[9] J. B. Pendry, D. Schurig, and D. R. Smith. Controlling electromagnetic fields. *Science*, 312(5781):1780–1782, 2006.

[10] N. Jiménez, W. Huang, V. Romero-García, V. Pagneux, and J.-P. Groby. Ultra-thin metamaterial for perfect and quasi-omnidirectional sound absorption. *Applied Physics Letters*, 109(12):121902, 2016.

[11] R. Porter. Plate arrays as a perfectly-transmitting negative-refraction metamaterial. *Wave Motion*, 100:102673, 2021.

[12] M. Farhat, S. Guenneau, S. Enoch, and A. Movchan. All-angle-negative-refraction and ultra-refraction for liquid surface waves in 2d phononic crystals. *J. Comput. Appl. Math.*, 234(6):2011–2019, 7 2010.

[13] C. P. Berraquero, A. Maurel, P. Petitjeans, and V. Pagneux. Experimental realization of a water-wave metamaterial shifter. *Phys. Rev. E*, 88:051002, 11 2013.

[14] H. Lamb. *Hydrodynamics*. University Press, 1924.

[15] J. J. Stoker. *Water waves: The mathematical theory with applications*, volume 36. John Wiley & Sons, 2011.

[16] A. Maurel, K. Pham, and J.-J. Marigo. Scattering of gravity waves by a periodically structured ridge of finite extent. *Journal of Fluid Mechanics*, 871:350–376, 07 2019.

[17] S. A. Cummer and D. Schurig. One path to acoustic cloaking. *New Journal of Physics*, 9(3):45, 2007.

[18] T. R. Neil, Z. Shen, D. Robert, B. W. Drinkwater, and M. W. Holderied. Moth wings are acoustic metamaterials. *Proceedings of the National Academy of Sciences*, 117(49):31134–31141, 2020.

[19] K. Donda, Y. Zhu, S.-W. Fan, L. Cao, Y. Li, and B. Assouar. Extreme low-frequency ultrathin acoustic absorbing metasurface. *Applied Physics Letters*, 115(17):173506, 2019.

[20] K.-J. Chang, J. Jung, H.-G. Kim, D. R. Choi, and S. Wang. An application of acoustic metamaterial for reducing noise transfer through car body panels. *SAE Technical Papers*, 06 2018.

[21] A. U. Jan and R. Porter. Transmission and absorption in a waveguide with a metamaterial cavity. *The Journal of the Acoustical Society of America*, 144:3172–3180, 12 2018.

[22] S. Zheng, R. Porter, and D. Greaves. Wave scattering by an array of metamaterial cylinders. *Journal of Fluid Mechanics*, 903, 08 2020.

[23] A. T. Chwang and A. T. Chan. Interaction between porous media and wave motion. *Annual Review of Fluid Mechanics*, 30:53–84, 11 2003.

[24] X. Garnaud and C. C. Mei. Wave-power extraction by a compact array of buoys. *Journal of Fluid Mechanics*, 635:389 – 413, 09 2009.

[25] J. N. Hunt. Viscous damping of waves over an inclined bed in a channel of finite width. *La Houille Blanche*, 7:836–842, 12 1952.

[26] C. C. Mei. *The applied dynamics of ocean surface waves*, volume 1. World scientific, 1989.

[27] S. W. Rienstra and A. Hirschberg. An introduction to acoustics. *Eindhoven University of Technology*, page 19, 01 2003.

[28] H. Lamb. *The dynamical theory of sound*. E. Arnold, 1910.

[29] V. A. Squire. Ocean wave interactions with sea ice: A reappraisal. *Annual Review of Fluid Mechanics*, 52, 01 2020.

[30] J. J. Stoker. Surface waves in water of variable depth. *Quarterly of Applied Mathematics*, 5:1–54, 1947.

[31] A. E. Heins. Water waves over a channel of finite depth with a dock. *American Journal of Mathematics*, 70:730–48, 1948.

[32] K. O. Friedrichs and H. Lewy. The dock problem. *Communications on Pure and Applied Mathematics*, 1(2):135–148, 1948.

[33] R. L. Holford. Short surface waves in the presence of a finite dock. i. *Mathematical Proceedings of the Cambridge Philosophical Society*, 60(4):957–983, 1964.

[34] R. L. Holford. Short surface waves in the presence of a finite dock. ii. *Mathematical Proceedings of the Cambridge Philosophical Society*, 60(4):985–1012, 1964.

[35] C. M. Linton. The finite dock problem. *Zeitschrift für angewandte Mathematik und Physik*, 52, 03 2000.

[36] R. Porter. Surface wave interaction with rigid plates lying on water. *Wave Motion*, 66, 06 2016.

[37] A. G. Greenhill. Wave motion in hydrodynamics. *American Journal of Mathematics*, pages 62–96, 1886.

[38] K. F. Graff. *Wave Motion in Elastic Solids*. Dover Books on Physics Series. Dover Publications, 1991.

[39] H. Chung and C. Fox. Calculation of wave-ice interaction using the wiener-hopf technique. *New Zealand Journal of Mathematics [electronic only]*, 31, 01 2002.

[40] H. Chung and C. M. Linton. Reflection and transmission of waves across a gap between two semi-infinite elastic plates on water. *Quarterly Journal of Mechanics and Applied Mathematics*, 58:1–15, 02 2005.

[41] R. Porter. Trapping of waves by thin floating ice floes. *The Quarterly Journal of Mechanics and Applied Mathematics*, 09 2018.

[42] V. A. Squire and T. W. Dixon. An analytic model for wave propagation across a crack in an ice sheet. *International Journal of Offshore and Polar Engineering*, 10, 09 2000.

[43] T. D. Williams and V. A. Squire. Wave propagation across an oblique crack in an ice sheet. In *The Twelfth International Offshore and Polar Engineering Conference*, volume 12, pages 157–162. OnePetro, 09 2002.

[44] H. Chung and C. Fox. Propagation of flexural waves at the interface between floating plates. *International Journal of Offshore and Polar Engineering*, 12, 08 2002.

[45] D. V. Evans and T. V. Davies. Wave-ice interaction. Technical report, Stevens Institute of Technology Hoboken NJ Davidson Lab, 1968.

[46] D. V. Evans and R. Porter. Wave scattering by narrow cracks in ice sheets floating on water of finite depth. *Journal of Fluid Mechanics*, 484:143 – 165, 06 2003.

[47] D. J. Griffiths and C. A. Steinke. Waves in locally periodic media. *Am. J. Phys.*, 69:137–154, 02 2001.

[48] P. Markos and C. M. Soukoulis. *Wave propagation*. Princeton University Press, 2008.

[49] P. G. Chamberlain and D. Porter. Decomposition methods for wave scattering by topography with application to ripple beds. *Wave Motion*, 22(2):201–214, 1995.

[50] R. Porter and D. Porter. Scattered and free waves over periodic beds. *Journal of Fluid Mechanics*, 483:129–163, 2003.

[51] P. A. Martin. N masses on an infinite string and related one-dimensional scattering problems. *Wave Motion*, 51(2):296–307, 2014.

[52] R. Porter and D. V. Evans. Scattering of flexural waves by multiple narrow cracks in ice sheets floating on water. *Wave Motion*, 43(5):425–443, 2006.

[53] Liu A. K., B. Holt, and P. W. Vachon. Wave propagation in the marginal ice zone: Model predictions and comparisons with buoy and synthetic aperture radar data. *Journal of Geophysical Research*, 96:4605–4621, 1991.

[54] R. Wang and H. H. Shen. Gravity waves propagating into an ice-covered ocean: A viscoelastic model. *Journal of Geophysical Research*, 115, 06 2010.

[55] W. E. Rogers and M. D. Orzech. Implementation and testing of ice and mud source functions in wavewatch iii. Technical report, Naval Research Lab Stennis, 05 2013.

[56] G. K. Batchelor. *An introduction to fluid dynamics*. Cambridge University Press, 2000.

[57] F. Ursell. The long-wave paradox in the theory of gravity waves. *Mathematical Proceedings of the Cambridge Philosophical Society*, 49(4):685–694, 1953.

[58] A. Zareei and M.-R. Alam. Cloaking in shallow-water waves via nonlinear medium transformation. *Journal of Fluid Mechanics*, 778:273–287, 09 2015.

[59] X. Hu and C. T. Chan. Refraction of water waves by periodic cylinder arrays. *Physical Review Letters*, 95:154501, 11 2005.

[60] Z. Wang, P. Zhang, X. Nie, and Y. Zhang. Focusing of liquid surface waves by gradient index lens. *EPL (Europhysics Letters)*, 108(2):24003, 10 2014.

[61] G. Dupont, O. Kimmoun, B. Molin, S. Guenneau, and S. Enoch. Numerical and experimental study of an invisibility carpet in a water channel. *Physical Review. E, Statistical, nonlinear, and soft matter physics*, 91:023010, 02 2015.

[62] T. Iida and M. Kashiwagi. Negative refraction of deep water waves through water channel network. *Journal of Hydrodynamics*, 31:1–8, 01 2019.

[63] A. Ourir, Y. Gao, A. Maurel, and J.-J. Marigo. *Homogenization of thin and thick metamaterials and applications*, pages 149–165. 04 2017.

[64] J.-J. Marigo and A. Maurel. Second order homogenization of subwavelength stratified media including finite size effect. *SIAM Journal on Applied Mathematics*, 77:721–743, 03 2017.

[65] R. Porter. Plate arrays as a water wave metamaterial. In *33rd International Workshop on Water Waves and Floating Bodies, Guidel-Plages, France*, pages 1–4, 2018.

[66] D. Porter and D. S. G. Stirling. *Integral equations: a practical treatment, from spectral theory to applications*, volume 5. Cambridge University Press, 1990.

[67] C. C. Mei and B. Vernescu. *Homogenization methods for multiscale mechanics*. World scientific, 2010.

[68] M. McIver. Diffraction of water waves by a moored, horizontal, flat plate. *Journal of Engineering Mathematics*, 19(4):297–319, 1985.

[69] C. M. Linton and P. McIver. *Handbook of mathematical techniques for wave/structure interactions*. Chapman and Hall/CRC, 2001.

[70] P. McIver. The dispersion relation and eigenfunction expansions for water waves in a porous structure. *Journal of Engineering Mathematics*, 34(3):319–334, 1998.

[71] T. D. C. Williams. *Reflections on Ice: The Scattering of Flexural-Gravity Waves by Irregularities in Arctic and Antarctic Ice Sheets*. PhD thesis, University of Otago, 01 2005.

[72] R. Porter. Complementary methods and bounds in linear water waves. *PhD. Bristol*, 1995.

[73] C. C. Mei and J. L. Black. Scattering of surface waves by rectangular obstacles in waters of finite depth. *Journal of Fluid Mechanics*, 38(3):499–511, 1969.

[74] D. V. Evans and C. A. N. Morris. Complementary approximations to the solution of a problem in water waves. *IMA Journal of Applied Mathematics*, 10(1):1–9, 1972.

[75] M. Abramowitz and I. A. Stegun. *Handbook of mathematical functions with formulas, graphs, and mathematical tables*, volume 55. US Government Printing Office, 1964.

[76] A. Erdelyi, W. Magnus, F. Oberhettinger, and F. G. Tricomi. *Tables of Integral Transforms: Vol.: 1.* McGraw-Hill Book Company, Incorporated, 1954.

[77] G. B. Whitham. *Linear and nonlinear waves*, volume 42. John Wiley & Sons, 2011.

[78] R. Porter. An extended linear shallow-water equation. *Journal of Fluid Mechanics*, 876:413–427, 10 2019.

[79] H. Chen, J. Yang, J. Zi, and C. T. Chan. Transformation media for linear liquid surface waves. *EPL (Europhysics Letters)*, 85:24004, 02 2009.

[80] R. Porter. Cloaking in water waves. In *World Scientific Handbook of Metamaterials and Plasmonics: Volume 2: Elastic, Acoustic, and Seismic Metamaterials*, pages 387–425. World Scientific, 2018.

[81] C. Marangos and R. Porter. Shallow water theory for structured bathymetry. *Proceedings of the Royal Society A: Mathematical and Physical Sciences*, 477(2254), 2021.

[82] R. Porter and D. V. Evans. Analysis of the effect of a rectangular cavity resonator on acoustic wave transmission in a waveguide. *Journal of Sound and Vibration*, 408:138–153, 11 2017.

[83] K. L. Tsakmakidis, A. D. Boardman, and O. Hess. Trapped rainbow storage of light in metamaterials. *Nature*, 450:397–401, 12 2007.

[84] J. Zhu, Y. Chen, X. Zhu, F. J. Garcia-Vidal, X. Yin, W. Zhang, and X. Zhang. Acoustic rainbow trapping. *Scientific Reports*, 3:1728, 04 2013.

[85] Z. Tian and L. Yu. Rainbow trapping of ultrasonic guided waves in chirped phononic crystal plates. *Scientific Reports*, 7:40004, 01 2017.

[86] C. Fox and H. Chung. Green's function for forcing of a thin floating plate. Technical report, Department of Mathematics, The University of Auckland, New Zealand, 1999.

[87] G. Kirchhoff. Über das gleichgewicht und die bewegung einer elastischen scheibe. *Journal für die reine und angewandte Mathematik (Crelles Journal)*, 1850(40):51 – 88, 1850.

[88] S. Howison. *Lubrication theory for fluids*, page 263–284. Cambridge Texts in Applied Mathematics. 2005.

[89] J. N. Newman. Propagation of water waves past long two-dimensional obstacles. *Journal of Fluid Mechanics*, 23(1):23–29, 1965.

[90] G. A. Kriegsmann. Scattering matrix analysis of a photonic fabry–perot resonator. *Wave Motion*, 37:43–61, 2003.

[91] M. Meylan and V. A. Squire. The response of ice floes to ocean waves. *Journal of Geophysical Research: Oceans*, 99(C1):891–900, 1994.

[92] M. J. Doble, G. D. Carolis, M. H. Meylan, J.-R. Bidlot, and P. Wadhams. Relating wave attenuation to pancake ice thickness, using field measurements and model results. *Geophysical Research Letters*, 42:4473–4481, 05 2015.

[93] P. Wadhams, V. A. Squire, D. J. Goodman, A. M. Cowan, and S. C. Moore. The attenuation rates of ocean waves in the marginal ice zone. *Journal of Geophysical Research: Oceans*, 93(C6):6799–6818, 1988.

[94] S. Cheng, W. E. Rogers, J. Thomson, M. Smith, M. J. Doble, P. Wadhams, A. L. Kohout, B. Lund, O. P. G. Persson, C. O. Collins, S. F. Ackley, F. Montiel, and H. H. Shen. Calibrating a viscoelastic sea ice model for wave propagation in the arctic fall marginal ice zone. *Journal of Geophysical Research: Oceans*, 10 2017.

[95] J. W. Brown and R. V. Churchill. *Complex variables and applications*. McGraw-Hill Book Company, 2009.

[96] J. B. Lawrie. Orthogonality relations for fluid-structural waves in a three-dimensional, rectangular duct with flexible walls. *Proceedings of the Royal Society A: Mathematical, Physical and Engineering Sciences*, 465(2108):2347–2367, 2009.

[97] F. Xu and D. Q. Lu. Wave scattering by a thin elastic plate floating on a two-layer fluid. *International Journal of Engineering Science*, 48(9):809–819, 2010.

[98] R. Mondal and T. Sahoo. Wave structure interaction problems for two-layer fluids in three dimensions. *Wave Motion*, 49(5):501–524, 2012.